A thesis submitted for the degree of Doctor of Philosophy

The Surface Structure and Growth of Natural Zeolites

by

Manisha Mistry

University College London

2005

Davy Faraday Research Laboratory,
The Royal Institution of Great Britain.

Centre for Theoretical and Computational Chemistry,
Department of Chemistry, University College London

ProQuest LLC
789 East Eisenhower Parkway
P.O. Box 1346
Ann Arbor, MI 48106-1346

ABSTRACT

A systematic study has been carried out in order to investigate two aspects of zeolite chemistry: to determine the external surface structure and to establish the mechanism of crystal growth. The natural zeolite edingtonite (EDI) was chosen as a model material and the surface structures were studied by finding the most stable termination for each face. For each of the four morphologically important faces the surface structure was found to minimise the number of broken bonds created upon cleaving the surface.

In the absence of experimental data, the crystal morphologies were used as a proxy indicator of relative growth rate of different faces. Qualitative inspection indicates that only the equilibrium morphology is able to reproduce the habit of the natural crystal. However, quantitative analysis with the crystal habit observed in SEM images reveals a discrepancy in aspect ratios. By predicting the crystal morphology by using a newly proposed, less demanding method of calculating the number of broken bonds upon cleaving the surface per surface area (N_{BB}/SA), one is able to accurately reproduce the crystal morphology with the correct aspect ratio.

The utility of the N_{BB}/SA method has been tested for a sample of zeolites, results show the N_{BB}/SA technique has correctly predicted the growth rate and crystal habit of merlinoite, analcime, natrolite, and zeolite A. The test on thomsonite was able to reproduce the correct order of stability for each face, however the aspect ratios were not precisely predicted.

By the use of atomistic and *ab-initio* methods, this research has also investigated the growth mechanism of EDI. The total and condensation energies of a range of possible solution fragments have been calculated and the most stable cluster along with the mechanism of formation has been suggested. The energetics of clusters along with the surface structural analysis has shown strong evidence that characteristic building units control the growth and aggregation of EDI, which dictates the extended crystal *structure* and the rate at which these building units condense onto the surface determines the crystal *shape*.

To Sandip

an exceptional person who has inspired me to believe that goals can be achieved by reaching beyond material concepts

ACKNOWLEDGEMENTS

I would firstly like to thank my supervisor Ben Slater for his encouragement, enthusiasm and guidance throughout my PhD. I would also like to acknowledge my secondary supervisors: Dewi Lewis for useful conversations, and C. Richard. A. Catlow for the opportunity to work at The Royal Institution of Great Britain. I am also grateful to Matt Johnson for his help with SEM experiments.

Personal thanks to my parents, Ramanbhai and Laxmiben Mistry, for their endless support, and giving me the opportunity to always achieve my goals. I am very grateful to my sister Mala Mistry, for her assistance with exhausting tasks. . I would also like to thank my fiancé Sandip Vekaria, who has always given me unparalleled strength and encouragement throughout the past four years.

Finally I would like to thank my friends Iman Saadoune, Dinah Parker, Ilona Franklin, Naseem Ramsahye, Donna Arnold, Dave Plant, David Coombes, Martin Foster, Dan Wilson and Misbah Sarwar, who have made working at the RI an unforgettable experience; and other close friends Sarah Harper, Lin Yan Liu and Sarah Choudhury.

TABLE OF CONTENTS

CHAPTER FOUR

CHAPTER FIVE

CHAPTER SIX

LIST OF FIGURES

LIST OF TABLES

CONVENTION

Throughout this thesis the following colour code has been used to represent atoms, unless otherwise stated.

Silicon

Aluminium

Oxygen

Hydrogen

Barium

CHAPTER ONE:

INTRODUCTION

1.0 OBJECTIVES

This thesis concerns the study of a class of microporous materials known as zeolites. Zeolites are of huge interest as a result of their structural diversity and their implementation in many 20th century industrial applications, for example, millions of tonnes are used each year in detergents to remove calcium from water by ion exchange. Zeolites are also widely used to catalyse the cracking process of long chain hydrocarbons in the petrochemical industry; and perform well as molecular sieves, for example to separate branched and chain hydrocarbons.

Many of the zeolites used within industrial applications are synthetically produced; this has inspired scientists to invest time into uncovering the mechanism of zeolite synthesis. By understanding zeolite growth new synthetic methods can be adopted to create new types of stable zeolite frameworks,[1-3] or adjustments in current methods may be used to modify current zeolites to increase their functionality.[4,5]

A recent review by Cundy and Cox[6] illustrates the wealth of research carried out in the area of zeolite synthesis, their paper discusses how the nature of hydrothermal synthesis has progressed from the early work by Barrer[7-9] and Milton[10] on the synthesis of zeolites A, B, and C, to recent studies, which show how the advances in structure determination and the characterisation of products and reaction mixtures give a greater insight into the nature of zeolite synthesis compositions. These studies have formed a significant part of zeolite chemistry, with the long term goal of understanding the mechanism by which zeolites form, such that crystals with specific channel and pore sizes can be engineered to be utilised within catalysis, ion exchange and molecular sieving roles in industrial applications.

The above examples are associated with the bulk zeolite structure, however the external surface also plays an important role in the functionality of the zeolite, for example by determining the size of cations or molecules allowed to enter or leave the zeolite framework. Recent studies have shown evidence that acid sites on the external surface structure can be used to break down branched alkanes which are too bulky to enter the bulk crystal.[11,12] There is very little known about the geometry of the external surface area, and since the importance of the external surface on influencing industrial processes has come to light, it has become essential to understand their structural and chemical properties.

The main objective of this study is to use simulation techniques to systematically model the external surfaces of zeolites, the structure of which have received rather less attention than the internal surface area. By finding suitable methods we are able to look at two different aspects of surface chemistry: (i) the prediction and characterisation of the surface structure, and (ii) obtain insight into the fundamental crystal growth processes. Both of these objectives challenge experiment and hence the role of simulation is to provide complementary and new information to this highly topical area of research.

The determination of the surface structure using computer modelling methods gives the structure and characteristics of the terminating surface to an atomic scale, for instance the distribution of aluminium and silicon on the exposed surface may be deduced. An insight into the surface structure can also help decipher what the principal clusters or units from which the material under examination could be constructed from and how they may react with the surface during growth to form the crystal. As we show in chapter 4, looking at the ratio of surface stability between morphologically important faces can in turn explain the relative growth rate of crystal faces, and by using the Wulff construction the morphology of the crystal can be visualised and compared to laboratory or synthetic samples. Understanding the surface structure and composition will be beneficial to experimentalists since it will provide valuable data, to make sense of ambiguous atomic force microscopy and electron microscopy scans. An example of how theoretical and experimental predictions can complement each other have been shown by the study on the zeolite beta C^{13} and the examination of various medium to large pore zeolites for the industrial application of phenol and acetone synthesis.[14]

In the following sections of this chapter the typical composition and structure of zeolites will be defined. The subsequent section will also describe why the structure of zeolites make them an ideal tool for industrial applications (*e.g.* catalysis, ion exchange), and also show specific examples of the role which the zeolite structure plays in chemical reactions within these applications.

1.1 Zeolites

Zeolite minerals were discovered and named in 1756 by Baron Cronstedt, the Swedish mineralogist,[15] the word 'zeolite' is Greek in origin and means 'boiling stones' as natural zeolites vigorously lose water when heated. The loss of water from zeolites leaves void space within the crystal; this allows the crystal to be used to carry out important chemical processes such as ion exchange and molecular sieving. The following section describes the environment in which zeolites are formed.

1.1.1 The geochemistry of natural zeolites

There are two main sources of natural zeolites, they are found in crystals of volcanic origin and in sedimentary and metamorphic rocks. Zeolites of volcanic origin are often formed as fine crystals, they are found lining the cavities and fractures of igneous rocks, in particular basaltic rocks. Volcanic zeolites are found as a mixture of more than one type of zeolite species (such as heulandite and stilbite), which is generally due to the replacement of one type of zeolite species by another, rather than co-crystallisation. Volcanic zeolites are also found dispersed over large areas, as a result they are not economically suitable for industrial purposes.

Larger deposits of zeolites occur as small crystal grains in sediments and metamorphic rocks; aqueous and generally alkaline solutions react with volcanic ash deposited in lakes and oceans, resulting in the formation of zeolites, such as phillipsite and clinoptilolite. Sediment beds which are rich in zeolites can be many hundreds of metres thick with some deposits made up primarily of one zeolite species. Consequently zeolites formed in sediments are used exclusively in commercial operations because

they can be readily extracted from a single mine site, and it is economically viable to obtain in large quantities within one location.

The following section will discuss how zeolites, both natural and synthesised are categorised by their structure.

1.1.2 Classification of zeolites

To date, there are approximately one hundred and forty identified zeolite minerals, both naturally occurring and synthetically produced, each with a unique structure, however they can be divided up into approximately one hundred and thirty different topologies or structural types. Each observed framework topology is given a unique framework code, according to IUPAC, depending on the extended manner in which the tetrahedral unit is interconnected in three dimensions.[16] For example, FAU is the three-letter code given for Linde X, Linde Y, faujasite, LZ-210 and SAPO-37 framework structures. It should be noted that a framework code and a common name (the name of the zeolite) are not the same. The common name describes the composition, whereas the framework code only gives insight into the framework topology and no information is provided into the composition. The structural details such as the bond lengths and angles for the framework components and the distribution of the non-framework species are dependent on the composition.

1.1.3 Structure and composition

The zeolitic group of solids has an intracrystalline microporous structure consisting of well-defined three dimensional structures which form frameworks containing silicon, aluminium and oxygen.[17]

Zeolites are primarily constructed from TO_4 tetrahedra, where T is the central tetrahedral species, *i.e.* $[SiO_4]^{4-}$ and $[AlO_4]^{5-}$ (see Figure 1. 1).

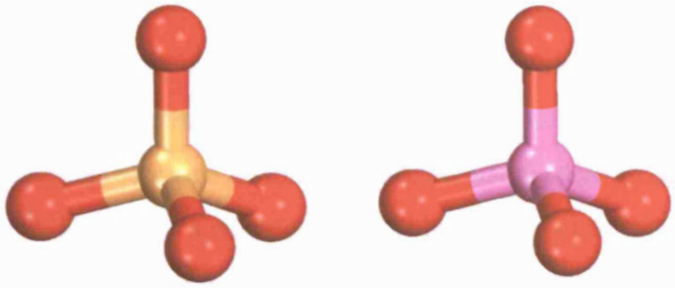

(a) (b)

Figure 1. 1: TO_4 tetrahedra, where T representes either (a) Si or (b) Al

Each apical oxygen atom is shared with an adjacent tetrahedron, thus there are no unshared oxygens on the framework, except where the macromolecule terminates at the external crystal surface and where there are large defects within the solid, in which case a proton may coordinate to the uni-coordinated oxygen atom giving rise to an acid site. Each TO_4 unit is a regular tetrahedron, however the shared oxygen linkage can accommodate a large range of average T-O-T bond angles from 120° to 180°. Each tetrahedron containing an aluminium atom possesses one unit of negative charge since the aluminium atom has a formal charge of +3 and each oxygen atom has a formal charge of –2. In order to maintain electrical neutrality alkali metals or alkali earth cations, such as Na^+, K^+, Ca^{2+}, Sr^{2+}, are present in the pores and channels of the aluminosilicate framework. These cations can be readily substituted which allows zeolites to be utilised as ion exchangers. The general formula of aluminosilicate zeolites can be written as:

$$Me_{x/n}\left[(AlO_2)_x(SiO_2)_y\right] \cdot MH_2O \qquad (1.1)$$

where *Me* is the metal cation and *M, x, y* and *n* are integers. The integer *x* represents the number of aluminium centred tetrahedra, *y* is the number of silicon centred tetrahedra, *M* is the number of water molecules and *n* represents the charge on the cation. The equation above (equation (1. 1)) applies to one unit cell of the of the zeolite structure, where the term in brackets relates to the zeolite framework composition, an example of this stoichiometry is shown by the natural zeolite gismondine which has a unit cell composition of $Ca_4[(AlO_2)_4(SiO_2)_{12}]\ 10H_2O$.

The distributions of Si and Al within the zeolite framework may be determined by Lowenstein's[18] and Dempsey's rules.[19] Lowenstein's rule states that the silicon to aluminium ratio must be greater or equal to one, as a result Al-O-Al bridges are forbidden. However, exceptions to this rule have been seen at high temperature by sodalite materials.[20] Dempsey's rule states that aluminium-aluminium distances will be maximized within a zeolite where the silicon to aluminium ratio is greater than one. In cases where the silicon to aluminium ratio is equal to one Al-O-Si-O-Al linkages would make up the framework. Investigations by Den Ouden *et al.*[21] and Catlow *et al.*[22] have shown and proved that the Al-O-Si-O-Al linkages are stable and help to bind divalent cations within the channels and cavities.

The tetrahedral units within a zeolite are often referred to as primary building units (PBUs), the tetrahedral units bridge together to form an infinite number of complex *nets* (*i.e.* rings and cages) however only a small number of these units are of low potential energy. Meier[23] identified a set of small units formed by a finite number of tetrahedra and defined them as secondary building units (SBUs) (see Figure 1. 2).

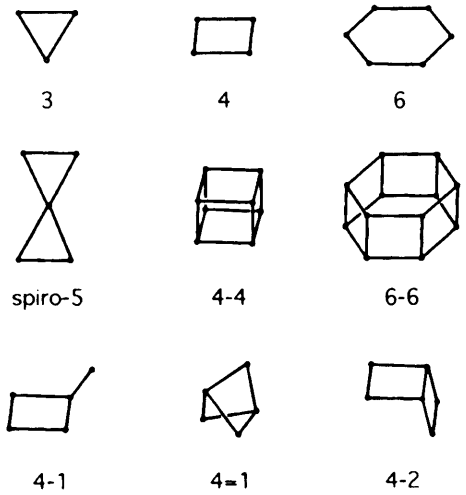

Figure 1. 2: Secondary Building Units. (Reproduced without permission from Atlas of zeolite Framework Types[24])

The purpose of deriving SBUs was to divide zeolites into groups, such that a group consisted of a set of zeolites where the entire zeolite framework could be described by

one type of SBU, for example natrolite is built of the 4=1* SBU, however it was noted that zeolites can also be formed by combinations of SBUs. It should be noted that SBUs are only theoretical topological building units and should not be assumed to be the species which may be in the solution or gel during the crystallisation of the zeolitic material. The identification of oligomeric units in the solution or gel during growth has been investigated with NMR studies by Knight *et al.*[25], this study will be discussed in chapter 6, in which the stability of precursors in solution are examined.

Taking all types of known zeolite structures into account Gottardi[26] proposed a modified set of structural units which consist of both infinite and finite component units, where the infinite units can be a chain or a layer and the finite units contain micropores of regular dimensions (as in Figure 1. 2). Using the modified classification of units the natural zeolites may be classified into six groups (see Figure 1. 3).

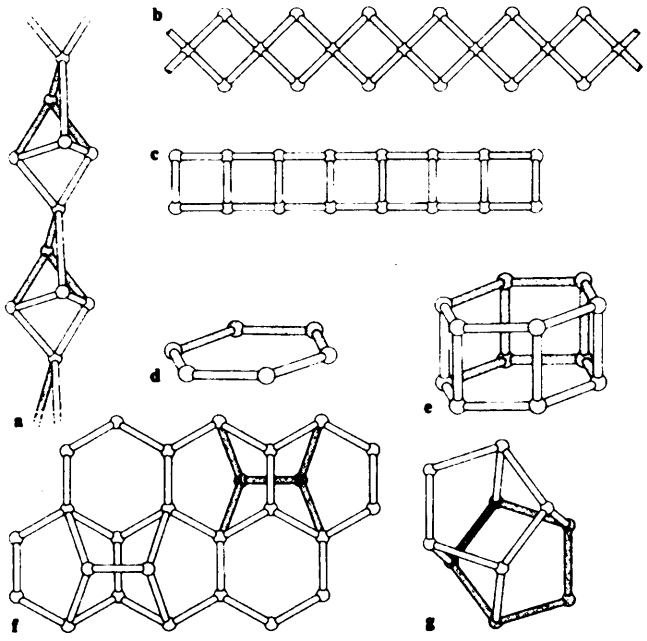

Figure 1. 3: Finite and infinite structural units which maybe used to assemble the zeolite framework: (a) The chain of fibrous zeolites, (b) The singly connected 4-ring chain, (c) The doubly connected 4-ring chain, (d) single 6-ring, (e) double 6-ring, (f) the hexagonal sheet with handles, as in mordenite, (g) The 4-4-1-1 heulandite unit. (Reproduced without permission from Natural Zeolites[27])

* The first number refers to the ring size, the second number denoted the number of other T atoms and the horizontal lines refers to the number of bonds connecting them, thus 4=1 is a 4T ring with two bonds to an additional T atom.

The six groups are: fibrous zeolites, which contain a chain of 4=1 units, zeolites with singly connected four ring chains, zeolites with doubly connected four ring chains, zeolites with 6-ring chains, zeolites of the mordenite group, which consist of a hexagonal sheet with handles and zeolites of the heulandite group which contain a 4-4-1-1 heulandite unit.

As SBUs join together they form channels and cavities which run throughout the zeolite structure, the voids within them are normally polyhedral. Many zeolites can be constructed by stacking one or more type of polyhedron in simple coordination. There are only five different types of polyhedra which stacked with others of the same kind in the same orientation can fill space. These five polyhedra include the 4-4 and 6-6 SBUs (as shown in Figure 1. 2), and two kinds of dodecahedron and one type of truncated octahedron (14-hedron), as shown in Figure 1. 4.

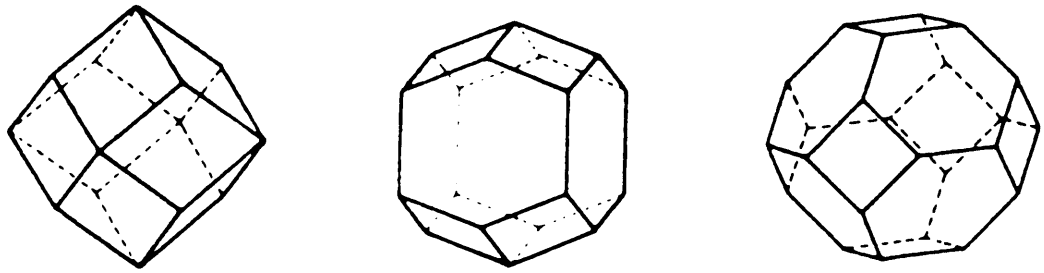

(a) (b) (c)

Figure 1. 4: Space filling polyhedra, (a) and (b) dodecahedron, (c) truncated octahedron. (Reproduced without permission from Barrer[28])

Entry into the void space within the zeolite is restricted by size of the windows on the surface of the crystal or by the window size of the polyhedra, the size of the window is determined by the number of T and oxygen atoms in the ring which defines them. For example the 14-hedron is found in sodalite and faujasite, the 14-hedron is stacked in 8-fold coordination with respect to other 14-hedron by sharing each of its 6-ring windows. The free diameter within the cavitiy is approximately 6.6Å, however access into the void is determined by the 6-ring windows which have a free diameter of ~2.3Å.

Figure 1. 5: Window sizes

Figure 1. 5 illustrates the windows which range from ~4Å for 8-membered ring structures such as zeolite A and ZK-4 (LTA), rho (RHO) and ZK-5 (KFI), through to 10.2Å for 18-membered ring structures such as VPI-5 (VFI).

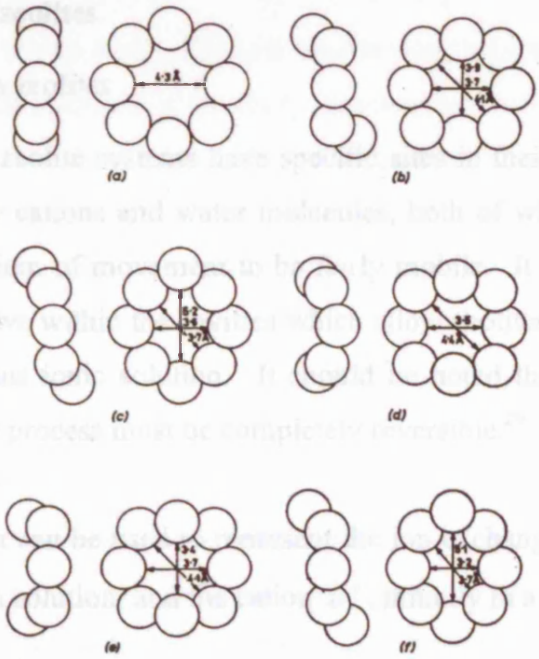

Figure 1. 6: 8-ring conformations for hydrated forms of (a) zeolite A, (b) chabazite, (c) erionite, (d) a hypothetical cubic zeolite, (e) gmelinite, and (f) levynite. (Reproduced without permission from Barrer[28])

The windows of the internal and external surface of the crystal vary in shape and dimension as a result of their ability to vary the T-O-T tetrahedral angle. For example, Figure 1. 6 illustrates how an eight membered ring window may change dimension as a

result of distortions in the T-O-T angle. A change in shape of the ring from planar, as in zeolite A, to boat and chair-shaped, as in chabazite and gmelinite respectively, this change shows a distinct alteration in the shape of the window from circular to elliptical.

The porosity of the crystal framework ensures the easy mobility of both the cations in ion exchangers, water molecules and of other guest species such as small organic molecules, *e.g.* methane. Additions and removals of guest molecules can be fully reversible, and so zeolites may be excellent sorbents of gases, vapors and liquids. The molecular dimensions of the intracrystalline channels and windows is selective of the character of the molecule or cation which may pass through, thus molecules that are too large or the wrong shape are unable to enter the zeolite, while smaller molecules of the right shape, can be copiously sorbed. Zeolites are therefore often termed molecular sieves.

1.2 Applications of zeolites

1.2.1 Ion exchange in zeolites

The crystal lattices of zeolite systems have specific sites in their channels and cavities which are occupied by cations and water molecules, both of which are loosely bound and have enough freedom of movement to be fairly mobile. It is these molecules and ions that are free to move within the cavities which allow zeolites to ion exchange when immersed in an aqueous ionic solution. It should be noted that for ion exchange to occur the ion exchange process must be completely reversible.[29]

The following equation can be used to represent the ion exchange equilibrium between a cation A^x, initially in solution, and the cation B^y, initially in a zeolite:

$$yA^x + x\underline{B^y} \Leftrightarrow y\underline{A^x} + xB^y \qquad (1.2)$$

Where x, y are the valences of the cations, and the underlined cations are within the zeolite structure.[30] Thus for a uni-univalent exchange one cation within the zeolite structure is replaced by another cation of same charge, whereas for a uni-divalent exchange one doubly charged cation is replaced by two singly charged cations.

The time taken for ion exchange to reach equilibrium is dependent upon the zeolite, for example, in open structured zeolites with low density, equilibrium for uni-univalent exchanges can be reached in roughly one week; whereas for ions with higher valences *i.e.* uni-divalent exchanges or even uni-univalent exchanges in more dense zeolites ion exchange can take months to reach completion.

The degree of cation exchange within zeolites is controlled by both the structure and energy barriers between channels: the size of the cavity and channel windows determines which ions are allowed to enter and leave the cavity. The relative sizes of the competing ions in their solvated states both inside and outside the zeolite play a large role in determining which ions are able to take part in ion exchange. The concentration of ions in the external solution together with the presence (or absence) of ligands other than water molecules effect the availability of ions in solution able to take part in ion exchange.

The binding energy of cation sites within the zeolite host can also affect the ease of ion exchange of a cation; for example, if the energy barrier for a cation to leave a cavity site within the zeolite is too large it is less likely to take part in ion exchange, however if the energy barrier is small, ion exchange would take place readily. The thermal conditions at which ion exchange takes place can influence the rate of reaction, at a high temperature all water molecules and ions would have more kinetic energy which would facilitate in crossing high energy barriers for moving in and out of the crystal.

The ion exchange properties of zeolites are used for a number of industrial applications, mainly since they have the advantage of being both environmentally friendly and cheap. A dominant industrial use of Na zeolite A and maximum aluminium zeolite P (also know as MAP) are as builders* in laundry detergents. There are approximately 800,000 tons per annum of zeolite A manufactured for this purpose alone.

Using zeolite A as an ingredient of laundry detergents meets two important requirements with respect to its ion exchange ability. As generally known the detergency in soft water is better than in hard water since there are less calcium deposits

* Detergent builders are chemical compounds that are added to a detergent product to improve its cleaning properties.

on textile fibres. Thus Zeolite A meets the first requirement of being able to strongly reduce the concentration of calcium ions by exchanging the calcium ions in hard water with sodium ions from within the zeolite without support by any other additives. The selectivity of calcium ions during ion exchange is so high that the equilibrium is reached after only one minute.[31,32]

A second requirement is the dissolution of calcium containing precipitate, which occurs after almost all the calcium hardness is removed from water. The dissolution process is considerably slower than the water softening process. Zeolite A alone does not have a very high rate of dissolution compared to citrate. Citrate is a water soluble complexing agent which works directly on adsorbing calcium precipitates. The addition of 10% citrate to 90% zeolite A gives almost the same values as citrate alone, which is very important when considering the time limited washing process.[33]

In the mid nineties Unilever developed MAP as the new zeolite detergent, MAP is a better builder than zeolite A for modern detergent products since it exchanges both calcium and magnesium more rapidly than zeolite A, particularly at low temperatures. The stability of sensitive components such as bleach is enhanced in the presence of MAP compared to zeolite A. These advantages arise as a result of the unusually flexible framework of MAP.[34,35]

Other applications of zeolites as ion exchangers include the use of clinoptilolite and chabazite for the treatment of mixed metal contaminated effluents.[36-38] Waste water from industries which manufacture fertiliser and animal feed will often contain high concentrations of ammonia, such that nitrification would be too costly. Clinoptilolite has been found to recover ammonia efficiently even in the presence of competing ions.[39-42]

1.2.2 Bulk catalysis

Zeolite based catalysts were primarily investigated for applications within the petrochemical industry and have been used as catalysts since the early 1960s. The interest in zeolite catalysts grew when it was discovered that rare earth zeolites are efficient catalytic cracking agents of petrochemicals. Cracking is the term used to

describe the process which breaks up large hydrocarbon molecules such as naphtha into smaller more useful hydrocarbon molecules, *e.g.* ethane which can be used for making plastic. The Mobil Company were the first to introduce cracking catalysts based on zeolite Y commercially, it was found that zeolite Y gave less coking, increased production capacity and improved gasoline yields by as much as 25% compared to silica-alumina catalysts.[43] A recent review by Corma[44] discusses the achievements made within the area of zeolite catalysis and also the challenges which the future of this field faces.

The advantages that zeolite catalysts have over silica alumina catalyst are two fold: they possess strong acidity and they are size selective. A Brønsted acid site is created on either the internal or external surface of a zeolite, when a Si atom is substituted by a trivalent metal, *i.e.* either an aluminium or a transition metal ion (in the case of metal substituted zeolites). Subsequently a negative charge is created within the lattice, which can be charge compensated by a proton. The proton is bonded to the bridging oxygen between the Si and the trivalent atom, see Figure 1. 7. The bridging hydroxyl group possesses strong Brønsted acid properties, and the O-Al-O bridges display Lewis base properties.[45]

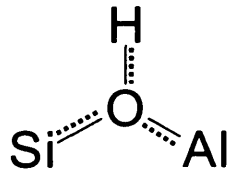

Figure 1. 7: A fully bridged oxygen with a bonded proton.

It can be assumed that the acid strength of the zeolite is based upon the total number of Brønsted sites, which in turn is dependent upon the number of framework Al^{3+} atoms. However it is recognised that all the acid sites in samples with high alumina content do not have the same strength, the acid strength is dependent on the number of aluminium atoms in nearest neighbour positions. A completely isolated aluminium tetrahedron with no aluminium nearest neighbours has the strongest type of framework Brønsted acid site. In practice, a reaction demanding low acidities are catalyzed using zeolites with low Si to Al ratios, whereas reactions requiring high acidic strength are catalyzed

with zeolites containing high Si to Al ratios, *i.e.* zeolites possessing isolated framework Al atoms.[46]

Zeolites are size and shape selective, as discussed in section 1.1.3 the structure of zeolites expose windows on the surface of the crystal which are the entrance to channels and pores. During a reaction, the well defined pore window dimensions are able to discriminate between reactants and products by size and shape, thus only molecules smaller than the pore window dimension will be allowed to enter the crystal. The window sizes of channels and cavities give the zeolite structure molecular sieving capability. Since acid sites are present throughout the molecular cage structure it can be used to simultaneously sieve and catalyse reactants.

A practical example of zeolites as selective catalysts is the use of medium sized zeolites with pore diameters in the range of 0.45–0.56nm (for example zeolite A type catalysts) for selective cracking of *n*-paraffins with respect to their branched isomers. Only the linear chains can enter the crystals and reach the acid sites, where as branched chain or cycloparaffins or aromatics are too bulky to enter the crystal. It follows that only the *n*-paraffins are selectively cracked while the other hydrocarbons are left unchanged.[47] The importance and influence of shape selectivity of zeolite catalysts during molecular sieving has been clearly examined in a paper by Degnan.[48]

The catalytic and size selective property of zeolites are well characterised within the bulk, the next section will give examples of how the external surface can also be exploited.

1.2.3 Surface catalytic processes

To date there has been relatively little work on the properties of zeolite external surfaces in comparison to the extensive research towards the properties of the bulk crystal and internal surface structure of zeolites. The internal surface area of zeolite crystals is of the order of several hundred square metres per gram whereas the typical external surface area is no more than 10 square metres per gram (for crystal approximately 1micrometer in size), however with the advent of membrane engineering and the tendency towards nanoscale fabrication processes, the ratio of internal and external

surface area is decreased. As a result the significance of understanding how the external surface influences industrial applications is of greater importance. Arguably, the significance of the external surface on catalytic activity and selectivity was not fully appreciated until a revolutionary paper was published in 1984 by Gilson and Derouane.[49] They demonstrated that the conversion of 1,3,5-trimethylbenzene, which is too bulky to enter the internal pores of medium sized zeolites (*e.g.* ZSM-5) is a suitable reaction to probe the outer surface activity of pentasil, and probably other medium sized zeolites.

To date three distinct catalytic surface mediated processes have been established, they are pore mouth selectivity, key-lock selectivity and the nest effect. Recent work by J.A. Martens and co-workers have shown that hydrocracking, isomerisation and monomethyl-branching of *n*-paraffin mixtures using Pt/ZSM-22 show evidence of both pore mouth and key-lock catalysis.[11,12,50] Hydrocracking differs from the conventional cracking process by utilising both hydrogen gas and a catalyst during the cracking process. Isomerisation is the process of converting a compound into an isomer of itself. Mono-methyl branching is the process of adding methyl branches onto the *n*-alkane carbon chain, skeletal branching of long alkane molecules leads to improved quality of diesel, aviation fuel and lubricating oils by altering properties such as the freezing point and the viscosity.

1.2.3.1 Pore mouth catalysis

The zeolite ZSM-22 has a TON structure, the 10-membered ring family has very narrow, parallel pores. In the case of monomethyl-branching, the formation of the branching in the carbon chain is catalysed by an acid site located at the entrance of the pore, where there is slightly more space than deeper in the pore. As a result the methyl side chain is formed on the part of the molecule located in the pore mouth, while the straight chain part of the molecule is positioned deeper into the pore. Figure 1. 8 illustrates where the long chain alkane sits within the pore mouth and the position where the methyl chain would attach. Methyl-branching of n-alkanes, where n ranges from 8 to 24 all show that the preferential site for methyl branching is at the C_2 position.[12] This type of monomethyl-branching is an example of 'pore mouth' catalysis.

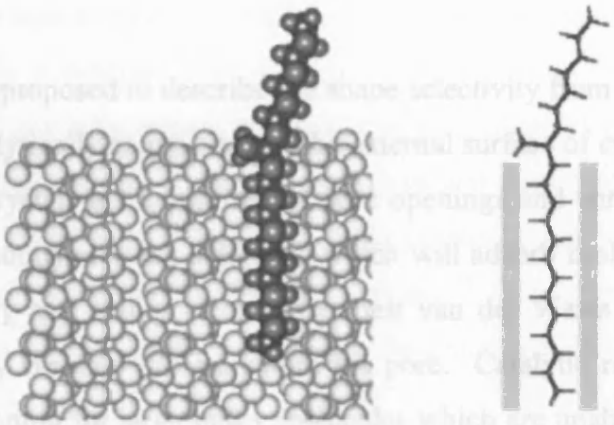

Figure 1. 8: Pore mouth catalysis (Reproduced without permission from Claude *et al.*[11])

1.2.3.2 Key-lock catalysis

In the case of longer alkyl chains, key-lock catalysis occurs, this mechanism involves the adsorption of *n*-alkanes onto the external zeolite surface. Both ends of the alkyl chain adsorbs on to adjacent pore mouths, this physisorption process 'locks' the hydrocarbon chain onto the external surface which then leads on to side chain branching at the pore mouth, see Figure 1. 9. The study by Claude *et al.*[11] on methyl branching of alkane chains, ranging from 8 to 24 carbons, have shown that branching occurs preferentially at roughly the centre of the chain, *i.e.* positions C_5-C_{12}.

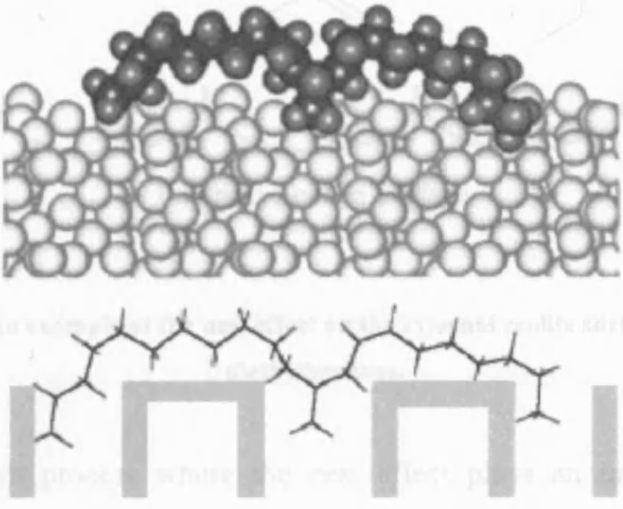

Figure 1. 9: Key lock catalysis (Reproduced without permission from Claude *et al.*[11])

1.2.3.3 Nest effect

The nest effect was proposed to describe the shape selectivity from the presence of non-shape selective catalytically active sites on the external surface of crystals. The external surface of zeolite crystals are composed of pore openings and cut channels, decorated with high concentrations of weak acid sites which will adsorb molecules depending on their stereochemistry and ability to optimise their van der Waals interaction with the framework, *i.e.* they are able to *nest* within the pore. Catalytic reactions *via* the nest effect are more common for large bulky molecules which are unable to diffuse into the zeolite due to steric constraints.

Experimental observations of the nest effect have been reported by Ducarme *et al.*[51] for the alkylation of aromatics over ZSM-5 type catalysts, the reaction was proposed to be activated by the catalytic site located in the half cavity on the external surface (see Figure 1. 10).

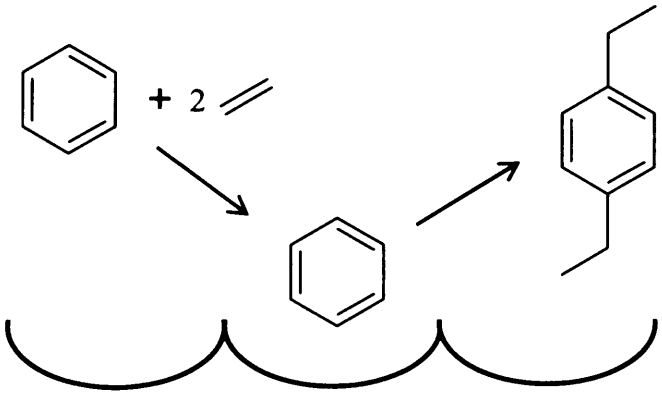

Figure 1. 10: An example of the nest effect on the external zeolite surface to produce diethylbenzene.

Another well known process where the nest effect plays an important role is the production of cumene (isopropylbenzene) and ethylbenzene by the alkylation of benzene over the solid acid catalyst MCM-22 (MWW). Cumene is an important chemical intermediate mainly used for the production of phenol and acetone.

MWW has a higher selectivity for propylene conversion compared to other larger pore zeolites, for example mordenite, USY (FAU), and zeolite beta (BEA).[52] The MWW structure consists of two independent pore systems, both of which have 10-member ring apertures. One system consists of large super cages and the other by sinusoidal pores parallel to the (010) plane. Initial theoretical studies computed very high energy barriers for cumene diffusion in the 10-membered ring pores.[14] These findings predicted that there would be little or no activity for cumene synthesis, this was incongruent to that found experimentally.

The inconsistency between experimental and theoretical results was clarified by the investigation of how these crystals grow and the analysis of the MWW crystal morphology. It was discovered that this crystal form as thin lamellae with a considerable amount of external surface area. The surface is composed of hemi-supercages resulting from the truncation of the supercages at the surface. Subsequent computation and experimental studies have provided evidence that the reaction occurs on the surface without any diffusion barriers but do possess shape selectivity.[14,53]

REFERENCES

1 A. Corma, M. T. Navarro, F. Rey and S. Valencia. *Chem. Commun.*, 1720 (2001)

2 W. T. A. Harrison, T. E. Gier and G. D. Stucky. *Zeolites* **13**, 242 (1993)

3 M. E. Leonowicz and D. E. W. Vaughan. *Nature* **329**, 819 (1987)

4 Y. Xu, H. D. Liu, J. H. Zhu, Z. Y. Yun, J. H. Xu, Y. Cao and Y. L. Wei. *New J. Chem.* **28**, 244 (2004)

5 C. T. O'Connor, K. P. Moller and H. Manstein. *Cattech* **5**, 172 (2001)

6 C. S. Cundy and P. A. Cox. *Chem. Rev.* **103**, 663 (2003)

7 R. M. Barrer. *J. Chem. Soc.*, 127 (1948)

8 R. M. Barrer, L. Hinds and E. A. White. *J. Chem. Soc.*, 1466 (1953)

9 R. M. Barrer and C. J. Marcilly. *J. Chem. Soc. A*, 2735 (1970)

10 R. M. Milton. *ACS Symp. Ser.* **1**, 398 (1989)

11 M. C. Claude and J. A. Martens. *J. Catal.* **190**, 39 (2000)

12 J. A. Martens, G. Vanbutsele, P. A. Jacobs, J. Denayer, R. Ocakoglu, G. Baron, J. A. M. Arroyo, J. Thybaut and G. B. Marin. *Catal. Today* **65**, 111 (2001)

13 B. Slater, C. R. A. Catlow, Z. Liu, T. Ohsuna, O. Terasaki and M. A. Camblor. *Angew. Chem.-Int. Edit.* **41**, 1235 (2002)

14 C. Perego, S. Amarilli, R. Millini, G. Bellussi, G. Girotti and G. Terzoni. *Microporous Mater.* **6**, 395 (1996)

15 A. F. Cronstedt. *Akad. Handl. Stockholm* **120**, 18 (1756)

16 R. M. Barrer. *Pure Appl. Chem.* **51**, 1091 (1979)

17 D. W. Breck. *Journal of Chemical Education* **41**, 679 (1964)

18 W. Lowenstein. *American Mineralogist* **39**, 92 (1854)

19 E. Dempsey, G. H. Kuhl and D. H. Olson. *Journal of Physical Chemistry* **73**, 387 (1969)

20 S. E. Tarling, P. Barnes and J. Klinowski. *Acta Crystallogr. Sect. B-Struct. Commun.* **44**, 128 (1988)

21 C. J. J. Den Ouden, R. A. Jackson, C. R. A. Catlow and M. F. M. Post. *Journal of Physical Chemistry* **94**, 5286 (1990)

22 C. R. A. Catlow, A. R. George and C. M. Freeman. *Chem. Commun.*, 1311 (1996)

23 W. M. Meier. in *Molecular sieves* 10 (Society of Chemistry Industry, London, 1968).

24 C. Baerlocher, W. M. Meier and D. H. Olson. *Atlas of zeolite framework types* (Elsevier, 2001)

25 C. T. G. Knight and S. D. Kinrade. *J. Phys. Chem. B* **106**, 3329 (2002)

26 G. Gottardi. in *Natural zeolites* (eds. L. B. Sand and F. A. Mumpton) 31 (Pergamon, Oxford, 1978).

27 G. Gottardi and E. Galli. *Natural zeolites* (Springer-Verlag, 1985)

28 R. M. Barrer. *Zeolites and clay minerals as sorbents and molecular sieves.* (Academic Press, London, 1978)

29 Marinsky. *Ion exchange* (Marcel Dekker, 1992)

30 A. Dyer. *An introduction to zeolites molecular sieves, chapter 6* (John Wiley & Sons, Chichester, 1988)

31 H. G. Smolka and M. J. Schwuger. *Coll Polym Sci* **256**, 270 (1978)

32 M. J. Schwuger and H. G. Smolka. *Coll Polym Sci* **254**, 1062 (1976)

33 C. P. Kurzendorfer, M. Liphard, W. von Rybinshi and M. J. Schwuger. *Coll Polym Sci* **265**, 542 (1987)

34 C. J. Adams, A. Araya, S. W. Carr, A. P. Chapple, K. R. Franklin, P. Graham, A. R. Minihan, T. J. Osinga and J. A. Stuart. in *Progress in zeolite and microporous materials, pts a-c* 1667 (1997).

35 E. V. Borgstedt, H. S. Sherry and J. P. Slobogin. in *Progress in zeolite and microporous materials, pts a-c* 1659 (1997).

36 S. Kesraoulouki, C. Cheeseman and R. Perry. *Environ. Sci. Technol.* **27**, 1108 (1993)

37 S. Kesraouiouki, C. R. Cheeseman and R. Perry. *J. Chem. Technol. Biotechnol.* **59**, 121 (1994)

38 S. K. Ouki and M. Kavannagh. *Waste Manage. Res.* **15**, 383 (1997)

39 B. W. Mercer, L. L. Ames, C. J. Tovhill, W. J. Slyke and R. B. Dean. *J. Wat. Pollut. Control Fed.* **42**, R95 (1970)

40 S. E. Jorgensen. *Water Research* **9**, 1187 (1975)

41 L. Liberti, G. Boari and R. Passino. *Water Research* **13**, 65 (1979)

42 L. Liberti, G. Boari, D. Petruzzelli and R. Passino. *Water Research* **15**, 337 (1981)

43 C. J. Plank, E. J. Rosinski and W. P. Hawthorne. *Ind. Eng. Chem. Prod. Res. Dev.* **3**, 165 (1964)

44 A. Corma. *J. Catal.* **216**, 298 (2003)

45 J. M. Thomas and W. J. Thomas. *Principles and practice of heterogeneous catalysis* (VCH Verlagsgesellschaft mbH, Germany, Weinheim, 1996)

46 L. A. Pine, P. J. Maher and W. A. Wachter. *J. Catal.* **85**, 466 (1984)

47 P. B. Weisz and V. J. Frilette. *Journal of Physical Chemistry* **64**, 382 (1960)

48 T. F. Degnan. *Journal of Catalysis* **216**, 32 (2003)

49 J. P. Gilson and E. G. Derouane. *J. Catal.* **88**, 538 (1984)

50 J. A. M. Arroyo, G. G. Martens, G. F. Froment, G. B. Marin, P. A. Jacobs and J. A. Martens. *Appl. Catal. A-Gen.* **192**, 9 (2000)

51 V. Ducarme and J. C. Vedrine. *Applied Catalysis* **17**, 175 (1985)

52 R. Millini, G. Perego, J. W. O. Parker, G. Bellussi and L. Carluccio. *Microporous Mater.* **4**, 221 (1995)

53 J. C. Cheng, T. F. Degnan, J. S. Beck, Y. Y. Huang, M. Kalyanaraman, J. A. Kowalski, C. A. Loehr and D. N. Mazzone. in *Science and technology in catalysis 1998* 53 (1999).

CHAPTER TWO:

CRYSTAL GROWTH: AN OVERVIEW OF THEORY AND EXPERIMENTAL TECHNIQUES

2.0 UNDERSTANDING THE CONCEPTS OF CRYSTAL GROWTH

The topic of evolution and growth has been a subject of investigation by many scientists over the course of many decades. The concept of *growth* has been studied over a range of diverse areas, from the spread of a fire through a wheat field to the evolution of common bacteria within living organisms.[1] To date, the field of crystal growth has been considered extensively.[2-4] The research presented in this thesis is concerned with understanding the growth mechanisms of zeolites, by recognising what factors influence the crystal topology or framework type which crystallises out of solution, and the process by which they grow. By uncovering information about crystal growth mechanisms, scientists may be able to engineer new materials with novel properties and applications, and modify existing zeolite crystal morphology, *e.g.* function of membranes to improve catalytic activity (an in-depth account of some applications of zeolites are stated in chapter one of this thesis). Studies by Foster *et al.*[5] have predicted new zeolite structures which may have very desirable properties, but because zeolite synthesis is entirely empirical, one cannot predict a priori what the product of the synthesis will be. By understanding the fundamental stages of growth, one can imagine that scientists would be able to design the porosity and topology of materials.

There are many different theories upon which crystal growth and nucleation may be modelled, such as heterogeneous and homogeneous nucleation, atomistic and continuum growth models. The following sections will briefly cover the process of homogeneous and heterogeneous nucleation, and then concentrate on outlining the atomistic modelling approach to crystal growth.

2.1 Crystal nucleation and growth

The nucleation and growth processes of a crystalline solid from a vapour phase can be described as a two step process. Nucleation describes the initial step, *i.e.* the development of tiny, microscopic particles within the gas phase clustering together to form the basis of a solid phase. The formation of nuclei has a positive free energy, meaning that nucleation is an activated process. If the free energy cost is very large, a huge thermal fluctuation is needed to overcome the barrier and form a microscopic crystal. Such fluctuations are extremely infrequent and may result in a metastable phase. A metastable phase appears to be in equilibrium since its properties do not vary with time, although it is not the true equilibrium phase. Conversely, if the free energy cost of forming a nucleus is not very high, then fluctuations leading to nucleation will occur frequently. The free energy cost of forming a microscopic nucleus of a new phase is important since it determines whether the phase will persist, become metastable, or transform to the equilibrium phase.

Nucleation is followed by the growth stage, which represents the interactions of further vapour phase atoms with the growing surface. Nucleation and growth may be understood in terms of the kinetics of formation; this concept is described within two models: homogeneous and heterogeneous nucleation.

2.1.1 Homogenous nucleation

Homogeneous nucleation is the process of forming a bulk condensed phase from a monoatomic vapour phase, this process initially starts by forming a small cluster with a similar atomic arrangement and density to the bulk condensed phase. The process of homogeneous nucleation may be thought of as a series of bimolecular reactions, where each reaction increases the size of the growing cluster, similar to:

$$\begin{aligned} A_1 + A_1 &\rightarrow A_2 \\ A_2 + A_1 &\rightarrow A_3 \\ &\vdots \\ A_{i-1} + A_1 &\rightarrow A_i \end{aligned} \qquad (2.1)$$

where A_{N+1} is larger than A_N.

The rate of such a process shown by the equations above is established by the concentration of clusters at each size, and the formation of a cluster at a particular size is determined by the energy of formation of the cluster relative to the monomolecular vapour phase. The free energy of formation (ΔG_i) for a cluster of size i may be calculated by summing up the pairwise interactions that occur in the course of bringing the molecules together, however this approach is not practical. In practice, an approximation can be made by assuming that the clusters can be described in terms of macroscopic thermodynamic properties and the total free energy of formation can be expressed as:

$$\Delta G_i = 4\pi r^2 \gamma + \left(\frac{4\pi r^3}{3}\right)\Delta G_v \qquad (2.\ 2)$$

where γ is the surface energy, r is the cluster radius and ΔG_v represents the volume free energy change.

The following equation relates the free energy of formation, ΔG_i, to the equilibrium concentration of clusters of size i (n_i):

$$n_i = n_1 \exp\left(\frac{-\Delta G_i}{kT}\right) \qquad (2.\ 3)$$

The relationship between equilibrium cluster concentration and the cluster size, *i.e.* equation (2. 3), is depicted in Figure 2. 1.

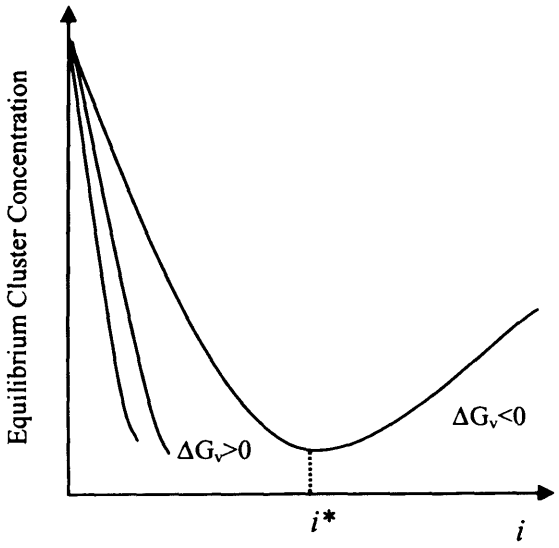

Figure 2. 1: Equilibrium cluster concentration as a function of cluster size, for various values of free energy change associated with condensation.

The graph in Figure 2. 1 shows that when the cluster size, *i*, is small the equilibrium cluster concentration is high, at this point the change in free energy accompanying condensation is positive, *i.e.* $\Delta G_v \geq 0$. As the change in free energy associated to condensation decreases the cluster size, *i*, increases and the equilibrium cluster concentration decrease. When the free energy accompanying condensation is less than zero, *i.e.* when $\Delta G_v < 0$, there is a minimum in the equilibrium cluster concentration and the equilibrium cluster size i^* is reached. As ΔG_v becomes more negative, the clusters continue to grow, *i.e.* *i* will continue to increase, and the concentration of clusters at that size also increases.

To calculate the nucleation frequency, *i.e.* the rate at which a stable growing crystal may form from the cluster concentration, a simple approach known as the Volmer-Weber theory[6,7] may be applied. The Volmer-Weber theory assumes that the equilibrium concentration of clusters of size i^* is maintained at all times, however once the cluster size increases by one unit to i^*+1, it is presumed that the cluster will then grow without limit and become a stable particle. The nucleation rate can be calculated using the expression:

$$J = A^* \omega n_{i^*} \tag{2. 4}$$

where A* is the surface area of the equilibrium cluster, ω is the impingement rate of condensation and n_{i^*} is the equilibrium concentration of clusters size i^* (as above). Although the Volmer-Weber theory is a clear and simple approach to the determination of the nucleation rate it has two limitations. Firstly, the theory assumes that clusters of a few molecules may be described by macroscopic values of surface and volume free energies. Secondly this model does not allow for the depletion of equilibrium sized clusters as they continue to develop into stable growing nuclei.

2.1.2 Heterogeneous nucleation

Heterogeneous nucleation contains two chemically distinct phases, it is a process where a condensed phase is formed on the pre-existing surface of a different substrate. In practice, the formation of a nucleus on a surface results in a substantial reduction of the energy barrier to nucleation (ΔG^*). Heterogeneous nucleation plays an important role in the formation of raindrops and dew. Practical applications include the growth of thin films on substrates of different materials for use in catalysis.

Heterogenous nucleation may be treated in the same manner as homogeneous nucleation. However, the main difference is that the cluster forms on a pre-existing surface as a spherical cap as shown in Figure 2. 2, where the angle θ is the contact angle of the cluster with the substrate.

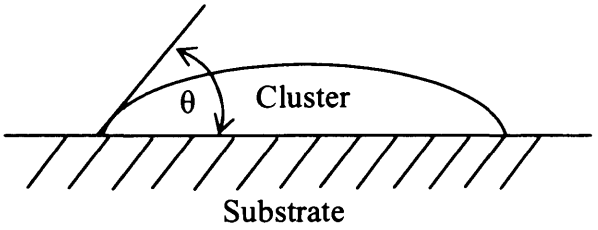

Figure 2. 2: The formation of a small cluster on an existing solid surface, θ is the contact angle. (Reproduced without permission from Hudson[8])

By applying the argument of bimolecular reactions, as in homogenous nucleation, the total free energy of formation of a cluster may be calculated using:

$$\Delta G_i = \left(\frac{4\pi r^3}{3}\right) f(\theta)\Delta G_v + 4\pi r^2 f'(\theta)\gamma_{nv} \tag{2. 5}$$

where $f(\theta) = (2+\cos\theta)(1-\cos\theta)^2/4$, $f'(\theta)$ is the first derivative and γ_{nv} is the surface energy of the cluster. The principle mechanism of cluster growth in heterogeneous nucleation is the addition of units *via* surface diffusion from the adlayer, and thus the nucleation rate may be expressed with the following expression:

$$J = L^* \omega n_{i^*} \tag{2. 6}$$

in which L^* is the perimeter length of the cluster, ω is the surface diffusion related impingement rate and n_{i^*} is the equilibrium concentration of clusters size i^*.

As with homogeneous nucleation, the nucleation rate equation has been tested against experimental data.[8] It has been found that in the case of condensation from slightly concentrated vapour, the results are within the error limits of theoretical predictions. However in the case of thin film growth by deposition from a vapour phase, the agreement is much worse which may be due to the very high concentration of the vapour phase.

The following sections will describe how crystal growth can be modelled atomistically.

2.2 Models of a crystal surface

An important breakthrough was made almost concurrently by Kossel[9] and Stranski[10] in the late 1920s and later by Stranski and Kaischew[11] in the understanding of both equilibrium and growth of ice crystals at low temperatures. The following sections will illustrate how these authors were able to describe complicated ideas of nucleation and growth of a crystal simply by the use of atomistic concepts based solely on the energies of bonds.

Kossel and Stranski were the first to show that crystal sites (described in-depth below), which play an important role during crystal growth, exist when there is an equilibrium

between a surface and the molecules in the vapour. In this state, there is equality between the chemical potential of the surface and the chemical potential of a molecule (or molecules) in the vapour, and an equality between the condensation and evaporation frequencies to or from the same site.

The key sites which play an important role in crystal growth can be differentiated from one another by considering the character of the surface which they are attaching to and the associated energy of attaching a single growth unit. The different characteristics of the surface can be classified as a selection of surface sites: a flat surface site, a stepped site and a kinked site. A flat surface site is on a smooth plane (this is also known as a terrace), a stepped site is located at the point of joining two flat surfaces with a monatomic height difference, and a kinked site is located at the point at which two stepped surfaces are joined perpendicular to one another.

In order to explain these sites we look at ideal surfaces in the form of a simple model known as a *Kossel* crystal. A *Kossel* crystal is based on an ideal crystal, the crystal can be thought of as a bulk crystal made up of a series of cubes held together by pair potentials. Since most pair potentials decay, it can be assumed that the most energy is gained or lost by the formation or breaking of bonds with the first nearest neighbour. If we cleave a *Kossel* crystal along the (001) plane, all seven key sites can be illustrated, see Figure 2. 3.

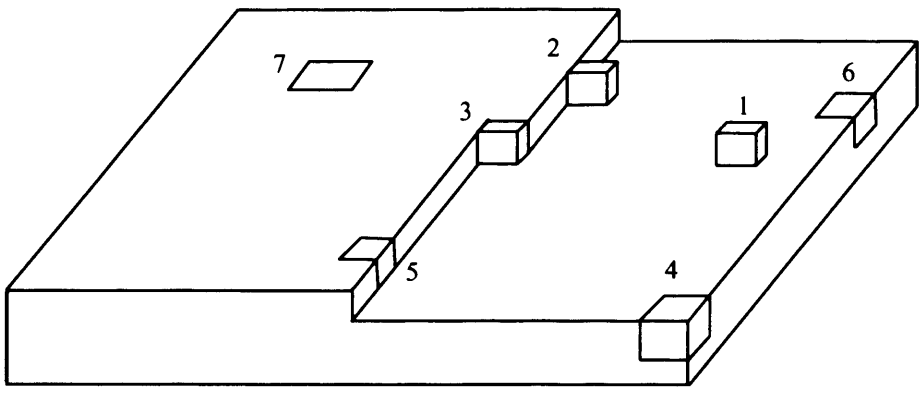

Figure 2. 3: A *Kossel* crystal cleaved along the (001) plane displaying seven key surface sites. (Reproduced without permission from Mutaftschiev[12])

The molecule labelled 1 is most loosely bound to the surface, it is adsorbed onto the flat surface with only one first nearest neighbour interaction. Molecule 2 has been adsorbed along a step with a monomolecular height, and this molecule has two first nearest neighbour interactions. Molecule 3 is in a kink site and has three first nearest neighbour interactions. Molecules 4 also has the equivalent energy as molecule 3, although it is located in a different site (at the edge of a terrace) it still has three first nearest neighbour interactions. Molecule 5, located within a molecular step, and molecule 6, integrated at the edge of two faces, also have the same number of first nearest neighbours, and hence the same energy. Finally the molecule with the strongest binding energy is molecule 7, it is embedded within the surface with five first nearest neighbours. This model is often described as the *terrace-ledge-kink model*, or *TLK* model.

It was later suggested by Burton, Cabrera and Frank[13,14] that three types of surfaces exist: F-type, K-type and faces that are subject to faceting (illustrated in Figure 2. 4).

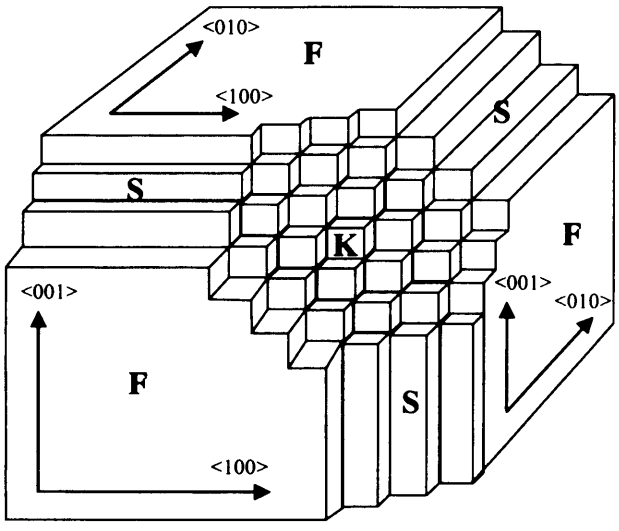

Figure 2. 4: A *Kossel* crystal illustrating the three different face types, F- faces, K- faces and S-faces. (Reproduced without permission from Mutaftschiev[12])

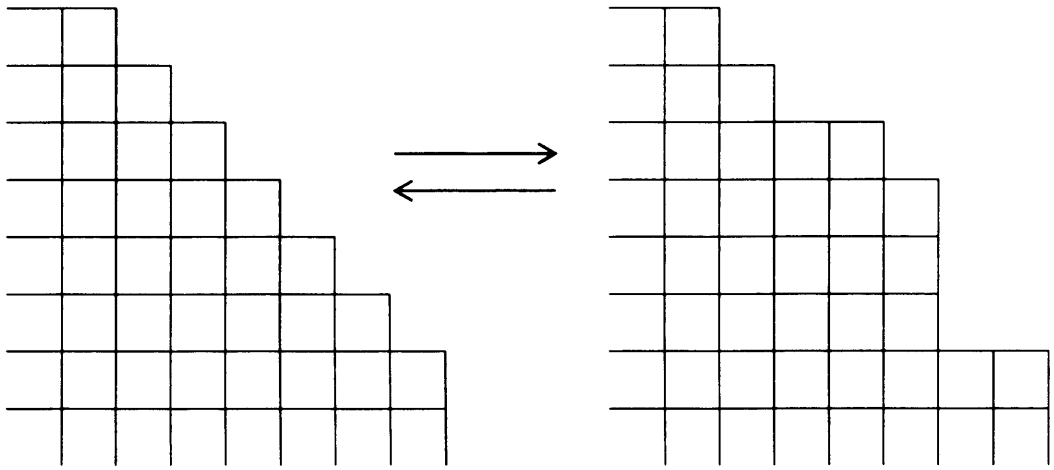

(a) (b)

Figure 2. 5: Two-dimensional model of a K-type face of a *Kossel* crystal

The last category of faces, are those subject to faceting, which is typical of ionic crystals. In this case, the size order of binding energy is the opposite of that in F-type faces:

$$\varphi_{ad} > \varphi_0 > \varphi_{in} \tag{2. 9}$$

In this case the binding energy of a molecule incorporated in the surface is negative, as a result the face breaks spontaneously give rise to large flat facets. It is common to these types of surfaces to change unexpectedly into other types of faces.

For completeness, it is also important to mention stepped faces (S-type faces) whose contour is intermediate between the F- and K-type faces (see Figure 2. 4). In this case if a molecule is adsorbed onto a step, a whole new row of molecules will be adsorbed onto every kink site until a new step is formed, whereas if an incorporated molecule is lost from a step edge, the whole line of molecules will be evaporated leaving no kink sites. As a result, the outline of the face will remain the same, however the steps may be distributed at a range of different heights.

An alternative nomenclature scheme places each of the surfaces into one of three categories: singular, vicinal and rough. F- and K- faces are known as singular surfaces, these surfaces are essentially smooth on an atomic scale, and are usually low index places such as the (110), (100) and (111) planes of cubic crystals. S- faces are often classed as vicinal surfaces. In order to describe a rough surface it would have to be completely disordered on the atomic scale even at very low temperatures. In this case is would not be possible to describe the surface in terms of a *Kossel* crystal or face types. It is easy to see how a connection can be made between a *Kossel* crystal and a rock salt crystal structure. However it can become difficult to describe porous materials, such as zeolites, in terms of the *Kossel* crystal since the definition of a step or kink may be very complicated.

2.2.1 Surface point defects

In real situations the growth of a crystal to macroscopic size will most likely contain some type of imperfections. Crystal faults of different kinds can be introduced by external factors such as impurities present in the mother phase and trapped within the crystal during growth, by thermal stress due to temperature differences or maybe as a result of the mechanism itself.

Surface point defects can be separated into two classes, those which are thermodynamically stable and those which are kinetically stable. Kinetically stable point defects include primary points of dislocation at the surface. Dislocations, such as line defects occur from mismatches in the bulk lattice of the crystal, and present in the bulk of almost all crystalline solids. They are generally present either as closed loops or networks within the crystal, or they terminate on the crystal surface. The orderly arrays of surface atoms are disrupted by these points of termination. There are two types of dislocations, edge dislocations and screw dislocations.

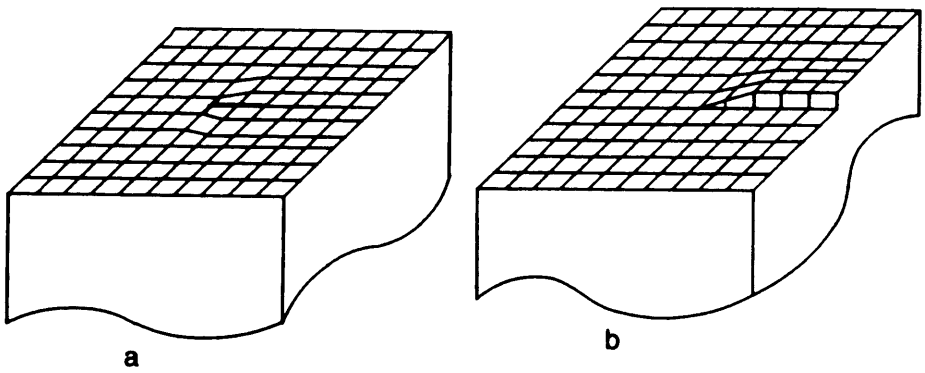

Figure 2. 6: (a) edge dislocation, (b) screw dislocation. (Reproduced without permission from Hudson[8])

The screw dislocation is formed by shearing one half of the crystal lattice with respect to the other half, in a portion of the crystal, (shown by the *Kossel* model in the Figure 2. 6). The occurrence of the screw dislocation creates a step on the surface of the crystal, with one side of the step tied to the point of origin of the screw dislocation. The presence of such defects plays a major role in the growth of crystals from the vapour phase or from the solution phase. A property of this type of defect is that it is continuously regenerated during the growth process since one side of the step is attached to the centre of the crystal which is the starting point of the dislocation.

The edge dislocation is formed by an extra half a plane of atoms in the bulk of the crystal. These sites are important in that they represent a different bonding configuration to normal surface atoms, thus they behave differently in gas-surface interactions. For example, at the point where the dislocation line emerges, it appears to be a preferential site for two-dimensional nucleation.[15]

The second class of surface point defects are thermodynamically stable, these defects are present at equilibrium above 0K. The stability of these defects is a result of the favourable entropy of mixing term related with creating disorder (*i.e.* creating defects) within an initially ideal system. These defects can be equated to the adsorbed molecules, vacancies or interstitial sites found at equilibrium in the bulk of the crystal, as shown by the *Kossel* crystal in Figure 2. 3, and are formed at flat faces, steps, kinks.

The energy of forming a thermodynamically stable defect can be calculated by taking into account the number of nearest neighbours, as described above in the introduction of

the *Kossel* crystal (see section 2.2). However, in general real crystals show that the nearest neighbour argument, although valid, does not produce accurate values for the energy of formation since it neglects the relaxation of the lattice around the defect, and also the effects of the interaction of the second or more distant neighbours with the defect. Nevertheless there are exceptions, for instance zeolites surfaces often undergo a small relaxation, in this case the number of nearest neighbours works well in predicting the thermodynamic stability.[16]

In order to take relaxation into account, both theoretical and experimental methods of investigating surface defects need further development so that the effects of lattice relaxation are taken into account. Well established methods used to minimise the energy around a defect or a cleaved surface are described in chapter 3 (methodology), within results chapter 4, a new simplified model of describing the stability of zeolite surface in terms of the number of broken bonds is proposed and tested in chapter 5.

2.3 Atomistic nature of crystal growth

The atomistic approach to crystal growth processes is focused primarily on the movement of atoms within the crystal and on the surface. In homogeneous and heterogeneous nucleation, where only small quantities of matter are involved, the importance of transportation is negligible. However in crystal growth, the effect of matter migrating across the surface can have a great impact, along with its diffusion length. Another important process which will be discussed is the sticking probability of molecules onto the surface.

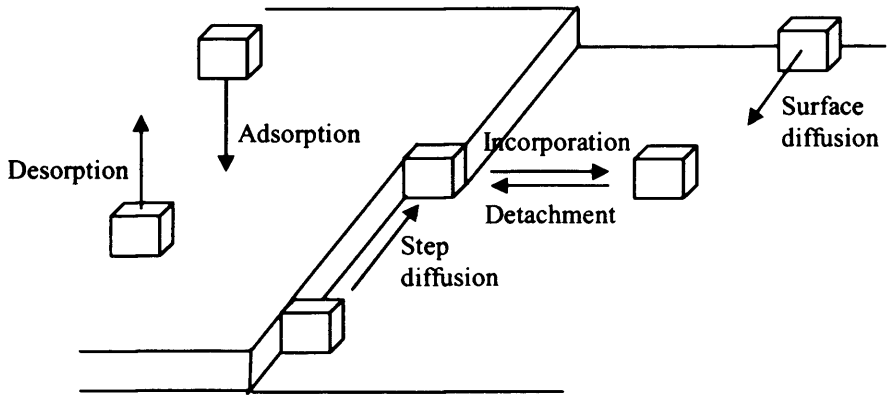

Figure 2. 7: Processes on the surface of an F- face (Reproduced without permission from Mutaftschiev[12])

The sequence of processes which may occur once a molecule in the gaseous phase has hit the surface can be explained via the use of a *Kossel* crystal (TLK model), as shown in Figure 2. 7. Following the impact of a gaseous molecule with the surface, the molecule may take one of two routes; it may be elastically reflected, without any energy transfer and return to the gaseous phase, or it may be captured by the surface after transferring its kinetic energy to the surface molecules. The probability of a gaseous molecule being captured by the surface is often expressed as a ratio of the number of molecules captured to the total number of molecules which have hit the surface; this ratio is often termed as the sticking coefficient. Once adsorbed onto the surface, the molecule can either desorb back into the vapour phase or diffuse to another adsorption site. During its migration along the surface, the adsorbed molecule may visit a number of adsorption sites. Another possible elementary process is the detachment of a molecule from a kink site back onto the surface. When the system is in equilibrium, the rate of detachment is equivalent to the rate of incorporation into a kink site. The flow of molecules into a kink site occurs via surface migration rather than direct exchange between the kink sites and vapour phase. The incorporation and detachment of molecules can also proceed *via* step diffusion. A detailed description of sticking probability, surface migration and surface diffusion is given in Mutaftschiev.[12]

In the context of zeolite crystal growth processes the sticking probability would be expected to change significantly between different zeolites. The zeolite surfaces could vary between a high density of under saturated bonds, and hence large sticking

probability, or a low density of under saturated bonds, and hence a small sticking probability. A study of the crystallisation of zeolite A by Agger *et al.*[16] have shown that there are multiple points of attachment on the (100) surface, and the probability of attaching building units to these sites have been calculated by Monte Carlo simulation.

2.4 Spiral growth model

Metals[17,18], semi-conductors[19] and ceramics[20] have been observed and modelled to grow by the presence of a dislocation, however there are a limited number of studies which show zeolites which grow by a spiral growth mechanism due to the presence of a screw dislocation. Unlike TLK models of growth, where the rate limiting step is the addition of a new growth unit attaching onto a flat surface, spiral growth models omit this step since the addition of new growth units results in the continuous regeneration of new step sites, as described below.

Spiral growth is the progression of growth resulting from the presence of a screw dislocation on the surface of a crystal (as discussed earlier in point 2.2.1). Growth on this type of defect leads to the addition of molecules in a coiled fashion, of which each layer of the coil spreads out from the centre in order to form a new layer. There are two points which hold true with this type of growth regardless of the shape of the crystal. Firstly the growth layer can not spread over the surface further than its radius of curvature, ρ. Secondly, once the critical radius, ρ^*, has been passed, the velocity of growth advances with a velocity approximately equal to that of a straight step.

The manner in which spiral growth occurs can be explained by the (001) face of the *Kossel* crystal which contains a screw dislocation in equilibrium with the vapour phase, see Figure 2. 8.

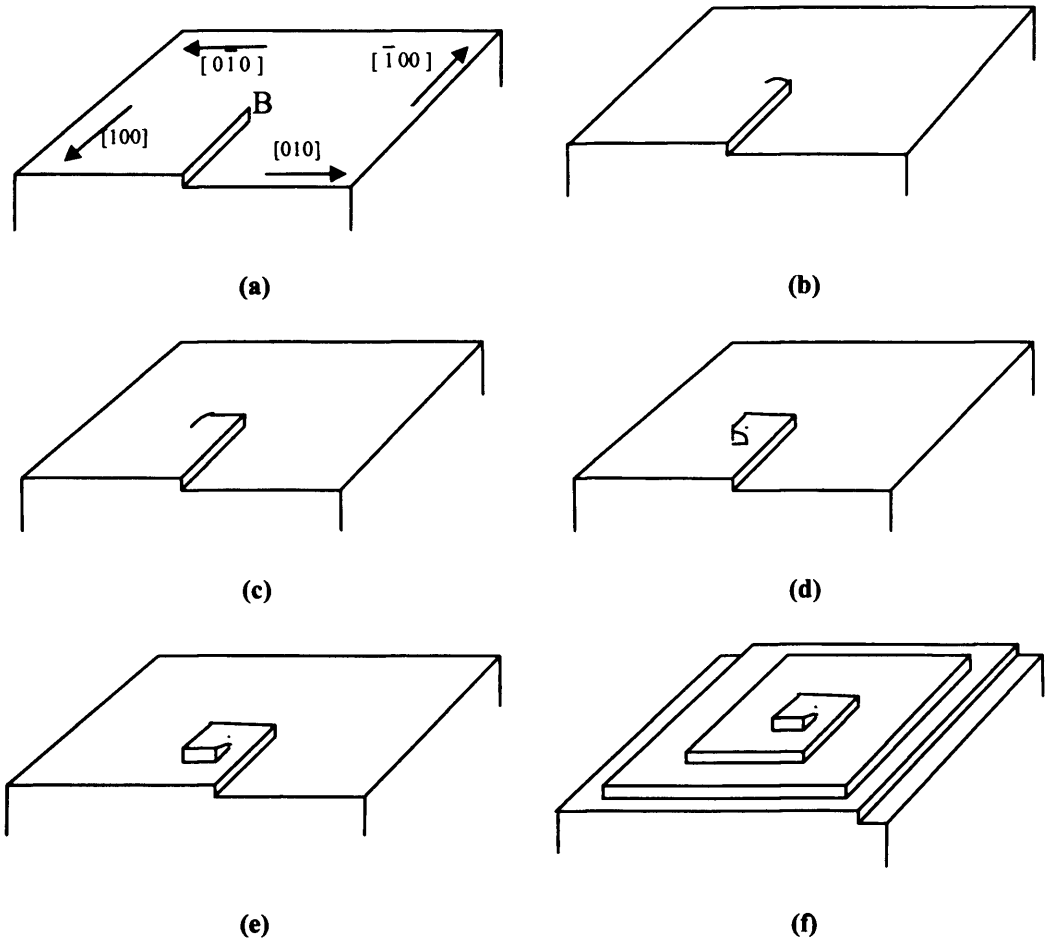

Figure 2. 8(a-f): Successive steps in the growth on a spiral defect. (Reproduced without permission from Mutaftschiev[12])

The surface contains a monomolecular straight step along the [010] orientation (see Figure 2. 8(a)). As growth commences, the step increases parallel to its initial path, however since the spiral is anchored at point B, a new step will start to appear (see Figure 2. 8(b)), this new step is only able to grow once its length reaches the critical radius in the given crystallographic direction. Once the step in the [$\bar{1}$00] direction exceeds $1/2\rho^*$ it starts to advance creating a new [0$\bar{1}$0] step (see Figure 2. 8(c)), this step only starts to advance once it also has reached the length $1/2\rho^*$. When the growing crystal has changed direction four times, a spiral is created as in Figure 2. 8(e), further growth of the spirals then take place. After multiple repetitions of the same cycle, a pyramidal coiled surface is formed (see Figure 2. 8(f)). The effect of an increase in molecules in the vapour phase will lead to the spires turning more rapidly, and the distance between each step decreasing.

An example of spiral growth within zeolites has been investigated by Dumrul *et al.*[21], they used atomic force microscopy to examine the crystal growth surface features on the (100) faces of zeolite A. They observed single, as well as pairs of growth spirals on the vicinal surface of synthetic zeolite A, as shown by the AFM images in Figure 2. 9. Measurements of the distances between single turns of these spirals indicated that spacing between two successive turns increased towards the centre of a spiral. The authors concluded that by observing growth spirals towards the end of the crystallization process of zeolite A indicates a screw dislocation mechanism takes place, although they were unable to speculate on the origin of these dislocations. However, a recent study by Walker *et al.*[22] has simulated screw dislocations on the (100) surface of zeolite A, and have predicted possible sites at which screw dislocations originate.

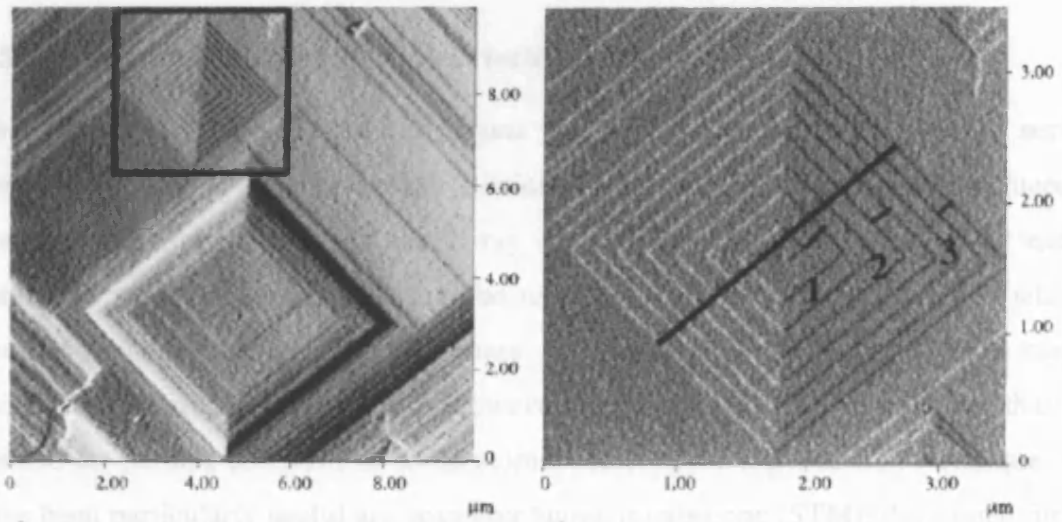

(a) **(b)**

Figure 2. 9: AFM image of a single growth spiral located on the upper layer of vicinal faces of zeolite A, (a) top view of the upper layers (growth spiral is highlighted with a box) (b) zoomed in top view of the growth spiral highlighted in (a). (Reproduced without permission from Dumrul *et al.*[21])

Studies by Binder *et al.*[23] and Yilmaz *et al.*[24] and have also observed evidence of spiral dislocations leading to spiral growth mechanisms within heulandite and ETS-4 respectively.

For further information regarding the theories of growth summarised within this chapter, the reader is directed to a comprehensive article written by Burton *et al*[14], which outlines the derivations of the equations which simulate atomistic crystal growth. Books by Hudson[8], Mutaftschiev[12] and Markov[25] also give an excellent account of the basic concepts of crystal growth and nucleation.

Up to this point, this chapter has described well known theoretical concepts used to model nucleation and growth of crystals, however, with advancements in experimental techniques there many methods which can be used to probe the surfaces of crystal, and gain an insight into how they grow. The remaining part of this chapter will discuss these experimental techniques and show examples of how they have been of use in the study of zeolites.

2.5 Experimental surface analytical techniques

There are many experimental techniques which can be used to analyse the surface composition and growth of a crystal. Particle size and crystallinity are often deduced by scanning electron microscopy and X-ray diffraction. Elemental analysis by energy dispersive x-ray analysis (EDX) may be used to follow the concentrations of silicate, aluminate and oxides in the liquid phase. Information on structural features can be gained by infrared spectroscopy. However there are very few techniques that can resolve the surface composition to an atomic scale. Two experimental techniques that have been particularly useful are scanning tunnel microscope (STM), developed further into atomic force microscopy (AFM) and high resolution transmission electron microscopy (HRTEM).

2.5.1 Scanning tunnelling microscope

Since the creation of the scanning tunnelling microscope (STM) in 1982 it has proven to be useful tool in the field of surface science. The STM was originally intended as a way to learn about the structure, electronic and growth properties of very thin insulating layers.[26] The aim of this work was to invent a method where by the diversity of the surface could be detected on samples no bigger than a few nanometers in size. Reviews of early work carried out using this method have been written by H. Rohrer[27] and R.M.

Feenstra[28]. This method uses a fine metal tip positioned within 1 nm of the surface to be studied and a voltage is applied between the sample and the tip. Under these conditions a small electronic current will flow from tip to sample or *vice versa* due to electronic tunnelling. Scanning the tip over the surface yields a real space image of the surface, where the outer electron density is probed rather than the geometrical surface. This type of imaging can be thought of as macroscopically drawing a pencil over a rough surface. Electronically processed two-dimensional scanning images or line scans can give a clear impression of the roughness and general morphology of a surface right down to atomic dimensions. Typically, the spatial resolution parallel to the surface is approximately 1Å and <0.1Å normal to the surface. A schematic diagram of a typical STM is shown below.

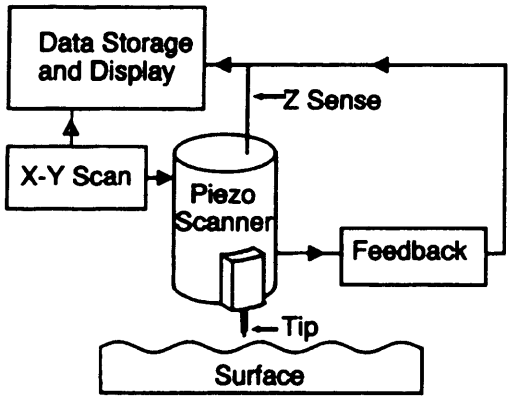

Figure 2. 10: A schematic diagram of a Scanning Tunnelling Microscope (STM) (Reproduced without permission from Husdon[8])

2.5.2 Atomic force microscope

The invention of the STM was quickly followed by the development of a whole family of related techniques.[29] The most important of which is undoubtedly the atomic force microscope (AFM). AFM operates by measuring attractive or repulsive forces between a tip and the sample.[30] In its repulsive contact mode, the instrument lightly touches a tip at the end of the cantilever to the sample. As a raster-scan drags the tip over the sample, a detection apparatus measures the vertical deflection of the cantilever, which indicates the local sample height. In contact mode the AFM measures hard sphere repulsion forces between the tip and the sample. Because the tip is in hard contact with the

surface, the stiffness of the lever needs to be less that the effective spring constant holding atoms together, which is on the order of 1 - 10 nN/nm. A drawback of the contact mode arises when the scans across a sample with a soft area, *i.e.* where the stiffness of the lever is greater than the spring constant, in this case the sample is easily deformed by the tip and a cavity or pit will appear in the AFM image. However, configurations AFM in contact mode with a force resolution of 1nN are able to give high quality scans with a depth resolution of 0.02nm, a typical AFM image is illustrated in Figure 2. 9.

In non-contact mode, the AFM derives topographic images from measurements of attractive forces, in this case the tip does not touch the sample.[31] AFM can achieve a resolution of 0.01nm and unlike electron microscopes it is possible to use this method to image samples in both air and under liquids, the added advantage to the non-contact method compared to the contact method is there is no damage to the surface of the sample.

AFM has been widely used to image the surface structures of a variety of natural zeolites, such as: scolecite, stilbite, faujasite and Heulandite.[32,33] Anderson *et al.*[34] were the first to use AFM to look at the crystal growth of the synthetic zeolite Y (FAU structure) and its hexagonal polymorph EMT. Three important features were observed from the AFM image; firstly the triangular faces of the images are rotated by 60° about (111) from the crystal edges. As the triangular faces enlarge they merge with other growing terraces on the other (111) faces to form the six faces of a truncated octahedron. This type of growth dictates that the crystal will grow in a uniform manner on all the (111) faces. Secondly the orientation of all triangular terraces are the same, this can be accounted for by the threefold symmetry of the faujasite layer as well as to the relationship to the interconnected layers. Lastly, the spacing between the terrace edges decreases towards the edges of the crystal. AFM has also been used to look at the growth mechanism of zeolite A,[16] this study has shown that, like zeolite Y, zeolite A grows by means of a layer mechanism.

2.5.3 Transmission electron microscopy

Transmission electron microscopy (TEM) is another method of direct imaging. TEM is an indispensable tool for material characterization because it is the only technique that provides information on the inner structure of materials, at a high spatial resolution, *i.e.* TEM can resolve objects that are ~0.1 nm apart. In a transmission electron microscope a high-energy electron beam penetrates an extremely thin slice of material to form a transmission image of the samples structure. Since the penetration depth of electrons through a solid material is limited to roughly 2-3nm for conventional TEMs with acceleration voltages below 200 KeV, the maximum thickness of the sample one can study is 1μm. Using high voltage instruments (acceleration voltages up to 3MeV), thicker samples can be investigated.

TEM can be used in a variety of ways to study thin films and overlayers, in experiments of island growth and 3D nucleation, the sample is evaporated onto the alkali halide surfaces prepared by cleavage in ultra high vacuum. Subsequently a deposited carbon film fixes the thin film consisting of more or less coalescent islands. Outside the ultra high vacuum chamber the alkali halide substrate is dissolved from the carbon film by water treatment and the films with the embedded sample clusters and islands are analysed with respect to shape, distribution and number of islands by conventional TEM techniques. More refined preparation techniques are needed to study the crystallographic quality of thin films.

In high-resolution transmission electron micrograph (HRTEM) even the atomic structure of an interface can be resolved. It must be emphasised, however, that the contrast seen in such high-resolution electron micrographs is not directly related to single atoms. Rows of atoms are imaged and an involved theoretical analysis (*i.e.* taking into account details of the electron scattering process) is necessary for a detailed interpretation of the dark and light spots in terms of atom positions. Nevertheless, information about the quality of an interface and in particular about the orientation of the lattice planes can be obtained by simple inspection.

HRTEM has been used as a tool to study the structure of both zeolite Y (FAU type structure) and EMT.[35-37] Terasaki *et al.*[35] was the first to observe the spatially correlated

intergrowths of cubic and hexagonal faujasite, however the material studies were dealuminated in order to improve the stability of the material in the electron microscope and this process may have altered the pores. Other studies include MCM22, MFI, Beta C and LTA, but to date no natural zeolite have been imaged. An example of a HREM image of Beta C is illustrated in Figure 2. 11

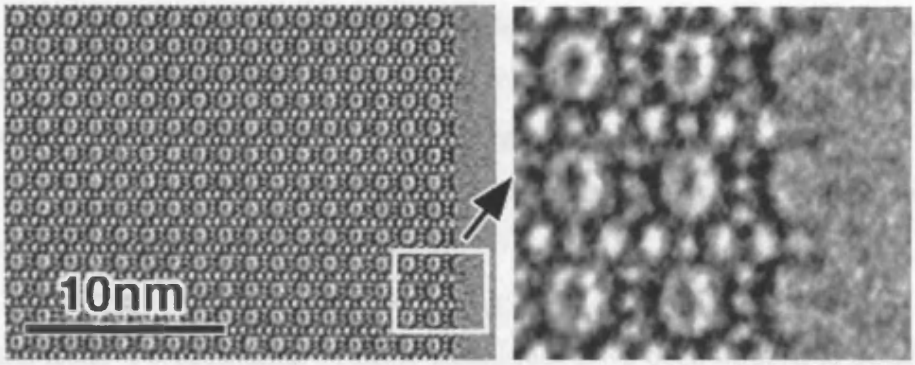

Figure 2. 11: HREM image of Beta C (reproduced without permission from Slater *et al.*[38])

2.5.4 Scanning Electron Microscopy

Scanning electron microscopy (SEM) can provide direct image of film morphology down to dimensions of 10Å in favourable cases. The SEM resolution is determined by the diameter of the electron beam. SEM is usually performed ex situ, *i.e.* films prepared under ultra high vacuum conditions have to be transferred through the atmosphere into the microscope. This may give rise to contamination induced changes to the film structure. Only in special cases is SEM equipment available with ultra high vacuum conditions and transfer units from the preparation chamber. It should also be noted that the SEM picture is produced by secondary electrons, whose emission intensity is affected by a number of factors, such as, geometrical factors *i.e.* type of surface and the inclination of the primary beam, and also by electronic properties of the surface, such as work function and the surface state density. As a result some of the intensity contrast in the image may therefore be related to electronically inhomogeneous areas and not to geometrical inhomogeneities.

2.5.5 Energy Dispersive X-ray Analysis

An energy-dispersive x-ray analyser (EDX) is a common accessory which gives the SEM a very valuable capability for elemental analysis. The electron beam in an SEM has an energy typically between 5,000eV and 20,000eV. The energy holding electrons in atoms (the binding energy) ranges from a few eV up to many kilovolts. As the electron beam hits the sample many of these atomic electrons are dislodged, thus ionising atoms of the specimen. Ejection of an atomic electron by an electron in the beam ionises the atom, which is then quickly neutralised by other electrons. In the neutralisation process an x-ray with an energy characteristic of the parent atom is emitted, and so by collecting and analysing the energy of these x-rays, the constituent elements of the specimen can be determined.

Within this study a combination of SEM techniques have been utilised to determine the morphology of two crystal samples of the natural zeolite edingtonite, along with the EDX methods to determine to composition of the crystals. These results have been presented in chapter 4. AFM experiments have been carried out on the same EDI crystals used in the EDX by Agger,* however since EDI is a very dense material accurate step heights could not be calculated.

REFERENCES

1 T. Halpinhealy and Y. C. Zhang. *Phys. Rep.-Rev. Sec. Phys. Lett.* **254**, 215 (1995)

2 J. Gavillet, J. Thibault, O. Stephan, H. Amara, A. Loiseau, C. Bichara, J. P. Gaspard and F. Ducastelle. *J. Nanosci. Nanotechnol.* **4**, 346 (2004)

3 C. W. Lan. *Chem. Eng. Sci.* **59**, 1437 (2004)

---

* Personal communication.

4 F. Iwasaki and H. Iwasaki. *J. Cryst. Growth* **237**, 820 (2002)

5 M. D. Foster, A. Simperler, R. G. Bell, O. D. Friedrichs, F. A. A. Paz and J. Klinowski. *Nat. Mater.* **3**, 234 (2004)

6 M. Volmer and A. Weber. *Z. Phys. Chem.* **119**, 277 (1926)

7 M. Volmer. *Z. Phys. Chem.* **102**, 267 (1922)

8 J. B. Hudson. *Surface science: An introduction* (John Wiley & Sons Inc., New York, 1992)

9 W. Kossel. *Nachr. Ges. Wiss. Gottingen.*, 135 (1927)

10 I. N. Stranski. *Z. Phys. Chem.* **136**, 259 (1928)

11 I. N. Stranski and R. Kaischew. *Z. Phys. Chem. (B)* **26**, 31 (1934)

12 B. Mutaftschiev. *The atomistic nature of crystal growth* (eds. R. Hull, R. M. Osgood Jr, H. Sakaki and A. Zunger) (Springer-Verlag, Berlin Heidelberg, 2001)

13 W. K. Burton and N. Cabrera. *Disc. Farad. Soc.* **5**, 33 (1949)

14 W. K. Burton, N. Cabrera and F. C. Frank. *Phil. Trans. Roy. Soc. (London) A* **243**, 299 (1951)

15 H. Bethge. *Phys. Stat. Sol. 2* **2**, 755 (1962)

16 J. R. Agger, N. Pervaiz, A. K. Cheetham and M. W. Anderson. *J. Am. Chem. Soc.* **120**, 10754 (1998)

17 S. Ismail-Beigi and T. A. Arias. *Physical Review Letters* **84**, 1499 (2000)

18 L. H. Yang, P. Soderlind and J. A. Moriarty. *Philos. Mag. A-Phys. Condens. Matter Struct. Defect Mech. Prop.* **81**, 1355 (2001)

19 F. Liu, M. Mostoller, V. Milman, M. F. Chisholm and T. Kaplan. *Phys. Rev. B* **51**, 17192 (1995)

20 G. W. Watson, E. T. Kelsey and S. C. Parker. *Philos. Mag. A-Phys. Condens. Matter Struct. Defect Mech. Prop.* **79**, 527 (1999)

21 S. Dumrul, S. Bazzana, J. Warzywoda, R. R. Biederman and A. Sacco Jr. *Microporous and Mesoporous Materials* **54**, 79 (2002)

22 A. M. Walker, B. Slater, J. G. Gale and K. Wright. *Nat. Mater.*, 1213 (2004)

23 G. Binder, L. Scandella, A. Schumacher, N. Kruse and R. Prins. *Zeolites* **16**, 2 (1996)

24 B. Yilmaz, P. Q. Miraglia, J. Warzywoda and A. Sacco. *Microporous and Mesoporous Materials* **71**, 167 (2004)

25 I. V. Markov. *Crystal growth for beginners: Fundamentals of nucleation, crystal growth and epitaxy* (World scientific publishing Co. Pte. Ltd., 1995)

26 G. Binning and H. Rohrer. *Helv. Phys. Acta.* **55**, 726 (1982)

27 H. Rohrer. *Surface Science* **299/300**, 956 (1994)

28 R. M. Feenstra. *Surface Science* **300**, 965 (1994)

29 C. F. Quate. *Surface Science* **299/300**, 980 (1994)

30 G. Binning, C. F. Quate and C. H. Gerber. *Phys. Rev. Lett.* **56**, 930 (1986)

31 T. R. Albrecht, P. Grütter, D. Horne and D. Rugar. *J. Appl. Phys.* **69**, 668 (1991)

32 J. E. Macdougall, S. D. Cox, G. D. Stucky, A. L. Weisenhorn, P. K. Hansma and W. S. Wise. *Zeolites* **11**, 429 (1991)

33 M. Komiyama and T. Yashima. *Jpn. J. Appl. Phys. Part 1 - Regul. Pap. Short Notes Rev. Pap.* **33**, 3761 (1994)

34 M. W. Anderson, J. R. Agger, J. T. Thornton and N. Forsyth. *Angew. Chem.-Int. Edit. Engl.* **35**, 1210 (1996)

35 M. W. Anderson, K. S. Pachis, F. Prebin, S. W. Carr, O. Terasaki, T. Ohsuna and V. Alfreddson. *J. Chem. Soc.-Chem. Commun.*, 1660 (1991)

36 O. Terasaki, T. Ohsuna, V. Alfredsson, J. O. Bovin, D. Watanabe, S. W. Carr and M. W. Anderson. *Chem. Mat.* **5**, 452 (1993)

37 T. Ohsuna, O. Terasaki, V. Alfredsson, J. O. Bovin, D. Watanabe, S. W. Carr and M. W. Anderson. *Proc. R. Soc. London Ser. A-Math. Phys. Eng. Sci.* **452**, 715 (1996)

38 B. Slater, C. R. A. Catlow, Z. Liu, T. Ohsuna, O. Terasaki and M. A. Camblor. *Angewandte Chemie-International Edition* **41**, 1235 (2002)

CHAPTER THREE:

METHODOLOGY

3.0 COMPUTATIONAL TECHNIQUES

The following sections discuss the theory behind the techniques used to produce high quality models for the simulation of bulk and surface properties of natural zeolites. This chapter will give a comprehensive overview of classical simulation methods which have been used in the studies of chapters 4 and 5, the *ab initio* techniques which are utilised in chapter 6, give a review of the codes used within this research to implement these techniques, and outline their capabilities.

Once a crystal structure of a natural zeolite has been found from experimental crystallographic studies, and a force field or basis set has been determined, modelling techniques may be used to resolve properties of a material, such as the crystal structure, *i.e.* unit cell lengths and coordinates, and the geometry of the structure, *i.e.* the bond lengths and bond angles. By investigating these properties of the unit cell, and comparing them with the original crystal structure determined *via* experimental techniques, one can assess how accurately the force field or basis set and functional is able to reproduce the simulated natural zeolite, post relaxation. The geometry changes during relaxation since the equilibrium geometry given by a force field or basis set and functional rarely corresponds exactly with experimental studies, however deviations from the crystal structure of up to 4% are classed as acceptable.

By using theoretical techniques we are able to differentiate between different structural models in order to find the most energetically favourable structure. Although this information can be found from experimental techniques, they are often very difficult to obtain and computer simulation findings can often be of great value and guidance.

3.1 Classical methods

In classical computer simulation techniques one specifies a potential model, *i.e.* the description in mathematical terms, either numerical or analytical, of the energy of the system as a function of particle coordinates.[1] In order for atomistic simulation techniques to be able to produce accurate results, a suitable set of potentials have to be parameterised. Potentials are fitted to primary physical properties, for example the cell lengths and atomic positions, and secondary physical properties, such as the dielectric and elastic constants, and the vibrational properties of a structure. An essential part of parameterising potentials is ensuring the model is producing a good representation of the observed structure.

Within this research the structure of the zeolite cell was simulated using an interatomic potential model. As stated above classical models make use of pair potentials, as opposed to electronic structure (*ab initio*) methods where the probability of finding electrons are described by wavefunctions, or in terms of electron densities (electronic structure methods discussed later in section 3.8). The main advantage of interatomic potential methods over *ab initio* methods is the calculations are computationally inexpensive and if parameterised correctly, very reliable.

The potential model used is based on the Born model for ionic solids,[2] the Born model assumes that there are two kinds of forces that interact between ions: long range electrostatic forces and short-range repulsive forces. These interactions can be used to calculate the total energy of the system:

$$E_L = \sum_{ij} \frac{q_i q_j}{r_{ij}} + \sum_{ij} \Phi_{ij}(r_{ij}) + \sum_{ijk} \Phi_{ijk}(r_{ijk}) + \ldots \qquad (3.1)$$

where i and j are atoms with charges q_i and q_j respectively. The first term refers to the long-range Coulombic interactions between the atoms i and j separated by the distance r_{ij}. The second, third and remaining terms represent the short-range interactions, where $\Phi_{ij}(r_{ij})$ represents the two body energy term, $\Phi_{ijk}(r_{ijk})$ represents

the three body energy, and the remaining terms are four body and higher order terms, which will not be addressed within this study.

3.1.1 Long range Coulombic interaction

3.1.1.1 Ewald summation

The summation of the long range term (first term in equation (3. 1)) presents problems due to slow convergence, this problem can be solved by use of the Ewald summation technique.[3] The Ewald summation is based on an infinite array of simulation cells, within each simulation cell each particle interacts with all other particles in the cell, and all their periodic images within other simulation cells. Figure 3. 1 illustrates a two dimensional representation of a three dimensional simulation box, the small squares represent simulation cells, which are periodically assembled, the circle represents spherical shape that would appear at the limit of the array of cells, and the large outer square represents the medium in which the simulation cells are embedded in, *e.g.* vacuum or water.

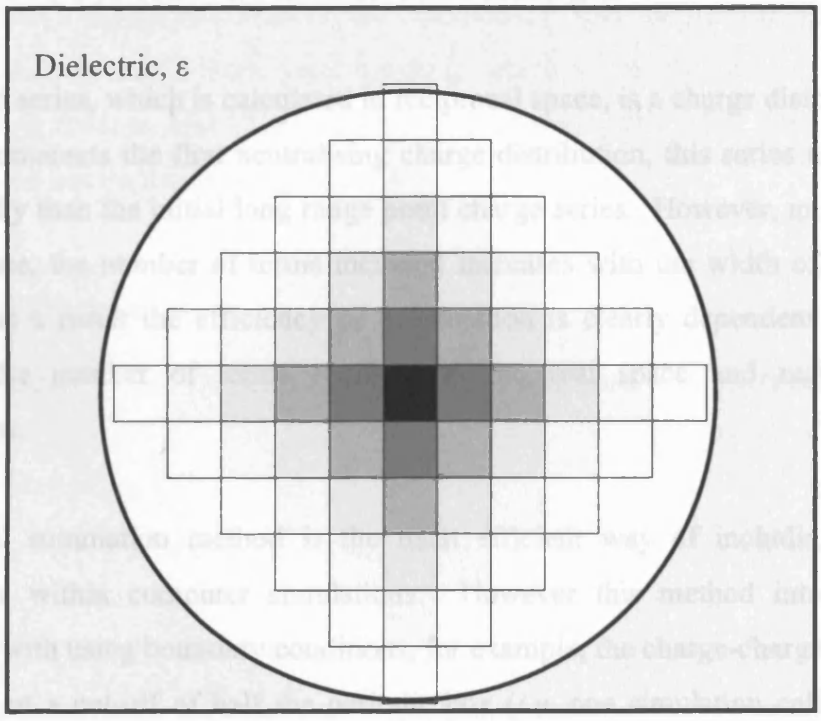

Figure 3. 1: A construction of a system of periodic simulation cells in the Ewald summation method. (Reproduced with out permission from Allen and Tildesley[4])

The total energy of the simulation box contains the contribution from the interactions of the constituents within the central cell (*i.e.* the black box in the centre of Figure 3. 1), the interactions between the central cell and the surrounding periodic images, and the interaction between the spherical array of cells and the surrounding medium. Since the series which calculates the total energy is conditionally convergent*, the order in which the terms are considered is very important.

The Ewald summation solves the problems associated with a conditionally convergent series and the slow rate at which the summation converges by transforming the long range terms into two series, one in real space and the other in reciprocal space, the combination of which results in a rapidly convergent electrostatic sum. The series in real space takes each charge to be surrounded by a charge of equivalent magnitude and opposite sign, hence neutralising the charge. Therefore the new series includes a summation of all point charges and their neutralising terms. The neutralising terms are described in the form of Gaussian charge distributions. The key aspect of the new summation is that the neutralising terms have rapid convergence; the broader the width of the Gaussian distribution the faster the series converges.

The second series, which is calculated in reciprocal space, is a charge distribution which exactly counteracts the first neutralising charge distribution, this series also converges more rapidly than the initial long range point charge series. However, unlike the series in real space, the number of terms included increases with the width of the Gaussian function, as a result the efficiency of this method is clearly dependent on a balance between the number of terms required in the real space and reciprocal space summations.

The Ewald summation method is the most efficient way of including long range interactions within computer simulations. However this method introduces errors associated with using boundary conditions, for example, the charge-charge interaction is minimised at a cut-off of half the periodic box (*i.e.* one simulation cell) length, also

* A conditionally convergent series contains both positive and negative terms, thus taking only positive or negative terms would lead to a divergent series, i.e. a series which would not sum up to a finite number.

instantaneous fluctuations within a cell are replicated throughout the system, rather than being damped out.

It has been shown that accurate electrostatic summation is needed to represent long range charged interactions found in ionic and semi-ionic solids, hence the Ewald summation has been applied throughout this work.

3.1.2 Short range potentials

The second, third and higher terms in equation (3. 1) represent the short-range interactions. The components of these terms include both the repulsive forces due to the overlap of ion charge clouds and the van der Waals attractions between neighbouring electron charge clouds. The terms of the type $\Phi_{ij}(r_{ij})$ are the two-body, central-force contributions to the short-range energy; they vary only with the distances between pairs of ions and have no angular components. The two body forces are unquestionably the most dominant component of the short-range energy. Terms of the type $\Phi_{ijk}(r_{ijk})$ represent the three-body terms, these forces are a function of the coordinates of three atoms. The three-body term has a small contribution to lattice energy, however they are known to have a significant effect on the vibrational properties and become increasingly important with deviation from ionic bonding, which is clearly important for zeolites. The following sections describe the potentials used within this study, parameters of each potential used can be found in appendix A.

3.1.2.1 Two-body terms

The best known of the van der Waals potential functions is the Lennard-Jones 12-6 potential:

$$E_{ij}(r) = 4\varepsilon\left[\left(\frac{\sigma}{r_{ij}}\right)^{12} - \left(\frac{\sigma}{r_{ij}}\right)^{6}\right] \qquad (3.2)$$

where r_{ij} is the distance between two atoms, ε represents the well depth and σ represents the collision diameter, *i.e.* the separation at which the energy is zero. When the energy is at a minimum, the equilibrium distance between the two atoms is found.

The Lennard-Jones 12-6 potential is characterised by an attractive term that varies as r^{-6} and a repulsive term that varies as r^{-12}. The r^{-6} variation is the same power-law relationship found for the leading term in theoretical treatments of the dispersion energy. There is no strong theoretical argument in favour for the repulsive term to be represented by r^{-12}, however the twelfth power term has been shown to describe rare gases well. The practical advantage of the twelfth power repulsive term is it is computationally inexpensive to square an r^{-6} term, in contrast to using, for example, a ninth power repulsive term.

It can be shown that the leading term of the electron-electron repulsion is of exponential character, an example of this is the Buckingham potential:

$$E_{ij}(r) = A_{ij} \exp\left[\frac{-r_{ij}}{\rho}\right] - \frac{C_{ij}}{r_{ij}^6} \qquad (3.3)$$

where A_{ij}, C_{ij}, ρ are adjustable parameters for the ion pair ij.

The exponential term is used to represent the size of 'hardness' of the ion whilst the C term controls the size of the induced dipole interaction within the solid. The Buckingham potential is often used to describe short-range interactions, however at very short distances the potential becomes strongly attractive which could lead to the nuclei being fused together. Both the Buckingham and Lennard-Jones potential are thought of as non-bonded potentials and are used to describe ionic and semi-ionic structures.

The Morse potential is the third functional form of a two body potential used within this work, which also has an exponential dependence and more accurately reproduces the shape of the potential energy surface. The Morse potential is expressed as:

$$E_{ij}(r) = D\{1 - \exp[\alpha(r - r_0)]\}^2 \qquad (3.4)$$

Where D is the dissociation energy of the bond, r_0 is the equilibrium bond length and α is the anharmonicity constant. The Morse potential is a bonded potential and generally used for better description of the interaction between atoms that are covalently bonded. The advantage of the Morse potential is that it is able to describe a wide range of atomic separations from the equilibrium bond length to the behaviour very close to bond dissociation.

The main difference between these three potential terms is in the repulsive term at short distances. The Morse and Buckingham potentials are able to give a higher quality description of bond energies, this is due to the fact that both the Morse and Buckingham potentials contain three adjustable parameters, whereas the Lennard-Jones potential only employs two parameters. In general, the quality of simulating bond energies is directly associated with the number of parameters, hence the greater the number of adjustable parameters within a potential, the more flexible the model will be. These potentials are parameterised by fitting to empirically observed properties, or to *ab initio* potential energy surfaces, however creating a more flexible potential with a greater number of adjustable parameters, requires more observables to fit to during parameterisation. Within this study the Morse and Buckingham potentials have been employed to model the two body interactions of the T-O bonds within zeolites, the three body term has also been applied to generate correct bond angles (see appendix A).

3.1.2.2 Three-body terms

In materials with some extent of covalency, such as zeolites, a three-body bond bending term may be required to model a T-O-T angle accurately. It is common to use the harmonic potential of the form:

$$E_{ijk}(\Theta) = \sum_{i,j\neq i,l\neq(i,j)} k_{ijl}\left(\Theta_{ijl} - \Theta'_{ijk}\right)^2 \qquad (3.5)$$

where K_{ijl} represents the three body force constant, Θ_{ijk} represents the angle between the bond between the atom pairs ij and il and Θ'_{ijk} represents the ideal bond angle, known from experiment.

Within this study, the three-body term has been used to accurately model the O-Si-O angle, and in the case of hydrated natural EDI the O-Si-O and O-Al-O angle.

3.2 Shell model

The shell model of Dick and Overhauser[5] is the simplest and most successful method of modelling the coupling between short-range repulsive forces and ionic polarisation. The model consists of a mechanism where the polarisable valence shell electrons are represented by a core and a mass-less shell connected *via* a harmonic spring, as shown in Figure 3. 2.

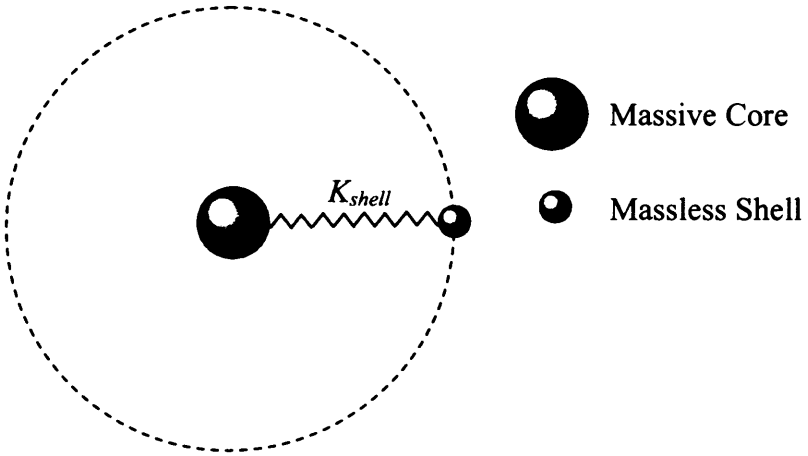

Figure 3. 2: The shell model: a massive core and a massless shell connected via a spring.

The total charge is the sum of the charges on the core and the shell. The following equation shows how the polarisability, α, is determined by the harmonic spring constant, k_{shell} and the charge of the shell, q_{shell}:

$$\alpha = \frac{(q_{shell})^2}{k_{shell}} \tag{3. 6}$$

The shell model parameters, *i.e.* the charge on the shell and the harmonic spring constant, are derived by a standard empirical fitting procedure, *e.g.* a least square method* until the measured elastic and dielectric properties of a material are reproduced.

Unlike the rigid ion model which does not allow an atomic dipole moment to be simulated, the shell model will allow the development of a dipole moment by the displacement of the shell relative to the core, *i.e.* the charges on the massless shell and core move away from each other. A dipole can be accounted for within rigid ion models by the use of partial charges for ions, as opposed to using formal charges. However, it has been found that rigid ion models often give rise to unphysical bond-angles particularly in zeolites, which is improved by the implementation of the shell model. Within this research the shell model has been utilised to reproduce the polarisability of the oxygen within a zeolite framework.

The following section will describe why cut-offs are often used and how they are able assist in running a simulation more efficiently.

3.3 Cut-offs

Cut-off distances describe the range in which the various potentials should be taken into account. Short-range terms converge rapidly, thus it is of little benefit to calculate what effects these forces would have at long ranged distances, and so cut-off limits are employed. These distances are chosen such that the short range energy is converged to a desired criterion, *i.e.* to a typical energy tolerance of 10^{-6} $kJmol^{-1}$.

When evaluating the long range Coulombic terms, the Ewald technique[3] (as discussed in section 3.1.1.1) is used to transform a highly unreliable and computationally expensive series summation, into two rapidly convergent series expansions. The Ewald technique allows the use of large cut-offs, hence a large volume of simulation space can

* The least square method chooses a set of experimental data to fit to, the 'error' for a given set of parameters equals the sum of squares of the differences between the observed and the calculated values. The force field is parameterised to minimise the error, this is done by assuming the properties are related to the force field by a Taylor series expansion.

be taken into account, this enables one to model isolated defects within a solid which do not interact with defects of their periodic images.

3.4 Modelling zeolites

Zeolites consist of silicon, aluminium, oxygen, extra framework cations and possibly water, bonded with partial covalent character (as stated in chapter one), they can be modelled using intermolecular potentials, such as the Lennard-Jones potential and more commonly the Buckingham potential. A correct description of the electrostatic interactions of a zeolite is essential to get accurate predictions of structure and their reactions with other materials, *e.g.* in catalysis and ion exchange. There are a number of potentials in literature which are constructed from either rigid ion or shell models, and their merits and short comings are now described.

The Sanders, Leslie and Catlow[6] model was created to be a transferable model for silicates, this potential model is a based on pair potentials, where each atom is assigned with their formal charge. All the variable parameters within this potential model were fitted using standard empirical methods, *i.e.* where the variables are adjusted until the measured cell parameters, atomic positions, elastic and dielectric constants of quartz (the densest form of SiO_2 at room temperature) were reproduced accurately compared with experiment. The two body pair potentials are described by the Buckingham potential, however the advantage of Sanders *et al.*[6] model lies within its description of bond bending term and also its ability to model polarisability. The O-Si-O bond bending terms are included in the form of a three body potential, which allows predictions of a large variety of framework species. The description of the polarisability of the oxygen atoms where included with the shell model.

The Sanders *et al.*[6] model has been used successfully to model properties of zeolites, such as reproducing the crystal parameters[7], determining the effects of hydration[8] and also observing the interactions of the external zeolite surface with hydrocarbons[9] and water[10].

Rigid ion potentials where partial charges have been used to describe the atomic charge have been developed by van Beest *et al.*[11,12] for silicas, aluminiophosphates and zeolites. The van Beest *et al.* model was based on *ab initio* cluster calculations combined with experimental information on the infinite system. They propose that the *ab initio* data is essential for ensuring the nearest neighbour interactions are properly described, however the incorporation of empirical data on the infinite system allows a better depiction of the long range interactions. The *ab initio* calculations were performed on H_4SiO_4 and $Al(OH)_4^-$ clusters, and the experimental information on an infinite system were taken from data on α-quartz and berlinite (the $AlPO_4$ analogue of α-quartz). The van Beest *et al.* ion pair potentials describe the Coulomb term by a single free parameter, which is the effective charge (*i.e.* the partial charge) on the atom, and describe the short range terms in the form of a Buckingham potential.

The van Beest *et al.* ion pair potentials have been used in a number of studies, such as investigating a wide range of properties from the diffusion of cations in silicates[13,14] and determining the stability of hydrated nano tubes.[15] Studies by Auerbach *et al.*[16,17] have shown how the combined use of the van Beest *et al.* ion pair potentials, along with the three-body potentials from Catlow *et al.*[18] can be used to model the diffusion of benzene in Na zeolite Y over the temperature range 100-500K *via* kinetic Monte Carlo simulations.

The Hill and Sauer[19,20] model is based on acidic zeolite crystals; the parameters of this molecular mechanics force field have been derived for silicate crystals solely from quantum chemical *ab initio* data. The Hill and Sauer approach has used *ab initio* data from typical structural units of zeolites, without the inclusion of empirical data of isolated molecules or of the extended crystal. With their force field model they have been able to reproduce the rigidity of the SiO_4 unit and also the flexibility within the Si-O-Si term, as found commonly within zeolite crystal structures. However, the Al-O bond length and Si-O(H)-Al bridge angle is not easily reproduced using this type of force field.

The Sanders *et al.*[6] potential has been utilised within this study, this set of potentials reproduces T-O bond lengths comparable to the van Beest *et al.* or the Hill and Sauer potential. However, the Sanders *et al.* potential contains both a shell model and a three

body term, which reproduces the T-O-T bond angle in zeolites with greater accuracy than the rigid bond potentials proposed by van Beest *et al.* or the Hill and Sauer potentials.

3.5 Energy minimisation techniques

Once the form of the force field has been established, the model is relaxed and compared to experiment. The object of energy minimisation is to remove all residual strain from the system; this is done by minimising the energy of the structure with respect to all nuclear coordinates *i.e.* by finding a point on the potential energy curve where the first derivative is zero:

$$\frac{\partial V}{\partial r} = 0 \tag{3.7}$$

where V represents the potential energy curve and r represents the coordinate system.

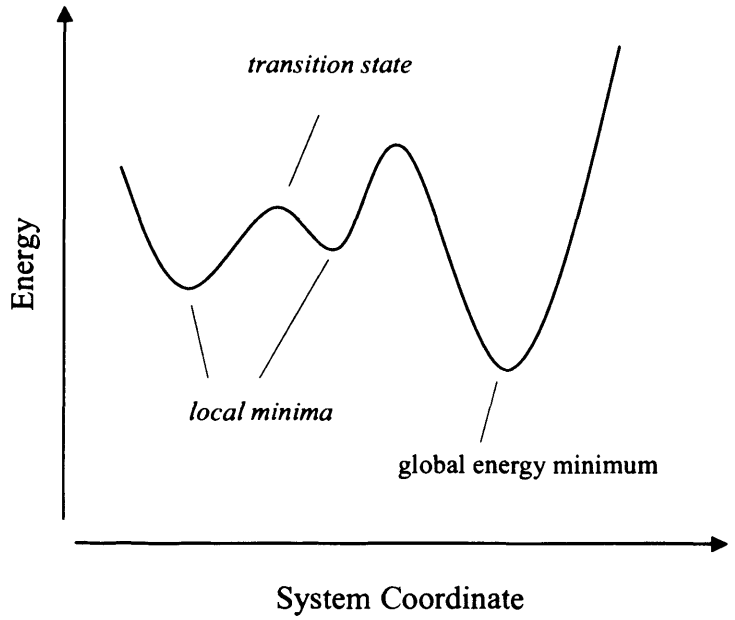

Figure 3.3: Local and global minima on the potential energy curve.

To locate the minimum point we employ an iterative numerical procedure that uses the first, and in certain cases the second derivative of potential energy. The first derivative describes the gradient of the curve, whereas the second derivatives provide information

about the curvature. It should be noted that potential energy curves could contain multiple local minima and transition states (see Figure 3.3) which satisfy the minimization criteria. These points should not be confused with the global energy minima.

3.5.1 Conjugate gradient technique

One of the simplest energy minimisation techniques is the conjugate gradient method, which requires the evaluation of both the energy and the first derivative. Within the conjugate gradient method the gradients at each point are orthogonal and the directions are conjugate. A property of conjugate gradients is that for a quadratic function of M variables, the minimum will be reached in M steps. The conjugate gradients method moves in a direction $\mathbf{v}_k$ from a point $\mathbf{x}_k$, where $\mathbf{v}_k$ is calculated from the gradient at the point and the previous direction vector $\mathbf{v}_{k-1}$, thus it follows the following equation:

$$v_k = -g_k + \gamma_k v_{k-1} \tag{3.8}$$

where γ_k is a scalar constant. The above equation can only be calculated from the second step onward, thus the first step would be calculated by another method. The conjugate gradients method works well at moderate to close distances from the energy minimum but has very slow convergence when very close to the minimum.

3.5.2 Newton Raphson technique

A rapid convergence can be achieved with the Newton Raphson technique, which uses an iterative procedure on the second derivative of the energy, this scheme relates the value of variables x at the $(i+1)^{th}$ iteration to its value at the i^{th} iteration by the following equation:

$$\vec{x}_{(i+1)} = \vec{x}_{(i)} - \vec{H}_{(i)} \cdot \vec{g}_{(i)} \tag{3.9}$$

where $\vec{g}_{(i)}$ represents the individual derivative vectors with respect to coordinates, $\vec{H}_{(i)}$ corresponds to the inverse of the second derivative matrix $\frac{\partial^2 E}{\partial x_g \partial x_h}$, this quantity is also known as the Hessian matrix.

The Hessian matrix need not be updated after every iteration, however, to increase convergence rate, the Hessian matrix is recalculated every 10-20 iterations depending on the course of minimisation. Although the Newton Raphson technique method does achieve rapid convergence in contrast to conjugate gradient techniques, it should be noted that it requires a large amount of memory when minimising large numbers of atoms because additional gradient components must be stored in memory.

3.6 Interatomic potential based codes

A brief review of the capabilities and applicability of the codes used within this research are presented in the following sections.

3.6.1 General utility lattice program

The general utility lattice program (GULP) is a classical potential based code initially developed for the treatment of periodic systems[21] and later developed to simulate surfaces[22]. GULP has been used within this study to relax only the bulk crystal structure. Since it is an impossible task to calculate the energetics of infinite systems, *i.e.* the evaluation of interactions between all species within the unit cell and their periodic replications to infinity, some finite cut-off must be placed. GULP overcomes this problem using the Ewald summation[3] (as described in section 3.1.1.1), for small to moderate sized systems this is the most efficient method of calculating the electrostatic energy. There are a variety of standard short-range two-, three- and four- body potentials in GULP to evaluate the short-range interactions, a full list of all potentials can be found within the GULP website.*

* See http://gulp.curtin.edu.au/potentials.cfm for full list of potentials available in GULP

The energy minimisation calculations in GULP are carried out using techniques that use the Newton Raphson methods since they prove to be most efficient. The default minimiser uses the exact second derivative calculated analytically to initialise the Hessian matrix for the minimisation variables, and then subsequently updates it using the Broyden-Fletcher-Goldfarb-Shanno (BFGS) algorithm. At each cycle, a line search is performed to obtain the optimum step length along the search vector. This method often leads to rapid convergence for most systems, however when there are particularly soft modes in the Hessian the rational function optimiser (RFO) is also available, which attempts to remove the imaginary modes from the Hessian, hence forcing the matrix to be positive definite. The disadvantage of the RFO method is that it is more expensive per cycle.

3.6.2 Minimisation and relaxation of vacancies and interstitials for neutral surfaces

MARVIN is an acronym for Minimisation And Relaxation of Vacancies and Interstitials for Neutral Surfaces and has been used to relax all surface structures reported here.[23] The simulation cell has planar 2D periodic boundary conditions parallel to the interface. The cell consists of one or more blocks, with each split into two regions, region I and region II (see Figure 3.4).

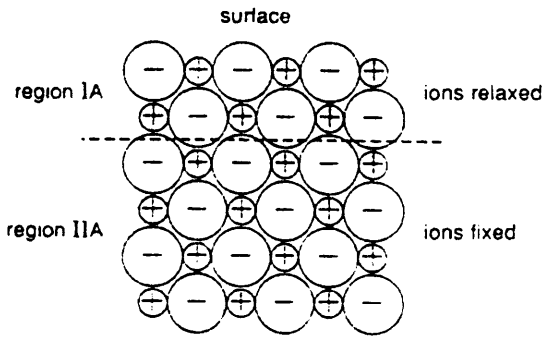

Figure 3.4: Regions in MARVIN (Reproduced without permission from Gay *et al.*[23])

Each region contains structural units, which can be in the form of ions or molecules. Each atom may be constructed by more than one particle; this is particularly useful when using the shell model[5] to describe polarisation. The calculations take place by relaxing the structural units in region I until there is zero force on each of them. The

region I layer represents the outer surface which may adsorb liquids, for example water. The structural units in region II are kept fixed to reproduce the long-range electrostatic effects of the bulk on the surface. The total energy of the system is calculated as all the energy of all the structural units in region I, and their interactions, the energy of all the structural units in region II, and the periodic images of both regions.

The total energy can be expressed as:

$$E_{total}^{\{2\}} = \sum_{a}^{N_I}\left[\frac{1}{2}\sum_{l\neq 0} V_{aa}(|l|) + \frac{1}{2}\sum_{b\neq a}^{N_I}\sum_{l} V_{ab}(|r_{ab}+l|) + \sum_{b}^{N_{II}}\sum_{l} V_{ab}(|r_{ab}+l|)\right] \tag{3. 10}$$

Where N_I is the total number of particles in all of region I, N_{II} is the total number of particles in all of region II, l denotes the 2D lattice vectors, and r_{ab} represents the vector length between particle a and particle b.

The first term in the equation describes the interactions between a particle and its periodic image, the second term describes the interactions between all regions I particles and their periodic images, both of which are divided by two to eliminate double counting. The third term describes the interactions between region I particles and region II particles. The expression above (equation (3. 10)) focuses on two-body interactions, however similar equations can be derived to apply the three- and four-body interactions.

3.6.2.1 Potentials

In ionic systems the greatest contribution to the energy comes from the electrostatic energy. In 3D systems the Ewald method is used to converge the energy, however for 2D systems, Parry[24,25] was the first to adapt the 3D Ewald summation for 2D slabs. A more complete treatment is given by Heyes *et al.*[26], they lead to the same result produced by Parry. The Heyes *et al.* algorithm has been applied within the MARVIN code.

There are a variety of potential types implemented into the code to describe the short-range repulsion and long range van der Waals attraction between atoms, for example the Buckingham, the Lennard-Jones and Morse potential; Gay and Rohl describe full lists of functional forms in their paper.[23] Subsequently other potentials and expressions have been added by Slater and Nygren.* Covalency can be described by the use of three- and four-body terms, MARVIN also implements the Dick-Overhauser shell model[5].

3.6.2.2 Energy minimisation

MARVIN has two different types of energy minimisers. The first is the conjugate gradient which is used at moderate to close distance from the energy minimum. The second method is a hybrid Newton minimiser, since the second derivatives which are used in this algorithm are very expensive, they are only explicitly calculated at the first step, or if the minimiser has a sharp change in direction on the energy surface. MARVIN allows the flexibility of using a combination of these minimisation throughout a particular calculation.

To minimise a structure which is far from the point of minimum, MARVIN has the ability to 'freeze' atoms in the code. Freezing atoms within a system is a technique which allows gradual minimisation, thus gross strain is removed from the system first, before the system is unfrozen and full minimisation can take place. When parts of the system are frozen their coordinates do not change post minimisation, however the presence of these atoms do have an effect on the system. The long range forces associated with the frozen atoms act up on the parts of the system which are not frozen, influencing the path the unfrozen atoms take on the potential energy surface.

Within MARVIN the freezing technique allows one to freeze a selection of atoms in region I, while allowing others to take part in the minimisation. Region II, which represents the bulk, is permanently frozen, since the atomic coordinates do not change, however the long range forces associated with region II affect region I. This cannot guarantee that the global minimum will be found, but it has proven to be effective in steering the system to equilibrium, particularly for zeolite surfaces where the potential energy surface tends to be very flat, and possess very shallow points of minima.

* See help file within MARVIN code.

3.7 Theoretical methodology

3.7.1 Simulating bulk structure

When simulating a bulk crystal structure (in this case of this study, zeolite bulk structures), there are many aspects that have to be taken into account in order to ensure that the bulk structure has been modelled correctly. Initially cell parameters and atomic coordinated are obtained from experimental data (*e.g.* XRD). The second step is to assemble a quality set of potentials in order to describe the zeolite accurately and efficiently. The quality of a set of potentials is based on their ability to reproduce the cell parameters, bond lengths and bond angle to a high degree of accuracy. Without using suitable parameters the structure under study will not give realistic results. The accuracy of potentials to reproduce the structure can be evaluated by comparison with experimental data, *e.g.* crystallographic data.

3.7.2 Simulating surfaces

Using the minimised bulk structure as a basis, the surfaces to be studied can be constructed in two techniques, however firstly it is critical to decide which Miller indices should be studied. The Miller index of a surface plane is a method of assigning a set of numbers (hkl) which quantify the intercepts that the plane has with the main crystallographic axes (*i.e.* a,b,c) of the solid bulk structure, and thus may be used to uniquely identify the plane or surface.

Deciding on which surface planes should be studied is based on the faces observed in the experimental morphology and the interplanar spacing, d_{hkl}, of the different crystal faces. It was proposed by Donnay and Harker that the rate of growth is inversely proportional to the d_{hkl}-spacing.[27] Thus, the larger the spacing between each layer the weaker the forces between them, as a result the surface will grow slower and be more dominant in the growth morphology.

When looking at each face of the crystal there are many possible different cuts or terminations, which can arise. To choose a particular cut the surface must satisfy two conditions. Firstly the surface must be charge neutral and secondly there must be an

overall zero dipole perpendicular to the surface. A study by Bertaut[28] has shown that when there is a dipole perpendicular to the surface, the surface energy diverges with increasing crystal size. In some cases the surface has to be reconstructed in order to create a stable surface. In order to reconstruct the surface atoms are moved from either the top of the surface to the symmetrical position at the bottom of the layer, or vice versa, this extinguishes the dipole moment.

There are often many different cuts on each face, for example, edingtonite requires analysing six different faces, with thirty-four terminations in total for siliceous edingtonite, all of which have to be investigated to find which is the most energetically favourable. Consequently, examining different permutations of surface termination and reconstructing surfaces to create stable surfaces is a very time consuming process.

When determining the size of the surface simulation cell, namely determining the size of region I and II; having more layers than required in region I will not produce errors within the calculation. However the number of particles in the simulation cell increase, thus the calculation becomes unnecessarily more expensive (since the calculation of energy is of order $N_{regionI}\left(N_{regionI}/2\right)+N_{regionI}N_{regionII}$). It reasonably simple to determine the correct size of both regions, a calculation is run which essentially keeps on adding layers to region II until the long range electrostatic sum has converged. If the surface has a dipole the effect of adding additional layers increases the dipole, thus the energy will not converge and surface must be reconstructed. Once the long-range electrostatics are correct, *i.e.* region II is behaving as bulk, layers are added to region I until the surface energy converges.

Another method of studying surfaces is by creating 3D slabs, where all three directions are infinitely periodic. Within 2D codes, such as MARVIN, only the x and y directions are infinitely periodic, however in 3D codes such as GULP, surface energies may be calculated from slabs. A slab is created by creating a 3D simulation box where part of the box contains the structure and the remaining part is a vacuum gap.

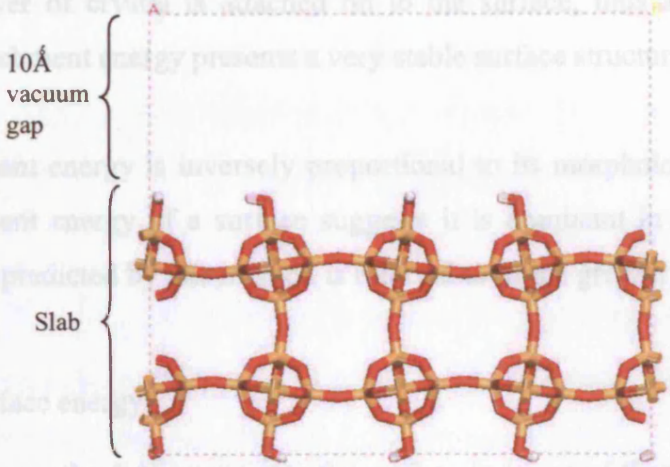

Figure 3. 5: A simulation box containing a slab of zeolite with a vacuum gap of 10Å

Figure 3. 5 is an example of an edingtonite slab, where the simulation cell contains two layers of edingtonite (determined by the method described above) and a 10Å vacuum gap. The amount of vacuum within the slab is determined such that the long range interactions of the bottom surface of the slab, does not interact with the top surface of the slab in its periodic image.

3.7.3 Assessment of surface stability

The stability of various faces and terminations can be evaluated by analysing the energy of the surface. When interpreting the minimised energies of the structures there are two methods that are commonly used: the attachment energy and the surface energy.

3.7.3.1 Attachment energy

The attachment energy, E_{att}, is the energy per molecule released when a new slice of depth d_{hkl} is attached onto the crystal face. It can be calculated as:

$$E_{att}(hkl) = \sum_{i=1}^{\infty} E_i(hkl) \qquad (3.\ 11)$$

where $E_i(hkl)$ is the interaction energy per molecule between a slice of thickness d_{hkl} and the i^{th} underlying slice. The attachment energy represents how strongly bound a

complete layer of crystal is attached on to the surface, thus a surface with a small absolute attachment energy presents a very stable surface structure.

The attachment energy is inversely proportional to its morphological importance, thus low attachment energy of a surface suggests it is dominant in the morphology. The morphology predicted by this method is referred to as the growth morphology.

3.7.3.2 Surface energy

J. W. Gibbs was the first investigate the surface in terms of thermodynamic properties, by examining the energetics of the 'dividing surface'. When considering the thermodynamics of bulk matter, the system is characterised by the volume, in this case the change in Gibbs free energy (dG) of the bulk is expressed as:

$$dG_{(b)} = -SdT + Vdp + \mu dN \tag{3.12}$$

where S is the entropy, V is the volume, μ is the chemical potential, and G is at a constant temperature, T, pressure, P, and number of particles, N. When a system is characterised by the surface, the change in Gibbs free energy of the surface ($dG_{(s)}$) contains an additional term which is dependent on the surface area, A, however according to the Gibbs convention the volume of the surface phase is nil, as a result the dV term disappears, giving the following:

$$dG_{(s)} = -S_{(s)}dT + \mu_{(s)}dN_{(s)} + \gamma dA \tag{3.13}$$

where $S_{(s)}$ is the entropy of the surface, $\mu_{(s)}$ is the chemical potential of the surface, G is at a constant temperature, T, and contains a constant number of surface particles, $N_{(s)}$. The basis of Gibbs'theory of the 'dividing surface', states that for a real crystal, the concentration of atoms or molecules may vary within the vicinity of the surface, however the system can be thought of as uniform up to the ideal interface, in which case the surface can be represented by f_s, which is then the surface free energy per unit area.

The integrated equation of the Gibbs free energy, which is often known as the surface free energy, is expressed per unit area by the following:

$$f_{(s)} = \gamma + \sum_i \mu_{i(s)} \Gamma_i \tag{3.14}$$

where $\Gamma_i = N_{i(s)} / A$, and is called the surface density of the i-th component. In the general case there is no equivalence between the surface free energy, $f_{(s)}$, and the surface tension, γ*, however they are often confused for one another. It should be noted that in the unique case when the sum of the chemical terms is equal to zero, the identity $f_{(s)} \equiv \gamma$ is true, and so the surface free energy and the surface tension are interchangeable.

The surface free energy or surface energy is the difference in energy of the surface ions compared to those in the bulk per unit surface area, as shown by the following equation:

$$\gamma(hkl) = \frac{\left[E_{total}(hkl) - \tfrac{1}{2} E_{boundary} - nE_{cr}\right]}{A(hkl)} \tag{3.15}$$

where E_{total} is the total energy of the system, $E_{boundary}$ represents the boundary energy, n is the number of unit cells in region I, E_{cr} represents the energy of one unit cell, and $A(hkl)$ is surface area of the simulation cell. The energy of the surface and bulk ions are evaluated against one another since the bulk ions are considered to be in the lowest energy configuration of the crystal structure.

During relaxation of the surface the surface energy decreases, a low surface energy implies that there is a small difference in energy between the surface and bulk ions, and so the surface ions are in a stable configuration. A high surface energy presents a large disparity between the energy of the surface and bulk ions, and can be interpreted as a highly unstable configuration.

* The surface tension is defined as the reversible work done required to create a new surface, *e.g.* the work done to cleave a bulk crystal to create new surfaces, where this process can be reversed.

Surface energies can also be used as an approach to determining the geometrical form of a crystal, and similarly to the attachment energy approach (see section 3.7.3.1), the surface energy is inversely proportional with the morphological importance. The crystal shape derived in this manner corresponds to crystal face being in thermodynamic equilibrium with its surroundings, and hence the entire crystal is in equilibrium, *i.e.* when the surface free energy of the crystal is at a minimum $d\gamma/dA=0$. When the crystal shape is determined by surface energies, the resulting structure is referred to as the equilibrium morphology.

3.7.4 Wulff construction

The morphology of the crystal (the crystal shape) can be constructed by the Wulff theorem. This states that the equilibrium form of a crystal can be found at the minimum of $\int \gamma dA$, which results when one draws a perpendicular line through $\gamma(\theta)$ and takes the inner envelope, this type of polar plot is referred to as the γ-plot or the σ-plot. The Wulff construction can be described qualitatively by looking at an example of a crystal, Figure 3. 6 displays a 2D cut of a γ-plot, where the length OP is perpendicular to the plane $\gamma(\theta)$, the crystal shape is taken as the inner loci of the planes, depicted by the bold line.

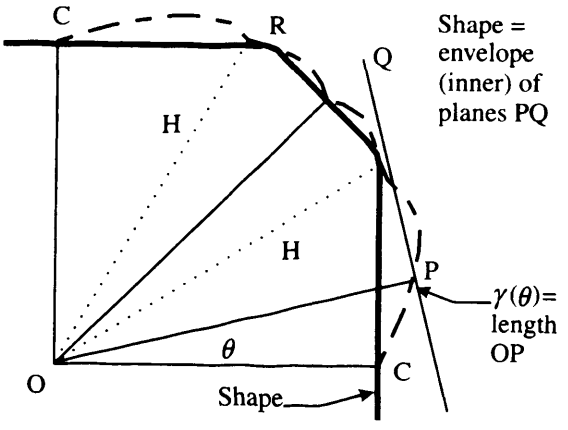

Figure 3. 6: The Wulff construction. A 2D plot of a γ-plot, this plot shows the existence of singular facets at C and rounded (rough) regions at R. (Reproduced without permission from Venables[29])

The deepest cusps, represented by C, are the singular facets and are always present in the equilibrium form. Other higher energy faces (shown by the cusps H) are most likely to be overgrown and unlikely to be present in the final morphology. Between the two singular faces there may be regions of a rough faces, R.

An example of determining the crystal morphology *via* the Wulff construction technique and by using the Donnay-Harker approach (*i.e.* looking at interplanar spacing, d_{hkl}) of surface stability is as follows. The crystal shape is dependent upon where the plane $\gamma(\theta)$ lies, which in turn is determined by the magnitude of the vector **OP**, in this case **OP** is equal to d_{hkl}, thus the higher index faces with smaller values for d_{hkl} are overgrown by the lower index faces with larger values of d_{hkl}. To create an equilibrium morphology (or growth morphology) the surface energies (or attachment energies) are used as the magnitude of the vector **OP** instead of d_{hkl}.

3.8 Electronic structure methods

The purpose of *ab initio* methods is to solve the Schrödinger equation to calculate the energy of an atom, molecules or a periodic system. The full Schrödinger equation is dependent on the position vector (r) and time (t), as shown by the following equation:

$$\hat{H}\Psi(r,t) = E\Psi(r,s,t) \tag{3.16}$$

where $\hat{H}$ is the Hamiltonian operator (described below), $\Psi(r,s,t)$ is the wavefunction, dependent on position (r), spin (s), and time (t), which characterises the particle's motion and E is the electronic operator.

When the external potential acting on the system is independent of time the wavefunction can be written as a product of the time part and the spatial part. We are mostly concerned with atoms and molecules without time dependent interaction since we are looking at a single snapshot in time, so we focus on the wavefunction dependent only on the position vector (and spin), the time independent Schrödinger equation can be written as:

$$\hat{H}\Psi(r,s) = E\Psi(r,s) \tag{3.17}$$

The description of the wavefunction, $\Psi(r,s)$, is very important, the wave function must be well behaved everywhere, in particular it must satisfy the condition of decaying to zero at infinity for an atom or molecule or obeying appropriate periodic boundary conditions for a regular infinite solid. The wavefunction must satisfy the Pauli exclusion principle, which states that only two electrons can occupy the same orbital and that they must possess opposite spins. The wavefunction is also required to contain the correct anti-symmetry, therefore in a system of fermions* (in this case electrons), the sign of the wavefunction must change when the coordinates (position, r, and spin, s) are interchanged.

The Hamiltonian operator consists of two quantities, the kinetic energy, $\hat{T}$, and the potential energy, $\hat{V}$:

$$\hat{H} = \hat{T} + \hat{V} \tag{3.18}$$

The potential operator can be separated into three parts:

$$\hat{V} = \hat{V}_{ne} + \hat{V}_{ee} + \hat{V}_{nn} \tag{3.19}$$

where $\hat{V}_{ne}$ is the nucleus-electron attraction energy operator, $\hat{V}_{ee}$ is the electron-electron energy operator and $\hat{V}_{nn}$ is the nucleus-nucleus repulsion energy. The nuclear-nuclear repulsion energy does not depend on electron coordinates and can be integrated to a constant. Consequently when solving the Schrödinger equation it is possible to separate out the nucleus-nucleus repulsion energy from the definition for the Hamiltonian. As a result, the Schrödinger equation can be solved for E with the nucleus-nucleus repulsion energy contained within the Hamiltonian or with the nucleus-nucleus repulsion energy separated out and then added once the is Schrödinger equation is solved. The separation of the nucleus-nucleus repulsion term is applicable whether one is solving the Schrödinger equation for a single nucleus or multiple nuclei.

* Fermions are the elementary particles which make up matter, e.g. electrons, protons neutrons.

The masses of nuclei are much greater than the mass of electrons, and hence their velocities are much smaller than those of the electrons. As a result, the solution to the Schrödinger equation can be approximated by separating the wavefunction into two parts, a solution is proposed by Born and Oppenheimer.[30] In the Born-Oppenheimer approximation it is recognised that the nuclei are much heavier than electrons, consequently the electrons react almost instantaneously without any change in position of the nuclei. As mentioned above, the wave function can be divided into two parts, one which describes the electronic wavefunction for fixed nuclear geometry and a second part which describes the nuclear wavefunction, where the energy from the electronic wave function describes the effective potential energy:

$$\Psi_{tot(nuclei,electrons)} = \Psi_{(electrons)}\Psi_{(nuclei)} \qquad (3.20)$$

When the Born-Oppenheimer approximation is used, we concentrate only on the electronic motions while the nuclei are considered fixed, thus for each arrangement of nuclei the Schrödinger equation is solved for the electrons alone within the field of the nuclei.

The Born-Oppenheimer approximation introduces very small errors into the system, however for systems with heavier nuclei the error decreases and the approximation becomes much better. There are very limited cases where the Schrödinger equation can be solved exactly; they are systems containing one electron, for example H_2^+, HD^+ and He^+. To obtain an absolute solution of the Schrödinger equation for most other atomistic models the calculation would contain many more electrons, for example a SiO_4 tetrahedral unit within a zeolite contains 46 electrons, and so the extended crystal would contain hundreds of electrons. In reality this would require masses of computing power and time, since this is not practical, approximations have to be introduced. There are two major approaches of implementing approximations to solve the Schrödinger equation, they are Hartree-Fock (HF) theory[31,32] and density functional theory (DFT).[31,33]

The HF method has not been used within this work due to two reasons; HF theory fails to include the interaction between electrons which are in anti-parallel spin states, as a result the effect of electron correlation is not included. The absence of electron

correlation in HF theory can lead to the failure of discriminating between two atomic spin states. The effects of electron correlation can be added to HF theory by methods such as configuration interaction and many body perturbation techniques.[31] However all these methods do increase the amount of computing power required, HF methods scale approximately to N^{4-5}, where N is the number of electrons, whereas DFT techniques are more computationally efficient, scaling to N^{2-3}. The reader is directed to textbooks by Jensen[31] and Leach[32] for a full explanation of the HF method. Within this study the DFT approximation has been used, which will be discussed in detail in the following sections.

3.9 Density Functional Theory (DFT)

Density Functional Theory (DFT) is based on the premise that there is a one to one correspondence between the wavefunction and the electron density, ρ. The electron density can be used to replace the complex N-electron wavefunction and the associated Schrödinger equation, such that the ground state electronic energy is determined entirely by the electron density.

The history of DFT begins in the 1920's with the work of Thomas and Fermi[34,35], their approach to solving the Schrödinger equation is based on a non-interacting uniform electron gas. The assumption of a non-interacting uniform electron gas does not calculate total energies of atomic or molecular systems well, with errors of roughly 15-50%. The main problem with the Thomas and Fermi approach is that the uniform electron gas model leads to a poor representation of bonding, for example it is unable to reproduce the regions of high and low electron densities in covalent bonds, as a result Thomas-Fermi theory is unable to model molecules. In 1964 a publication by Hohenberg and Kohn[36] explained the fundamental theorems, showing that the ground states estimated by the Thomas-Fermi model can be used as an approximation to the exact density functional theory. Before the proof shown by Hohenberg and Kohn, density functional theories were perceived as useful only for idealised models, which could not be used to calculate reliable energies for real chemical systems.

3.9.1 Hohenberg and Kohn theorems

For an *N*-electron system, where $N \geq 1$, described by the Hamiltonian, both the ground state energy and the ground state wavefunction are determined by minimisation of the energy functional* $E[\Psi]$. However, within the *N*-electron system, the external potential $v(r)$ fixes the Hamiltonian, thus the ground state properties are determined by N and $v(r)$.

The first Hohenberg-Kohn theorem proves that the two variables N and $v(r)$ can be replaced by the electron density, ρ, where the electron density is defined as the number of electrons per unit volume. As a result, the external potential $v(r)$ and the number of electrons N can be determined by the electron density. Consequently it is the electron density alone which can be used as a basic variable to determine all properties of the ground state, such as the ground state wavefunction and all other electronic properties of the system such as the kinetic energy, $T[\rho]$, potential energy $V[\rho]$ and the total energy $E[\rho]$.

The second Hohenberg-Kohn theorem is a variation principle analogous to that in wave mechanics. The variation principle states that given an approximate electron density which is assumed to be positive definite everywhere, *i.e.* $\rho(r) \geq 0$, and integrates to the number of electrons *N*, *i.e.* $\int \rho(r) dr = N$, then the calculated energy given by the trial density is always greater than or equal to the exact ground state energy, as shown by the following equation:

$$E[\rho] \geq E_0 \tag{3.21}$$

where $E[\rho]$ is the exact energy functional and E_0 is the exact ground state energy. In general it is found that the closer approximation of the trial density to the exact density, the lower the calculated energy of they system under consideration.

* A functional is a function of a function. It is a method of producing a number from a single or number of functions, where a function by definition is a process of calculating a number dependant on a number of variables.

DFT theory has been further advanced by Kohn and Sham[37], by the introduction of orbitals, they were able to develop a scheme which split the kinetic energy functional into two parts: the kinetic correlation energy which can be calculated exactly and the exchange correlation energy which is a small correction term which can be solved separately. This indirect approach to calculating the kinetic energy into two parts thereby allowed DFT to be used as a practical tool for rigorous calculations. In order to understand the Kohn-Sham orbital method and how the two parts originate we firstly look at the exact formula for the ground state kinetic energy, T, given by the following:

$$T = \sum_{i}^{N} n_i \left\langle \psi_i \left| -\frac{1}{2}\nabla^2 \right| \psi_i \right\rangle \quad (3.22)$$

where ψ_i represents the natural spin orbitals, n_i represents their occupation numbers which are in the range $0 \leq n_i \leq 1$, i represents the electron number, which range from $1 < i < N$, where N is the maximum number of electrons in the system, and ∇^2 is the second differential operator $\frac{\partial^2}{\partial x^2} + \frac{\partial^2}{\partial y^2} + \frac{\partial^2}{\partial z^2}$.

In the hypothetical case of non-interacting electrons, the Schrödinger equation can be solved exactly by a Slater determinant† composed of orbitals, φ_i, and so the expression for which the exact kinetic energy determined by Slater determinants, T_s, is given as:

$$T_s = \sum_{i}^{N} \left\langle \varphi_i \left| -\frac{1}{2}\nabla^2 \right| \varphi_i \right\rangle \quad (3.23)$$

However in reality there are interacting electrons, in this case the kinetic energy is determined by the Slater determinant and is an approximation to the real kinetic energy. The general term for the energy determined by DFT is expressed as:

$$E_{DFT}[\rho] = T_s[\rho] + E_{ne}[\rho] + J[\rho] + E_{xc}[\rho] \quad (3.24)$$

---

* Equation (3.22) uses the *bra-ket* shorthand notation of writing complex conjugates of orbitals. The *bra* $\langle n|$ represents the complex conjugate orbital, n, on the left hand side of the operator, |, and the *ket* $|m\rangle$ represents the orbital, m, on the right hand side of the operator.

† A Slater determinant is a method which incorporated the anti-symmetry within the wavefunction.

where $T_s[\rho]$ represents the kinetic energy determined by Slater determinants (as defined in equation (3. 24)), $E_{ne}[\rho]$ represents the nuclear – electron energy, $J[\rho]$ is the Coloumb integral, and $E_{xc}[\rho]$ represents the exchange correlation energy.

The Coloumb integral classically represents the repulsion between two charges, and is calculated by the following:

$$J[\rho]=\frac{1}{2}\iint\frac{\rho(r)\rho(r')}{|r-r'|}drdr' \tag{3. 25}$$

where $\rho(r)$ represents the charge density at position r, $\rho(r')$ represents the charge density at position r', and $r-r'$ is the distance between the two charge densities.

The exchange correlation term contains the difference between the real kinetic energy and the calculated kinetic energy assuming non-interacting orbitals. Therefore the exchange correlation term is defined as the difference between $E[\rho]$ and $E_{DFT}[\rho]$:

$$E_{xc}[\rho]=(T[\rho]-T_s[\rho])+(E_{ee}[\rho]-J[\rho]) \tag{3. 26}$$

The first parenthesis within this expression can be thought of as the kinetic correlation energy, while the second contributes to the exchange and potential correlation energy. The exchange correlation energy is a relatively small part of the overall energy, however it plays a vital role, since without its inclusion the ionisation energy and atomisation energies would be much smaller than they are in reality.

3.9.2 Exchange correlation functionals

A major challenge within DFT is deriving suitable formulas for the exchange correlation term, however since there is little guidance from theory as to how suitable formulas can be derived, different routes have been taken forming many different functional forms of the exchange correlation term. Consequently one of the main

differences between DFT methods is the choice of the functional form of the exchange correlation term.

In order to derive an exchange correlation term, it is often divided into two parts, a pure exchange part, E_x, and a pure correlation part, E_c:

$$E_{xc}[\rho]=E_x[\rho]+E_c[\rho] \tag{3.27}$$

The exchange energy, E_x, includes the sum of contributions from both the up ($n_\uparrow$) and down ($n_\downarrow$) spin densities. Since the electron-electron potential energy obeys the Pauli exclusion principle, which states that no two electrons of the same spin may be found together at the same point in space, the exchange energy does not include the contributions from interactions between the same spin. The correlation energy, E_c, includes the effects of electron-electron Coulomb repulsion on the wavefunction.

Although there are many different functional forms of the exchange correlation energy this discussion will focus on three of the most popular forms: local density approximation, generalized gradient approximation and exact-exchange hybrid.

3.9.2.1 Local density approximation

Within the Local Density Approximation (LDA) it is assumed that the local density is treated as a uniform electron gas. Within this system the electrons are subjected to a constant external potential, as a result the charge density is constant. The system is consequently described by a single number: the value of the constant electron density. The uniform electron gas formula was initially utilised by Thomas-Fermi[34,35] to derive a functional form for the kinetic energy, and then later combined with the Dirac formula[38] to determine the exchange part of the exchange correlation energy, leading to a modification from the Thomas-Fermi method to form the Thomas-Fermi-Dirac method. However the inclusion of the Dirac exchange functional did not lead to any significant improvements mainly due to the poor representation of the kinetic energy by the Thomas-Fermi method.

The introduction of Kohn-Sham orbitals lead the kinetic energy to be calculated more rigorously, leading to the uniform electron gas approximation being used solely for the determination of the unknown exchange correlation energy, hence the local density approximation is applied exclusively to the exchange correlation energy. The total exchange correlation energy is described by:

$$E_{xc}^{LDA}[\rho]=\int\rho(r)\varepsilon_{xc}(\rho)dr \tag{3.28}$$

where $\varepsilon_{xc}(\rho)$ represents the exchange and correlation energy per particle of a uniform electron gas of density ρ. Since $E_{xc}(\rho)$ can be divided into separate exchange, E_x, and correlation E_c parts (see equation (3. 27)), the LDA has already been previously applied to the exchange energy, as was proposed by the Dirac exchange formula[38], as shown below:

$$E_x^{LDA}[\rho]=-C_x\int\rho(r)^{4/3}dr \tag{3.29}$$

where the constant C_x is:

$$C_x=\frac{3}{4}\left(\frac{3}{\pi}\right)^{1/3} \tag{3.30}$$

In the general case where the $n_\uparrow$ and $n_\downarrow$ spin densities are not equal, the LDA is replaced by the Local Spin Density Approximation (LSDA), in this case each individual spin density is raised to the power 4/3 before summation, as shown below:

$$E_x^{LSDA}\left[\rho_{n_\uparrow,n_\downarrow}\right]=-2^{1/3}C_x\int\left[\rho_{n_\uparrow}^{4/3}+\rho_{n_\downarrow}^{4/3}\right]dr \tag{3.31}$$

For closed shell systems where the number of $n_\uparrow$ and $n_\downarrow$ spins are equivalent, LSDA is identical to LDA. An example of an open shell system is a chlorine atom, where the outer shell contains seven electrons, three pairs and one single unpaired electron whereas a chlorine molecule is an example of a closed system, where there are no unpaired electrons.

The correlation energy of a uniform electron gas has been determined by simulating the homogeneous electron gas with numerical quantum Monte Carlo methods, this yields essentially exact results.[39] In order to use the Monte-Carlo results to produce a correlation functional which gives useful DFT results, the correlation energy has been fitted by a number of analytical forms.[40-43] A popular correlation functional has been constructed by Vosko, Wilk and Nusair,[42] by fitting an interpolation formula they have been able to give an accurate fit for a broad range of structures.

Since LDA is based on homogeneous electron gas results, it gives accurate results when applied to systems with slowly varying densities and chemical trends are well reproduced.[44] However it is a major and well known failure of LDA that the asymptotic behaviour of overlapped orbitals during bond formation is not correctly reproduced, thus bond dissociation energies are described poorly. It is also found that the exchange energy is generally underestimated and the correlation energy is overestimated, these errors tend to cancel each other out. An example of the errors in estimating the exchange and correlation energy has been demonstrated by a study on bulk silicon.[45] In general, LDA functionals, such as those based on the VWN functional, overestimates binding energies (typically by 20-30%) predicting shorter bond lengths.[33]

3.9.2.2 Gradient corrected approximation

To improve the accuracy of the LDA, non-local dependence in the energy functional is introduced by gradient corrected approximations, more specifically the accuracy is improved by taking the first Gradient Expansion Approximation (GEA). This is done by making a Taylor series expansion of the energy in terms of the gradient of the density. The first GEA appeared in the original Hohenberg-Kohn[36] and Kohn-Sham papers[37] and is based on the polarisability of the homogeneous electron gas. Although this GEA was not tested with actual calculations in the original papers, it was known that this method is limited to systems with slowly varying densities. In later calculations on atoms and molecules this GEA was shown to fail since the approximation of the exchange hole* does not satisfy the condition of normalising to

* The exchange hole (also known as the Fermi hole) is defined by the area around an electron where there is a reduced probability of finding another electron of the same spin.

minus one,[46,47] other investigations also found that the GEA does not converge for strongly inhomogeneous systems.[48,49]

Advancements in gradient corrected methods of finding the exchange correlation energy were developed from the early eighties by the development of functionals known as Generalised Gradient approximations (GGA).[50-59] Unlike LDA methods, GGAs consider a non-uniform electron gas by adopting a functional form which satisfies the normalisation condition of the wavefunction and ensures that the exchange hole is negative definite.[51] The resulting energy functional depends on both the density and its gradient but retains the analytic properties of the exchange correlation hole* intrinsic in the LDA. In general the GGA functional is developed to describe to the highest accuracy by the relation below:

$$E_{xc}^{GGA}\left[\rho_{n_\uparrow}, n_\downarrow\right] = \int f\left(\rho_{n_\uparrow}, \rho_{n_\uparrow}, \nabla\rho_{n_\uparrow}, \nabla\rho_{n_\downarrow}\right) dr \tag{3.32}$$

where $\rho_{n_\uparrow}, \rho_{n_\downarrow}$ represents the spin densities and $\nabla\rho_{n_\uparrow}$, $\nabla\rho_{n_\downarrow}$ represents the first derivative of the spin densities. The introduction of GGAs has lead to the development of a large number of different exchange and correlation functionals, however the following sections shall only discuss the two functionals, PW91 and PBE, which were utilised within this study.

3.9.2.2.1 PW91

The Perdew-Wang-91 (PW91)[58,60] functional is one of the most widely utilised GGAs, is contains no empirical parameters and is therefore constructed entirely from *first principles*. Perdew and Wang argued that the gradient expansion for the exchange correlation hole around an electron in real space is an expansion in the distance from the electron as well as its derivative. They developed a more accurate description of the exchange functional by cutting off the inaccurate long-range contributions in real space, and continued to use a wave-vector space for correlation energy.

* The correlation hole is defined by the area around an electron where there is a reduced probability of finding another electron of opposite spin. Thus the exchange-correlation hole is the area around an electron where the probability of finding an electron of either spin is reduced. The exchange-correlation hole contains a deficit of exactly one electronic charge.

In a variety of tests for atoms, molecules, solids and surfaces, it has been shown that the PW91 approximation is on average, more accurate than the LSDA or earlier GGAs.[61,62] It is shown that the atomisation energies are highly accurate for seven hydrocarbon molecules with an error of 0.1eV per bond for PW91 compared to the 0.7eV error per bond for LSDA and 2.4eV error per bond for Hartree-Fock theory. [58] PW91 corrects the LDA overestimate of atomisation energies for molecules and solids in almost all cases, it enlarges the equilibrium bond lengths and lattice spacings, reduces the vibrational frequencies,[63] and improves activation barriers.[64] In general the PW91 functional reduces exchange energy errors from 10% in LDA to 1% and correlation errors from 100% to about 10%.[58,59] However neither the LDA or PW91 can describe the long-range part of the exchange correlation hole, fortunately this does not seem to be an important limitation for most properties of interest in quantum chemistry,[58] unless one is studying metal surface energy where the long-range tail of the exchange correlation hole must be taken into account.[65]

3.9.2.2.2 PBE

The Perdew-Burke-Ernzerhof (PBE) functional[66-69] has been constructed in a manner such that all the essential conditions of the reliability of the LDA are maintained; this is due to a number of papers validating the success of the LDA,[70-72] arguing that it obeys a number of physical constraints such as the normalisation constraint on the exchange-correlation hole. The PBE functional also aims to solve the problems associated with the PW91 functional by deriving a simple new GGA functional where all parameters (except those in $\varepsilon_{xc}^{unif}\left(\rho_{n_\uparrow},\rho_{n_\downarrow}\right)$) are fundamental constants. The PBE functional eliminates the problem of over-parameterisation by introducing a simple exchange enhancement function:

$$F_x(s)=1+\kappa-\frac{\kappa}{\left(\left(1+\mu\, s^2\right)/\kappa\right)} \tag{3.33}$$

where κ=0.804, μ=0.21951 and F_x depends on the reduced density gradient, s:

$$s = \frac{|\nabla \rho|}{2k_F \rho} \tag{3.34}$$

where $k_F = (3\pi^2 \rho)^{1/3}$. The constants μ and κ are chosen in such a way, that the gradient expansion around s=0 should give the correct linear response of the homogeneous electron gas, and the local Lieb-Oxford bound[73] must be satisfied. The Lieb-Oxford bound states that the following inequality is satisfied:

$$\begin{aligned} E_x[\rho_{n\uparrow,n\downarrow}] &\geq E_{xc}[\rho_{n\uparrow,n\downarrow}] \\ E_x[\rho_{n\uparrow,n\downarrow}] &\geq -1.679e^2 \int d^3 r \rho(r)^{4/3} \end{aligned} \tag{3.35}$$

The PBE exchange correlation energy can be written in the following form:

$$E_{xc}^{PBE} = d^3 r \rho(r) \varepsilon_{xc}^{PBE}(r_s(r), s(r), \zeta(r)) \tag{3.36}$$

where $\zeta = (\rho_{n\uparrow} - \rho_{n\downarrow})/\rho$ is the spin polarisation and $r_s = (4\pi\rho/3)^{-1/3}$.

The authors of the PBE functional state that all parameters in the PBE functional are fundamental constants, however the κ term is fixed by the *local* Lieb-Oxford bound condition (*i.e.* $\varepsilon_x(r) \geq 1.68\rho(r)^{3/4}$ for all r), although this is sufficient, it is an unnecessary criterion for the *integrated* Lieb-Oxford bound (as stated in equation (3. 35)). The removal of the *local* Lieb-Oxford constraint has led to Zhang and Wang's construction of the revPBE[74,75] exchange functional, which has the same correct formal properties as the PBE except the κ coefficient has been modified to 1.245. The revPBE systematically improves the atomization energies[74] and chemisorption energies[76].

The main concern with revPBE is that is does not fulfil the *local* Lieb-Oxford criterion, Hammer *et al.*[76] have developed an alternative functional, named RPBE, which like revPBE improves the description of molecules, however at the same time satisfies the *local* Lieb-Oxford bound.

The exchange enhancement functions of the three functions, PBE, revPBE and RPBE are compared in Figure 3. 7, this figure shows the deviation of revPBE from the *local* Lieb-Oxford bound.

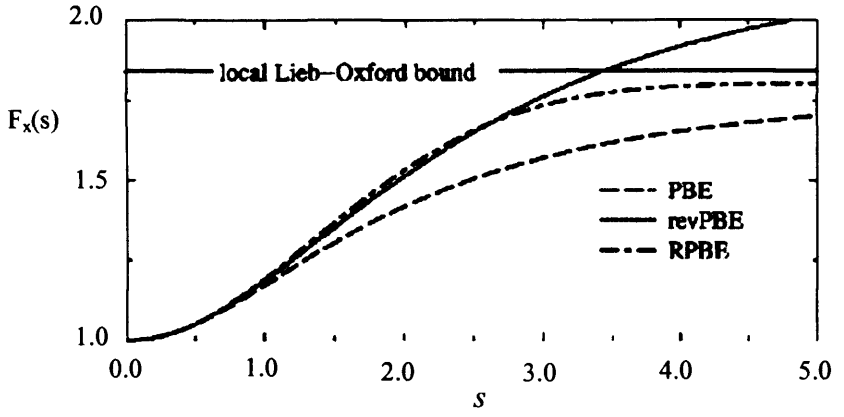

Figure 3. 7: The exchange enhancement factor for the different GGA functionals as a function of the reduced density gradient, *s*. (Reproduced without permission from Hammer *et al.*[76])

Contrary to previous articles it has also been shown by Kurth *et al.*[77] by tests on molecular and solid state systems that properties such as the exchange and correlation surface energies (of jellium) and the equilibrium unit cell volume of bulk solids, calculated with the RPBE and revPBE functionals are in larger disagreement with experimental results, than the same properties calculated with the original PBE functional.

Investigations of GGA for the exchange and correlation functional of DFT for atoms, clusters and crystals has shown that the atomic total energy and first ionisation energy by the PBE functional are far more accurate than the LDA, and comparable to the PW91 functional.[66,78] The over binding of clusters in solids by LDA are either corrected or overcorrected by PBE.[67,78] The PBE functional gives realistic binding energy curves for rare-gas dimmers, whereas other GGAs are known to fail.[79,80] In solid state physics, it improves lattice constants and magnetic properties of many metals and pressures for phase transition.[81] However it is found that PBE does not always improve on LDA lattice constants, and in the case of Ge less accurate lattice constants were predicted. PBE, and other GGAs, are also found to significantly underestimate exchange energies of surfaces.[82]

Overall it is found that the accuracy of the GGA is usually comparable to conventional quantum chemistry methods such as Hartree-Fock theory but at a much lower computational cost. On the whole, GGAs also offer significant improvements in the calculation of molecular properties compared to their predecessor the LDA.

3.9.2.3 Exact-exchange hybrid

A third class of functionals used to estimate the exchange correlation energy are known as hybrid methods.[83] The hybrid model contains two parts to the exchange correlation energy, the first is an exchange energy part as given exactly by Hartree-Fock theory and the second is an approximation using DFT. Using the LDA and GGA as the DFT part results in a method known as the generalised version of the Half-and-Half method. The generalised Half-and-Half method may be defined by writing the exchange energy as a suitable combination of LDA, exact exchange and a gradient correction term. The correlation energy may in the same way be taken as the LDA formula plus a gradient correction term, as shown below:

$$E_{xc}^{Hybrid} = (1-a)E_x^{LDA} + aE_x^{exact} + b\Delta E_x^{GGA} + E_c^{LDA} + cE_c^{GGA} \qquad (3.37)$$

where the parameters *a, b* and *c* are determined by fitting to experimental data and depend on the form chosen for E_C^{GGA}.

Hybrids give significant improvement over GGAs for many molecular properties, consequently they are a very popular choice of functional in quantum chemistry. The most popular hybrid functional has been the B3LYP scheme proposed by Stephens *et al.*[84], which is a combination of exact HF exchange energy with local gradient-corrected exchange terms derived by Becke,[83] and a the LYP correlation functional developed by Lee *et al.*.[57] The parameters in the Becke exchange functional have been obtained by fitting data from heats of formation of small molecules. The LYP correlation functional, which is a modification of the correlation energy formula proposed by Colle

and Salvetti,[85] is based on a treatment of the helium atom and only really treats correlation between opposite spins.[57]

Investigations of seven exchange and correlation functionals by Curtiss *et al.*[86] on the G2 natural test set* show that the B3LYP method performs the best, with an average absolute deviation from atomisation energy of 3.11kcal/mol. The BLYP method performs best out of the nonhybrid DFT methods.

Ab initio calculations testing the B3LYP functional with LDA and GGA functionals have also been carried out in order to test the accuracy of these methods.[84,87] They found that the IR-adsorption spectra calculated with B3LYP is in impressive agreement with experiment, where as the BLYP (a GGA functional which combines the Becke88[56] exchange functional with the LYP[57] correlation functional) and LDA functionals are unable to predict all peaks and correct intensities.[84]

This research has made use of non-local GGA functionals since they are more sophisticated at calculating total energies and are able to predict structural properties without overbinding, as observed with LDA. The PBE functional has been utilised to minimise small silicate and aluminosilicate clusters, and the PW91 functional has been used in preliminary calculations to minimise slab structures.

3.10 Basis sets

The fundamental nature of *ab initio* methods is to derive information about systems by solving the Schrödinger equation without fitting to any parameters to experimental data. As stated earlier there are very limited cases where the Schrödinger equation can be solved exactly, and so approximations such as HF and DFT are used. To determine the performance of these approximate methods, experimental data is used as a point of reference, thus experimental data is used as guides rather than directly entered into the method, as in classical methods (as in section 3.1).

* The G2 natural test set is a set of 148 molecules, having well-established enthalpies of formation at 298K. The G2 set set includes 29 radicals, 35 nonhydrogen systems, 22 hydrocarbons, 47 substituted hydrocarbons and 15 inorganic hydrides. It is hoped that this test set will provide a means for assessing and improving new theoretical models.

An approximation common with both HF and DFT methods is the use of basis sets to describe an unknown function, for example molecular orbitals. Basis sets describe unknown functions by expanding a set of known functions, thus if an infinite number of known functions are used, the basis set is not an approximation since it is said to be complete. In practice, it is impossible to use an infinite number of functions, as a result a finite number of functions are used. The smaller the basis set the poorer the representation but at a much cheaper the computational cost. However the type of basis function used also influences the accuracy.

3.10.1 Slater and Gaussian type orbitals

There are two types of basis functions (also known as atomic orbitals) used to create basis sets: Slater Type Orbitals (STO) and Gaussian Type Orbitals (GTO). STOs are based on exponential functions, which ensure a rapid convergence with increasing number of functionals. It is relatively straightforward to evaluate integrals of STOs involving one- or two centres when based on different nuclei, however three- and four-centre integrals are very difficult to evaluate when based on different nuclei. As a result STOs are mainly used for atomic and diatomic systems where a high level of accuracy is required.

The second type of basis function is known as the GTO, and is of the general form:

$$\chi(x,y,z) = x^a y^b z^c e^{-\zeta r^2} \tag{3.38}$$

where $e^{-\zeta r^2}$ represents the Gaussian function, ζ represents the radial extent or spread of the Gaussian, thus large values of ζ has a small spread, whereas small values of ζ has a large spread. The type of orbital is determined by the powers of the Cartesian variables x^a, y^b, z^c, for example $a+b+c=1$ is a p-orbital.

Unlike the STO which forms a cusp at the nucleus, the r^2 dependence of the exponential in of Gaussian functions give GTOs a zero gradient at the nucleus, as a result GTOs

have problems representing the behaviour at the nucleus. Another failing of the GTO is that it decays to zero too rapidly far from the nucleus, thus the tail of the wavefunction is represented poorly. As a result of these shortcomings it is found that the replacing a STO with a GTO leads to a large reduction in accuracy.

The accuracy of GTOs can be increased by using a number of Gaussian basis functions, this leads to a three times the number of Gaussian functions required compared to STOs to obtain the same level of accuracy. However unlike STOs, the integrals in GTOs are far easier to calculate, therefore in terms of computational expense GTOs are preferred.

A graphical representation of the 1s STO and four Gaussian expansions is shown by Figure 3. 8, this graph clears displays how the fit improves with an increase in the number of Gaussian functions. However the cusp at the nucleus and exponential tail is still not accurately represented; as a result Gaussian functions tend to underestimate long range overlap between atoms and the charge and spin density at the nucleus.

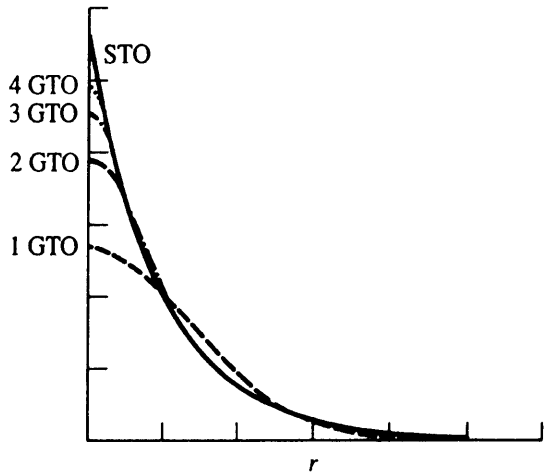

Figure 3. 8: Comparison of 1s Slater-type orbital and Gaussian expansions with up to four terms. (Reproduced without permission from Leach[32])

3.10.2 Multiple basis functions

An important factor which needs to be taken into account, regardless of the type of basis function and where they are centred, is the number of functions in the basis set. The smallest number of functions is known as a minimum basis set. A minimal basis set contains only the number of functions that are required to accommodate all the filled orbitals in each atom, for example hydrogen and helium would only have a single s-type function.

The minimal basis set can improved on by doubling the number of basis functions in the minimal basis set to produce a Double Zeta* basis (DZ), thus two s-type functions (1s and 1s') are used to represent hydrogen. By doubling the number of basis functions, the electron distribution in different directions and different types of bonds (*e.g.* σ- and π-bonds) can be described in greater detail. The number of basis functions can be increased further to Triple Zeta (TZ), *i.e.* tripling the number of basis functions in the minimal basis set, Quadruple Zeta (QZ), Quintuple Zeta (5Z) and so on. Although an increased number of basis functions improves the description of the electron distribution, in cases where atoms are polarised increasing the number of functions does improve the accuracy.

3.10.2 Polarisation functions

Polarisation functions implement the effect of polarisation by adding additional orbitals which are not present within the minimal basis set. For example, the electron cloud of a hydrogen atom is represented by a spherical s-orbital, however when a hydrogen atom in present in a molecule, *i.e.* HCN, the electrons are attracted to other nuclei, thus the electrons are distorted. The perturbed electrons can be best described by mixing p-orbital character into the s-orbital of the hydrogen to form a sp-hybrid.

In general polarisation functions are higher angular momentum functions, hence they correspond to p-orbital character for polarising s-orbitals. d-orbital character for polarising p-orbitals, and so on. Polarisation functions are denoted by an asterisk (*) or

* The term zeta originates from the fact that the STO and GTO basis functions is often symbolized by the Greek letter ζ

a 'P', *e.g.* STO-3G* represents three Gaussian functions used to represent each STO with polarisation, and DZP represents a Double Zeta basis set with Polarisation.

In this work a double basis set with a polarisation function has been used to minimise silica and aluminosilicate fragments.

3.11 Density functional theory codes

3.11.1 DMol^3

DMol^3 is an *ab initio* quantum chemistry code designed to perform calculations using DFT methodology.[88] The DMol^3 code can be used for a large variety of molecules or structures which are entered as either finite molecular systems. DMol^3 allows the user to calculate the electronic energy of molecular orbitals within a chemical system, predict the molecular geometry, determine the harmonic vibrational frequencies and calculate thermodynamic properties, orbital eigenvalues and occupations. The effects of solvents on a molecular system can also be investigated through the implementation of the COSMO[89] model.

When solving DFT equations it is convenient to expand molecular orbitals in terms of a linear combination of atomic orbitals (LCAOs):

$$\phi_i = \sum_{\mu} C_{i\mu} \chi_{\mu} \qquad (3.39)$$

where the atomic orbitals χ_{μ} are often referred to as atomic basis functions and $C_{i\mu}$ is the molecular orbital expansion coefficient. DMol^3 operates by using numerical functions to describe the atomic basis functions. The numerical basis functions are based on numerical values derived on an atomic-centred spherical-polar mesh, rather than analytical functions (*e.g.* STOs or GTOs). The angular portion of each function is the appropriate spherical harmonic and the radial component is generated by solving the DFT equations for each individual atom numerically. The accuracy of the atomic basis

sets minimises superposition error and an excellent description of even weak bonds are possible.

Once the solutions to the DFT equations have been found, DMol^3 is able to provide the molecular wavefunctions and electron densities, which can be used to evaluate the energetics properties of the system. In addition, evaluation of the energy gradients provides a convenient method for determining the equilibrium geometry of the system. The results calculated by DMol^3 provide a reliable predictive method for theoretically exploring the properties of compounds.

3.11.1.1 COSMO

As many chemical reactions take place in solvents it is important to simulate a solvated environment to consider the solvent effects on the behaviour of the system. Where the solvent molecules are directly involved within the reaction it is necessary to model them explicitly. However in systems where the solvent doesn't directly interact with the solute, the dielectric properties of the solvent can be modelled with COSMO, hence the solvent molecules are modelled implicitly. Here the solvent acts as a perturbation on the gas-phase behaviour of the system, which can be modelled *via* continuum solvent models.[90] A considerable number of models have been devised for use in both classical and quantum models,[91-95] however we shall concentrate on the COnductor-like Screening MOdel (COSMO) applied within DMol^3.

COSMO[89] is a type of polarisable continuum model,[96] where the solute molecule forms van der Waals surface type cavity within a dielectric continuum of permittivity which represents the solvent. The charge distribution of the solute molecule polarises the dielectric continuum generating a screen of charges on the cavity surface (see Figure 3. 9).

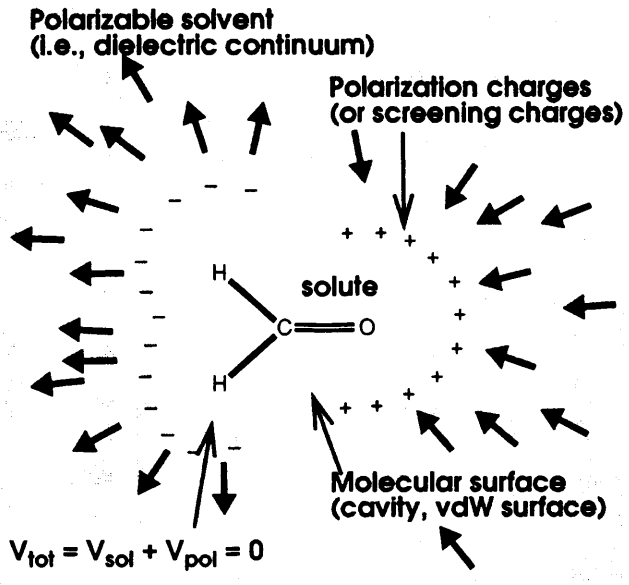

Figure 3. 9: COSMO model: illustrating how the solute molecule polarises the dielectric continuum. (Reproduced without permission from the DMol^3 manual)[97]

The COSMO model is a simplified version of other continuum models, which does not need to resolve complicated boundary conditions of a dielectric in order to determine screening charges of the cavity surface. Although the COSMO approximation is a simplified model, deviations tested by both Klamt and Schüürmann[89] and Anderzelm *et al.*[98] have shown that results do depend on the choice of van der Waals radii used to evaluate the cavity surface, and energies do depend on parameters such as the DFT functional and basis set, however they are of high quality. For example, the DMol^3/COSMO model can predict solvation energies for neutral solutes with an accuracy of about 2kcal/mol.[98]

Within this study DMol^3 has been utilised to determine the stability of small clusters, and their minimum energy configurations. These calculations have been carried out in vacuum and solution *via* the COSMO model. The COSMO model has been utilised to recreate the aqueous environment in which zeolites crystallise. By comparing the stability and conformation of units in vacuum and solution, the effect of an aqueous environment on the clusters is determined, and by doing so, the validity of using additional computational expense to model a solvated medium can be concluded. These calculations can also provide data to reveal which clusters may play an important role

within zeolite growth, this is done by comparing the stability of these units, and as a result, the order in which units may amalgamate to form small clusters during crystal formation may be established.

For completeness, the following sections describe the CASTEP code and the background of pseudopotentials. In this study, preliminary 3D periodic energy minimisation calculations (as described in section 3.7.2) were carried out to determine the ground state energy and structure of zeolite slabs.

3.11.2 CASTEP/ New CASTEP

The quantum mechanical package CASTEP was originally developed in the Theory of Condensed Matter Group as Cambridge University, UK,[99] thus the acronym CASTEP stands for Cambridge Sequential Total Energy Package. CASTEP is capable of applying DFT to a number and type of atoms in a system which is periodic, however CASTEP can also be applied to supercells constructed to study defects, molecules or surfaces/ interfaces. By applying DFT methods, CASTEP is able to simulate electronic relaxation for the ground state, capable of calculating forces acting on atoms and stress on the unit cell. Atomic forces can be used to either predict properties such as lattice constants, the equilibrium structure or to perform molecular dynamics simulations (either canonical or microcanonical ensemble). CASTEP also contains the function of calculating elastic constants, band structures, density-of-states, charge densities and wave functions and optical properties.

3.11.2.1 Pseudopotentials

CASTEP solves DFT equations by using a total energy plane-wave pseudopotential (PW-PP) scheme. The design of the pseudopotentials (also known as effective core potentials) method is to solve DFT equations by considering only valence electrons, core electrons are excluded under the assumption that their charge density is not affected by the changes in the chemical environment, thus the core electrons are represented by a suitable function. [100,101]

The pseudopotential function gives a wavefunction with the same shape as the true wavefunction outside the core region, but with fewer nodes inside the core region, as shown by Figure 3. 10.

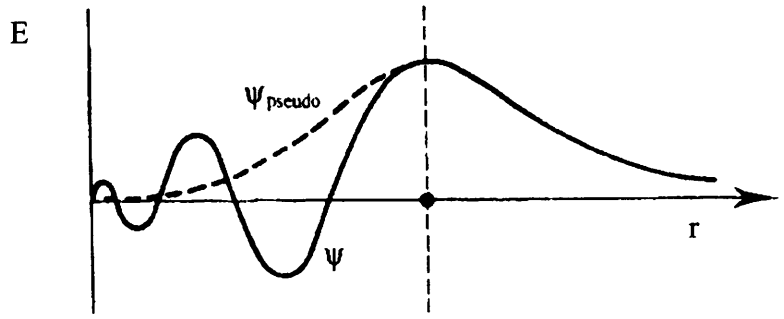

Figure 3. 10: Schematic illustration of all-electron (solid lines) and pseudopotential (dashed line) potentials and their corresponding wavefunctions (Reproduced without permission from Payne *et al.*[99])

The pseudopotential approximation has the advantage of the exclusion of relativistic effects which are mainly due to core electrons and also eliminates the problem of having to use large number of basis functions to expand the corresponding orbitals which are necessary to describe the valence orbitals in standard potentials.

3.11.2.2 Plane-waves basis set

Bloch's theorem* states that the electronic wavefunctions at each **k** point† can be expanded in terms of discrete plane-wave basis set, this leads to a three-dimensional Fourier series representation of the wavefunction. Each electron wavefunction can be written as a sum of plane-waves, where plane-waves are written in an exponential form. In principle, an infinite plane-waves basis set is required to expand the electronic wavefunctions, however application of Bloch's theorem allows the electronic wavefunction to be expanded in terms of a discrete set of plane waves. By introduction

* Bloch's theorem states that in a periodic solid each electronic wavefunction can be written as a product of a cell periodic part and a wavelike part.

† A set of **k** points are used to map out electronic states, a set of **k** points are determined by the boundary conditions that apply to the bulk solid in question.

of an energy cutoff to the discrete plane-wave basis set, a finite basis set is produced. By applying cutoffs to the energy, errors are introduced into the calculation, however the magnitude of error may be reduced by increasing the energy cutoff until the calculated total energy has converged.

Although plane-waves have the advantage that the quality of the basis set depends on a single parameter, they are mathematically simple and their derivatives are products in **k**-space, one of the major disadvantages it that all space is treated with the same quality. Thus empty space also has the same high quality representation as regions of interest, as a result the computational cost of the calculation is increased for regions which are of no interest, whereas DMol^3 has the advantage of only representing the area of interest.

Plane-waves are often linked with pseudopotentials since only pseudo-wave functions can be represented with a small number of Fourier components without compromising in accuracy. It is also a relatively straightforward task to Fourier transform the pseudo-wave function from real to reciprocal space or vice versa. The CASTEP program allows approximations to the exchange correlation energy with functionals constructed by LDA or GGA. In general the PW-PP method is more efficient and less expensive as there are fewer electronic states in the solid state calculation.

A new version of CASTEP has been completely rewritten in Fortran-90 by the CASTEP development group and released in 2001.[102] The new code was designed and specified in advance, with a consistent design philosophy throughout. The aim of new CASTEP is to deliver a clean, stable, portable code which would be easy to maintain and develop. The code was to be designed from the start as a parallel code, and to use Vanderbilt ultrasoft pseudopotentials to represent the ionic potentials efficiently.

The following chapters will describe how the theory and methodology described throughout this chapter has been applied to natural zeolites to determine ground state energies, stable structural configurations and crystal morphologies.

REFERENCES

1 C. R. A. Catlow and A. Cheetham. *New trends in material chemistry*

2 M. Born and K. Huang. *Dynamical theory of crystal lattices (international series of monographs on physics)* (Oxford, University Press, 1954)

3 P. P. Ewald. *Ann. Physik.* **64**, 253 (1921)

4 M. P. Allan and D. J. Tildesley. *Computer silmulation of liquids* (Oxford University Press, Oxford, 1987)

5 B. G. Dick and A. W. Overhauser. *Physical Review* **112**, 90 (1958)

6 M. J. Sanders, M. Leslie and C. R. A. Catlow. *J. Chem. Soc. Chem. Commun.*, 1271 (1984)

7 R. Grau-Crespo, E. Acuay and R. R. Ruiz-Salvador. *Chem. Commun.*, 2544 (2002)

8 G. Maurin, R. G. Bell, S. Devautour, F. Henn and J. C. Giuntini. *J. Phys. Chem. B* **108**, 3739 (2004)

9 L. Whitmore, B. Slater and C. R. A. Catlow. *Phys. Chem. Chem. Phys.* **2**, 5354 (2000)

10 B. Slater, C. R. A. Catlow, Z. Liu, T. Ohsuna, O. Terasaki and M. A. Camblor. *Angew. Chem.-Int. Edit.* **41**, 1235 (2002)

11 B. W. H. van Beest, G. J. Kramer and R. A. van Santen. *Physical Review Letters* **64**, 1955 (1990)

12 G. J. Kramer, N. P. Farragher, B. W. H. Vanbeest and R. A. Vansanten. *Phys. Rev. B* **43**, 5068 (1991)

13 B. Palmieri and D. Ronis. *Phys. Rev. E* **68**, art. no. (2003)

14 M. Rarivomanantsoa, P. Jund and R. Jullien. *J. Chem. Phys.* **120**, 4915 (2004)

15 N. H. de Leeuw, Z. M. Du, J. Li, S. Yip and T. Zhu. *Nano Lett.* **3**, 1347 (2003)

16 S. M. Auerbach, N. J. Henson, A. K. Cheetham and H. I. Metiu. *Journal of Physical Chemistry* **99**, 10600 (1995)

17 E. Jaramillo and S. M. Auerbach. *J. Phys. Chem. B* **103**, 9589 (1999)

18 C. R. A. Catlow, C. M. Freeman, B. Vessal, S. M. Tomlinson and M. Leslie. *J. Chem. Soc. Far. Trans.* **87**, 1947 (1991)

19 J. R. Hill and J. Sauer. *Journal of Physical Chemistry* **98**, 1238 (1994)

20 J. R. Hill and J. Sauer. *Journal of Physical Chemistry* **99**, 9536 (1995)

21 J. D. Gale. *J. Chem. Soc.-Faraday Trans.* **93**, 629 (1997)

22 J. D. Gale and A. L. Rohl. *Mol. Simul.* **29**, 291 (2003)

23 D. H. Gay and A. L. Rohl. *J. Chem. Soc. Far. Trans.* **91**, 925 (1995)

24 D. E. Parry. *Surf. Sci.* **49** (1975)

25 D. E. Parry. *Surf. Sci.* **54**, 195 (1976)

26 D. M. Heyes, M. Barber and J. H. R. Clarke. *J. Chem. Soc. Far. Trans.* **73**, 1485 (1977)

27 J. D. Donnay and G. Harker. *Am. Mineral.* **22**, 446 (1937)

28 F. Bertaut. *Comp. Rend.* **246**, 3447 (1958)

29 J. A. Venables. *Introduction to surface and thin film processes* (Cambridge University Press, 2000)

30 W. Kolos and L. Wolniewicz. *Journal of Chemical Phys.* **41**, 3663 (1964)

31 F. Jensen. in *Introduction to computational chemistry* 53 (Wiley, 1999).

32 A. R. Leach. in *Molecular modelling: Principles and applications* 25 (Longman, 1996).

33 N. M. Harrison. in *Computation material science* (eds. C. R. A. Catlow and E. Kotomin) 45.

34 L. H. Thomas. *Proc. Camb. Phil. Soc.* **23**, 542 (1927)

35 E. Fermi. *Rend. Accad. Lincei* **6**, 602 (1927)

36 P. Hohenberg and W. Kohn. *Physical Review* **136**, B864 (1964)

37 W. Kohn and L. J. Sham. *Physical Review* **140**, A1133 (1965)

38 P. A. M. Dirac. *Proc. Camb. Phil. Soc.* **26**, 376 (1930)

39 D. M. Ceperley and B. J. Alder. *Physical Review Letters* **45**, 566 (1980)

40 J. P. Perdew and A. Zunger. *Phys. Rev. B* **23**, 5048 (1980)

41 U. von Barth and L. Hedin. *J. Phys.* **C5**, 1629 (1972)

42 S. J. Vosko, L. Wilk and M. Nusair. *Can. J. Phys.* **58**, 1200 (1980)

43 J. P. Perdew and Y. Wang. *Phys. Rev. B* **45**, 13244 (1992)

44 N. Wilson and J. Muscat. *Mol. Simul.* **28**, 903 (2002)

45 R. Q. Hood, M. Y. Chou, A. J. Williamson, G. Rajagopal, R. J. Needs and W. M. C. Foulkes. *Physical Review Letters* **78**, 3350 (1997)

46 Y. Yang, J. P. Perdew, J. A. Cevary, L. D. Macdonald and S. H. Vosko. *Physical Review A* **41**, 78 (1990)

47 J. P. Perdew. *Physical Review Letters* **55**, 1665 (1985)

48 J. P. Perdew, D. C. Langreth and V. Sahni. *Physical Review Letters* **38**, 1030 (1977)

49 S.-K. Ma and K. A. Brueckner. *Physical Review* **165**, 18 (1968)

50 D. C. Langreth and J. P. Perdew. *Phys. Rev. B* **21**, 5469 (1980)

51 J. P. Perdew and W. Yue. *Phys. Rev. B* **33**, 8800 (1986)

52 J. P. Perdew. *Phys. Rev. B* **33**, 8822 (1986)

53 J. P. Perdew. *Phys. Rev. B* **34**, 7406 (1986)

54 D. C. Langreth and M. J. Mehl. *Phys. Rev. B* **28**, 1809 (1983)

55 J. P. Perdew. *Phys. Rev. B* **40**, 3399 (1989)

56 A. D. Becke. *Physical Review A* **38**, 3098 (1988)

57 C. T. Lee, W. T. Yang and R. G. Parr. *Phys. Rev. B* **37**, 785 (1988)

58 J. P. Perdew, J. A. Chevary, S. H. Vosko, K. A. Jackson, M. R. Pederson, D. J. Singh and C. Fiolhais. *Phys. Rev. B* **46**, 6671 (1992)

59 J. P. Perdew, J. A. Chevary, S. H. Vosko, K. A. Jackson, M. R. Pederson, D. J. Singh and C. Fiolhais. *Phys. Rev. B* **48**, 4978 (1993)

60 K. Burke and J. P. Perdew. *Int. J. Quantum Chem.* **56**, 199 (1995)

61 M. Ernzerhof, J. P. Perdew and K. Burke. in *Density functional theory i* 1 (1996).

62 J. P. Perdew, K. Burke and M. Ernzerhof. in *Chemical applications of density-functional theory* 453 (1996).

63 K. Burke, J. P. Perdew and M. levy. in *Modern density functional theory: A tool for chemisty* (eds. J. M. Seminario and P. Politzer) (Elsevier, Amsterdam, 1995).

64 B. Hammer, K. W. Jacobsen and J. K. Norskov. *Physical Review Letters* **70**, 3971 (1993)

65 D. C. Langreth and J. P. Perdew. *Phys. Rev. B* **26**, 2810 (1982)

66 J. P. Perdew, K. Burke and M. Ernzerhof. *Physical Review Letters* **77**, 3865 (1996)

67 M. Ernzerhof and G. E. Scuseria. *J. Chem. Phys.* **110**, 5029 (1999)

68 A. Zupan, K. Burke, M. Ernzerhof and J. P. Perdew. *Journal of Chemical Phys.* **106**, 10184 (1997)

69 J. P. Perdew, M. Ernzerhof, A. Zupan and K. Burke. *Journal of Chemical Phys.* **108**, 1522 (1998)

70 O. Gunnarsson, M. Jonson and B. I. Lundqvist. *Phys. Rev. B* **20**, 3136 (1979)

71 K. Burke, J. P. Perdew and M. Ernzerhof. *J. Chem. Phys.* **109**, 3760 (1998)

72 R. O. Jones and O. Gunnarsson. *Rev. Mod. Phys.* **61**, 689 (1989)

73 E. H. Lieb and S. Oxford. *Int. J. Quantum Chem.* **19**, 427 (1981)

74 Y. Zhang and W. Yang. *Physical Review Letters* **80**, 890 (1998)

75 J. P. Perdew, K. Burke and M. Ernzerhof. *Physical Review Letters* **80**, 891 (1998)

76 B. Hammer, L. B. Hansen and J. K. Norskov. *Phys. Rev. B* **59**, 7413 (1999)

77 S. Kurth, J. P. Perdew and P. Blaha. *Int. J. Quantum Chem.* **75**, 889 (1999)

78 I. H. Lee and R. M. Martin. *Phys. Rev. B* **56**, 7197 (1997)

79 Y. Zhang, W. Pan and W. Yang. *J. Chem. Phys.* **107**, 7921 (1997)

80 D. C. Patton and M. R. Pederson. *Physical Review A* **56**, R2495 (1997)

81 A. Zupan, P. Blaha, K. Schwarz and J. P. Perdew. *Phys. Rev. B* **58**, 11266 (1998)

82 J. P. Perdew, S. Kurth, A. Zupan and P. Blaha. *Physical Review Letters* **82**, 2544 (1999)

83 A. D. Becke. *J. Chem. Phys.* **98**, 1372 (1993)

84 P. J. Stephens, F. J. Devlin, C. F. Chabalowski and M. J. Frisch. *Journal of Physical Chemistry* **98**, 11623 (1994)

85 R. Colle and D. Salvetti. *Theor. Chim. Acta.* **37**, 329 (1975)

86 L. A. Curtiss, K. Raghavachari, P. C. Redfern and J. A. Pople. *J. Chem. Phys.* **106**, 1063 (1996)

87 A. D. Becke. *J. Chem. Phys.* **98**, 5648 (1993)

88 B. Delley. *Journal of Physical Chemistry* **91**, 508 (1990)

89 A. Klamt and G. Schuurmann. *J. Chem. Soc.-Perkin Trans. 2*, 799 (1993)

90 P. E. Smith and B. M. Pattitt. *Journal of Physical Chemistry* **98**, 9700 (1994)

91 M. Born. *Zeitschrift fur Physik* **1**, 45 (1920)

92 L. Onsager. *American Chemical Society* **58**, 1486 (1936)

93 J. G. Kirkwood. *J. Chem. Phys.* **2**, 351 (1934)

94 A. A. Rashin and K. Namboodiri. *Journal of Physical Chemistry* **91**, 6003 (1987)

95 A. A. Rashin. *Journal of Physical Chemistry* **94**, 1725 (1990)

96 S. Miertus, E. Scrocco and J. Tomasi. *Chemical Physics* **55**, 117 (1981)

97 *Dmol 96.0/4.0.0 quantum chemistry user guide* (Molecular Simulations, San Diego, 1996)

98 J. Andzelm, C. Kolmel and A. Klamt. *J. Chem. Phys.* **103**, 9312 (1995)

99 M. C. Payne, M. P. Teter, D. C. Allan, T. A. Arias and J. D. Joannopoulos. *Rev. Mod. Phys.* **64**, 1045 (1992)

100 G. Frenking, I. Antes, M. Bohme, S. Dapprioh, A. W. Ehlers, V. Jonas, A. Nauhaus, M. Otto, R. Stegmann, A. Veldkamp and S. F. Vyboishchikov. *Rev. Comput. Chem.* **8**, 63 (1996)

101 T. R. Cundari, M. T. Benson, M. L. Lutz and S. O. Sommerer. *Rev. Comput. Chem.* **8**, 145 (1996)

102 M. D. Segall, P. J. D. Lindan, M. J. Probert, C. J. Pickard, P. J. Hasnip, S. J. Clark and M. C. Payne. *J. Phys.-Condes. Matter* **14**, 2717 (2002)

CHAPTER FOUR:

AN ATOMISTIC STUDY OF EDINGTONITE

4.0 INTRODUCTION

The aim of the work presented within this chapter is to use atomistic techniques to accurately model the bulk structure of a natural zeolite, which can then be used as a starting point to model a number of surface terminations to determine the most thermodynamically stable surface structure. The most stable surface of each face can then be used to predict the morphology of the crystal, by determining the inter-planar spacing, the attachment energy or the surface energy (as described in chapter 3, section 3.7.2).

The natural zeolite edingtonite (EDI) was selected for this study since it contains only 50 atoms per unit cell, which is small in comparison to, for example faujasite, which contains 182 atoms per unit cell, therefore computational expense is minimised and it also allows one to carry out *ab initio* calculations which, cannot be performed on large numbers of atoms (>150). EDI has also been well characterised experimentally, and is known to have an ordered silicon and aluminium framework, with distinct aluminium positions.[1] Also, the atomic positions of molecular water within the framework are well known,[2] which allows a precise model to be constructed for the starting point. All of these considerations make EDI an ideal material to develop a systematic approach to deducing thermodynamically stable surface structures and predicting crystal morphology.

4.1 Edingtonite (EDI) crystal structure.

Edingtonite is a rare Barium zeolite first described by Haidinger[3] in 1825. The structure was first solved by Taylor and Jackson[4] in 1933 and subsequently refined by Galli[5] in 1976, Kvick and Smith[1] in 1983 and by Mazzi *et al.*[2] in 1984. The ideal composition of

Edingtonite is $Ba_2Al_4Si_6O_{20}.8H_2O$ (with a 3:2 Si:Al ratio); with the structure type EDI. The chemical composition of all the edingtonites are very similar, the only discrepancy is in the amount of water present in each sample.

The symmetry of the edingtonite structure is $P\bar{4}2_1m$, however ordering of the Si and Al in the tetrahedra reduces the symmetry down to $P2_12_12$. The structure in this space group has an orthorhombic cell with cell dimensions of a=9.550Å, b=9.665Å and c=6.523Å and $\alpha=\beta=\gamma=90°$. EDI belongs to the fibrous family of zeolites, the main attribute of the structure is the presence of chains of SiO_4 and AlO_4 tetrahedra parallel to the c axis. Each chain is linked through the O bridges to four neighbouring chains to form a three-dimensional framework, two sets of intersecting channels delimited by eight-membered rings run throughout the structure normal to c. The minimum free diameter of each of these channels is 2.8×3.8Å assuming the effective radius of the O to be 1.35 Å. Each Ba cation is coordinated to six framework oxygens and four water oxygens and lies in the centre of the channel, with the hydrogen atoms from the water molecule bent away from the Ba atom. Figure 4. 1 illustrates the bulk crystal structure of natural hydrated EDI.

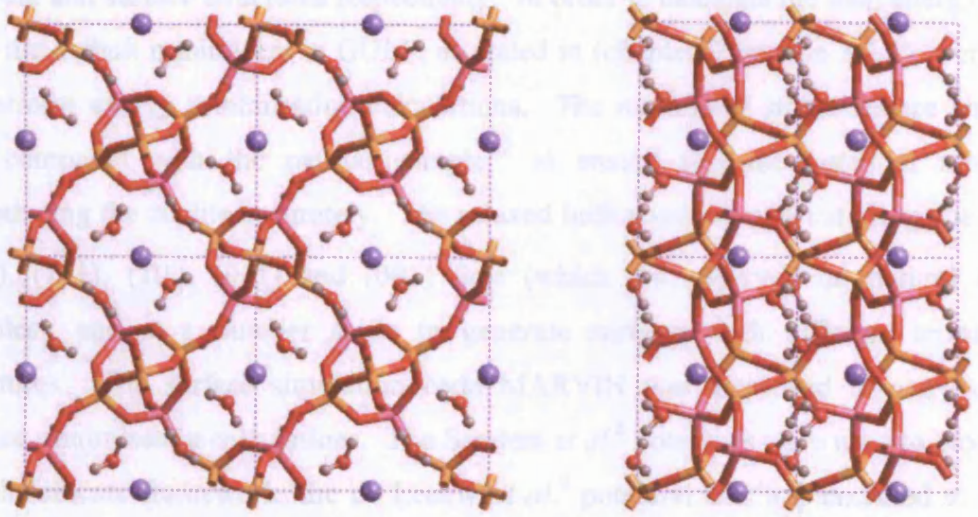

View along the [001] **View along the [100]**

Figure 4. 1: Edingtonite (the purple spheres represent the barium cations)

Within this study, the determination of the surface structure and prediction of morphology was performed on the siliceous form of EDI and then on the hydrated aluminosilicate form of EDI. Siliceous EDI is a siliceous analogue of natural EDI, constructed from a silicon and oxygen framework (as opposed to a silicon, aluminium and oxygen framework), and no extra framework cations or molecular water within the channels or pores. By studying a siliceous analogue of EDI the number of atoms per unit cell is reduced from 50 to 30, decreasing the amount of computing time required and reduces the complexity of the model. By investigating siliceous EDI, we are also able to determine the importance of the presence of extra framework cations and water within the channel system, in the context of crystal growth.

From this point onwards the simulated hydrated natural EDI crystal will be referred to as hydrated aluminosilicate EDI and the experimentally characterised geological sample of EDI will be referred to as natural EDI.

4.2 Methodology

GULP[6] and MARVIN[7] were used to perform energy minimisation calculations at 0K of the bulk and surface structures respectively. In order to calculate the total energy of the bulk the default minimisers in GULP, as stated in (chapter 3, section 3.6.1), were used to perform energy minimisation calculations. The minimised structures are analysed and compared with the natural sample[1,2] to ensure that the potential model is reproducing the zeolite accurately. The relaxed bulk structure was cut along the (1 1 0), (1 0 0), (1 1 1), ($1\bar{1}1$), (0 1 1) and (0 0 1) face (which are observed on natural crystal samples), and at a number shifts to generate surfaces with different terminating structures. The surface simulation code MARVIN was employed to carry out all surface minimisation calculations. The Sanders *et al.*[8] potentials were used to model the aluminosilicate framework, the de Leeuw *et al.*[9] potential was implemented to model the molecular water, the barium-oxygen pair potential was fitted for this study (method of fitting is described by appendix A), and the hydroxyl groups were described by the Schröder *et al.*[10] potential, the details of each potential have been tabulated in appendix A.

4.3 Results and discussion

4.3.1 Bulk analysis

Table 4. 1 contains the cell lengths for the energy minimised bulk structure of both siliceous EDI and hydrated aluminosilicate EDI compared to the cell lengths of natural EDI.

	Lattice Data			
Crystal structure	A (Å)	b (Å)	c (Å)	Volume (Å^2)
Natural EDI	9.550	9.665	6.523	602.078
Siliceous EDI	9.551	9.551	6.359	580.071
	(0.01)	(-1.18)	(-2.51)	(-3.66)
Hydrated aluminosilicate	9.689	9.721	6.400	602.826
EDI	(1.46)	(0.58)	(-1.89)	(0.12)

Table 4. 1: Cell lengths and volume of the relaxed bulk structure and natural EDI. Percentage deviation from the natural sample are given in parenthesis.

Looking at the percentage changes in volume and lattice parameters it is immediately observed that the potentials have reproduced the hydrated aluminosilicate crystal structure very well. The hydrated aluminosilicate EDI model has the best agreement with the crystal structure of the natural sample, this is what would be expected when the potentials accurately reproduce the structure, since the hydrated aluminosilicate EDI model contains the exact unit cell composition as the natural sample. However it is important to analyse the deviation that each cell length has from the natural sample as the cell parameters can cancel each other to give good comparison of the cell volume. The cell lengths for the hydrated aluminosilicate compare very well to the natural sample, with a maximum deviation of 1.89%. It should be noted that if the cumulative error of each cell length is considered without taking the sign into account, it is found that the hydrated aluminosilicate deviates further from the experimental crystal structure (by 0.3%) than siliceous EDI, suggesting that the potentials for water or the barium-framework need modifying.

Dehydrated siliceous EDI displays a small contraction of 3.66% in cell volume, and the cell parameters are in fair agreement with the natural crystal structure, with the maximum difference of cell length being 2.51% in the c parameter. It should be reiterated that siliceous EDI only contains a silicon and oxygen framework and no extra framework cations or water, thus by comparing with natural EDI we are comparing materials with different compositions, nevertheless siliceous EDI gives a reasonable reproduction of the framework of the natural material.

Table 4. 2 list the bond angles and Table 4. 3 contain the bond distances of the two simulated forms of EDI and the natural sample. The T-O bond lengths differ by less than 1%, the O-T-O bond angles differ by less than 0.05% and the T-O-T angles differ by less than 2.5%, these results compare well with the results found experimentally, confirming the potentials used to represent the zeolite framework have reproduced the structure successfully and more importantly suggest they will be reliable for the prediction of the surface structures. Given the absence of experimental data of the surface it is crucial that the potentials are able to reproduce the crystal bulk.

	Bond Angles (°)				
Crystal Structure	O-Si-O	O-Al-O	Si-O-Si	Si-O-Al	H-O-H
Natural EDI	109.455	109.447	141.389	137.351	106.550
Siliceous EDI	109.393		144.626		
Hydrated aluminosilicate EDI	109.432	109.421	138.473	138.200	105.823

Table 4. 2: Average bond angles of natural sample and relaxed bulk structures.

	Bond Lengths (Å)		
Crystal Structure	Si-O	Al-O	Water O-H
Natural EDI	1.619	1.743	0.946
Siliceous EDI	1.606		
Hydrated aluminosilicate EDI	1.620	1.742	0.946

Table 4. 3: Bond lengths of the natural sample and relaxed bulk structures.

Siliceous EDI has yet to be synthesised, as a result there is no experimental data to compare with, however Civalleri *et al.*[11-13] have carried out Hartree-Fock and density functional calculations on bulk siliceous EDI. Within their calculations a reduced unit cell was created by decreasing the a and b parameters, and keeping the c parameter the same as the original unit cell. The reduced unit cell contains five T atom arranged as the spiro unit, and corner sharing oxygen atoms which link the spiro units together. Table 4. 4 lists the values of the a, b and c cell parameters, and the Si...Si length within the spiro unit calculated from this study using classical techniques and from the Civalleri *et al.*[13] study calculated using HF and B3LYP.

	a and b	c	Si...Si
Classical (this study)	6.897	6.359	3.721
HF[13]	6.917	6.453	3.731
	(0.29)	(1.46)	(0.27)
B3LYP[13]	7.000	6.492	3.773
	(1.47)	(2.05)	(1.38)

Table 4. 4: Cell parameters and Si...Si distance within the spiro unit of siliceous EDI, all values are given in angstroms (Å). Values in parentheses state the percentage difference between the parameters calculated by this work and those calculated by *ab initio* methods.

A comparison between the all three parameters shows that the values calculated by this study are between 0.2 and 1.5% smaller than HF values and between 1.3 and 2.1% smaller than B3LYP values, all these parameters are in fair agreement with the results obtained by this work. They calculated the average O-Si-O angle of 109.3° and average Si-O distance of 1.611Å. These results compare very well with the observed results (see Table 4. 2 and Table 4. 3), with a O-Si-O angle difference of 0.085% and a Si-O distance difference of 0.311%, thus the potentials describing the Si-O framework are reproducing the structure accurately. A true value of all these parameters are approximated between the HF and B3LYP values, since HF methods do not calculate electron correlation, and so predict much larger bond lengths and consequently larger cell parameters. Whereas B3LYP methods take electron correlation into account, however they are also known to often underbind bonds, hence giving larger bond lengths and cell parameters, as a result, it is reasonable that this classical study predicts smaller cell lengths than the *ab inito* studies.

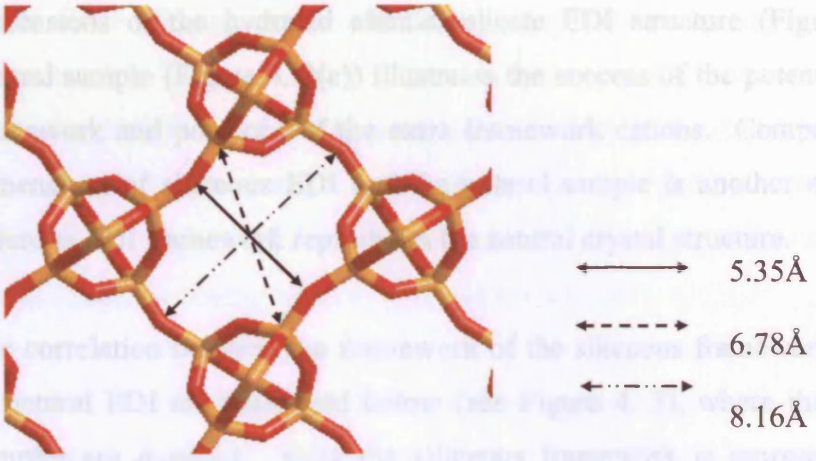

(a) Siliceous EDI

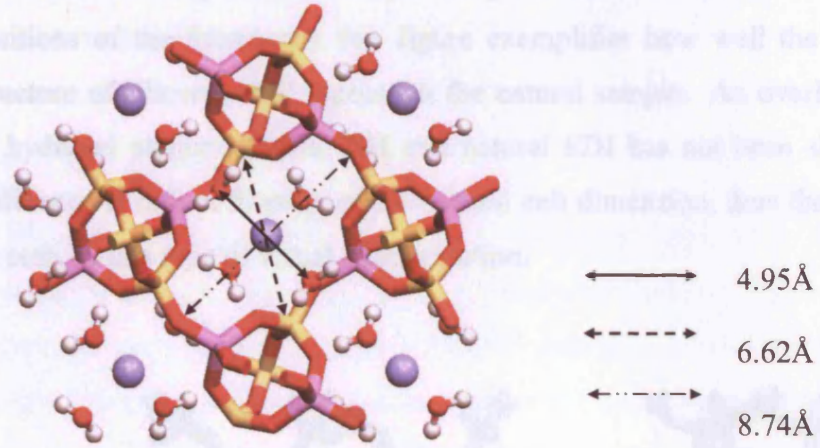

(b) Hydrated aluminosilicate EDI

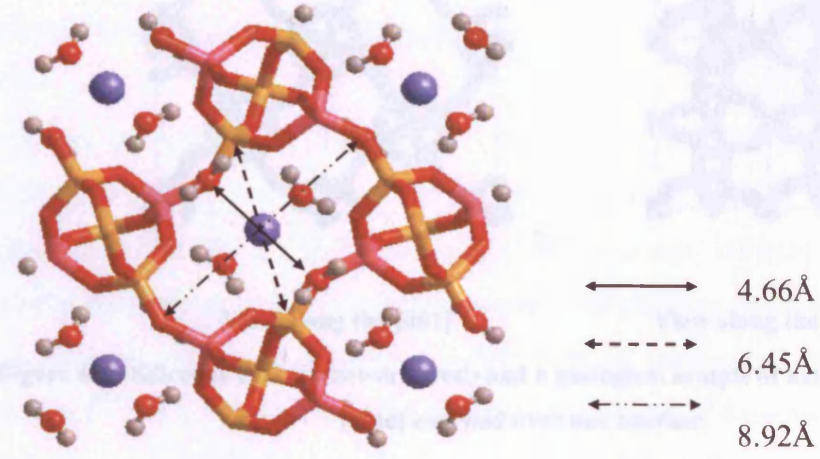

(c) Natural EDI

Figure 4. 2: (a)-(c) Channel dimensions of EDI (purple spheres represent barium cations)

Figure 4. 2(a)-(c) show the channel dimensions of the simulated siliceous EDI, the simulated hydrated aluminosilicate and natural EDI. The similarity between the channel

dimensions of the hydrated aluminosilicate EDI structure (Figure 4. 2(b)) and the natural sample (Figure 4. 2(c)) illustrates the success of the potentials to reproduce the framework and positions of the extra framework cations. Comparison of the channel dimensions of siliceous EDI and the natural sample is another example of how well siliceous EDI framework reproduces the natural crystal structure.

The correlation between the framework of the siliceous framework and the framework of natural EDI are illustrated below (see Figure 4. 3), where the framework of both samples are overlaid. Here the siliceous framework is represented in red and the framework of the geological sample is represented in blue, by concentrating on the atom positions of the framework this figure exemplifies how well the periodic framework structure of siliceous EDI represents the natural sample. An overlay of the framework of hydrated aluminosilicate EDI and natural EDI has not been shown here since the difference is only a fraction of the overall cell dimension, thus the different would not be seen by this type of visual representation.

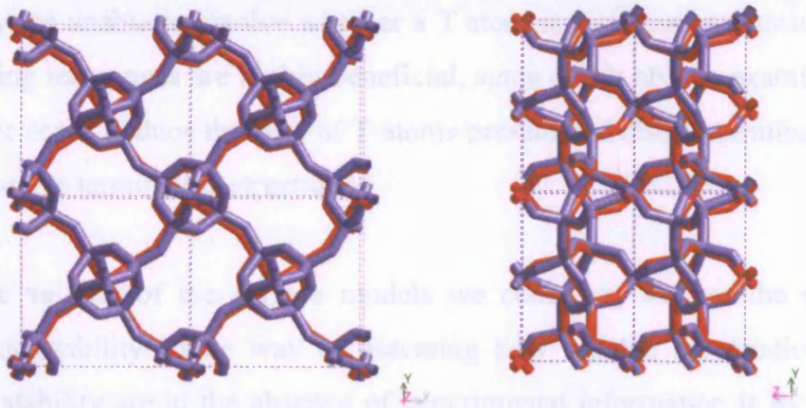

View along the [001] **View along the [010]**

Figure 4. 3: Siliceous EDI framework (red) and a geological sample of natural EDI framework (blue) overlaid over one another.

Despite the absence of experimental data, the classical calculations for siliceous EDI agree well with the natural EDI crystal structure and the *ab-initio* structures calculated for siliceous EDI by Civalleri *et al.* It is also calculated that the energy per SiO_2 unit of siliceous EDI is 19kJmol^{-1} higher in energy than α-quartz and therefore less stable. This would suggest that purely siliceous EDI if synthesised would be thermodynamically

stable, since calometric data has shown that siliceous faujasite which has an energy of approximately 25kJmol^{-1} greater than α-quartz per SiO_2 is thermodynamically stable.[14] As a result it will be useful to consider siliceous EDI (*i.e.* only the EDI framework) in order to predict the surface structure and properties of natural EDI, as it has the advantage of containing less atoms per unit cell, as so will contain less degrees of freedom and the computation will be more tractable.

Now that suitable bulk models have been created for both siliceous and hydrated aluminosilicate EDI, the relaxed crystal structures can used to create surfaces in order to determine the terminating structure. The following section will present and discuss the results obtained by this analysis.

4.3.2 Surface analysis

As discussed in chapter 2 section 2.6, it is extremely difficult to determine the surface structure at an atomistic scale *via* experimental techniques. State of the art scanning techniques such as AFM[15] and HRTEM[16] can not achieve atomic scale resolution, therefore they are unable to resolve whether a T atom is a silicon or aluminium. As a result modelling techniques are highly beneficial, since one is able to examine surfaces to an atomistic scale, deduce the type of T atoms present and also discriminate between stable and unstable terminating structures.

To assess the validity of the surface models we construct, we use the criterion of thermodynamic stability. One way of assessing how reliable the predicted surface energies and stability are in the absence of experimental information is by a proxy of inferring the correct surface energy and surface structure to correlate to the morphology of a material, this is a technique often seen in studies of metal oxides[17-21] and organics.[22-29] It is assumed that the relative aspect ratio of each face in the morphology plot is closely related to the relative stability of the faces, therefore if the experimentally observed morphology can be reproduced, it can be deduced that the model of surface energies is accurate and as a result we have the correct surface structure.

In order to determine the morphology of edingtonite the surfaces with the following Miller indices were investigated: (110), (001), (111), ($1\bar{1}1$), (100), (011). These planes

were chosen since the first four planes appear in the experimentally determined morphology of naturally occurring tetragonal EDI,[30] A schematic diagram of the morphology of tetragonal edingtonite is shown in Figure 4. 10(c). An SEM image of natural EDI[30] is shown in Figure 4. 4, from this image one can visualise the (110), (001), (111), ($1\bar{1}1$) faces present in the crystal morphology. The (100) and (011) faces were predicted by the Donnay-Harker (*i.e.* the interlayer spacing) prediction of morphology, as a result these six faces were investigated in this study.

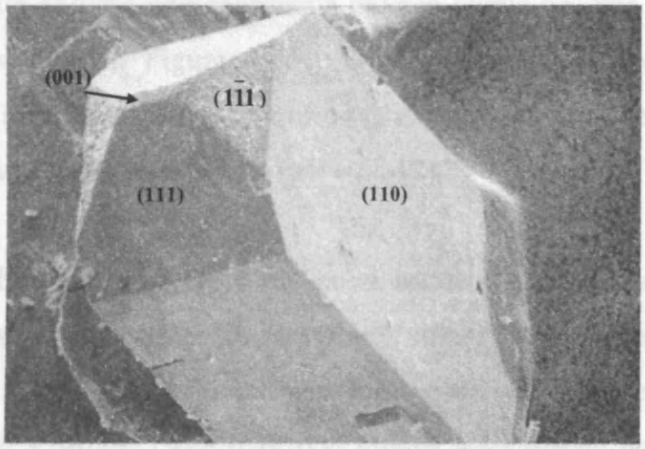

Figure 4. 4: SEM of Edingtonite (Reproduced without permission from Gottardi and Galli30)

In order to create surfaces each face was cut at numerous positions parallel to the surface. These surfaces were selected such that each termination was charge neutral, did not cut through any atoms, and had a net zero dipole or could be reconstructed in a manner stated in section 3.7.2 such that a net zero dipole could be achieved. By systematic analysis *via* energy minimisation calculations of all possible terminations, we hope to have sampled all reasonable surface structures so that our lowest energy surface structure corresponds to the global minimum.

We expect that terminations which cut through a minimal number of bonds to be relatively stable. We assume that surfaces which cut through closed structures would entail breaking a larger number of bonds and will be unfavourable, whereas surfaces containing complete ring structures and cages would be expected to be relatively stable. The act of slicing in order to create surfaces is a mechanical one and therefore cleaving of bonds leads to the exposure of under-coordinated sites, *i.e.* typically three-coordinated silicon and one-coordinated oxygen atoms. We expect that these under-

coordinated sites are unstable. Figure 4. 5 illustrates bulk EDI cleaved along the (110) plane resulting in three-coordinate silicon and one-coordinate oxygen.

Since zeolites are synthesised under hydrothermal conditions it may be possible for the under-coordinated sites on the surface to undergo a reaction with water. In this model it is assumed that water dissociates into a proton and hydroxyl group, both of which react with the under coordinated sites, and results in all the under-coordinated sites satisfying their coordination shell. The three-coordinate silicon atoms, (or aluminium atoms), become four-coordinate and the one-coordinate oxygen atoms become two-coordinate, as shown by the last step in Figure 4. 5. During synthesis water may undergo hydrolysis, however a large amount of hydroxyl ions are present in solution since synthesis takes place in alkaline conditions (pH ~11-12).

When modelling hydroxylated surfaces the most stable surface is selected, *i.e.* the surface with the lowest energy, and each unsaturated silicon (and aluminium in the case of hydrated aluminosilicate EDI) is capped with a hydroxyl group and each unsaturated oxygen is capped with a proton. The hydroxyl groups were placed on the surface by finding similar oxygen in the bulk and positioning the hydroxyl oxygen in the same direction with a bond distance of 1.6Å. The protons were placed perpendicular to the surface with a bond distance of 0.95Å. The fact that the orientation of the hydroxyl group is selected arbitrarily using chemical intuition means that we cannot systematically measure the degree of relaxation of the hydroxyl groups, since we cannot be sure that the starting geometry is correct. The potentials for the framework are the same as those used for the bulk. The potentials used to model the interaction of the hydroxyl groups with the framework have been taken from Schröder *et al.*[10], which have been fitted for a bridging hydroxyl group within a zeolite cage (parameters are listed in appendix A).

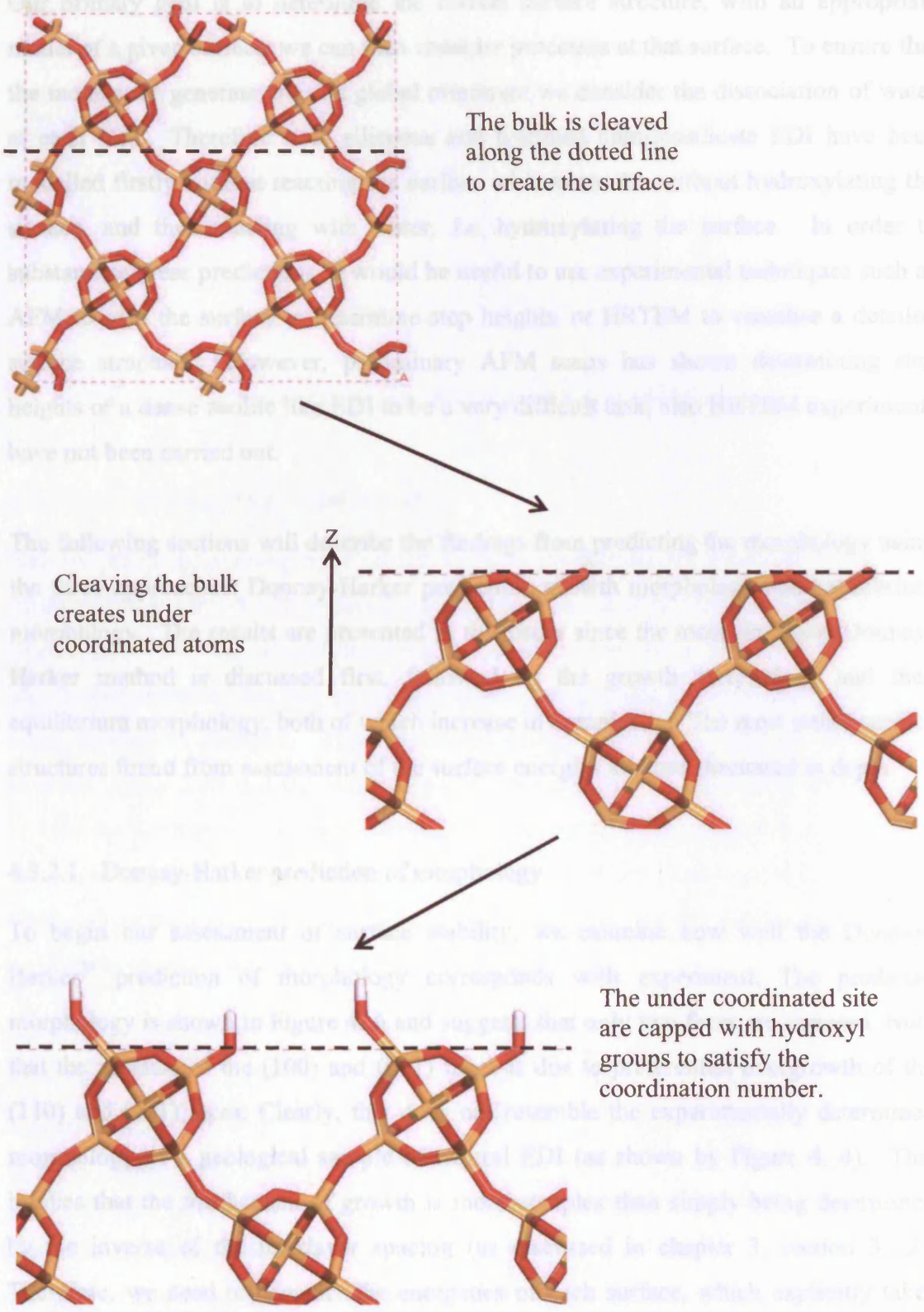

Figure 4. 5: Cleaving of the surface to expose under coordinated sites, which are subsequently hydroxylated

Our primary goal is to determine the correct surface structure, with an appropriate model of a given surface; we can then consider processes at that surface. To ensure that the models we generate are at a global minimum we consider the dissociation of water at each face. Therefore both siliceous and hydrated aluminosilicate EDI have been modelled firstly without reacting the surface with water, *i.e.* without hydroxylating the surface, and then reacting with water, *i.e.* hydroxylating the surface. In order to substantiate these predictions, it would be useful to use experimental techniques such as AFM to scan the surface to determine step heights, or HRTEM to visualise a detailed surface structure. However, preliminary AFM scans has shown determining step heights of a dense zeolite like EDI to be a very difficult task, also HRTEM experiments have not been carried out.

The following sections will describe the findings from predicting the morphology using the three approaches: Donnay-Harker prediction, growth morphology and equilibrium morphology. The results are presented in this order since the most simplistic Donnay-Harker method is discussed first, followed by the growth morphology and then equilibrium morphology, both of which increase in complexity. The most stable surface structures found from assessment of the surface energies are then discussed in depth.

4.3.2.1 Donnay-Harker prediction of morphology

To begin our assessment of surface stability, we examine how well the Donnay-Harker[31] prediction of morphology corresponds with experiment. The predicted morphology is shown in Figure 4. 6 and suggests that only two faces are exposed. Note that the absence of the (100) and (011) faces is due to preferential overgrowth of the (110) and (001) faces. Clearly, this does not resemble the experimentally determined morphology of a geological sample of natural EDI (as shown by Figure 4. 4). This implies that the mechanism of growth is more complex than simply being determined by the inverse of the interlayer spacing (as discussed in chapter 3, section 3.7.2). Therefore, we need to consider the energetics of each surface, which explicitly takes into account the strength of bonding within and between layers, by assessing the attachment and surface energy.

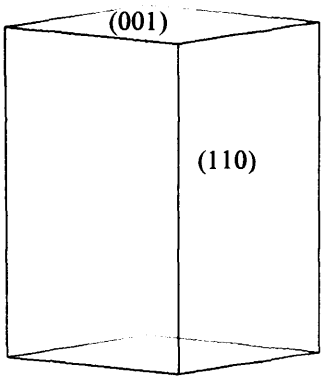

Figure 4. 6: Donnay-Harker predicted morphology

4.3.2.2 Analysis of attachment energies

Relaxed attachment energies of all the surfaces considered are shown in Table 4. 5. Morphological importance is based on the absolute value of the attachment energy, where slow growing morphologically important faces are associated with small attachment energies; and fast growing, quickly extinguished faces are associated with large attachment energies. The attachment energy reflects the strength of binding between layers. Note that the magnitude of the numbers vary considerably, up to a ratio of 1:10 for the lowest to highest energies. In the experimental morphology, the aspect ratio between faces is interpreted as being indicative of the relative growth rate. This highly disparate spread of values immediately indicates that the relative energies are unlikely to correlate well with experimental growth rates.

Miller plane	(110)	(100)	(001)	(011)	(111)	$(1\bar{1}1)$
Siliceous EDI						
Unhydroxylated	-14.807	-24.240	-74.221	-68.873	-115.775	-109.223
Hydroxylated	-14.946	-24.256	-74.504	-66.870	-111.288	-112.033
Hydrated aluminosilicate EDI						
Unhydroxylated	-0.509	-0.946	-2.082	-2.187	-3.303	-3.046
Hydroxylated	-0.452	-0.941	-2.062	-2.135	-3.155	-3.539

Table 4. 5: Attachment energies in $eVmol^{-1}$

A prediction of growth morphology can be made by correlating morphological importance to the reciprocal of attachment energy. This allows us to make a rapid, qualitative and visual analysis of whether the strength of interlayer binding is indeed related to growth rate, and is shown by Figure 4. 7.

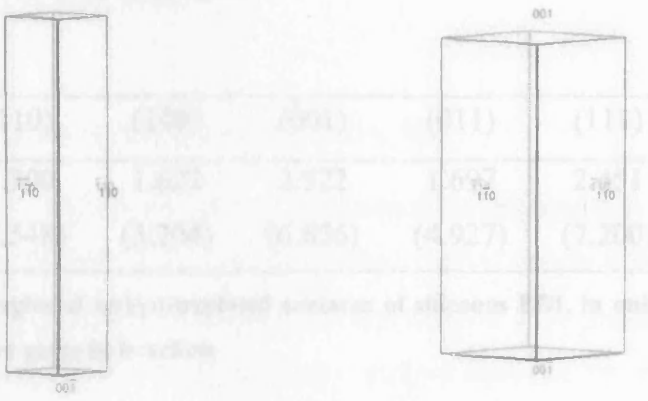

(a) Siliceous EDI **(b) Hydrated aluminosilicate EDI**

Figure 4. 7: Growth Morphology

It is immediately clear that only two of the four faces are present and the predicted morphology shows no resemblance to the morphology established by SEM of natural EDI. It is also clear that the predictions for the two structures are somewhat different. These findings show that the growth of EDI cannot be thought of a simple layer-upon-layer growth mechanism, *i.e.* growth *via* one complete layer simply attaching itself onto the bulk or growing crystal surface. It suggests we need to understand the chemistry and energetics of the different fragments which make up the layer and how they emerge out of solution and attach onto the bulk.

We do not have an experimentally deduced morphology plot for siliceous EDI, however since the framework of siliceous EDI is corresponds very well to the natural sample, the siliceous EDI morphology will be compared to the natural EDI crystal shape. By comparison of the siliceous and natural EDI morphology, it is evident that the morphology does not display all four faces, this is similar to what was observed with hydrated aluminosilicate EDI. From these results it is clear that that the attachment energies do not seem to be a suitable tool for predicting the morphology of EDI and possibly other zeolite structures, therefore, we next consider the surface energy of each face.

4.3.2.3 Analysis of surface energies

4.3.2.3.1 Unhydroxylated purely siliceous EDI

The results from the energy minimisation calculations are shown in Table 4. 6, only the energies for the relaxed most stable surfaces are shown. It was necessary to consider and relax a total of 42 surface structures.

Miller plane	(110)	(100)	(001)	(011)	(111)	$(1\bar{1}1)$
Siliceous EDI	1.300	1.622	2.522	1.697	2.451	2.174
	(2.548)	(3.204)	(6.656)	(4.927)	(7.200)	(7.200)

Table 4. 6: Surface energies of unhydroxylated surfaces of siliceous EDI, in units of Jm^{-2}. Initial, pre-minimised values are given in brackets

All surface energies, (as expected) were found to have decreased upon minimisation since the total energy of the surface would be expected to decrease during minimisation, the largest decrease occurring on the $(1\bar{1}1)$ surface. It is noticed that the degree of relaxation increases with decreasing d_{hkl}. The surface energies show the following trend in surface stability:

$$(110) > (100) > (011) > (1\bar{1}1) > (111) > (001)$$

Trends of the surface stability (where we assume stability is correlated with morphological importance) of tetragonal EDI have been observed experimentally to be:

$$(110) > (1\bar{1}1) > (111) > (001).^{30}$$

Cleary, the post minimisation trend of surface stability of unhydroxylated siliceous EDI is in agreement with experimental observations.

On relaxation surface energies were observed to become much closer in magnitude, thus decreasing the dominance of the (110) and (100) faces and increasing the dominance of the other surfaces with smaller interlayer spacing.

The magnitude of the surface energies are consistent with typical surface energies reported for silica materials such as α-quartz[32] and other zeolites.[33,34] Unlike the attachment energies, the spread of surface energies (*i.e.* the relative ratio of which we expect to correlate with aspect ratio) is more reasonable. However, the relatively stable (100) and (011) faces are not observed in the experimental morphology and this point will be discussed later in section 4.3.7.

4.3.2.3.2 Unhydroxylated hydrated aluminosilicate EDI

The values in Table 4. 7 show the energy minimised surface energies of the hydrated aluminosilicate EDI surfaces. As in the calculations carried out on siliceous EDI, these surfaces have not had the under-coordinated sites capped with protons or hydroxide ions. Despite the fact that the bulk structures contain different compositions, it was found that the most stable structure on each face had an identical termination to those found in siliceous EDI, hence they are the equivalent cuts and contain the same number of undercoordinated sites.

Miller plane	(110)	(100)	(001)	(011)	(111)	$(1\bar{1}1)$
Hydrated aluminosilicate EDI	1.203	1.545	2.615	1.521	2.092	1.476
	(2.698)	(3.404)	(4.967)	(4.280)	(5.625)	(5.625)

Table 4. 7: Surface energies of unhydroxylated surfaces of hydrated aluminosilicate EDI, in units of Jm^{-2}. Initial, pre-minimised values are quoted in brackets.

The surface energies were observed to undergo a large decrease on minimisation and stabilise in the following order:

$$(110) > (1\bar{1}1) > (011) > (100) > (111) > (001)$$

Assuming that stability can be correlated with morphological importance, this trend agrees well with experiment. However, again on the basis of surface energy alone, the (011) and (100) faces would be expected to be observed, which in reality is not the case.

4.3.2.3.3 Hydroxylated siliceous EDI

The surface energies for hydroxylated siliceous EDI are shown in Table 4. 8 and have been corrected to account for the self energy of the hydroxyl species we introduce upon the surface (see appendix B).

Miller plane	(110)	(100)	(001)	(011)	(111)	$(1\bar{1}1)$
Number of hydroxyls	2	2	8	8	8	8
Siliceous EDI	1.116	1.543	4.279	2.604	2.995	2.954

Table 4. 8: Corrected surface energies of hydroxylated siliceous EDI surfaces, in units of Jm^{-2}

The trend in stability does not change on relaxation and remains as:

$$(110) > (100) > (011) > (1\bar{1}1) > (111) > (001)$$

If one concentrates on the faces seen explicitly on the crystal morphology of natural EDI, *i.e.* by ignoring the (100) and (011) faces, the trend above agrees with that found for the unhydroxylated siliceous surfaces and also that observed experimentally. Hydroxylating the (110) and (100) surface (*i.e.* creating two hydroxyls) have shown a decrease in the surface energies in relation to the unhydroxylated surfaces, whereas the surface energy of the remaining four surfaces all increase. This would suggest that for siliceous EDI only these two surfaces are stable with respect to dissociative adsorption of water.

4.3.2.3.4 Hydroxylated aluminosilicate EDI surfaces

Hydrated aluminosilicate EDI contains both silicon and aluminium, thus hydroxyl groups have been attached to both silicon and aluminium atoms at the surface. In order to correct the surface energies the type of atom to which the hydroxyl group is attached must be noted and corrected for since as one might anticipate, the affinity for hydroxyl groups is higher for silicon than aluminium. The higher attraction for silicon is due to the fact that the silicon ion possesses a greater positive charge than the aluminium ion

thus it is more attractive to the hydroxyl group. (See appendix B for calculation of correction factor)

Miller plane	(110)	(100)	(001)	(011)	(111)	$(1\bar{1}1)$
Number of hydroxyls	2	2	8	8	8	8
Hydrated aluminosilicate EDI	1.103	1.108	2.835	1.797	2.230	2.075

Table 4. 9: Corrected surface energies of hydroxylated natural EDI surfaces, in units of Jm^{-2}

The corrected surface energies, shown in Table 4. 9, give the following trend of stability:

$$(110) > (100) > (011) > (1\bar{1}1) > (111) > (001)$$

Hydrating the surface has the effect of increasing the stability of the (110) and (100) face and decreasing the stability of the remaining four faces, consequently we anticipate that only these two faces are stable with respect to hydration. This is consistent with that seen by analysis of siliceous EDI surfaces. Again, we find qualitative similarity between the siliceous and dehydrated natural EDI structures and energies.

4.3.3 Analysis of hydration energies

The energy of hydration or energy for dissociative adsorption of water on each face for both siliceous and hydrated aluminosilicate EDI has been calculated by the Born-Haber cycle discussed in appendix B and values have been listed in Table 4. 10. Looking at the signs of each value shows that hydration of the (110) and (100) surface are exothermic reactions and therefore we expect these reactions to occur. Whereas the hydration of the other four surfaces, excluding the (111) hydrated aluminosilicate EDI surface, have an endothermic energy of reaction and would not expect the reaction to occur. This is consistent with the findings from analysis of the surface energies.

Miller plane	(110)	(100)	(001)	(011)	(111)	$(1\bar{1}1)$
Siliceous EDI	-134.684	-57.1993	847.317	759.968	292.175	472.719
Hydrated aluminosilicate EDI	-115.02	-218.063	487.151	311.970	-47.365	309.687

Table 4. 10: Hydration energies for siliceous and natural EDI surfaces in units of $kJmol^{-1}$

We considered that the reactivity to water could be attributed to the number of under-coordinated sites on each surface per unit area, *i.e.* the density of these 'defects'. The (110) and the (100) surface both have two under-coordinated sites, thus two hydroxyl groups are formed. As a result there is approximately one hydroxyl group per $42Å^2$ on the (110) surface and one hydroxyl group per $30Å^2$ on the (100). On the other four faces there is one hydroxyl group every 11-$18Å^2$. Intuitively, one might expect that the density of under-coordinated sites per unit area is correlated with reactivity; specifically reaction with water, which is clearly present during synthesis. However, we find the reverse is true and the reason for this is discussed in the following section. It is also interesting to find that the same trends are found with both siliceous and hydrated aluminosilicate EDI surfaces despite the fact that chemically the two are highly dissimilar.

The magnitude of the surface energies for unhydroxylated surfaces are similar to those found in the paper by de Leeuw *et al.*[32] on quartz, *i.e.* within the range of 1.5-2.5Jm^{-2}. However the hydroxylated surface energies in this study appear to me slightly too high (approximately 0.5Jm^{-2}), this may be due to the error in the correction factor used, since the correction is based on α-quartz and gibbsite rather than EDI. Another source of discrepancy between this study and the work by de Leeuw *et al.* is in the potentials used for the hydroxyl groups, this study uses a partial charge rigid ion model, where as the de Leeuw paper uses a shell model for the hydroxyl oxygen which is likely to allow more flexibility. The positions of the hydroxyl groups can be verified by carrying out periodic *ab initio* calculations. Preliminary DFT calculations have been carried out and have shown that the SiOH angle in the classical calculations are calculated to be 20° too large, this is due to an inadequate representation of the hydroxyl groups by the potentials. The inconsistency of the surface energy and hydration energy of the (111)

surface of hydrated aluminosilicate EDI is found to be a result of the surface structure; a more detailed analysis is discussed below.

4.3.4 Surface structural analysis

Combining the surface energy and hydration data, we can present models for the most stable terminations for each of the Miller indices we have considered:

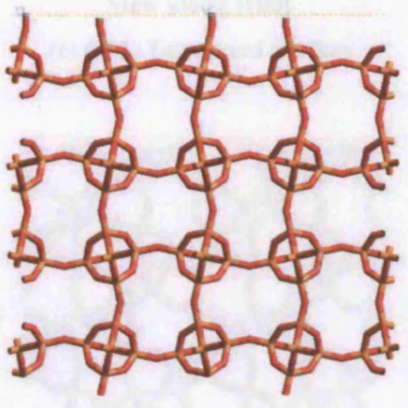

view along [011]
(a) (110) Unrelaxed surface

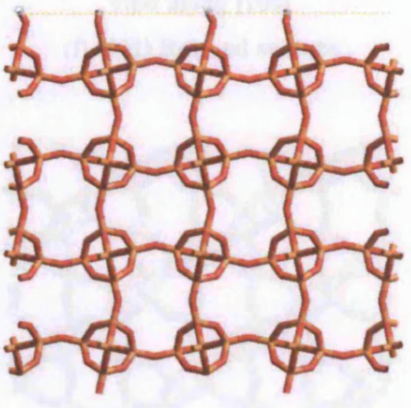

view along [011]
(b) (110) Relaxed surface

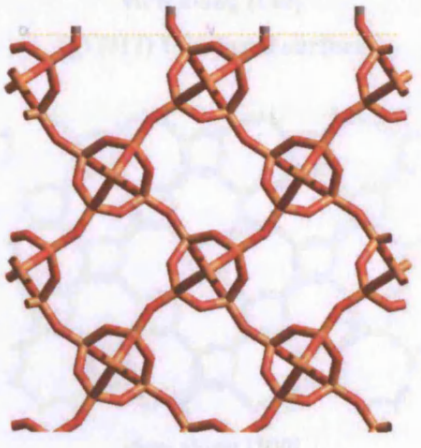

view along [001]
(c) (100) Unrelaxed surface

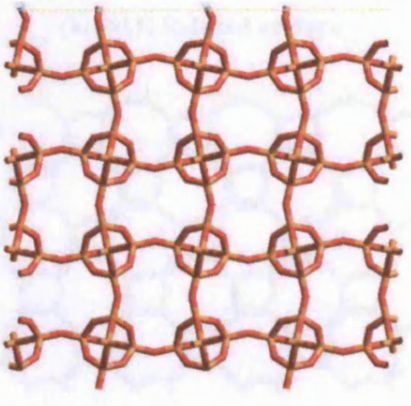

view along [001]
(d) (100) Relaxed surface

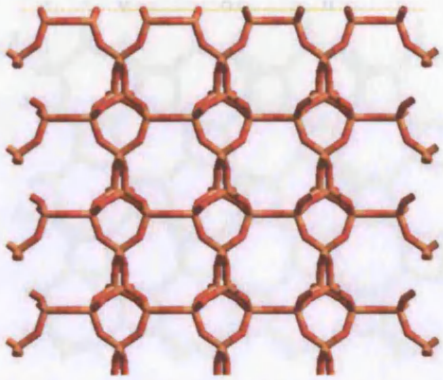

view along [100]

(e) (001) Unrelaxed surface

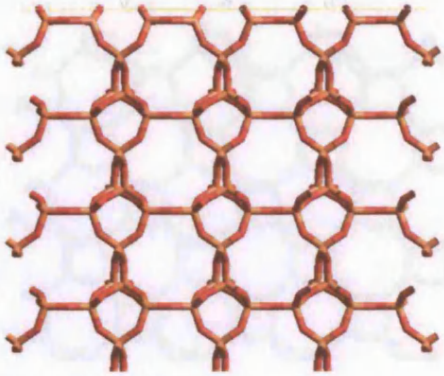

view along [100]

(f) (001) Relaxed surface

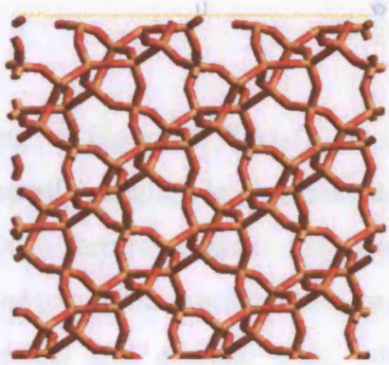

view along [110]

(g) (011) Unrelaxed surface

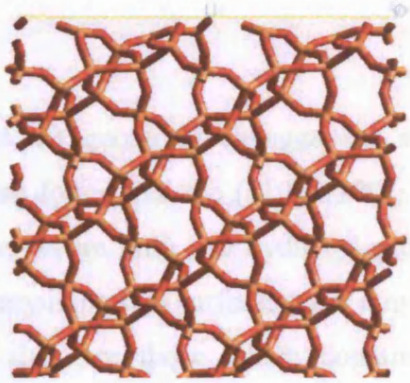

view along [110]

(h) (011) Relaxed surface

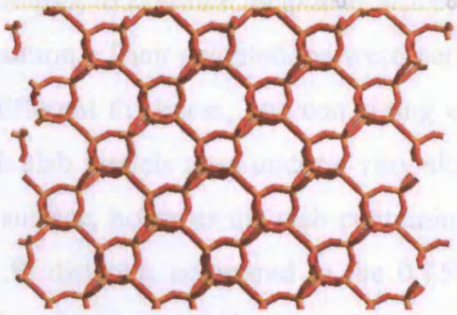

view along [100]

(i) (111) Unrelaxed surface

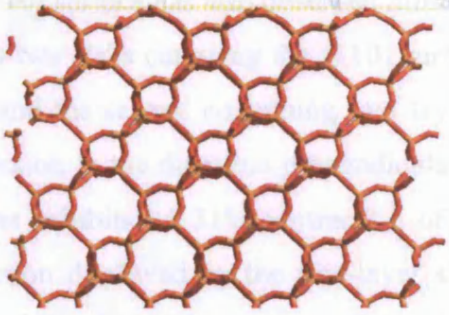

view along [100]

(j) (111) Unrelaxed surface

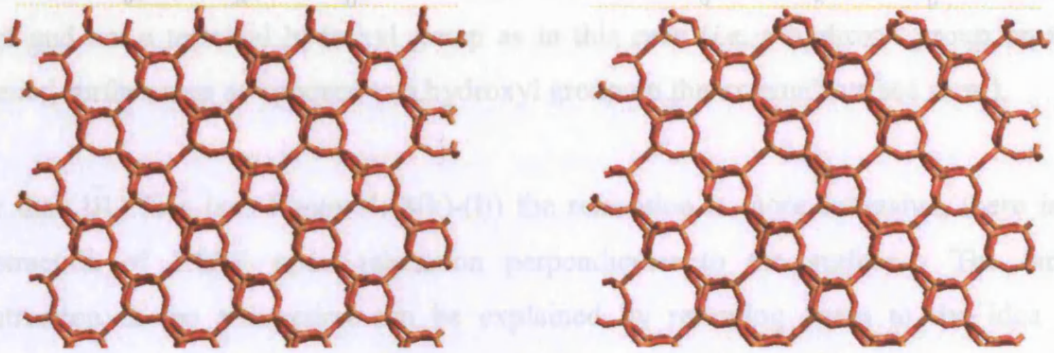

view along [100] **view along [100]**

(k) ($1\bar{1}1$) Unrelaxed surface **(l) ($1\bar{1}1$) Relaxed surface**

Figure 4. 8: (a)-(l) Unrelaxed and relaxed surfaces of most stable terminations on each face of siliceous EDI

Looking at Figure 4. 8(a)–(h) it is noticed that the geometry changes are almost (structurally) negligible on minimisation. It is also found that the (110), (100), (011) and (001) surfaces contain only terminal sites, *i.e.* where only one hydroxyl group is attached to a three coordinate silicon atom. The remaining two surfaces have a mixture of terminal and geminal sites, where geminal sites are those which contain two hydroxyls attached to the same silicon atom, this finding of different sites can be verified by spectroscopy measurements. Civalleri *et al*[13] who used quantum mechanical techniques to examine the purely siliceous EDI (110) surface has also observed minimal relaxation. Their calculations were performed on two slabs cut along the (110) surface of different thickness, one containing one layer and the second containing two layers. Both slab models goes under a very slight contraction in the direction perpendicular to the surface, however the slab containing one layer exhibits a 0.31% contraction of the Si…Si distance, compared to the 0.15% contraction displayed by the two-layer slab. Within this study we have modelled two layers within the surface region of the (110) face, the relaxed surface also shows a 0.30% contraction of Si….Si bond distance perpendicular to the surface, which is consistent with the trends shown by quantum mechanical studies.

Civalleri *et al.* also found that the average Si-O-H angle in the relaxed slabs were 123.5°, whereas in this the average Si-O-H angle was found to be 138°, This shows an inadequacy of the Si-O-H three body potential taken from Sanders *et al*[8], due to the fact

that the O-H potential was been fitted for a bridging hydroxyl group within a zeolite cage and not a terminal hydroxyl group as in this case (*i.e.* a hydroxyl group on the internal surface area as opposed to a hydroxyl group on the external surface area.).

For the $(1\bar{1}1)$ face (see Figure 4. 8(k)-(l)) the relaxation is more extensive, there is a contraction of 1.86% upon relaxation perpendicular to the surface. The large contraction in the z-direction can be explained by returning again to the idea of reactivity correlated to density of under coordinated sites. It might be expected that the high index faces with many dangling bonds would be highly hydrophilic and stabilised by dissociative adsorption of water. However on closer inspection of the $(1\bar{1}1)$ surface it is found that these surfaces undergo a form of 'reconstruction' whereby the surfaces stabilise by significant relaxation, which results in an increase in the coordination number of the under-coordinated sites. An example of this is the $(1\bar{1}1)$ unhydroxylated siliceous surface (see Figure 4. 8(k)&(l)), on relaxation some of the under-coordinated silicon and oxygen form bonds increasing their coordination number and therefore are stabilised. This form of 'reconstruction is also seen on the $(1\bar{1}1)$ face of natural EDI (see Figure 4. 9, the water molecules within the cell have been removed for clarity). This picture illustrates how a 2-coordinated silicon (green) becomes 3-coordinate creating a new bond of length 1.59Å, which is the approximate value of a typical Si-O bond length. In this manner, the (111) and $(1\bar{1}1)$ faces are all able to passivate their surfaces and are hence relatively hydrophobic.

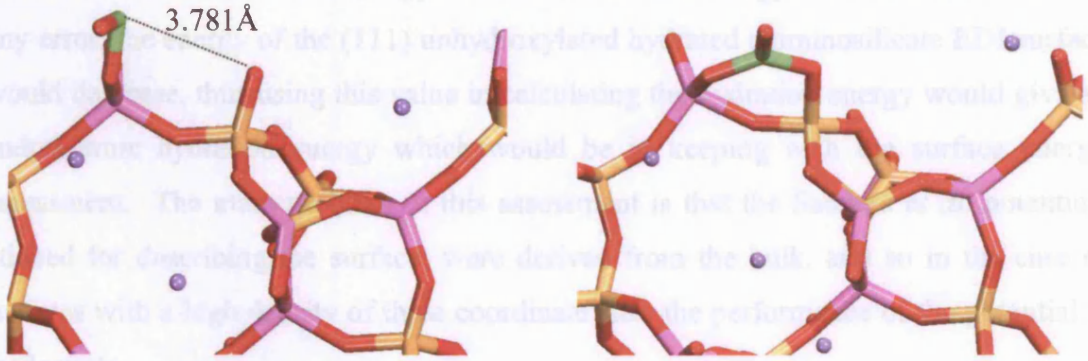

(a) Unrelaxed Surface **(b) Relaxed Surface**

Figure 4. 9: Relaxed and unrelaxed $(1\bar{1}1)$ face of hydrated aluminosilicate EDI (purple spheres represent barium cations)

The (111) surface and $(1\bar{1}1)$ surface have very similar terminations, this results in comparable surface energies and surface structures on minimisation. Our calculations show that the relaxed hydroxylated surfaces for both the (111) and $(1\bar{1}1)$ surface have very similar surface structures and surface energies, however the relaxed unhydroxylated surface energies differ by almost 8eV per unit area for siliceous EDI and 5eV per unit area for hydrated aluminosilicate EDI. The difference in energy between the (111) surface and $(1\bar{1}1)$ is a result of the (111) surface may be in a local minimum *i.e.* not reaching its global minimum. As a result, it is still in a high energy configuration, and so the (111) surface structure is still strained. Once the (111) surface has found its global minimum, the under coordinated bonds on the surface would be expected to increase its coordination number in the same way as the $(1\bar{1}1)$, which in turn would decrease the surface energy to be in parity with the $(1\bar{1}1)$ surface.

In the assessment of hydration energies (see section 4.3.3, Table 4. 10), the value for the (111) hydrated aluminosilicate EDI surface was exothermic and not in keeping with the surface energy results. When examining the surface energies to determine whether the surface should be hydrated, one simply looks at the surface energy difference between the hydroxylated and unhydroxylated surface. Whereas the calculation of the hydration energy (see appendix B) completes the Born-Haber cycle to determine the energy gain or penalty in attaching hydroxyl groups to the surface. Thus the anomaly between the results from hydration energy and surface energy is due to the error of calculating the total energy of the surface producing a systematic error throughout any calculation where the value of the total energy is used. If the total energy were calculated without any error, the energy of the (111) unhydroxylated hydrated aluminosilicate EDI surface would decrease, thus using this value in calculating the hydration energy would give an endothermic hydration energy which would be in keeping with the surface energy assessment. The main problem in this assessment is that the Sanders *et al.* potentials utilised for describing the surface, were derived from the bulk, and so in the case of surfaces with a high density of three coordinate sites the performance of the potential is inadequate.

As remarked upon previously, the pre- and post-minimised geometry of these surfaces are both very similar for both siliceous and natural EDI surfaces. Although, figures

18(a)-(l) show the pre and post minimised structures of siliceous EDI surfaces, the hydrated aluminosilicate EDI surfaces are found to be almost identical and have been omitted for brevity.

4.3.5 Morphology

Figure 4. 10 shows the morphology of a geological sample of EDI determined experimentally and the equilibrium morphology, based up on surface energy, determined from the Wulff approach.

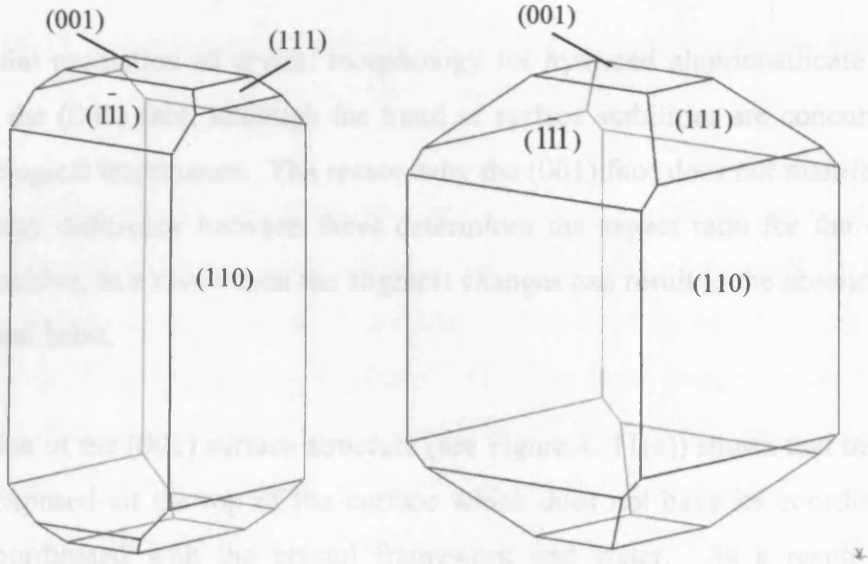

(a) Siliceous EDI **(b) Natural EDI**

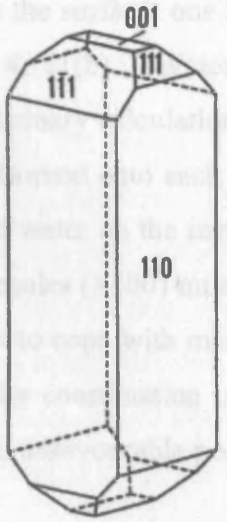

(c) Schematic diagram based on geological sample[30]

Figure 4. 10: (a)-(c) Equilibrium morphology of EDI

The (100) and (011) faces have not been included in this prediction. A qualitative inspection of the general characteristics of the crystal indicate that the siliceous and natural crystal have been reproduced well in both cases. Both models have reproduced the experimental morphology with remarkable accuracy, displaying all four stable surfaces as in the geological EDI sample and reproduces the aspect ratio of each face well. This allows us to conclude that the reason stability of surfaces is a reasonable indicator of growth rate, with the exceptions of the (100) and (011) faces which are discussed below (section 4.3.7).

The initial prediction of crystal morphology for hydrated aluminosilicate EDI did not display the (001) face, although the trend of surface stabilities are concurrent with the morphological importance. The reason why the (001) face does not manifest is because the energy difference between faces determines the aspect ratio for the (001) face is very sensitive, as a result even the slightest changes can result in the absence of a face in the crystal habit.

Inspection of the (001) surface structure (see Figure 4. 11(a)) shows that there is barium cation exposed on the top of the surface which does not have its coordination sphere fully coordinated with the crystal framework and water. As a result the partially coordinated barium cation is in an unfavourable and unrealistic chemical state. In order to stabilise the surface, one layer of water was added on top of the surface as depicted by Figure 4. 11(b). (Water surrounds the crystal during the crystallisation process.) From preliminary calculations (not presented here) it is observed that at least a layer of water is adsorbed onto each crystal face, however generating reasonable configurations of layers of water on the surface of a crystal is not a straightforward task because many water molecules (>100) must be modelled in random positions, thus potentials must be very robust to cope with many molecules. The effect of the water on the (001) surface increases the coordination of the barium cation, hence reducing the movement of the cation to an unfavourable position during minimisation of the surface structure.

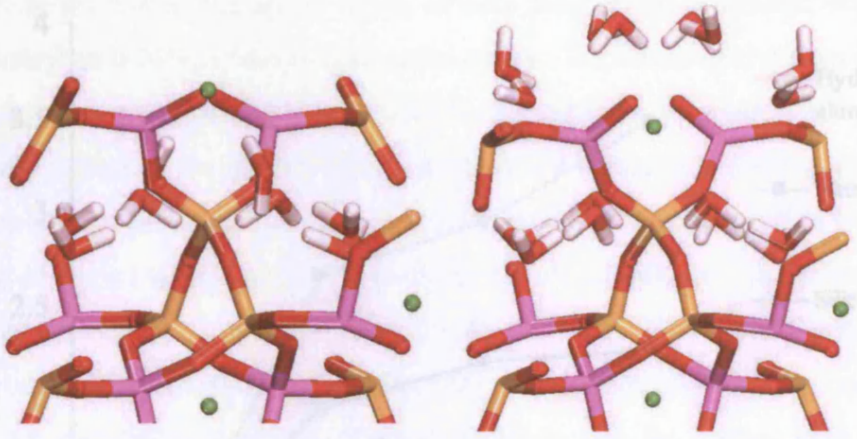

(a) (b)

Figure 4. 11: (a) minimised (001) unhydroxylated surface, (b) minimised (001) unhydroxylated surface with a monolayer of water

Calculating the correct crystal morphology furthermore indicates that we have almost certainly determined the correct surface structure for each of the faces, out of the many possible structural permutations. Since the relative stability of faces, can be predicted correctly for EDI by studying the purely siliceous form, suggests that the growth of natural EDI must be relatively insensitive to framework and extra framework constituents. Therefore presence of aluminium, extra framework cation and water must not play a significant role in determining the rate of growth. since the growth can be followed by studying the purely siliceous form.

4.3.5.1 Quantitative analysis of the EDI morphology

To determine the aspect ratio of the natural crystal and the two simulated crystals quantitatively, the surface area of each face was calculated from the schematic diagram of the SEM (Figure 4. 10(c)). Each surface area was then manipulated into a percentage of the total surface area, the percentages were then used to create a morphology plot within the Cerius^2 visualisation package from which the aspect ratios were deduced. The growth rates of all three crystals have been normalised to the (110) face and have been compared in the graph below.

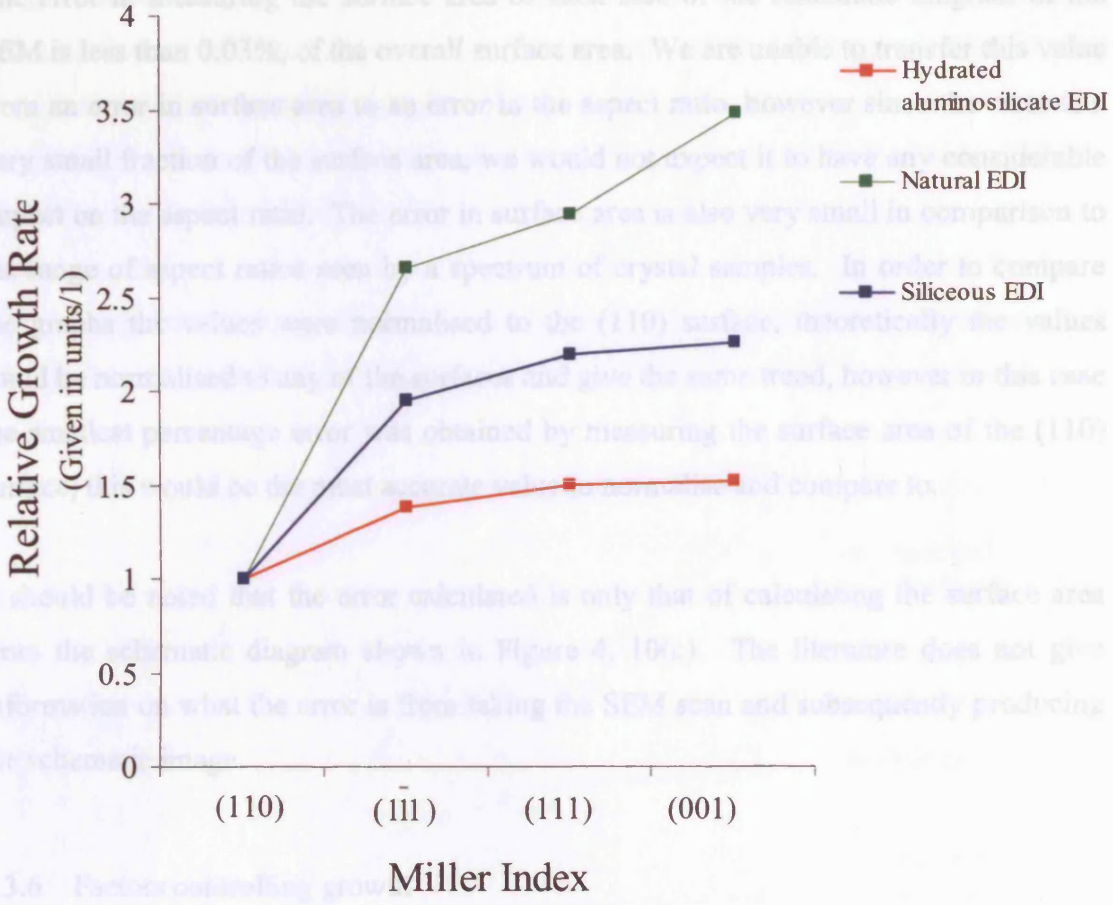

Figure 4. 12: Comparison of the growth rates of simulated siliceous EDI, simulated natural EDI and a geological sample of EDI

Here we can see that both the simulated siliceous EDI and simulated hydrated aluminosilicate EDI growth rates follow the same trend as the growth rate of the natural sample, however surprisingly the siliceous EDI gives better correspondence with the geological growth rate than natural EDI. Hence, this shows that the ratio between surface stabilities for each face of siliceous EDI is in closer agreement with natural EDI than that shown by hydrated aluminosilicate EDI. This discrepancy may be due to the fact that all stress has not been removed from the surface structure of the (110) face, which decreases the difference in aspect ratio between the (110) face and the remaining three faces, and decreases the stability of the (110) with respect to the other three morphologically important faces.

The error in measuring the surface area of each face of the schematic diagram of the SEM is less than 0.03%, of the overall surface area. We are unable to transfer this value from an error in surface area to an error in the aspect ratio, however since the error is a very small fraction of the surface area, we would not expect it to have any considerable impact on the aspect ratio. The error in surface area is also very small in comparison to the range of aspect ratios seen by a spectrum of crystal samples. In order to compare the graphs the values were normalised to the (110) surface, theoretically the values could be normalised to any of the surfaces and give the same trend, however in this case the smallest percentage error was obtained by measuring the surface area of the (110) surface, this would be the most accurate value to normalise and compare to.

It should be noted that the error calculated is only that of calculating the surface area from the schematic diagram shown in Figure 4. 10(c). The literature does not give information on what the error is from taking the SEM scan and subsequently producing the schematic image.

4.3.6 Factors controlling growth

Since the observations above show that a surface energies are able to reproduce the crystal morphology, the next step in this investigation was to deduce which aspect of surface energy was accountable for determining the growth rate. A range of components which make up the surface energy where investigated, such as the two body energy, three body energy, electrostatic energy, and the surface excess energy*, however none of these quantities correlated to the growth rate of the natural crystal. The surface energy produces the correct growth trend, yet there is a lack of correlation between the growth rate and the surface excess energy, this intuitively exposes that the growth rate must be dependent on the surface area. It is apparent that surface area must play a role in the growth rate, since the surface energy can reproduce the aspect ratios, whereas surface excess energy does not, hence the difference between calculating both quantities is the surface area.

In order to test the hypothesis that surface area plays a role in the growth rate the surface area was normalised with the (110) surface (as done above) and compared with

* Surface excess energy = Surface energy × Surface area.

the growth rate, this did not produce the correct growth trend. The number of bonds per unit area that are broken upon creation of the crystal surface was then investigated, this trend is shown in the graph below (see Figure 4. 13). Immediately one can see a strong correlation between the number of broken bonds per unit area for both simulated forms of EDI and natural growth rate.

Figure 4. 13 also displays how this simple quantity gives a much better reproduction of the relative crystal growth rate than the surface energy prediction.

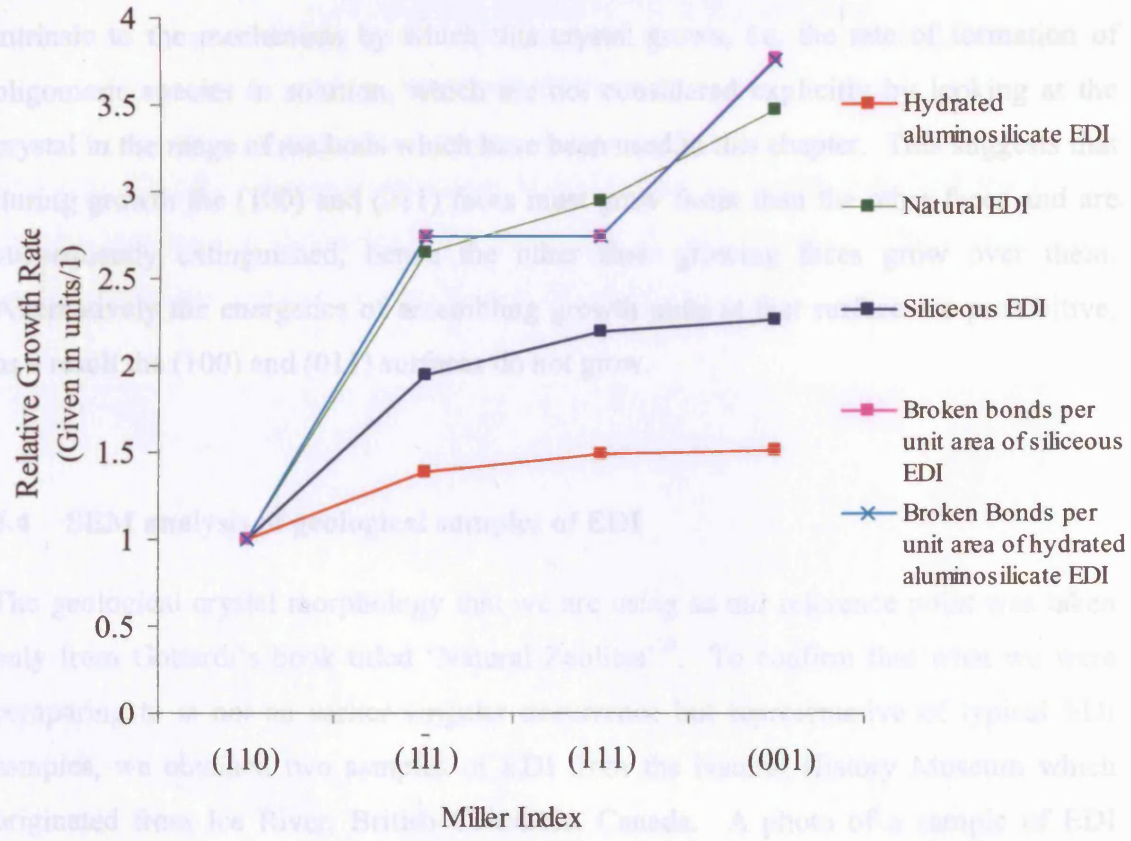

Figure 4. 13: A comparison between the geological growth rate determined experimentally and the simulated growth rate of natural and siliceous EDI determined via surface energies and the number of broken bonds upon creating the surface per unit area

4.3.7 (100) and (011) surfaces

For both siliceous EDI and natural EDI it is found that the (100) face is stable in the hydroxylated form and the (011) face is stable in the unhydroxylated form. According to the surface energy analysis they should appear in the equilibrium morphology,

however literature and our own SEM experiments (See section 4.4) show that they are not present in the experimentally determined morphology. Calculating the crystal morphology by looking at the number of unsaturated bonds per surface area also suggests that the (100) and (011) surfaces should be present. This would suggest that determining the morphology of this crystal requires more than simply looking at the energetics of the surfaces or investigating simple quantities such as broken bonds on creating the surface or surface area. The reasons for this are not clear, it may be that our model is not representative of the surface structure of natural EDI, though this is unlikely. We believe that the answer behind why these surfaces are not present is intrinsic to the mechanism by which this crystal grows, *i.e.* the rate of formation of oligomeric species in solution, which are not considered explicitly by looking at the crystal in the range of methods which have been used in this chapter. This suggests that during growth the (100) and (011) faces must grow faster than the other faces and are subsequently extinguished, hence the other slow growing faces grow over them. Alternatively the energetics of assembling growth units at that surface are prohibitive, as a result the (100) and (011) surfaces do not grow.

4.4 SEM analysis of geological samples of EDI

The geological crystal morphology that we are using as our reference point was taken only from Gottardi's book titled 'Natural Zeolites'[30]. To confirm that what we were comparing to is not an earlier singular occurrence but representative of typical EDI samples, we obtained two samples of EDI from the Natural History Museum which originated from Ice River, British Columbia, Canada. A photo of a sample of EDI crystals are shown by the photo in Figure 4. 14

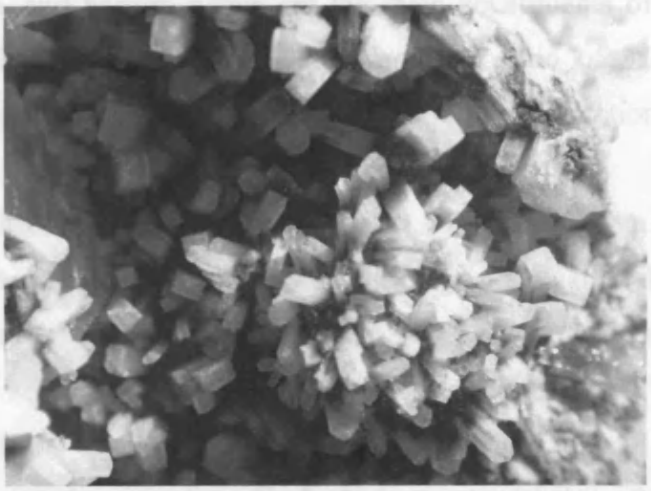

Figure 4. 14: Sample of EDI crystals formed in Ice River, British Columbia, Canada, obtained from the natural history museum

The Jeol J35 SEM apparatus was used to investigate the morphology and the EDAX method was used to determine the composition of both crystals. The crystals were carbon coated and analysed at a voltage of 20KeV at 100mA.

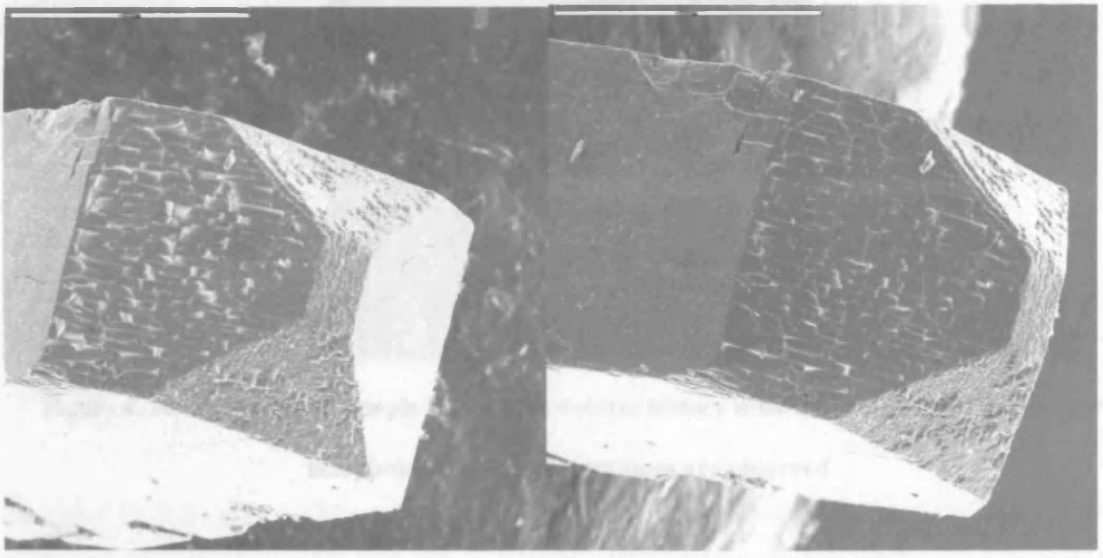

Figure 4. 15: SEM image of sample A of EDI obtained from the natural history museum. All four morphologically important faces are observed*

Figure 4. 15 illustrates the SEM images of the first sample (sample A), here all four faces are observed clearly and with similar aspect ratio, to that seen in previous literature (see Figure 4. 4). The major composition of sample A consisted of oxygen,

* The flakes on the top of the (111) face were easily removed when the beam was fired onto the surface, this could easily change the composition taken by EDAX measurements.

aluminium, silicon, and barium which are the main constituents of a formula unit of EDI crystal, within the correct silicon to aluminium ratio of 3:2 thus we can be confident that this crystal sample is EDI, however no x-ray diffraction was carried out.

Figure 4. 16 visualises the second sample (sample B) obtained from the natural history museum, this SEM scan shows this crystal morphology posses only the three of the four faces shown by the other EDI crystal samples. The (001) face is not observed and would cap the top and bottom of the crystal. The reasons why the (001) is absent on this crystal could be attributed to a variety of environmental factors, such as temperature, pH and cations species, all of which can change the rate of growth. In this case the (001) face is the minor face, so any small change in the relative growth rate of the (001) and (111) would lead to the presence of the (001) cap or uncapped crystal.

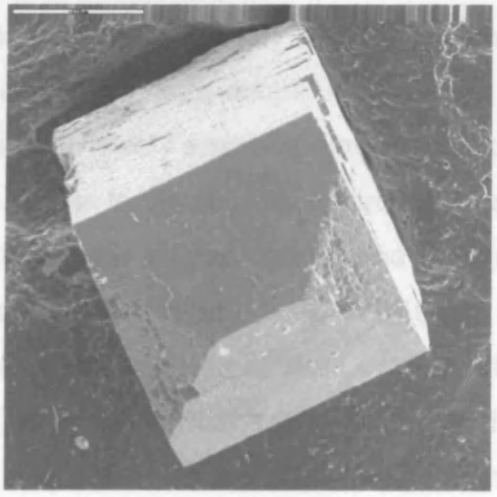

Figure 4. 16: SEM scan of sample B from the natural history museum. Only three of the four morphologically important faces are observed

The values in Table 4. 11 show the percentage of an element within each of the two EDI samples taken *via* EDAX measurements (the EDAX facility is built into the SEM instrument).

	Elemental (%)	
Element	Sample A	Sample B
O	27.36	53.13
Al	11.88	10.02
Si	18.06	15.70
Ba	40.62	21.50
Zn	1.97	0.35
Ca	0.10	0.52

Table 4. 11: Values represent the percentage of a particular element in a sample taken from EDAX experiment.

Both samples contain the correct 3:2 silicon to aluminium ratio as natural EDI, however the main difference between the two samples is the amount of extra framework cations. Sample A contains almost double the quantity of extra framework cations of sample B for the same amount of aluminium, with sample A containing 40% barium and sample B containing 20% barium, this is very surprising since in both cases the amount of extra framework cation are in excess to the amount required to create a charge neutral cell. Another difference between these natural crystals and the simulated crystals are the natural samples contain a small percentage (between 0.10 and 2%) of calcium and zinc as well as barium cations. The ionic radii of these varying cations are all smaller than the ionic radii of barium,* they range from half to two thirds the value of barium. The reduction in ionic radii may influence the formation of framework structure during growth.

In order to form a complete analysis, the errors in the values calculated by EDAX must be taken into account. The elemental values from EDAX are based upon the overall elemental percentage which is prone to error from the beam current. If the beam current it set too high the structural water may evaporate during the scan decreasing the amount of oxygen. Since all the values are normalised to one hundred the loss of oxygen increases the percentage amount of the remaining elements. Also, the chemical analysis revealed that the amount of calcium within sample A is at the edge of the error limit of detection, implying that this value may be dubious.

* Ionic Radii of Ba^{2+} = 136pm, Ca^{2+} = 100pm, Zn^{2+} = 75pm.[35]

It is unclear exactly how cation concentration affects the crystal morphology but it is likely this influences the rate at which the (001) surface forms and may extinguish during growth of sample two.

4.5 Conclusions

This study describes the first attempt to model the surface structure of a hydrated aluminosilicate zeolite. By carrying out a systematic investigation of the four morphologically important faces of siliceous and hydrated aluminosilicate EDI, surface energy analysis has resolved the most stable terminating structure in all four cases. For both polymorphs of EDI the terminating structure are identical, *i.e.* the cut has been made at the same position in the crystal framework, resulting in the same number of under-saturated sites. A key finding is that the lowest thermodynamic stability of each face is correlated to the surface termination that breaks a minimal number of bonds, *i.e.* a surface that contains the least number of under-saturated sites. Assessment of the surface also highlights that the surface structure can be readily understood by considering the siliceous analogue.

Preliminary work on the hydration of crystal faces has shown that it is a thermodynamically favourable process, and affects the rate of growth. By understanding the process of hydration (and dehydration), the change in surface structure, and dissociative reactivity of water with the surface can be understood. Insights into the role that water plays in the process of crystallisation can be deduced.

Using the relaxed surface energies for these four faces the equilibrium morphology has been predicted using the Wulff construction. Qualitatively the crystal habit of both siliceous and hydrated aluminosilicate EDI has been reproduced well; this implies that the thermodynamic stability of each face is correlated to the rate of growth. From this analysis one can conclude that the relative growth rates of the surface are apparently relatively insensitive to the aluminium distribution and water content. A quantitative analysis of the morphology shows a discrepancy between the aspect ratio of the simulated crystal and the natural crystal.

A new method or indicator has been found, which assumes that the most stable surface termination is that which exposes the minimum number of dangling bonds. This assumption is based upon the findings from the surface energy approach, which indicates maximum thermodynamic stability is correlated with minimal broken bonds. By applying the broken bonds (N_{BB}/SA) technique, the relative quantities for each crystal face expressed through a Wulff plot, predict the correct crystal habit of EDI. Quantitative analysis reveals that the aspect ratio of each face is reproduced to a high degree of accuracy. This finding implies that the *density* of under-saturated sites plays an important role in dictating the relative growth rate of each face. This is the first time a critical and comparative study of morphology prediction methods has been undertaken for zeolites.

Discovering that the density of under-saturated sites on the surface of a crystal determines the growth rate of a crystal is a significant finding. If this theory can be extended to other zeolite systems it can bring crystal engineers one step closer to answering the enduring question of what factors determine crystal growth and by what mechanism they crystallise.

REFERENCES

1 A. Kvick and J. V. Smith. *J. Chem. Phys.* **79**, 2356 (1983)

2 E. Mazzi, E. Galli and G. Gottardi. *Neues Jahrb. Miner. Monatsh.*, 373 (1984)

3 W. Haidinger. *Ann. Phys. Lpz.* **5**, 193 (1825)

4 W. H. Taylor and R. Jackson. *Z. Kristallogr.* **86**, 53 (1933)

5 E. Galli. *Acta. Cryst.* **B32**, 1623 (1976)

6 J. D. Gale. *J. Chem. Soc.-Faraday Trans.* **93**, 629 (1997)

7 D. H. Gay and A. L. Rohl. *J. Chem. Soc. Far. Trans.* **91**, 925 (1995)

8 M. J. Sanders, M. Leslie and C. R. A. Catlow. *J. Chem. Soc.-Chem. Commun.*, 1271 (1984)

9 N. H. de Leeuw, G. W. Watson and S. C. Parker. *J. Chem. Soc.-Faraday Trans.* **92**, 2081 (1996)

10 K. P. Schroder, J. Sauer, M. Leslie, C. R. A. Catlow and J. M. Thomas. *Chem. Phys. Lett.* **188**, 320 (1992)

11 B. Civalleri, C. M. Zicovich-Wilson, P. Ugliengo, V. R. Saunders and R. Dovesi. *Chem. Phys. Lett.* **292**, 394 (1998)

12 P. Ugliengo, B. Civalleri, R. Dovesi and C. M. Zicovich-Wilson. *PCCP Phys. Chem. Chem. Phys.* **1**, 545 (1999)

13 B. Civalleri, S. Casassa, E. Garrone, C. Pisani and P. Ugliengo. *J. Phys. Chem. B* **103**, 2165 (1999)

14 N. J. Henson, A. K. Cheetham and J. D. Gale. *Chem. Mater.* **6**, 1647 (1994)

15 G. Binnig, C. F. Quate and C. Gerber. *Phys. Rev. Lett.* **56**, 930 (1986)

16 J. O. Bovin. *Ultramicroscopy* **13**, 419 (1984)

17 R. C. Baetzold and H. Yang. *J. Phys. Chem. B* **107**, 14357 (2003)

18 S. Hamad, S. Cristol and C. R. A. Callow. *J. Phys. Chem. B* **106**, 11002 (2002)

19 D. J. Binks, R. W. Grimes, A. L. Rohl and D. H. Gay. *J. Mater. Sci.* **31**, 1151 (1996)

20 M. J. Davies, S. C. Parker and G. W. Watson. *J. Mater. Chem.* **4**, 813 (1994)

21 M. A. Nygren, D. H. Gay and C. R. A. Catlow. *Surf. Sci.* **380**, 113 (1997)

22 D. S. Coombes, C. R. A. Catlow, J. D. Gale, M. J. Hardy and M. R. Saunders. *J. Pharm. Sci.* **91**, 1652 (2002)

23 G. Pfefer and R. Boistelle. *J. Cryst. Growth* **208**, 615 (2000)

24 J. C. Givand, R. W. Rousseau and P. J. Ludovice. *J. Cryst. Growth* **194**, 228 (1998)

25 G. Clydesdale, K. J. Roberts, G. B. Telfer and D. J. W. Grant. *J. Pharm. Sci.* **86**, 135 (1997)

26 L. J. P. Vogels, R. F. P. Grimbergen, C. S. Strom, P. Bennema, S. A. Roberts and R. F. Blanks. *Chem. Phys.* **203**, 69 (1996)

27 L. J. P. Vogels, M. A. Verheijen and P. Bennema. *J. Cryst. Growth* **110**, 604 (1991)

28 L. J. P. Vogels, P. Bennema, M. H. J. Hottenhuis and M. C. Elwenspoek. *J. Cryst. Growth* **108**, 733 (1991)

29 R. Docherty and K. J. Roberts. *J. Cryst. Growth* **88**, 159 (1988)

30 G. Gottardi and E. Galli. *Natural zeolites* (Springer-Verlag, 1985)

31 J. D. H. Donnay and D. Harker. *Am. Mineral.* **22**, 446 (1937)

32 N. H. de Leeuw, F. M. Higgins and S. C. Parker. *J. Phys. Chem. B* **103**, 1270 (1999)

33 A. A. Shubin, C. R. A. Catlow, J. M. Thomas and K. I. Zamaraev. *Proc. R. Soc. London Ser. A-Math. Phys. Eng. Sci.* **446**, 411 (1994)

34 B. Slater, C. R. A. Catlow, Z. Liu, T. Ohsuna, O. Terasaki and M. A. Camblor. *Angew. Chem.-Int. Edit.* **41**, 1235 (2002)

35 P. W. Atkins. *Physical chemistry* (Oxford University Press, 1994)

CHAPTER FIVE

INVESTIGATION OF SELECTED NATURAL ZEOLITES

5.0 BACKGROUND

In the previous chapter (chapter 4) an in depth analysis and discussion was presented on the prediction of the external surface structure and crystal morphology of the natural zeolite EDI *via* atomistic simulation methods. It was established that two out of the four approaches used to establish morphology performed very well in reproducing the experimental crystal shape. By examining surface energies of a number of cuts parallel to the Miller index being investigated, the most stable terminating surface structure was obtained for each face, this lead to a set of surface energies which were normalised to the most stable face and used as the aspect ratio values for predicting crystal morphology. The surface energy approach lead to a striking qualitative agreement between the simulated morphology and the experimental morphology determined by SEM for both siliceous and hydrated aluminosilicate EDI, however quantitative comparison of the trend of aspect ratios, illustrated there was a large error margin.

The second method used to determine crystal morphology of EDI was by calculating the number of broken bonds created on cleaving the surface per unit area (N_{BB}/SA) for each face. By normalising the values to the smallest number, which was the (1 1 0) face for EDI, the aspect ratios of the relative growth rates used to create the morphology were deduced. Previously there have been studies which have made use of the number of broken bonds created upon cleaving the surface, such as the Born-Stern[1] procedure which calculates the bond cleavage energy per unit area, *i.e.* by calculating the surface energy by determining the work necessary to cleave a crystal along a plane and dividing it by twice the surface area since two surfaces are created. Another method, known as the 'broken bond rule' which has been utilised on metals, states that surface energy $\gamma(hkl)$ needed to create a surface with a Miller index (hkl) reduces to the product of the surface energy of the surface with the smallest number of broken bonds and the ratio of

the first-neighbour broken bonds N(hkl).[2] So in the case where the smallest number of broken bonds is for the (111) face and where N(111)=3, the surface energy will be:

$$\gamma(hkl) = \frac{N(hkl)}{3}\gamma(111) \qquad (5.1)$$

The broken bond rule has been shown to accurately predict the surface energies of noble metals.[3]

The two broken bond methods described above require calculating the work done for breaking the bond or looking at the ratio of one surface to another, however determining the morphology of a crystal by the N_{BB}/SA method (as used in chapter 4 for EDI) is a new approach, and has not been seen in literature for any previous studies. The concept behind the N_{BB}/SA method of determining crystal shape is undemanding, one needs to only deduce the number of broken bonds on the most stable termination; and so it does not require any laborious analysis of the surface energetics of the minimised surface. In this method the strength of bonds on each face are assumes to be equal. This assumption is reasonable for zeolites since the bonds can be stretched and twisted with almost zero energetic penalty.[4] By comparing the trends of surface area of each face from the SEM scan of EDI quantitatively with the surface area from the N_{BB}/SA morphology for both siliceous and hydrated aluminosilicate EDI illustrated that this method is able to give almost identical aspect ratios.

The work based on EDI clearly demonstrates that the N_{BB}/SA method can be used to determine crystal morphology of EDI, however within this study it is proposed that the N_{BB}/SA can also be utilised as a powerful crystal morphology predictive tool for other natural zeolites. In order to test this hypothesis, *i.e.* that the N_{BB}/SA is able to predict the growth rate of each face of a natural zeolite crystal, a variety of natural zeolites constructed from different SBUs need to be tested.

The following sections present a full surface energy analysis of merlinoite and analcime, along with a comparison of the equilibrium and N_{BB}/SA morphology with the crystal shape deduced experimentally *via* SEM. The latter half of this chapter deduces

the strength of the N_{BB}/SA method as a predictive tool alone, without any surface energy assessment, for natrolite, zeolite A, laumontite, and thomsonite.

5.1 Merlinoite

Merlinoite is rare natural zeolite, first discovered in 1977 by Passaglia *et al.*[5] from Cupaello, Rieti, Italy, the structure was later refined by Galli *et al.*[6] Merlinoite is a low-silica zeolite with typical composition of $K_6Ca_2Al_9Si_{23}O_{64}.24H_2O$, it is an orthorhombic, is a small-pore material with the MER topology. The MER structure belongs to the category of zeolites which consists of doubly connected 4-ring chains (see Figure 1.3(c) in chapter 1), which assemble to form a three-dimensional pore system consisting of intersecting 8-ring channels. MER does not contain an ordered distribution of aluminium within the framework, to date there have not been any studies of distinct aluminium positions throughout the entire crystal structure, however there have been studies using NMR spectroscopy that show evidence of two crystallographic distinct tetrahedral sites which may be framework aluminium sites.[7,8] The examination of EDI shows that it is the framework structure which contributes to the determination of the morphology and not the composition of the framework, the extra framework cations or molecular water, and so the simulations described here are based on a purely siliceous analogue of MER (See Figure 5. 1). The crystallographic data used in this simulation has been taken from Galli *et al.*[6]

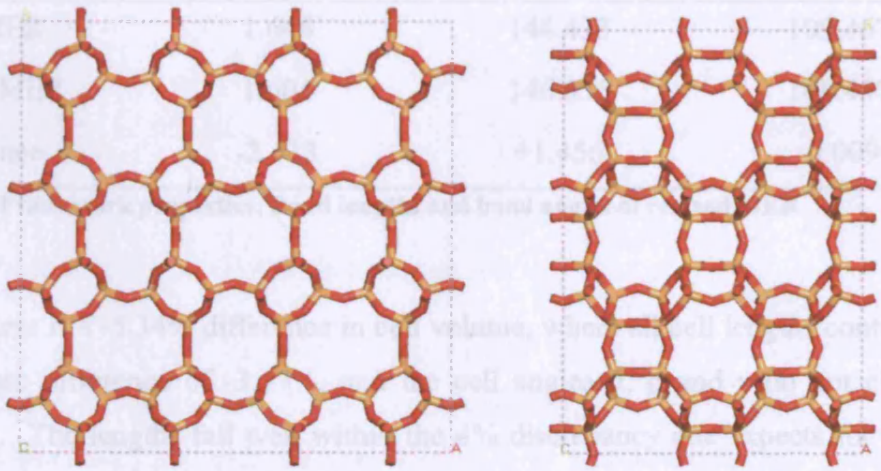

view along [001] **view along [100]**

Figure 5. 1: Siliceous analogue of MER

5.1.1 Bulk study

The bulk unit cell of siliceous MER has been simulated using the Sanders *et al.*[9] potentials (see appendix A), the accuracy of the potentials in simulating the unit cell of MER is tested by a comparison of the cell lengths, bond angles and bond lengths of the simulated siliceous MER with natural hydrated MER. An assessment between siliceous and natural hydrated MER is made since there is no evidence in literature of a natural or synthesised sample of siliceous MER to make a direct comparison.

The cell parameters of the simulated sample and the natural hydrated sample of MER have been tabulated in Table 5. 1 and Table 5. 2.

	Cell lengths (Å)			Cell angles (°)		
	a	b	c	α	B	γ
Natural MER	14.116	14.229	9.946	90.000	90.000	90.000
Siliceous MER	14.012	14.012	9.631	90.000	90.000	90.000
% Difference	-0.737	-1.525	-3.167	0	0	0

Table 5. 1: Cell parameters (lengths and angles) of relaxed siliceous MER

	Bond length	Bond angle	
	Si-O (Å)	Si-O-Si (°)	O-Si-O (°)
Natural MER	1.644	144.433	109.467
Siliceous MER	1.604	146.536	109.457
% Difference	-2.433	+1.456	-0.009

Table 5. 2: Framework properties: Bond lengths and bond angles of relaxed MER

Overall there is a -5.34% difference in cell volume, where all cell lengths contract, with a maximum difference of -3.17%, and the cell angles α, β and γ do not change on relaxation. The lengths fall well within the 4% discrepancy one expects for atomistic calculations. The mean Si-O bond length has reduced by 2.4% and the mean bond angle has increased by 1.5%. The errors within this comparison are in part due to the fact that we are not making a comparison of the exact same structure, the simulated

siliceous MER structure is composed of silicon and oxygen while the hydrated natural sample contains silicon, aluminium and oxygen framework with calcium and potassium extra framework cations and molecular water within the channel system. Therefore the average bond length would be expected to decrease since Si-O bond lengths are shorter than Al-O bond lengths, consequently a contraction in the cell parameters would be expected. This analysis shows that the bond angles and lengths do have values as would be expected from a siliceous zeolite structure. Another systematic error which is built into this model is due to the fact that this structure is dehydrated, this results in a contraction in the lattice.[10,11]

Another source of error may arise from the experimental measurements taken of the natural sample, this contribution can not be quantified since the crystallographic data does not suggest an error bar for these measurements.

Once a suitable bulk structure has been simulated, the surfaces are created by cleaving the bulk crystal and minimised to find stable surface terminations.

5.1.2 Surface study

To establish which faces should be investigated, the work of Gottardi *et al.*[12] was considered, they observed the morphology of a natural sample of MER *via* SEM experiment. They found the presence of two faces: the (110) and (111) face. These two faces were subsequently used to predict the morphology of the crystal using the well established technique of calculating surface energies to predict an equilibrium morphology (method outlined in section 3.7.3), and the new N_{BB}/SA technique.

5.1.2.1 Surface energy and hydration energy assessment

To find the structure of the terminating surface, the minimised bulk structure of siliceous MER was cleaved at a total of nine different cuts along the (110) and (111) face, such that each cut satisfied the conditions of not directly cutting through any atoms. In addition creating a charge neutral cell and the resulting surface has zero dipole perpendicular to the surface (or a cut could be made such that the surface could

be reconstructed to eliminate the dipole in the z-direction). All nine terminations were minimised to find the most thermodynamically stable surface structure. To form a complete analysis, both unhydroxylated and hydroxylated surfaces* were examined to establish whether the most stable termination was hydrated. As with EDI the hydroxyl groups are corrected for by the method shown in appendix B. Results of these calculations are presented in Table 5. 3.

	Surface Energies (Jm^{-2})	
Miller plane	(110)	(111)
Unhydroxylated	1.838	1.877
Hydroxylated	1.845	2.290

Table 5. 3: Surface energies of both faces in the unhydroxylated and hydroxylated state, in units of Jm^{-2}

A comparison between the surface energies for each MER face show that the (110) face is more stable than the (111) face, this is identical to what is found from experiment. Also the energies presented in Table 5. 3 show that both surfaces would be most favourable in an unhydroxylated state, *i.e.* without a dissociative reaction with water. However the energy difference between the unhydroxylated and hydroxylated (110) surface is very small ($\sim 0.007 Jm^{-2}$), thus calculating the hydration energy would give further insight into which form of the surface would exist.

Miller plane	(110)	(111)
Hydration energy	-70.771	479.948

Table 5. 4: Hydration energies of MER surfaces, in units of $kJmol^{-1}$. Calculated by the method shown in appendix B

Table 5. 4 contains the calculated hydration energies for both faces of MER, the hydration energy of (111) is endothermic, implying that dissociative reaction of water with this surface is unfavourable; this is in agreement with the surface energy predictions. However the (110) face has an exothermic reaction energy, implying that this surface would be more favourable in a hydroxylated state, this is contrary to surface

* Potentials used to model hydroxyl groups were fitted by Schröder *et al.*[13]

energy predictions. This ambiguity can be explained by examining the surface structures of each face.

5.1.2.2 Surface structure

The most stable surface structure of the two morphologically important faces of MER are illustrated below (see Figure 5. 2 and Figure 5. 3).

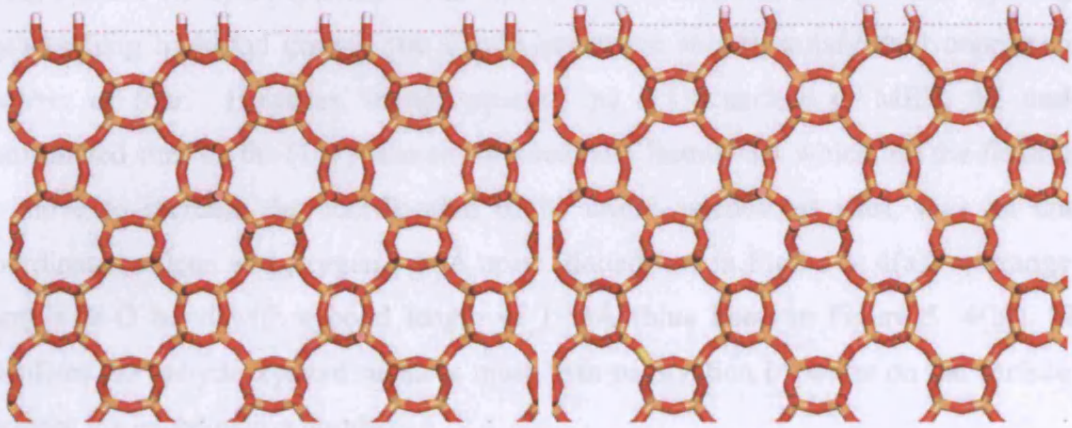

(a) (b)

Figure 5. 2: (a) Unrelaxed and (b) relaxed surface structure of (110) MER face

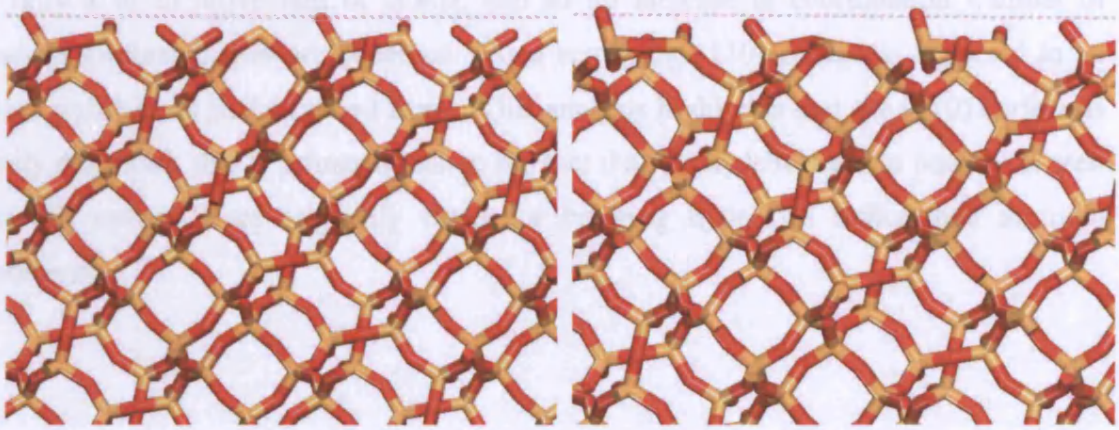

(a) (b)

Figure 5. 3: (a) Unrelaxed and (b) relaxed surface structure of (111) MER face.

As with EDI, if the reactivity of water is considered to be correlated to the number of under-coordinated sites per surface area, the (110) surface contains one under-

coordinated site approximately every 24Å^2, and one under-coordinated site approximately every 20Å^2 on the (111) surface. Along with this assessment, the proximity of the under-coordinated sites to other under-coordinated sites and the flexibility of the framework to move to a site in which increased coordination can take place are also very important.

Examining the surface highlights that both the surfaces are terminated from different types of silicon atoms. The (110) surface contains only terminal hydroxyls, whereas the (111) surface (if hydroxylated) would contains both terminal and geminal hydroxyls. By attaching hydroxyl groups, the silicon atoms are able to satisfy their coordination number of four. However, in this case of the (111) surface of MER, the under-coordinated sites on the (111) face are situated on a framework which has the flexibility to move to increase the coordination of its under-coordinated sites, thus an under coordinated silicon and oxygen 3.56Å apart (dotted line in Figure 5. 4(a)) rearrange to form a Si-O bond with a bond length of 1.53Å (blue bond in Figure 5. 4(b)). This stabilises the unhydroxylated surfaces more than passivation by water on the surface to increase the coordination number.

On the other hand, the surface structure of the under-coordinated sites on the (110) are 3.56Å apart, however since the surface atoms are in a rigid position, on relaxation there is only a small movement of atoms, and so no increase in coordination number of under-coordinated sites are observed. As a result, the (110) surface is expected to be more stable in its hydroxylated form. This analysis highlights that the (110) surface is badly described, this is primarily due to the fact that the hydroxyl group potentials used for this system were originally fitted for bridging hydroxyls rather than terminal hydroxyls.

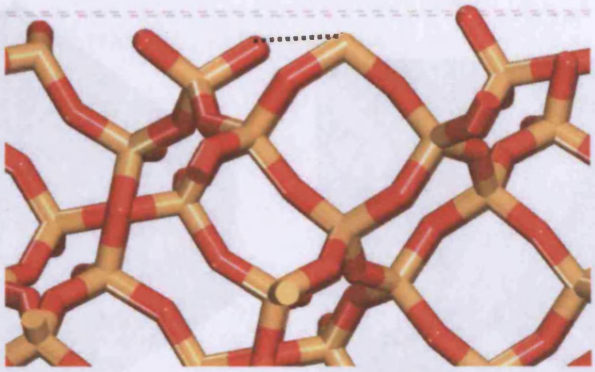

(a) Before minimisation

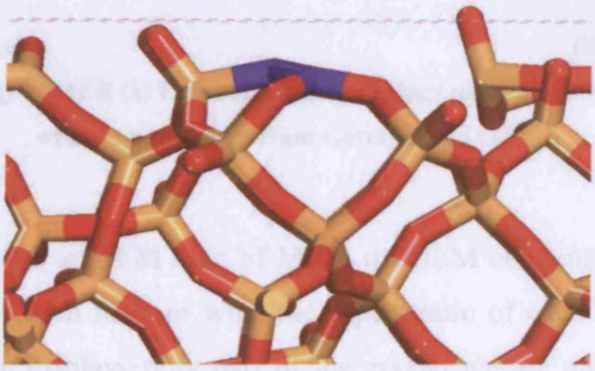

(b) Post minimisation

Figure 5. 4: The increase in coordination number of an under-coordinated site on the (111) surface.

From this analysis the hydroxylated surface structure must be trapped in a local minimum and contain some strain within the framework. If all strain were removed from the framework we would see a decrease in surface energy, leading a more stable hydroxylated surface compared to the unhydroxylated surface, which would be analogous to the prediction from hydration energies.

5.1.2.3 Equilibrium morphology

The equilibrium morphology of MER is predicted from the surface energies of the minimised surface structures and gives the form shown in Figure 5. 5(a). The predicted morphology exhibits both the morphologically important faces, however the aspect ratios of both faces are almost identical giving very similar total surface area values for both faces.

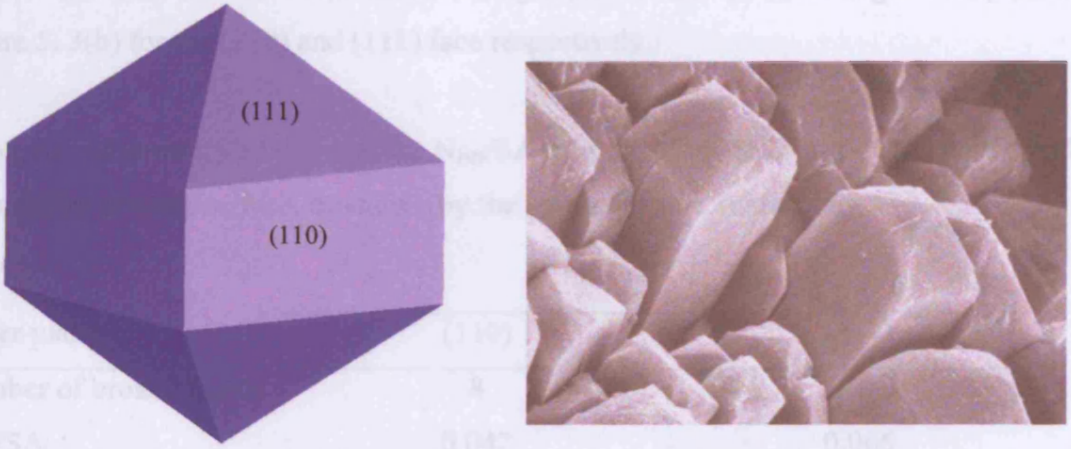

(a) (b)

Figure 5. 5: Morphology of MER (a) Equilibrium morphology plot, (b) SEM of MER (Reproduced without permission from Gottardi and Galli[12])

Figure 5. 5(b) illustrates an SEM scan of MER, the SEM contains no quantitative data of the surface area of each face, or what the aspect ratio of each face is. In addition, since the SEM image displays only part of the crystal we are unable to calculate the surface area (in a similar fashion to how the surface area of EDI was calculated). A qualitative analysis of the predicted crystal morphology displays both faces, however aspect ratios of both faces are clearly not alike, this is due to the potentials incorrectly representing the hydroxyl groups on the (110) surface. With the correct representation of the (110) surface the ratio between the (110) and (111) surface would be expected to increase.

5.1.2.4 N_{BB}/SA assessment

To find the most stable terminating surface structure, it is assumed that the surface which cuts through the least bonds is the most stable, and therefore most likely be the surface structure of that particular face. The cut along the (111) face which was considered as the most stable termination, contained a total of eighteen broken bonds. the same process was repeated for the (110) face, for this face only one cut could be made which satisfied the three conditions stated above (see section 5.1.2.1), this termination comprised of eight broken bonds. The terminations found by the N_{BB}/SA method are the same those found in the surface energy assessment, for brevity the

surface structures have not been illustrated again, and can be found in Figure 5. 2(a) and Figure 5. 3(b) for the (110) and (111) face respectively.

Using the rudimentary analysis of the N_{BB}/SA method, produced values which indicated the stability of each surface, as shown by the second row in Table 5. 5.

Miller plane	(110)	(111)
Number of broken bonds	8	18
N_{BB}/SA	0.042	0.066
Normalised value	1	1.568

Table 5. 5: N_{BB}/SA assessment of MER, and the values are normalised to the (110) surface and are given in units/1

In order to make use of the data to create the crystal morphology, the figures were normalised to the smallest number, which in this case was for the (110) face. The normalised values are subsequently used to predict the crystal morphology (see Figure 5. 6) *via* a Wulff construction (as described in chapter 3, section 3.7.4).

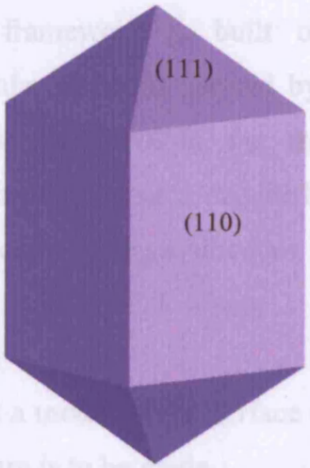

Figure 5. 6: Morphology prediction using the number of broken bonds per surface area prediction

Although we do not have quantitative data for the natural crystal we can see from a comparison with the SEM (see Figure 5. 5(b)) that the aspect ratios of the siliceous sample *via* the N_{BB}/SA method are in fair agreement. A comparison between the MER

morphology predicted by the N_{BB}/SA method (Figure 5. 6), the equilibrium morphology (Figure 5. 5(a)) and the SEM image of the natural crystal (Figure 5. 5(b)) shows the new N_{BB}/SA method gives a far superior prediction than the equilibrium morphology.

The next section will use the same analysis techniques to make a prediction of the crystal shape of analcime.

5.2 Analcime

The earliest report of analcime was by Dolomieu in 1784, however since then there have been many studies to determine the crystal structure. The structure of analcime was first resolved *via* XRD by Taylor[14], and refined by Calleri and Ferraris[15], Knowles *et al.*[16] and Ferraris *et al.*[17]. All these reports have referred to analcime in a cubic space group, however analcime is known to deviate from the cubic space group.[18] Mazzi and Galli have shown analcime to have the tetragonal and orthorhombic structures.[19] Within this study we have used the cubic structure of analcime, since the morphology of the natural crystal is identified to be in the cubic space group.

The structure code of analcime is ANA, where one unit cell of ANA consists of $Na_{16}(Al_{16}Si_{32}O_{96}).16H_2O$, the framework is built of a complex aluminosilicate framework connected *via* irregular channels formed by highly distorted 8 rings. As with MER, aluminium is disordered within the framework, however since the hypothesis of predicting the morphology of a crystal by the N_{BB}/SA is based of the framework position and not its constituents a siliceous analogue of ANA will be used within this study.

As with previous studies, before a model of the surface can be constructed, an accurate representation of the bulk structure is to be made.

5.2.1 Bulk study

The Sanders *et al.*[9] potential was used to model siliceous ANA, and the bulk structure was relaxed within the classical program GULP[20]. As with MER, the cell parameters

have been compared with the cell parameters of a natural sample of ANA since there has been no evidence of a study on siliceous ANA within the literature. Table 5. 6 list the cell parameters and Table 5. 7 give the bond lengths and bond angles of both the natural ANA and simulated siliceous ANA.

	Cell lengths (Å)			Cell angles (°)		
	a	b	c	α	β	γ
Natural ANA	13.730	13.730	13.730	90.000	90.000	90.000
Siliceous ANA	13.420	13.420	13.420	90.000	90.000	90.000
% Difference	-2.258	-2.258	-2.258	0	0	0

Table 5. 6: Cell parameters of natural analcime and simulated siliceous analcime, cell lengths are given in angstroms (Å) and cell angles are given in degrees (°)

	Bond length (Å)	Bond angle (°)	
	Si-O	Si-O-Si	O-Si-O
Natural ANA	1.648	144.253	109.498
Siliceous ANA	1.603	146.295	109.486
% Difference	-2.731	1.416	-0.011

Table 5. 7: Bond lengths and bond angles of natural analcime and siliceous analcime, bond lengths are given in angstroms (Å) and bond angles are given in degrees (°)

Overall the simulated siliceous ANA cell volume contracts by 6.6% compared to natural ANA, with a reduction of 2.3% on each cell length, a, b, and c. A factor which contributes to the contraction in cell lengths is that all the bonds in the framework are Si-O, thus the average bond length is much shorter than the average bond length in natural ANA, which contains both silicon and aluminium T atoms. On the whole, the cell parameters, bond lengths and angles are within the range expected of a siliceous zeolite, such as silicalite which has an Si-O bond length of 1.61Å[21], as a result surface energy calculations and equilibrium morphology predictions will be made from the starting point of the relaxed siliceous ANA bulk structure.

5.2.2 Surface study

By examining the morphology of a synthetic sample of cubic ANA from a SEM scan taken by Ghobarkar *et al.*[22] illustrates the (100) and (211) face. An SEM study of a natural sample of cubic ANA by Gottardi and Galli[12] show two types of crystal habits, one exposing only the (211) face and others with both the (100) and (211) face. As a result, surface energy analysis was conducted on these two surfaces, using the classical energy minimisation package MARVIN.[23]

5.2.2.1 Surface energy assessment

To determine the external surface structure on each face of the ANA crystal, energy minimisation calculations were carried out on thirteen different shifts on the (100) surface and nine different shifts on the (211) surface, in each case the surface was cleaved according to conditions of creating a zero dipole perpendicular to the surface, not cutting through any atoms, and constructing a charge neutral surface. As with previous investigations of both EDI and MER, the surface energies of both unhydroxylated and hydroxylated surfaces were examined, the energies of the most stable surfaces are listed in Table 5. 8.

	Surface Energies (Jm^{-2})	
Miller plane	(211)	(100)
Unhydroxylated	1.647	1.810
Hydroxylated	2.490	1.980

Table 5. 8: Surface energies for the most stable shifts on both faces of ANA, in Jm^{-2}

The surface energies show that both the (211) surface and (100) are more stable in their unhydroxylated form, *i.e.* without reaction with water in a dissociative manner. It would be expected that the surfaces are more stable in the hydroxylated form, however it has been seen previously with both EDI and MER that structural reconstruction upon minimisation to increase the coordination number of under-coordinated sites lead to a more stable surface that hydroxylating the surface. This point will be discussed further in section 5.2.2.3.

According to SEM scans of natural samples of ANA the (211) face is dominant, with the (100) face appearing as a minor face in some samples, thus the (211) face should have a lower surface energy than the (100), on the other hand the synthetic sample of ANA illustrates a much larger surface area for the (100) face compared to the (211) face. The surface energies listed in Table 5. 8 predicts that the (211) face is more stable than the (100) face, this prediction agrees with the results from SEM studies of natural ANA.

5.2.2.2 Hydration energy assessment

The energy of hydroxylating each face of ANA by the method shown in appendix B has been given in Table 5. 9. The hydration energies for both surfaces are endothermic, hence it would be unfavourable to react the surface with water in a dissociative manner. The evaluation of hydration energies is analogous with surface energy predictions. The hydration energy for each water molecule is $+77kJmol^{-1}$ for the (211) surface and $+66kJmol^{-1}$ for the (100) surface, this is higher than the hydration energies calculated for the EDI (-5 – $+60kJmol^{-1}$ per water molecule) and MER (-8 – $+34kJmol^{-1}$ per water molecule). The high hydration energies may be due to the potentials failing when a large number of under-coordinated sites are present at the surface. The potential model by Sanders *et al.*[9] used within this study was originally designed for the crystal bulk, where all atoms are fully coordinated. This problem was not observed previously where there where a maximum of fourteen under-coordinated sites, where as for ANA contains almost twice as many under-saturated atoms (twenty-two).

Miller plane	(211)	(100)
Hydration energy	1863.600	1060.467
Hydration energy/water molecule	77.650	66.279

Table 5. 9: Hydration energies of analcime faces, given in $kJmol^{-1}$

To determine why thermodynamic energies suggest that the surface would be found in its unhydroxylated form, examination of the surface structure is required (this is discussed in the next section).

5.2.2.3 Surface structure analysis

Figure 5. 7(a and b) and Figure 5. 8(a and b) represent the unrelaxed and relaxed surface structure of the most stable terminations on both the (211) and (100) face respectively, all terminations have not been shown here for brevity.

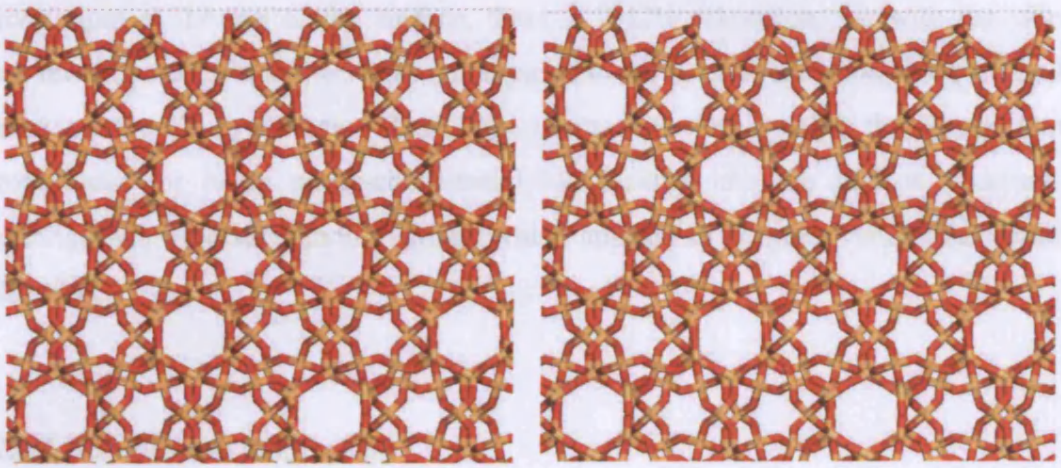

view along [121] **view along [121]**

(a) **(b)**

Figure 5. 7: (211) surface of ANA, (a) unrelaxed, (b) relaxed.

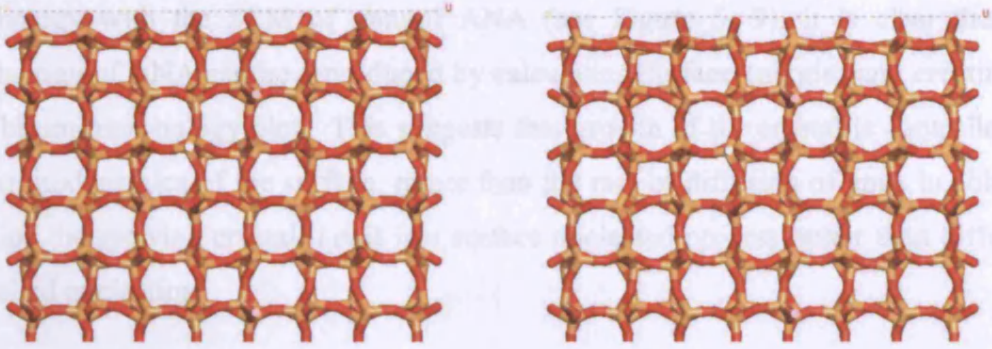

view along [010] **view along [010]**

(a) **(b)**

Figure 5. 8: (100) surface of ANA, (a) relaxed, (b) relaxed

Previous work suggests that the surface with the least number of bonds cleaved are the most stable, both the (211) and (100) faces are consistent with this prediction, thus the termination with the minimal number of bonds cleaved is shown to be the most stable according to surface energy assessment.

Upon minimisation the (211) surface shows an increase in coordination of under-saturated sites, the (211) surface contains under-saturated silicon atoms and under-saturated oxygen atoms at a distance of 3.71Å. During minimisation these two under-saturated sites join together to form a bond of length 1.62Å, this results in 24 under-saturated sites reducing to 20. The (100) surface does not show an increase in coordination on relaxation, however if we measure the degree of relaxation of the silicon atom at the top of the surface, there is 2.42% relaxation, *i.e.* with the silicon atom moving closer in to the surface, compared to the 0.77% relaxation observed by the silicon on the (211) surface. This large contraction implies that the silicon atoms compensates for being under-coordinated by relaxing into the surface structure to coordinate with the surrounding atoms, which appears to be more stable than reacting with water.

5.2.2.4 Equilibrium morphology

The minimised surface energies were used to create an equilibrium morphology plot of ANA, see Figure 5. 9. The equilibrium morphology displays both faces, however the (211) face is dominant and the (100) face is minor. Comparing the equilibrium morphology with the SEM of natural ANA (see Figure 5. 9), it is clear that the morphology of ANA can be reproduced by calculating surface energies and creating an equilibrium morphology plot. This suggests that growth of the crystal is controlled by the thermodynamics of the surface, rather than the rate of diffusion of units in solution reaching the growing crystal, *i.e.* it is a surface nucleated process rather than diffusion controlled nucleation.

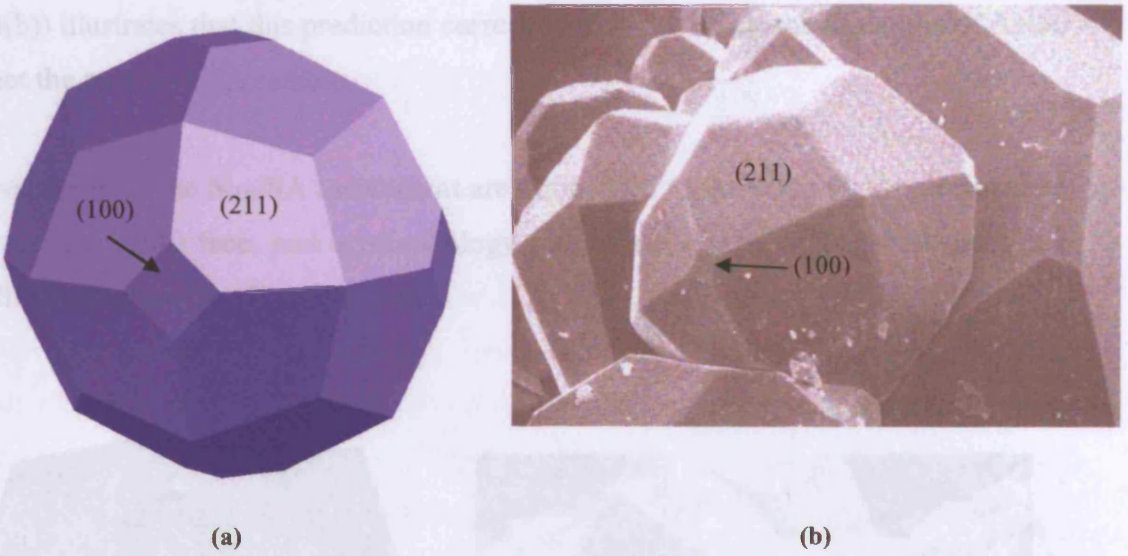

(a) (b)

Figure 5. 9: Morphology of ANA, (a) equilibrium morphology of siliceous ANA, (b) SEM image of natural ANA.

5.2.2.5 N_{BB}/SA assessment

To test the method of predicting crystal morphology with the N_{BB}/SA, the surface termination which cleaves the least number of bonds were identified. The minimum number of bonds cleaved on the (100) and (211) surface was 8 and 24 respectively, however it was found that more than one distinctive cut could be made on each face to achieve this result, with one cut on each surface being identical to the surface found using the surface energy assessment. The results obtained from the N_{BB}/SA are shown in Table 5. 10.

	(211)	(100)
Number of broken bonds	24	8
N_{BB}/SA	0.054	0.044
Normalised value	1.227	1

Table 5. 10: N_{BB}/SA test on siliceous ANA

The N_{BB}/SA test predicts that the (100) surface is more stable than the (211) face, this is the reverse to what is predicted by the surface energy assessment. A comparison of the stability trend with the trend shown by the two SEM samples (Figure 5. 9(b) and Figure

5. 10(b)) illustrates that this prediction corresponds well with synthetic sample of ANA, but not the natural ANA sample.

The values from the N_{BB}/SA assessment are normalised to the value for the most stable face, *i.e.* the (100) face, and a morphology plot of the crystal is predicted using the Wulff construction (see Figure 5. 10).

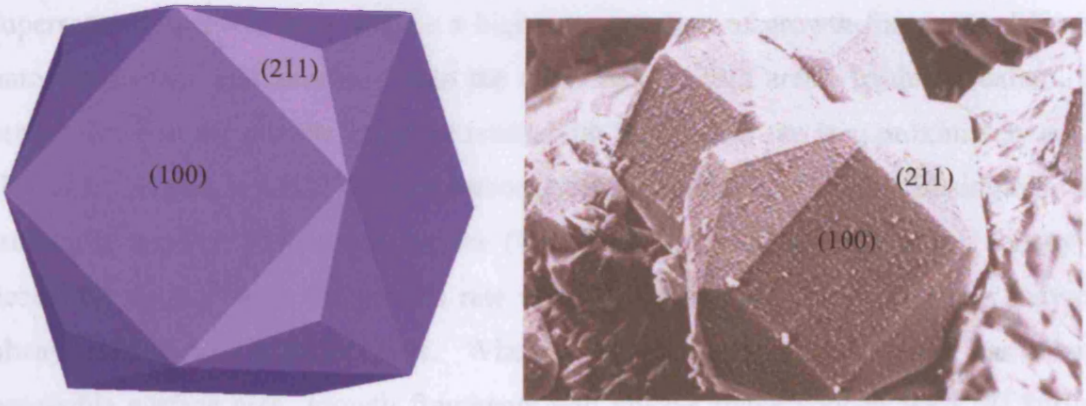

Figure 5. 10: Morphology of ANA determined by the number of broken bonds per surface area

A comparison of the predicted crystal habit with the SEM scans of the natural and synthetic sample illustrates that the N_{BB}/SA approach reproduces the synthetic sample well, with the ratio of surface areas of each of the two faces reasonably predicted.

Overall it is seen that in the case of ANA both the equilibrium and N_{BB}/SA morphology are able to reproduce the crystal habit of ANA, the equilibrium morphology reproduces the natural sample of ANA, whereas the N_{BB}/SA approach works successfully in reproducing the synthetic sample. As observed with EDI it is seen that crystal morphologies can vary within a given batch of crystals, this difference may arise from additional cations which could be present in small quantities which can alter the growth rates of each face, in the crystal. Where as the composition of synthetic sample can be thought of as accurate since the all reactants are known, and so one can be confident that the sample is pure ANA. However, it is important to note that the natural sample has crystallised over a long period of time, whereas the synthetic sample crystallised in

60 days. Therefore, a different crystal habit may be observed, depending upon the rate of formation of individual building units.

The difference between the growth rate predicted by surface energy and N_{BB}/SA could be rationalised in terms of the level of solution supersaturation. If the surface structures of the (211) and (100) surface are examined (topographically), the (100) face contains a smaller density of accessible surface sites, whereas the (211) surface is flatter and contains a larger density of accessible surface sites. In conditions where there is a high supersaturation level, there will be a high concentration of growth fragments diffusing onto the surface and attaching onto the accessible surface area. In this situation, the probability that the growth fragment reacts with the surface site is approximately equal. However, if there is a low supersaturation level, the number of units diffusing onto the surface is smaller. Therefore, on the (100) face, where there is a lower density of accessible surface sites, the growth rate will be slower since the growth unit may not always collide with a surface site. Whereas, on the (211) surface which has a large accessible surface area, growth fragments will always make contact with the surface sites. As a result, the relative growth rate will be faster, and so the (100) surface will be more dominant than that of the (211) face.

In this study, both the surface energy and N_{BB}/SA methods have been able to predict the morphology of different crystal samples. Both approaches divide by the total surface area, however the N_{BB}/SA method appears to be acutely sensitive to the density of terrace nucleation sites. It was observed that the N_{BB}/SA approach was able to predict the synthetic crystal, this could be indicative that the supersaturation levels of the synthetic crystal are quite low.

All these factors can place a large role in crystal growth of ANA , as the crystal habit of natural ANA has been observed with either a dominant or minor (100) face. A through investigation of the origins of this discrepancy is beyond the scope of this thesis.

5.3 Number of bonds per unit area tests

To examine the ease of obtaining reliable predictions of crystal morphology solely by applying the N_{BB}/SA test, natrolite, zeolite A, laumontite, and thomsonite were examined. This test will help establish the versatility of the N_{BB}/SA approach to predicting the crystal morphology for zeolites built up from various secondary building units.

5.3.1 Natrolite

Natrolite (NAT) is a natural zeolite which belongs to the fibrous group, within this classification of zeolite the framework is built up of chains of spiro units, with each spiro unit containing 5T atoms. NAT is an orthorhombic zeolite, with one unit cell made up of $Na_{16}(Al_{16}Si_{24}O_{80}).16H_2O$, thus it is constructed from an aluminosilicate framework with sodium extra framework cations and molecular water within the channels. However within this work we do not believe that the extra framework cations, water or aluminium content within the framework has an effect on the crystal morphology, thus this test will be carried out on a siliceous framework, see Figure 5. 11.

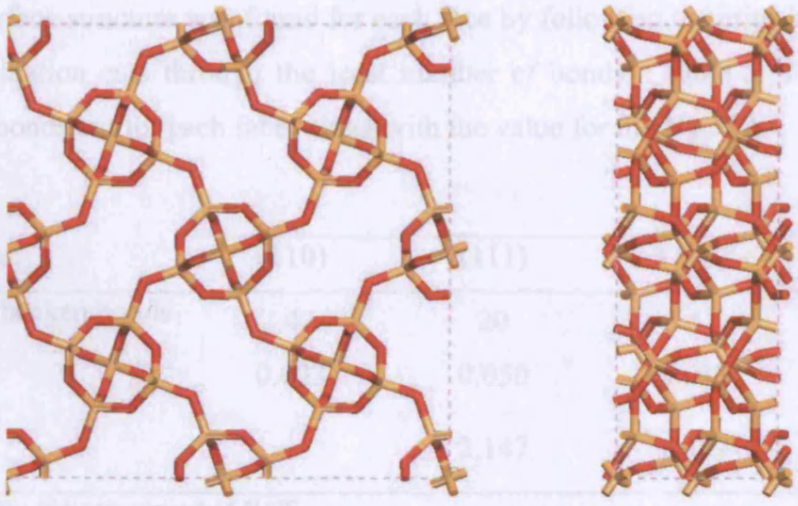

view along [001] **view along [100]**

Figure 5. 11: Siliceous analogue of NAT

5.3.1.1 Crystal morphology

The morphology of natural NAT exposes four faces, the (110) and (111) are dominating faces with a smaller (100) and (010) faces (see Figure 5. 12(a)and (b)), however a tetranatrolite crystal has a form which displays only the (110) and (111) face (see Figure 5. 13(b)).

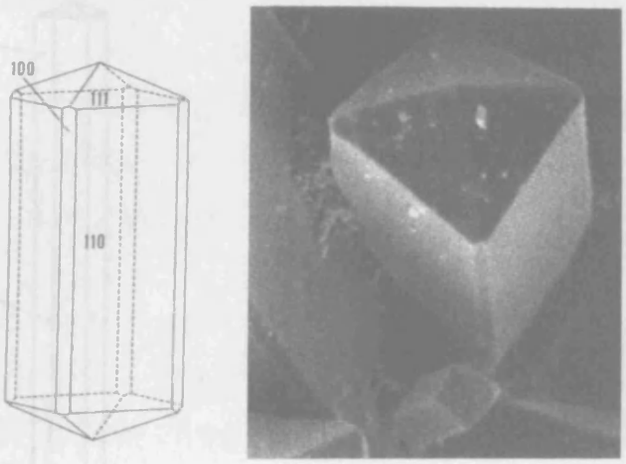

(a) (b)

Figure 5. 12: (a) Schematic image of an SEM of natrolite, (b) SEM image of synthetic of natrolite. ((a) reproduced without permission from Gottardi and Galli[12], (b) reproduced with without permission from Ghobarkar *et al.*[22])

A stable surface structure was found for each face by following the criteria that the most stable termination cuts through the least number of bonds. Table 5. 11 displays the number of bonds cut for each face, along with the value for the N_{BB}/SA.

Miller plane	(110)	(111)	(100)	(010)
Number of broken bonds	4	20	4	4
N_{BB}/SA	0.023	0.050	0.032	0.032
Normalised values	1	2.147	1.389	1.389

Table 5. 11: N_{BB}/SA assessment of NAT

Since the N_{BB}/SA value is inversely proportional to the morphological importance of the face, this assessment illustrates that the (110) face is the most dominant. As a result, to predict the crystal shape, each N_{BB}/SA value is normalised to the (110) face, giving the values shown in the second row of Table 5. 11. Using the normalised values with the Wulff construction gives the following morphology.

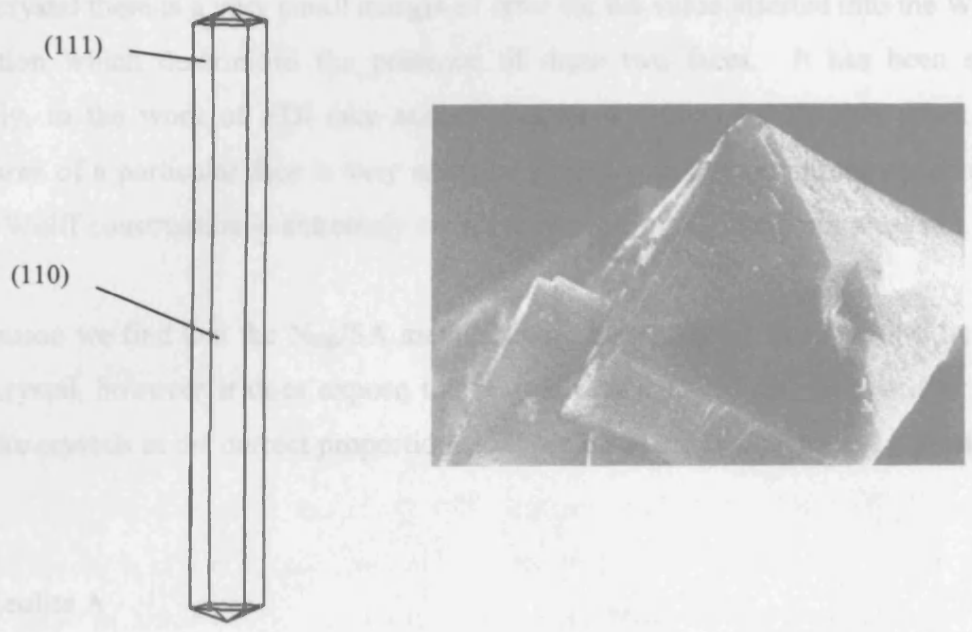

(a) (b)

Figure 5. 13: (a) Predicted crystal morphology of natrolite using the N_{BB}/SA assessment, (b) SEM of tetranatrolite from Ilimaussaq, Greenland. (reproduced without permission from Gottardi and Galli[12])

The above predicted morphology only exhibits two out of the four morphologically important faces, they are the (110) and (111) face. A comparison between this predicted morphology and the SEM of the natural natrolite crystal shown in Figure 5. 12(a) shows that the ratio between the two faces look very similar to what is found in nature, *i.e.* a long crystal, dominated by the (110) face and capped with the (111) face. However it is found that due to the pseudo-tetragonality of the natrolite crystal, tetranatrolite crystals exist, which is constructed from a reduced natrolite unit cell. Tetranatrolite has been identified to have the same structure and composition as Gonnardite.[24] In this case the morphology only contains the (110) and (111) face, as shown in Figure 5. 13(b). The predicted crystal is in very close agreement with crystal shape of tetranatrolite.

The (100) and (010) faces are absent from this prediction, implying that these two faces are fast growing and extinguished by the slow growing (110) and (111) faces. Figure 5. 12 illustrates that the (100) and (010) have a very small surface area in comparison to the total surface area of the natural crystal, and in some cases, *i.e.* tetranatrolite, these faces do not exist at all. Since the (100) and (010) faces are a small percentage of the over all crystal there is a very small margin of error for the value inserted into the Wulff construction which determines the presence of these two faces. It has been seen previously, in the work of EDI (see section chapter 4 section 4.3.4), that when the surface area of a particular face is very small its presence in the morphology predicted with the Wulff construction is extremely sensitive to even small changes in the ratio.

In conclusion we find that the N_{BB}/SA method does not exhibit all faces, shown by the natural crystal, however it does expose the two dominant faces, and does create thin needle like crystals in the correct proportions to those observed by the natural crystal.

5.3.2 Zeolite A

Zeolite A is synthetic zeolite, and belongs to the family of LTA (Linde Type A) structures. The structure contains a 3-dimensional channel system with channels running perpendicular to each other. The framework is made of secondary building units 4, 6, 8, and 4-4 (see Figure 1.2 in chapter 1). The pore diameter is defined by an eight member ring of 4.2Å, this leads into a larger cavity of minimum free diameter 11.4Å. The cavity is surrounded by eight sodalite cages (truncated octahedra) connected by their square faces in a cubic structure. The unit cell of zeolite A has an ordered Si/Al ratio of 1.0, however zeolite A has recently been made in the pure siliceous form. The siliceous analogue of zeolite A is illustrated in Figure 5. 14.

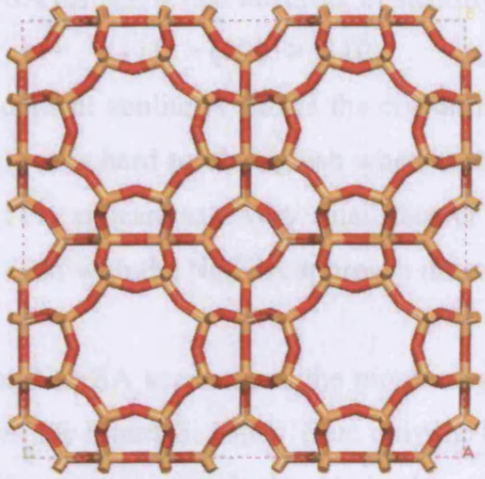

Figure 5. 14: Siliceous zeolite A

5.3.2.1 Crystal morphology

SEM studies have observed three distinct morphologies of zeolite A, a truncated octahedral showing the (100) and (111) face, a chamfered-edge cube with (100) and (110) faces and a sharp edged cube exhibiting pure (100) character.[25] The most common form of zeolite A is the sharp edge cube, however the production of the chamfered edge cube is of technological interest for the detergent industry. Synthesis of zeolite A has shown that there is a large difference in the morphology of the crystal depending upon the aluminium content and temperature used.

For this study the (100), (111) and (110) faces have all been investigated, the surface terminations with the least number of bonds cut have been found and the N_{BB}/SA test has been carried out, results of which have been give in Table 5. 12.

Miller plane	(100)	(111)	(110)
Number of Broken Bond	16	24	14
N_{BB}/SA	0.026	0.023	0.033
Normalised value	1.155	1	1.434

Table 5. 12: N_{BB}/SA test for zeolite A.

The results from the N_{BB}/SA test show that the order of stability of faces is

$$(111) > (100) > (110)$$

The SEM of high silica content zeolite A shows the crystal in a truncated octadehron habit (see Figure 5. 15(b)), it is hard to distinguish whether the (100) or (111) is more dominant, however the (111) appears as a very small face or in some cases not at all, thus a comparison of the SEM with the N_{BB}/SA approach illustrates a similar trend.

Using the values from the N_{BB}/SA assessment, the morphology of zeolite A is plotted *via* the Wulff construction, see Figure 5. 15(a). Here only the (100) and (111) faces are observed, the (110) face does not appear. It should also be noted that in this prediction the (111) face appears to be more dominant than the (100) face, which implies that the (111) is slower growing. A qualitative analysis of the overall shape of the crystal proves to be consistent with the high silica samples.

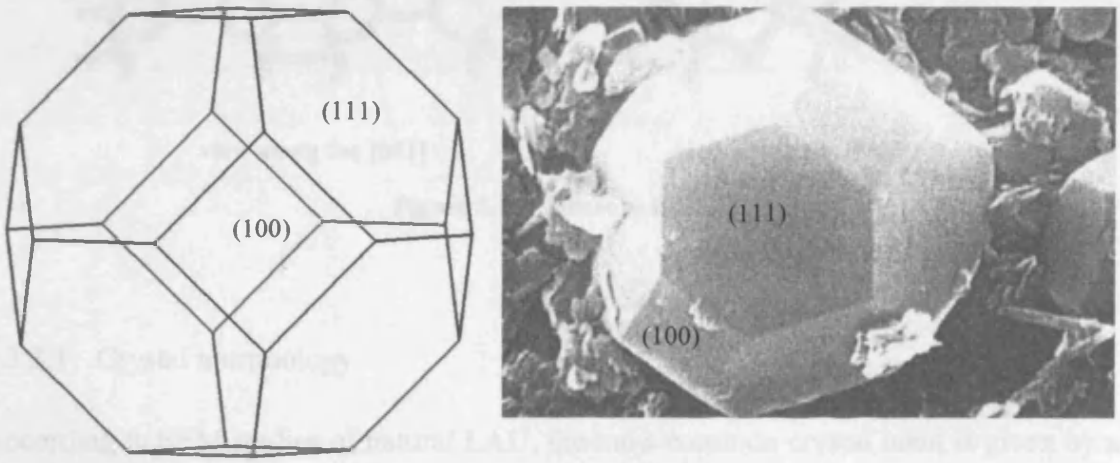

Figure 5. 15: Morphology of zeolite A, (a) simulated with N_{BB}/SA approach, (b) SEM (Reproduced without permission from Basaldella *et al.*[25])

5.3.3 Laumontite

Laumontite (LAU) is a natural zeolite, with a unit cell composition of $Ca_4(Al_8Si_{16}O_{48}).16H_2O$. The crystal structure was resolved almost concurrently by Bartl and Fischer[26], and Amiroc *et al.*[27], and later refined by Schramm and Fischer[28], which is the structure used within this study. LAU belongs to the group of zeolites

constructed from singly connected four ring units, in the LAU structure the four ring units are arranged in sheets. The aluminium distribution within the tetrahedral framework of natural LAU is well known, however as within the previous tests, we are concerned only with the position of the framework atomic positions and not the positions of the extra framework cations or molecular water, as a result the siliceous analogue of LAU is used (see Figure 5. 16).

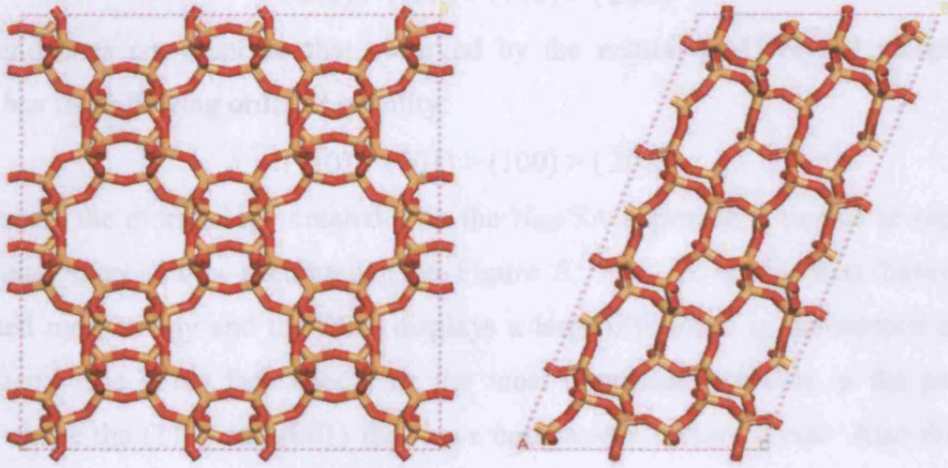

view along the [001] **view along the [100]**

Figure 5. 16: Siliceous LAU

5.3.3.1 Crystal morphology

According to SEM studies of natural LAU, the most common crystal habit is given by a combination of $(\bar{2}01)$, (110), with some crystals displaying (001) and (100) faces, (see Figure 5. 17).[12] A study by Ghobarkar *et al.*[29] have used hydrothermal synthesis methods to form LAU at a range of temperatures, and have observed various crystals shapes ranging from long prismatic single crystal forming at 30°C, single crystals which look like the morphology of natural LAU at 365°C, to thin plates at 450°C.

To predict the crystal morphology four faces are investigated (the $(\bar{2}01)$, (110), (001) and (100) faces) to find a termination which cuts through the least number of bond, results are shown in Table 5. 13.

	$(\bar{2}01)$	(110)	(001)	(100)
Number of broken bonds	18	12	4	8
N_{BB}/SA	0.047	0.059	0.040	0.043
Normalised value	1.191	1.30	1	1.097

Table 5. 13: N_{BB}/SA assessment of LAU

The N_{BB}/SA method shows the following stability of faces:

$$(001) > (100) > (110) > (\bar{2}01)$$

this trend does not relate to that observed by the natural LAU crystal morphology, which has the following order of stability:

$$(110) > (001) > (100) > (\bar{2}01)$$

As a result, the morphology created with the N_{BB}/SA approach is unable to reproduce the crystal morphology accurately (see Figure 5. 17). A comparison between the predicted morphology and the SEM displays a large difference in the surface areas of each face. The (110) face should be the most dominant, however in the predicted crystal shape the (110) and (001) face have comparable surface areas. Also the (100) and $(\bar{2}01)$ faces are more dominant in the predicted crystal implying that they are slower growing faces.

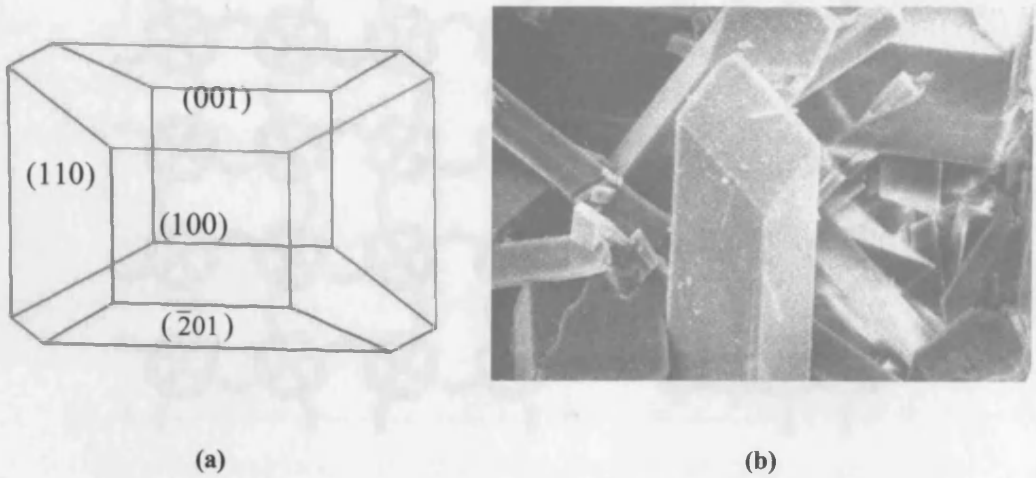

(a) **(b)**

Figure 5. 17: (a) predicted morphology using the N_{BB}/SA approach, (b) SEM of natural LAU (reproduced without premission[12])

Since the N_{BB}/SA procedure is a basic approach to determining crystal shape there are many factors, such as temperature, and the pH of the solution in which LAU

crystallises, all of which could alter the relative rates of the crystal and are not considered here.

In order to improve the prediction of the crystal the correct surface structure may be predicted by carrying out a surface energy assessment. It would also be useful to work with an aluminosilicate framework with extra framework species, rather than the siliceous framework, to establish if the composition of the cell affects the growth rate of each face for this material.

5.3.4 Thomsonite

The Thomsonite (THO) framework was described by Taylor *et al.*[30] in 1933, however later refinements made by Meier[31] proposed a larger unit cell with a doubling of the c parameter. The structure was further refined and all cation and water sites were found by Alberti *et al.*[32] A typical unit cell of THO has a composition of $Na_4Ca_8(Al_{20}Si_{20}O_{80}).24H_2O$. THO belongs to the fibrous group of zeolites, and so like EDI the framework is constructed from a chain of spiro units, as shown in Figure 5. 18.

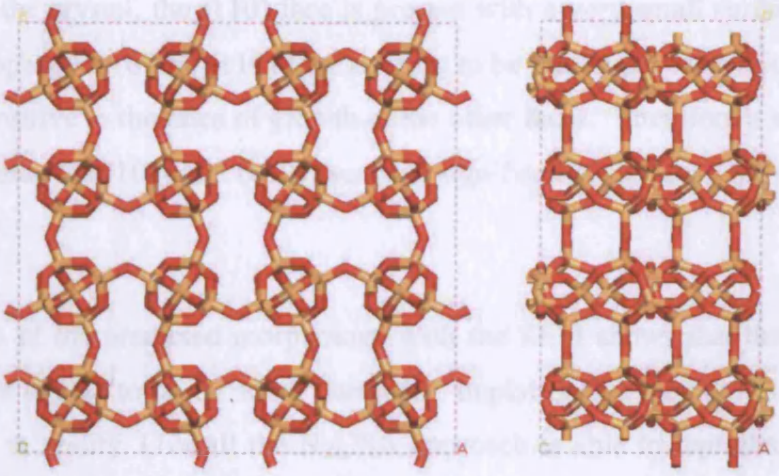

view along [001] **view along [100]**

Figure 5. 18: Siliceous structure of THO

5.3.4.1 Crystal morphology

A natural sample of THO exposes four faces, the (100), (110), (010) and (001) face (see Figure 5. 19(a)), and so these faces were used in the N_{BB}/SA assessment. The values calculated for the most stable termination, by methods described above, of each face are listed in Table 5. 14.

Miller plane	(010)	(100)	(110)	(001)
Number of broken bonds	4	4	8	8
N_{BB}/SA	0.023	0.023	0.033	0.044
Normalised value	1	1	1.415	1.893

Table 5. 14: N_{BB}/SA assessment of THO

The N_{BB}/SA approach gives the following trend of stability:

(010) and (100) > (110) > (001)

which is the same trend of stability as that shown by the SEM image of natural THO. In order to determine if the correct surface structure has been deduced the morphology of the crystal is predicted using the Wulff construction, as shown by Figure 5. 19(c). On first sight this crystal shape shows only three out of the four faces, however on closer inspection of the crystal, the (110) face is present with a very small surface area. This decrease in appearance of the (110) face is likely to be due to the expression of this face being very sensitive to the rates of growth of the other faces. Therefore a slight increase in the dominance the (100) and (010) face will significantly decrease the dominance of the (110) face.

A comparison of the predicted morphology with the SEM shows that the (100), (010) and (001) face appear to be far more dominant, implying that they are far more stable than they are in reality. Overall the N_{BB}/SA approach is able to reproduce the correct order of surface stability, however it is unable to calculate accurate magnitudes to create a morphology with aspect ratios similar to that seen in nature. In this case it would be useful to carry out a surface energy assessment to determine if the predicted surface terminations are the most stable.

(a)

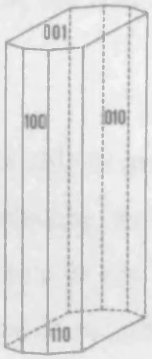

(b)

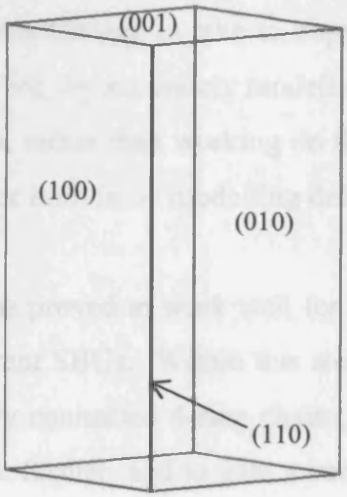

(c)

Figure 5. 19: (a) SEM of natural THO, (b) schematic diagram of THO, (c) predicted morphology using the N_{BB}/SA approach.

5.4 Conclusions

A critical test of the capability of the N_{BB}/SA method has been carried out. The aim was to predict relative growth rates and determine crystal morphology, using the assumption that the most thermodynamically stable surface termination is the one that breaks the minimal number of bonds between crystal planes.

By carrying out a number of tests on selected materials, this work has shown that the N_{BB}/SA is able to provide a reasonably successful route to predict the crystal habit of a zeolite. The tests on the natural zeolites MER, ANA, and NAT. and the synthetic zeolite A illustrate that the N_{BB}/SA method is able to predict the relative rate of growth

of faces and also predict the morphology. In the case of MER the N_{BB}/SA prediction is far superior than the equilibrium morphology prediction.

The test on THO illustrated that in some cases this method is able to predict the correct order of the rate of growth, however a problem lies in transferring those rates into the relative magnitude of growth, and the sensitivity of growth rate of one face to another. It is also found that the N_{BB}/SA prediction of LAU is unable to predict the correct aspect ratios of faces, which results in the incorrect prediction of the crystal habit. These problems may originate from a number of factors, since the N_{BB}/SA method is such a simplified model. A sensible step to take to improve these models would be to correctly represent the framework, by accurately modelling the crystal composition and then using the N_{BB}/SA method, rather than working on the siliceous analogue; this will also remove the systematic error built in by modelling dehydrated structures.

Overall the N_{BB}/SA method has proved to work well for predicting the crystal shape of a zeolite with a range of different SBUs. Within this study zeolites constructed from a chain of fibrous zeolites, singly connected 4-ring chains, doubly connect 4-ring chains and 6-rings. To take this work further, and to gain a complete picture of how well the N_{BB}/SA method works on zeolites built from all structural units this technique should be tested for zeolites constructed from double 6-rings, the hexagonal sheet with handles and the 4-4-1-1 heulandite unit.

By carrying out this work, the N_{BB}/SA test has proved to be a useful method in calculating the relative growth rates and also predicting the crystal morphology of a number of zeolites. This method is also capable in giving insights into the mechanism of growth. When the N_{BB}/SA method is able to correctly predict the aspect ratio, one can deduce that there are key sites on the surface that are the rate-determining steps during growth. As a result, the rate-determining process in growth can be deduced to be nucleation at a surface terrace site, rather than diffusion limited growth.

REFERENCES

1 M. Born and O. Stern. *Sitz. Ber. Preuss. Akad. Wiss.* **48**, 901 (1919)

2 I. Galanakis, G. Bihlmayer, V. Bellini, N. Papanikolaou, R. Zeller, S. Blugel and P. H. Dederichs. *Europhys. Lett.* **58**, 751 (2002)

3 I. Galanakis, N. Papanikolaou and P. H. Dederichs. *Surf. Sci.* **511**, 1 (2002)

4 J. B. Nicholas, A. J. Hopfinger, F. R. Trouw and L. E. Iton. *Journal of the American Chemical Society* **113**, 4792 (1991)

5 E. Passaglia, D. Pongiluppi and R. Rinaldi. *Neues Jahrb Miner Montsh* (1977)

6 E. Galli, G. Gottardi and D. Pongiluppi. *Neues Jahrb Miner Montsh*, 1 (1979)

7 S. B. Hong, D. Y. Han, O. H. Han and I. S. Nam. *Chem. Commun.*, 1719 (2000)

8 G. J. Kennedy, M. Afeworki and S. B. Hong. *Microporous Mesoporous Mat.* **52**, 55 (2002)

9 M. J. Sanders, M. Leslie and C. R. A. Catlow. *J. Chem. Soc. Chem. Commun.*, 1271 (1984)

10 N. Almora-Barrios, A. Gomez, A. R. Ruiz-Salvador, M. Mistry and D. W. Lewis. *Chem. Commun.*, 531 (2001)

11 D. W. Lewis, A. R. Ruiz-Salvador, N. Almora-Barrios, A. Gomez and M. Mistry. *Mol. Simul.* **28**, 649 (2002)

12 G. Gottardi and E. Galli. *Natural zeolites* (Springer-Verlag, 1985)

13 K. P. Schroder, J. Sauer, M. Leslie, C. R. A. Catlow and J. M. Thomas. *Chem. Phys. Lett.* **188**, 320 (1992)

14 W. H. Taylor. *Z Kristallogr.* **74**, 1 (1930)

15 M. Calleri and G. Ferraris. *Atti Accad. Sci. Torino 98*, 821 (1964)

16 C. R. Knowles, F. F. Rinaldi and J. V. Smith. *Indian Mineral* **6**, 127 (1965)

17 G. Ferraris, D. W. Jones and J. Yerkess. *Z Kristallogr.* **135**, 240 (1972)

18 D. S. Coombs. *Mineral. Mag.* **30**, 699 (1955)

19 F. Mazzi and E. Galli. *Mineral. Mag.* **60**, 448 (1978)

20 J. D. Gale. *J. Chem. Soc.-Faraday Trans.* **93**, 629 (1997)

21 E. M. Flanigen, J. M. Bennett, R. W. Grose, J. P. Cohen, R. L. Patton, R. M. Kirchner and J. V. Smith. *Nature* **271**, 512 (1978)

22 H. Ghobarker, O. Schaf, Y. Massiani and P. Knauth. *The reconstruction of natural zeolites* (Kluwer Academic Publishers, 2003)

23 D. H. Gay and A. L. Rohl. *J. Chem. Soc. Far. Trans.* **91**, 925 (1995)

24 G. A. Rtioli and E. G. Alli. *American Mineralogist* **84**, 1445 (1999)

25 E. I. Basaldella and J. C. Tara. *Mater. Lett.* **34**, 119 (1998)

26 H. Bartl and K. F. Fischer. *Neues Jahrb Miner Montsh*, 33 (1967)

27 S. T. Amirov, V. V. Ilyukhin and N. V. Belov. *Dokl Akad Nauk SSSR* **174**, 667 (1967)

28 V. Schramm and K. F. Fischer. *Molecular sieve zeolites. I. Am Chem Soc Adv Chem Ser* **101**, 259 (1970)

29 H. Ghobarkar and O. Schaf. *Microporous Mesoporous Mat.* **23**, 55 (1998)

30 W. H. Taylor, C. A. Meek and W. W. Jackson. *Z Kristallogr.* **84**, 373 (1933)

31 W. M. Meier. in *Molecular sieves* 10 (Society of chemical Industry, London, 1968).

32 A. Alberti, G. Vezzalini and V. Tazzoli. *Zeolites* **1**, 91 (1981)

CHAPTER SIX:

A DENSITY FUNCTIONAL THEORY STUDY OF SILICATE AND ALUMINOSILICATE CLUSTERS

6.0 INTRODUCTION

The importance of sol-gel processes in synthesising inorganic ceramics and glass materials was first recognised in the mid-1800s from studies by Ebelman[1,2] and Grahams[3] on silica gels. Subsequently the interest in sol-gel methods of synthesis has developed to include various studies, for example, there is the occurrence of *liesegang* rings* formed from gels.[4] It was also recognised by Roy *et al.*[5-8] that high levels of chemical homogeneity could be achieved in colloid gels, consequently sol-gel methods were used to form large numbers of novel ceramic oxides which could not be formed previously by other methods. A review by Hench and West[9] gives a thorough account of the achievements through the use of sol-gel processes.

This study is focused upon exploring the use of sol-gel methods to form low and high density silicates and aluminosilicates. In particular this research will focus on the use of hydrothermal methods in the synthesis of microporous materials. A significant amount of information has been concluded from a wealth of studies, to determine the factors controlling and optimising the synthetic process,[10,11] however atomistic understanding of the underlying mechanistic process of these methods are sparse. As a result, this work will concentrate on using simulation techniques to model the species in solution during hydrothermal synthesis, at an atomisic level.

Early ideas on the mechanism of zeolite growth were proposed by Barrer,[12] he suggested that zeolites are formed by the successive addition of small, preformed units (*i.e.* SBUs). However, the view that distinct stable clusters exist in solution was

* *Liesegang* rings are the formation of patterns during precipitation. *Liesegang* patterns, which are often rings in circular geometries and bands in linear geometries. These are formed by the nonuniform spatial distribution of crystals in a precipitation reaction in a gel.

doubted until the 1980s, when NMR studies were able to prove the existence of such structures in aqueous alkali metal and alkylammonium silicate solutions.[13-17] A range of silicate structures have been identified from a single monomer to linear chains to cyclic and cubic units. Recent studies on the synthesis of MFI and MEL by Ravishankar *et al.*[18-20] have identified polycyclic silicate anions, which they describe as the precursor species which self assemble to build up the crystal structure. A paper by Knight *et al.*[21] has challenged the prediction of the precursor species predicted by Ravishankar *et al.* stating no evidence of these clusters have been seen in solution, however a recent study by Ramanan *et al.*[22] has provided TEM and AFM evidence of *nanoslabs* which have an in-plane dimension of $4\times4nm^2$ and a thickness of approximately 1.2-1.3nm. Given the complex nature of this topic and the apparent disagreement between different experiments, simulation methods offer timely adjunct information.

Alongside experimental methods, computational techniques have also been implemented to study crystal growth, for example a recent study by Bussemer *et al.*[23] has used *ab initio* methods to simulate the ^{29}Si NMR spectra of all-silica zeolites. Comparison of their results with chemical shifts calculated with observed structures show that the simulated data are able to reproduce experimental results, and hence provides confidence in the use of this technique. This allows accurate chemical shifts to be predicted for species unknown in solution, which can aid experimentalist to interpret ambiguous data. *Ab initio* methods have also been utilised to investigate the stability of silicate fragments by Sauer[24] and Catlow *et al.*[25] Their work has identified the thermodynamic stability of clusters, and unlike experimental investigations, they have been able to suggest the conformation of these units and make predictions on the extent of intra-molecular hydrogen bonding. However, they have not been consistent throughout their approach. For smaller clusters they have used a non-local DFT-BLYP/TNP level of approximation and a local DFT-BHL/DNP level of theory for larger clusters.

6.1 Objectives

There have been many papers published on the subject of hydrothermal synthesis, however there are no definitive conclusions; as a result this area is still an active area of research with many outstanding questions. The purpose of this study is to gain a deeper understanding of the precursors which are present in solution during synthesis and to determine a mechanistic pathway for the formation of a zeolite crystal. Development into understanding the area of zeolite growth mechanisms will be carried out by establishing the mechanism of growth for EDI.

In chapter 4 the underlying information of the EDI crystal surface was revealed; the crystal habit was modelled and the surface structure of each face visible in the morphology was determined. Using this basic structural information, a set of silicate and aluminosilicate fragments likely to be present in solution can be proposed. By understanding the energetics of the individual fragments, a series of stability for the set of fragments considered will be developed and a mechanistic pathway of condensation reactions which occur during the formation of EDI may be suggested.

6.2 Proposed building units

To determine a set of fragments to be investigated, our knowledge of the most stable surface structure was used as starting point. From the classical study and the N_{BB}/SA approach it was concluded that the density of under-saturated bonds on each face determine the growth rate, hence it is the formation of these bonds on each face which is the rate determining step during the crystallisation of EDI. Since these crucial bonds appear between each layer of EDI, and it is already known from the prediction of growth morphology that growth does not occur by addition of fully formed layers, crystallisation must proceed *via* the attachment of small fragments present within one layer. By examining the surface structure of each face of the crystal, it was concluded that each surface contained an integer number of formula units, however on each surface the formula unit is arranged in a different configuration. These units could be arranged such that on each face, a formula unit in a particular configuration could tessellate from the bulk structure up to the surface termination without any excess atoms. One formula unit of EDI has a composition of three silicons, two aluminiums,

four oxygens and a barium cation, *i.e.* $BaSi_3Al_2O_4$, this is the same silicon to aluminium ratio as on the unit cell of the EDI crystal, hence the repetition of a formula unit throughout the structure allows the correct silicon to aluminium ratio as found in the extended crystal. Each formula unit appears twice within one layer, where one layer on each face contains the same constituents as one unit cell of EDI.

The following sections describe the repeat fragment found on each face and describe how they relate to the rate determining bonds on each surface termination. Each of these fragments is cut out of the surface framework, the under-coordinated oxygens are capped with hydrogens and the undercoordinated T atoms are capped with hydroxyl groups to construct a charge neutral cluster.

6.2.1 (110) surface

Figure 6. 1(a) displays the surface structure of the (110) face, with the repeat units highlighted in green and lilac. The highlighted fragment has been cut out and enlarged to show the arrangement of the constituent atoms (see Figure 6. 1(b)).

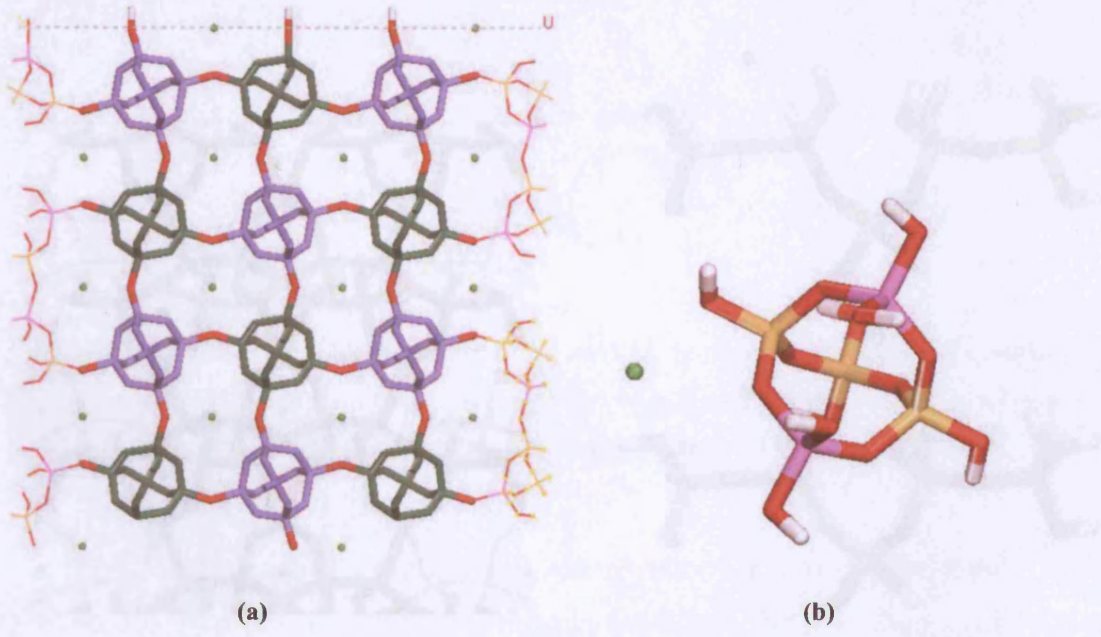

(a) (b)

Figure 6. 1: (a) Repeat unit highlighted in green and lilac on the (110) surface, (b) highlighted fragment enlarged displaying, displaying both the silicon (yellow) and aluminium (magenta) atoms within a spiro unit arrangement.

The enlarged fragment displays a 3:2 silicon (yellow) to aluminium (magenta) ratio, with all five tetrahedral (T) atoms arranged as three 4-membered rings. From this point onwards we shall refer to this arrangement as a spiro unit. The (110) surface contains two broken bonds per surface area, and so two spiro units attach on to the growing surface, with each spiro unit forming one rate determining bond.

6.2.2 (001) surface

Figure 6. 2(a) displays the repeat units highlighted upon the (001) surface, with Figure 6. 2(b) illustrating an enlarged image of the repeat fragment. There are two repeating fragments with respect to each crystal layer on the (001) surface, both are arranged as a v-shaped chain, with alternating silicon and aluminium atoms in the following series: Si-Al-Si-Al-Si, or aluminium atoms at either end Al-Si-Si-Si-Al. Within these chains the oxygen atoms between each T atom have been omitted to represent the order of the aluminosilicate in a concise form. The (001) surface termination exposes eight rate determining bonding sites per surface area, in this case one fragment attaches on to all eight sites.

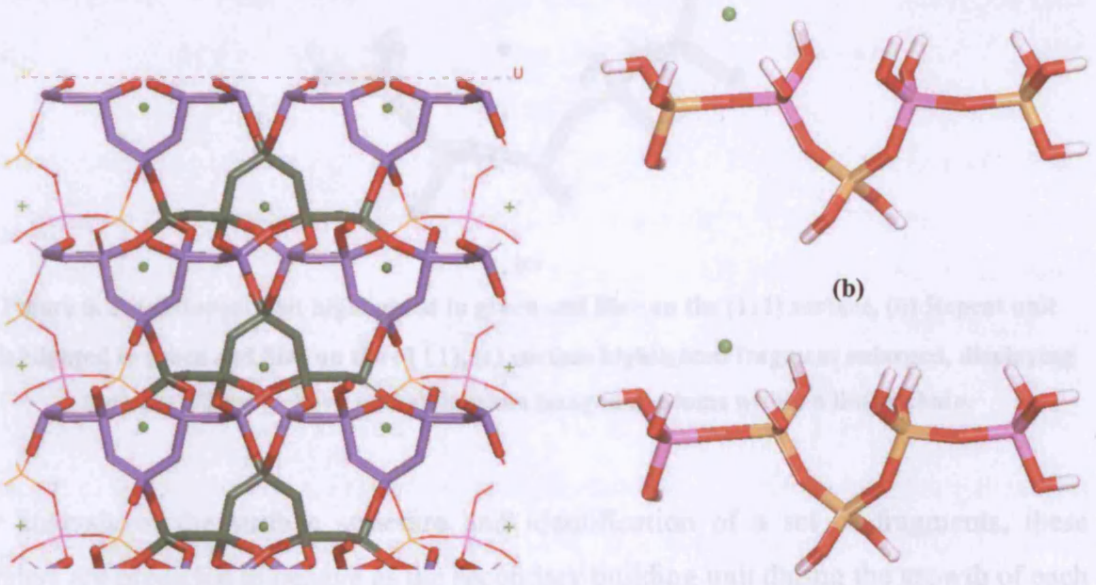

Figure 6. 2: (a) Repeat unit highlighted in green and lilac on the (001) surface, (b) and (c) highlighted fragment enlarged, displaying both the silicon (yellow) and aluminium (magenta) atoms within a v-shaped linear arrangement.

6.2.3 (111) and $(1\bar{1}1)$ surface

The (111) and $(1\bar{1}1)$ surface both have the same 5T linear chain translated throughout the bulk and to the surface (see Figure 6. 3(a) and (b)), with a Si-Al-Si-Si-Al sequence (see Figure 6. 3(c)).

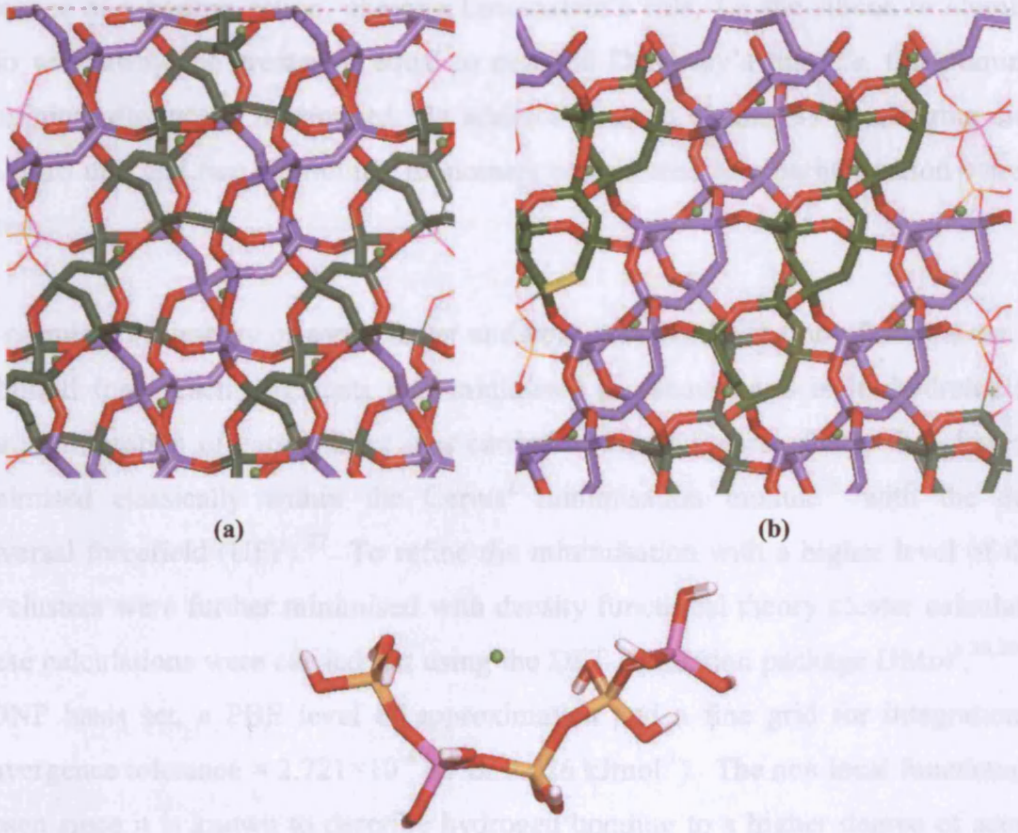

Figure 6. 3: (a) Repeat unit highlighted in green and lilac on the (111) surface, (b) Repeat unit highlighted in green and lilac on the $(1\bar{1}1)$, (c) surface highlighted fragment enlarged, displaying both the silicon (yellow) and aluminium (magenta) atoms within a linear chain.

By analysis of the surface structure and identification of a set of fragments, these clusters are predicted to behave as the secondary building unit during the growth of each face. This prediction is investigated by the determination of the overall stability of each cluster by DFT calculations.

6.3 Methodology

In order to calculate the stability of smaller fragments also present in solution a series of silicate and aluminosilicate clusters have been examined. All siliceous fragments with the formula $Si_xO_y(OH)_z$ with x ranging from 1 to 5 were investigated, also the equivalent aluminosilicate cluster with two aluminium atoms has also been tested, with each cluster formed conforming to the criterion of being charge neutral, *i.e.* by the presence of a barium cation, obeying Lowenstein's rule, *i.e.* the silicon to aluminium ratio will always be greater or equal to one and Dempsey's rule, *i.e.* the aluminium-aluminium distance is maximised. In addition to open chains, 4T closed ring cluster, the spiro unit and two aluminium monomers coordinated to a barium cation were also tested.

To calculate the energy of each cluster and hence the configuration of the cluster in its stabilised form, each fragments was minimised in vacuum and in its hydrated form. The minimisation of each cluster was carried out in two parts, firstly the cluster was minimised classically within the Cerius[2] minimisation module[26] with the default universal forcefield (UFF).[27] To refine the minimisation with a higher level of theory the clusters were further minimised with density functional theory cluster calculations. These calculations were carried out using the DFT simulation package DMol[3],[28,29] with a DNP basis set, a PBE level of approximation and a fine grid for integration (*i.e.* convergence tolerance = 2.721×10^{-4} eV or 0.026 $kJmol^{-1}$). The non local functional was chosen since it is known to describe hydrogen bonding to a higher degree of accuracy that local functionals, this was combined with a double numerical basis set since previous studies by Pereira *et al.*[30,31] have shown a very small (0.02%) improvement in energy by using a triple basis set.

To minimise the clusters in a hydrated medium, the DMol[3] code was used together with the COSMO method to represent the clusters in a water solvent. In the COSMO model[32] the water models are represented implicitly, as described in chapter 3 section 3.11.1.1. As with minimisation calculations in vacuum, a DNP basis set with a PBE level of approximation with a fine grid of integration was used, the COSMO dielectric constant was set to 78.4 to represent water. The COSMO model has been parameterised

with a DNP basis set, and so by combining the COSMO model with TNP will induce errors, thus using DNP is a more favourable choice in this work.

Unlike previous studies[25,30,31,33-35] which have used both LDA and various GGA functionals, this research uses a consistent approach, where all silica clusters are studied with the same well defined GGA functional, and for the first time the aluminosilicate equivalent of all clusters are also considered and compared with pure silica fragments.

6.4 Results and discussion

In the following sections a detailed analysis of the conformations and energetics of each cluster will be discussed. Along with a comparison between siliceous and aluminosilicate clusters, open and closed (spiro and ring type) structures and the changes in acidity of hydroxyl groups. The affect of water on the thermodynamic stability and configuration of each cluster will also be analysed. Where possible these findings are compared with findings of other studies. For reference it should be noted that atoms with subscript *t* represent to terminal atoms, and atoms with subscript *b* signify to bridging atoms.

6.4.1 Siliceous clusters

6.4.1.1 Silica monomer

Two different confirmations of the silica monomer (S1 and S2) have been minimised within this study, both of which are shown in Figure 6. 4. Only the configuration of the S2 monomer predicted in this study is the same to the conformation found by DFT calculations using the BLYP/TNP[25] functional and Hartree-Fock (HF)[24] approximations. Both of these calculations present the same two conformations of the silica monomer with point symmetries of D_{2d} and S_4, where the point symmetry S_4 represents the silica monomer at the global minimum and the point symmetry represents D_{2d} a local minimum.

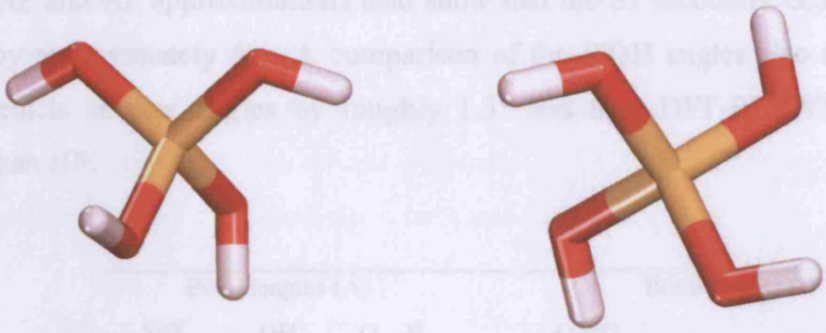

(a) S1 - C_1 symmetry **(b) S2 - S_4 symmetry**

Figure 6. 4: $Si(OH)_4$ Cluster optimised at the DFT-PBE/DNP level of approximation

The structure of the S1 silica monomer minimised in this study does not belong to either of these categories, the position of two of the hydroxyl groups lie in the same direction as within the D_{2d} configuration and the remaining two hydroxyl groups lie in the same direction at the S_4 configuration, thus the S1 monomer is in the C1 point group. The S2 monomer is -0.017eV (-1.63kJmol^{-1}) more stable than the S1 monomer, this value can not be compared with the work by Catlow *et al.*[25] and Pereira *et al.*[30,31] since they have not calculated the energy of the silica monomer in the C1 symmetry, however the energy difference between the D_{2d} and S_4 conformers is -0.078eV (-7.53kJmol^{-1}) at the BLYP/DNP level of theory, this suggests that the S_4 conformation is the most stable, with the D_{2d} configuration being the least stable and the stability of C_1 monomer lying in between the two. At 300K, it would be feasible for the structures in the C1 and D_{2d} conformation to rotate to form the S_4 monomer, as a result all three monomers would be predicted to exist in solution, with the S4 monomer present in the highest concentration.

A comparison of the bond angles and lengths of the S1 monomer in this study with the DFT prediction by Catlow *et al.*[25] and HF prediction by Sauer[25] is tabulated in Table 6. 1. The SiO_t and OH bond lengths match exactly with that of the DFT-BLYP/TNP approximation and only 0.02Å and 0.03Å larger than the HF study respectively. Both the DFT-BLYP/TNP and HF approximation do not show any evidence of hydrogen bonding, whereas this study may be considered to show evidence of a very weak indirect hydrogen bond of 2.56Å, this may simply be a product of this conformation resembling a structure with some residual strain. The range of O_tSiO_t angles for the S1 monomer is smaller than the S2 monomer, a comparison these angles with DFT-

BLYP/TNP and HF approximations also show that the S1 monomer O_tSiO_t angles are smaller by approximately 4°. A comparison of the SiOH angles also show that this study predicts smaller angles by roughly 1.3° less than DFT-BLYP/TNP and 3.6° smaller than HF.

	Bond lengths (Å)			Bond Angles (°)	
	SiO_t	OH	O...H	O_tSiO_t	SiOH
S1-DFT-PBE/DNP	1.65	0.97	2.56	102.43-112.86 (109.53)	114.43-115.80 (115.17)
S2-DFT-PBE/DNP	1.65	0.97		106.12-116.55 (109.55)	114.77-115.54(115.16)
DFT-BLYP/TNP[25]	1.65	0.97		106.6-115.4	116.5
HF/6-31G**[24]	1.63	0.94		106.6-115.4	118.8

Table 6. 1: A comparison of bond lengths and angles of the S1 and S2 monomer from this study and other computational methods of the silica monomer. Figures in parentheses represent the average value

The S2 monomer (Figure 6. 4(b)) minimises into a configuration which lies in the S_4 point group, which according to the DFT study by Catlow *et al.*[25], the HF study by Sauer[24] and the energies calculated from this study is the global minimum configuration for a silicon monomer. The bond lengths and angles of the S2 monomer are as listed in the second row of Table 6. 1. The bond lengths of both the S1 and S2 monomers are exactly the same, with the average bond angles in agreement within one decimal place. The bond lengths and O_tSiO_t angle of the S2 monomer are in agreement with hybrid B3LYP methods and have a maximum 3% difference with HF methods. The average SiO_tH angle from this study is approx 1% lower than the hybrid method and 3% lower than the HF method. Both the PBE and hybrid BLYP functionals produces very similar results, with figures ranging within in the same values, as a result the PBE/DNP functional can be regarded are a suitable level of theory for investigating this structure. Typically HF methods do not include the effects of electron correlation, which reduces the accuracy of the minimised structure, methods such as configuration interaction may be used to include electron correlation, however they do increase the computational expense.

Table 6. 2 lists the Mulliken and Hirshfeld charges[36] of both the silica monomer studied in this research, and the charges of the silica monomer investigated by Pereira *et al.*[30]

The Mulliken and Hirshfeld charges calculated in this study for both monomers are comparable. An evaluation of the hydrogen and oxygen charges between this study and the Pereira *et al.* study show that the Mulliken charges predict the hydrogen atoms in this study to be almost half as acidic, however the Hirshfeld charges predict similar charge densities (within 5%) of all three monomers.

	Mulliken			Hirshfeld		
	Si	O_t	H	Si	O_t	H
S1-PBE/DNP	1.458	-0.636 – -0.667	0.281 – 0.288	0.500	-0.288 – -0.300	0.166 – 0.169
S2-PBE/DNP	1.475	-0.654 – 0.657	0.287	0.504	-0.295	0.169 – 0.170
BLYP/TNP[30]	1.151	-0.809	0.522	0.509	-0.289	0.161

Table 6. 2: Mulliken and Hirshfeld charges of the silica monomer.

6.4.1.2 Silica dimer

Figure 6. 5 illustrate the confirmation of the minimised silica dimer, in this case the total energies vary extensively with the amount of hydrogen bonding present within the minimised cluster. Within the case of the silicon dimer the extent of intra-molecular hydrogen bonding may be attributed to the to the SiO_bSi angle, however since there are no experimental results for the silicon dimer in vacuo, we can only compare to other theoretical studies.

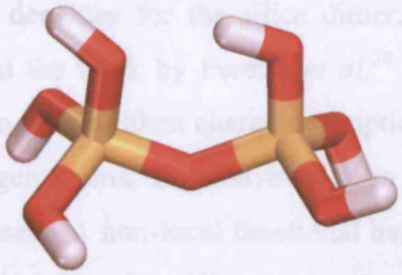

Figure 6. 5: Silica dimer: $Si_2O(OH)_6$ cluster optimised at the DFT-PBE/DNP level of approximation

The structural properties of the minimised dimer from this study, *i.e.* using the DFT-PBE/DNP approximation, and a study by Pereira *et al.*[30] with the DFT-BLYP/TNP approximation have been tabulated in Table 6. 3. Both the average OSiO and SiO_tH angles calculated have a broader range of values than the range calculated by Pereira *et*

al., however the values are realistic and the average value is found to lie within the range calculated using the BLYP/TNP method. The SiO_bSi angle is almost 5° larger in this study compared to the BLYP/TNP level of approximation, however the 137° angle predicted in this study seems a reasonable quantity since the SiO_bSi angle in zeolites are known to adopt a large range of angles (as explained in chapter 1). Although there is an increase in the SiO_bSi angle, the PBE/DNP approximation produces a stronger intra-molecular hydrogen bond than the BLYP/TNP approximation. All other bond lengths from both approximations compare very well.

	DFT Method	
	PBE/DNP	BLYP/TNP[30]
Bond Lengths (Å)		
SiO_t	1.64 – 1.66 (1.65)	1.64 – 1.66
SiO_b	1.64 – 1.66 (1.65)	1.65
OH	0.97	0.97
O...H	2.05	2.52
Bond Angles(°)		
SiO_bSi	137.00	132.1
OSiO	103.34 – 116.25 (109.51)	107.8 – 113.7
SiO_tH	113.15 – 116.29 (115.02)	114.1 – 117.7

Table 6. 3: Geometry of silica dimer, with bond lengths given in Å and bond angles in °. Figures in parentheses represent the average value

Table 6. 4 lists the charge densities for the silica dimer, a comparison between the findings from this study and the work by Pereira *et al.*[30] display very similar results. The only difference occurs in the Mulliken charge description of hydrogen, this research predicts more acidic hydrogen atoms, this maybe due to two factors, the number of basis sets or the functional used. A non-local functional has been used in this study and the work of Pereira *et al.*, therefore the difference in charge is most likely due to the difference in the number of basis sets used. The work by Pereira[37] has noted a drastic change in silica dimer dipole moment (from 1.09 for DNP and 0.85 for TNP) by changing the number of basis sets, and hence concluded that the use of a greater number of basis sets may not increase the reliability of the calculated values.

	Mulliken		Hirshfeld	
	PBE/DNP	BLYP/TNP[30]	PBE/DNP	BLYP/TNP[30]
Si	1.521 – 1.550	1.762	0.507 – 0.521	0.537
O_b	-0.870	-0.826	-0.2929	-0.304
O_t	-0.635 – 0.704	-0.601	-0.263 – -0.298	-0.290
H	0.280 – 0.317	0.151	0.131 – 0.177	0.162

Table 6. 4: Mulliken and Hirshfeld charges of the silica dimer

6.4.1.3 Silica trimer

The minimised silica trimer is illustrated in Figure 6. 6, the linear trimer has relaxed into a quasi cyclic configuration, with the formation of two intra-molecular hydrogen bonds completing the ring. The same cyclic conformation was found with the DFT-local and non-local methods by Catlow *et al.*[25] and Pereira *et al.*[30]. Both papers investigated the quasi cyclic chain and linear chain structures, at both the local and non-local approximation the quasi cyclic conformation was found to be more stable. They have also investigated the cyclised silica trimer which they find to have a small positive condensation energy, however according to experimental evidence this is observed in solution.

At the local DFT-BHL/DNP* level of approximation the hydrogen bonds are overestimated, this is exemplified by the short O...H distance of approximately 1.64Å and the OH bond of the acceptor groups are too long (1.02Å), this is typical of local DFT methods. At the non-local DFT-BLYP/DNP level of approximation two direct intra-molecular hydrogen bonds are formed, the O...H and OH bond lengths are 1.83Å and 1.00Å respectively, this is more in line with what would be expected.[25,30] The trimer from this study has O...H bond lengths of 1.90Å and 1.91Å with OH bond lengths of 0.99Å, these values compare very well with results from the above mentioned non-local methods, the sensible values of the OH bond lengths provides evidence that the O...H bonds are unlikely to be overestimated.

* The local BHL functional calculates the exchange and correlation functionals separately, by using the functional developed by von Barth and Hedin[37,38] and Hedin and Lundqvist.[39]

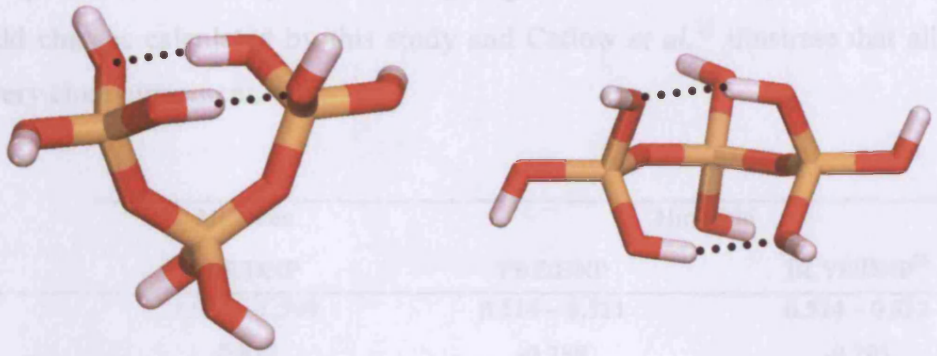

Figure 6. 6: Silica trimer: $Si_3O_2(OH)_8$ cluster optimised at the DFT-PBE/DNP level of approximation. Hydrogen bonds are highlighted with a dotted line

Table 6. 5 contains a comparison of all bond angles and bond lengths for the silica trimer minimised in this study by the DFT-PBE/DNP approximation and the DFT-BLYP/DNP approximation by Catlow *et al.*[25] As a whole all bond lengths and bond angles compare very well, which is what we would expect as we are comparing two non-local approximations.

	DFT- PBE/DNP	DFT- BLYP/DNP[25]
Bond Lengths (Å)		
SiO_t	1.64 – 1.67 (1.65)	1.66 – 1.69
SiO_b	1.64	1.65 – 1.66
OH	0.97 – 0.99	0.98 – 1.00
O…H	1.90, 1.91	1.83
Bond Angles(°)		
SiO_bSi	144.38 – 144.57 (144.48)	140.4 – 145.0
O_bSiO_b	111.64	112.4
O_tSiO_t	103.06 – 113.01 (109.35)	106.9 – 112.7
SiO_tH	114.42 – 116.47 (115.41)	111.4 – 114.2

Table 6. 5: Structural properties of the silica trimer at the DFT-PBE/DNP and DFT-BLYP/DNP level of approximation. Figures in parentheses represent the average value

Both the Mulliken and Hirshfeld charge distribution of the silica trimer (see Table 6. 6) illustrate that the most acidic hydrogen atoms are at the two ends of the chain, these are the hydrogen atoms which take part in intra-molecular hydrogen bonds. The least acidic hydrogen atoms are part of the hydroxyls which are attached to the central silicon atom,

i.e. at a point furthest away from the hydrogen bonds. A comparison between the Hirshfeld charges calculated by this study and Catlow *et al.*[25] illustrate that all values are in very close agreement.

	Mulliken	Hirshfeld	
	PBE/DNP	PBE/DNP	BLYP/DNP[25]
Si	1.554 – 1.599	0.516 – 0.521	0.524 – 0.532
O_b	-0.873	-0.288	-0.293
O_t	-0.639 – -0.710	-0.252 – -0.304	-0.243 – -0.303
H	0.284 – 0.335	0.117 – 0.177	0.107 – 0.174

Table 6. 6: Mulliken and Hirshfeld charges of the silica trimer

6.4.1.4 Silica tetramer

As with the silica trimer, the chain silicon tetramer is most stable in a quasi cyclic arrangement (see Figure 6. 7), in this configuration two intra-molecular hydrogen bonds with length 1.91Å and 1.97Å are present, the occurrence of these bonds close the ring to form two rings, a 3T and 4T ring. The hydrogen bonds have been shown by the dotted lines in Figure 6. 7, this figure clearly illustrates the formation of the two rings. This structure appears to be reasonable, since the bond lengths of the OH group associated with the hydrogen bonds are 0.98Å, this is a value predicted by OH groups where no hydrogen bonding is present, implying that the hydrogen bond is not over estimated.

In comparison, Catlow *et al.*[25] have minimised a open chain silica tetramer using the local DFT-BHL/DNP level of approximation, their study also predicted a quasi cyclic conformation with the presence of five intra-molecular hydrogen bonds within the range of 1.51-1.68Å, however unlike this study, the quasi cyclic conformation produced only one 4T ring. The short hydrogen bonds along with the long bond lengths (1.01-1.05Å) of the associated OH groups is typical of the over estimation of hydrogen bonding consistent with a local density functional.

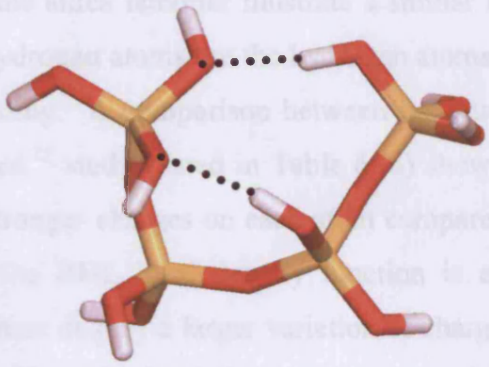

Figure 6. 7: Silica tetramer: $Si_4O_3(OH)_{10}$ cluster optimised at the DFT-PBE/DNP level of approximation

Table 6. 7 contains all structural properties of the silica tetramer minimised with the non-local DFT-PBE/DNP approximation from this work and the local DFT-BHL/DNP[25] approximation. The SiO_t and SiO_b bond lengths from both approximations compare well, however a decrease is observed in the OH bond length in this study to values between 0.97Å and 0.98Å, this is a result of the PBE/DNP approximation improving the prediction of hydrogen bond strengths (as discussed above). The average O_tSiO_t and SiO_tH bond angles lie within the range of bond angles found with the DFT-BHL/DNP approximation. However the average SiO_bSi angle is 10.05° larger than the largest SiO_bSi angle found with DFT-BHL/DNP, the increase in this angle is a contributing factor to the decrease in hydrogen bonding.

	DFT- PBE/DNP	DFT- BHL/DNP[25]
Bond Lengths (Å)		
SiO_t	1.64 – 1.67 (1.65)	1.62 – 1.67
SiO_b	1.62 – 1.66 (1.65)	1.64 – 1.66
OH	0.97 – 0.98 (0.97)	0.98 – 1.03
O…H	1.91, 1.97	1.51 – 1.68
Bond Angles(°)		
SiO_bSi	130.10 – 147.43 (138.05)	121.7 – 128.0
O_bSiO_b	106.34 – 113.799 (110.07)	108.5 – 109.7
O_tSiO_t	103.66 – 115.91 (109.43)	106.8 – 112.5
SiO_tH	112.58 – 117.62 (115.61)	104.7 – 118.0

Table 6. 7: Structural properties of the silica tetramer at the DFT-PBE/DNP and DFT-BHL/DNP[25] level of approximation. Figures in parentheses represent the average value.

The charge densities of the silica tetramer illustrate a similar trend as observed by the trimer, the more acidic hydrogen atoms are the hydrogen atoms which take part in intra-molecular hydrogen bonding. A comparison between the Hirshfeld charges from this work and the Catlow *et al.*[25] study (listed in Table 6. 8) show that the PBE functional from this study predict stronger charges on each atom compared to the BHL functional, this is surprising since the BHL local density function is expected to overestimate hydrogen bonding and hence display a larger variation of charge. The Mulliken charges of the tetramer minimised with the BHL local density functional have not been calculated, and so there is no data from literature to compare to, however a comparison with the Mulliken charges of the silica trimer exhibit very similar trends.

	Mulliken	Hirshfeld	
	PBE/DNP	PBE/DNP	BHL/DNP[25]
Si	1.528 – 1.599	0.506 – 0.532	0.461 – 0.485
O_b	-0.869 – -0.883	-0.286 – -0.301	-0.215 – -0.274
O_t	-0.628 – -0.709	-0.238 – -0.306	-0.231 – -0.291
H	0.281 – 0.344	0.111 – 0.186	0.104 – 0.182

Table 6. 8: Mulliken and Hirshfeld charges of the silica tetramer.

The second 4T silica fragment investigated was the closed ring which is minimised into a distorted crown configuration (see Figure 6. 8), unlike the chain tetramer the ring structure does not present any hydrogen bonding. The Catlow *et al.*[25] study on the silica tetramer ring predicts two conformations, a planar and crown configuration. The crown structure is more stable since it allows a strong cyclic system of four strong hydrogen bonds (1.61-1.62Å), however they suggest that the use of a local basis set has lead to the over estimation in the strength of hydrogen bonding.

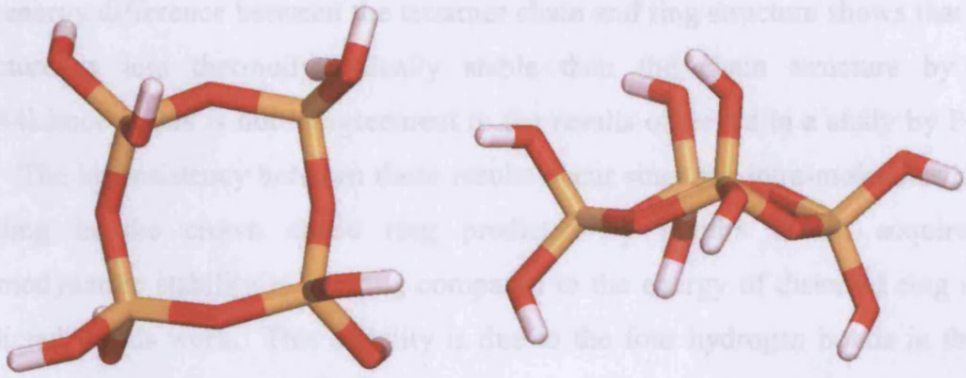

Figure 6. 8: 4T Silica ring: $Si_4O_4(OH)_8$ cluster optimised at the DFT-PBE/DNP level of approximation.

Analysis of the structural properties of the tetramer ring from this study and the two conformations investigated in the Catlow *et al.* study shows similar SiO bond lengths between all three structures. The OH bond length is similar to the distorted crown planar structure, however due to the extensive intra-molecular hydrogen bonding in the crown structure the OH bond lengths are larger than that found in this work. The SiO_bSi bond angle appears to be much bigger in the cluster from this study and the planar structure compared to the crown structure, as seen with the previous clusters, it is this quantity which affects the extent of hydrogen bonding within the fragment. The OSiO angles are similar between all three structures.

	DFT- PBE/DNP	DFT- BHL/DNP[25]	
	Distorted crown	Planar	Crown
Bond Lengths (Å)			
SiO_t	1.64 – 1.65 (1.64)	1.64	1.62 – 1.66
SiO_b	1.63 – 1.66 (1.64)	1.62	1.64 – 1.65
OH	0.97	1.98	0.98 – 1.03
O…H			1.61 – 1.62
Bond Angles(°)			
SiO_bSi	137.38 – 153.24 (144.75)	160.40	125.80 – 126.30
O_bSiO_b	108.99 – 110.33 (109.56)	109.5	111.20 – 112.20
O_tSiO_t	105.74 – 113.84 (109.47)	106.00	113.20 – 114.80
SiO_tH	114.71 – 117.84 (115.77)	112.00 – 112.50	106.20 – 114.30

Table 6. 9: Structural properties of the silica tetramer ring at the DFT-PBE/DNP and DFT-BHL/DNP[25] level of approximation. Figures in parentheses represent the average value.

The energy difference between the tetramer chain and ring structure shows that the ring structure is less thermodynamically stable than the chain structure by 0.34eV (32.44kJmol^{-1}), this is not in agreement to the results observed in a study by Pereria *et al.*[30] The inconsistency between these results occur since the intra-molecular hydrogen bonding in the crown shape ring predicted by Pereira *et al.* acquires more thermodynamic stability in the ring compared to the energy of distorted ring structure predicted in this work. This stability is due to the four hydrogen bonds in the crown shape ring creating a circle of hydrogen bonds which essentially forms a quasi ring.

The charge distribution of the ring conformation has been listed in Table 6. 10, these results show that the charge on each atom of the same element are very similar, this implies that one hydrogen atom is not more acidic than another. A comparison with the Pereria *et al.* study shows that the oxygen charges are very similar to the planar configuration, and the hydrogen charge distribution lie within the wide spread of values calculated for the crown structure. The hydrogen atoms of the chain tetramer are predicted to be more acidic than the ring tetramer, this would be expected since analysis of the dimer and trimer shows that acidity appears to be correlated to the extent of intra-molecular hydrogen bonding. Since the distorted ring structure does not exhibit any intra-molecular hydrogen bonding, strong acid sites would not be expected.

	Si	O_b	O_t	H
Mulliken				
PBE/DNP	1.581 – 1.610	-0.857 – -0.889	-0.629 – -0.652	0.280 – 0.284
Hirshfield				
PBE/DNP	0.515 – 0.528	-0.278 – -0.305	-0.272 – -0.294	0.164 – 0.175
BHL/DNP[25] (planar)	0.478	-0.272	-0.278 – -0.282	0.175 – 0.179
BHL/DNP[25] (crown)	0.482 – 0.485	-0.266 – 0.270	-0.244 – -0.265	0.107 – 0.186

Table 6. 10: Mulliken and Hirshfeld charges of the silica tetramer ring.

6.4.1.5 Silica pentamer

Two conformations of the silica pentamer have been investigated (see Figure 6. 9), an open silica chain and a silica spiro unit. Both of these clusters are the silicon equivalent of fragments found in the surface structure of EDI, as discussed in section 6.2.

The chain structure contains two hydrogen bonds with lengths of 1.75Å and 1.81Å, however unlike the trimer and the tetramer a quasi cyclic conformation is not adopted by this chain. A pentamer chain optimised at the local DFT-BHL/DNP level of theory adopts the expected quasi cyclic form and contains four strong hydrogen bonds with lengths ranging from 1.60-1.68Å.[30]

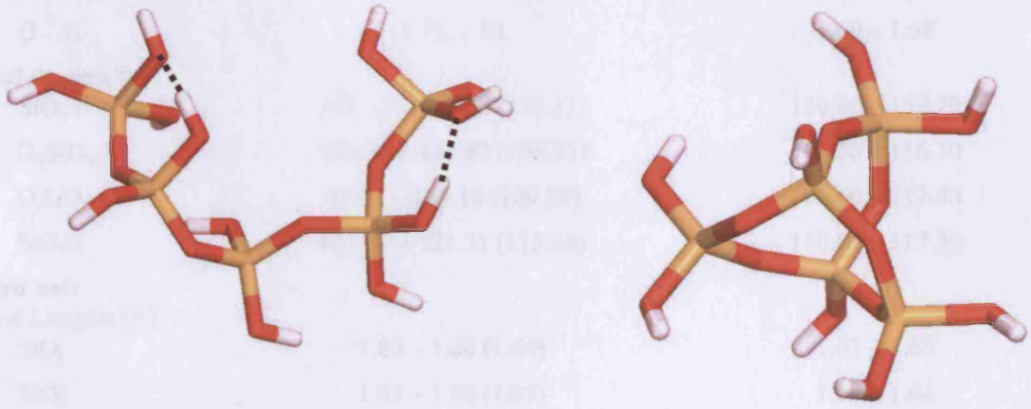

Chain **Spiro**

Figure 6. 9: Silica pentamer: $Si_5O_4(OH)_{12}$ chain cluster and $Si_5O_6(OH)_8$ optimised at the DFT-PBE/DNP level of approximation

The silica spiro unit contains only one intra-molecular hydrogen bond, this is due to the fact that the spiro is a high constrained structure, and unlike the pentamer chain which is free to rotate at every bridging oxygen, this structure is confined by the closed rings. The energy difference between the silica 5T chain and spiro unit shows that the 5T chain is more stable by 0.44eV (42.91kJmol^{-1}). Hence the 5T chain structure is more thermodynamically stable than the ring structure, this is consistent to what was observed by the tetramer chain and 4T ring.

All bond lengths and bond angles of both pentamer conformations have been listed in Table 6. 11, a comparison of chain structure minimised with a GGA function and an LDA functional show that the SiO bond lengths predicted by the GGA in this study range from the same value, up to values almost 0.2Å larger. The SiO_tH and O_tSiO_t angles predicted by GGA also have a larger spread of values, with angles ranging from 10° smaller to 8° larger in value compared to the LDA. However the spread of values for the SiO_bSi and O_bSiO_b angles, and OH bond lengths have decreased by using GGA.

	DFT- PBE/DNP	DFT- BHL/DNP[30,31]
Chain structure		
Bond Lengths (Å)		
SiO_t	1.63 – 1.83 (1.72)	1.61 – 1.67
SiO_b	1.63 – 1.81 (1.69)	1.62 – 1.66
OH	0.97 – 1.00 (0.97)	0.98 – 1.02
O...H	1.75, 1.81	1.60 – 1.68
Bond Angles(°)		
SiO_bSi	129.12 – 132.68 (131.11)	130.40 – 159.20
O_bSiO_b	103.55 – 111.87 (108.73)	105.80 – 116.10
O_tSiO_t	95.52 – 120.18 (109.30)	106.60 – 112.40
SiO_tH	107.89 – 121.31 (115.58)	110.00 – 117.70
Spiro unit		
Bond Lengths (Å)		
SiO_t	1.63 – 1.66 (1.64)	1.63 – 1.65
SiO_b	1.63 – 1.66 (1.65)	1.62 – 1.66
OH	0.97 – 0.98 (0.97)	0.98 – 1.00
O...H	1.99	1.81 – 1.82
Bond Angles(°)		
SiO_bSi	135.93 – 146.24 (141.29)	126.60 – 140.90
O_bSiO_b	107.40 – 112.09 (109.32)	106.60 – 117.60
O_tSiO_t	105.44 – 113.09 (109.54)	108.00 – 114.30
SiO_tH	113.97 – 116.57 (115.58)	111.50 – 120.10

Table 6. 11: Structural properties of the silica pentamer at the DFT-PBE/DNP and DFT-BHL/DNP level of approximation. Figures in parentheses represent the average value.

A comparison between the structural properties of the silica spiro unit show the average bond length predicted in this study are almost identical to that predicted with BHL/DNP. A discrepancy occurs in the SiO_bSi bond angle, this study predicts angles up to 6° larger than the BHL/DNP approximation. However, the spiro unit is a closed structure, therefore a change in one structural parameter (*i.e.* bond length/angle) will have an effect on the remaining structure, in this case the increase in bond angles has been balanced by a reduction of up to 5° in the O_bSiO_b angle.

The Mulliken and Hirshfeld charge densities of both chain and spiro units are displayed in Table 6. 1, both predictions show that the spiro structure contains stronger acid sites than the silica chain. This is not consistent with previous results, where the trimer and

tetramer structures show the strongest acid sites are associated with the chain structures. However it is consistent with the trend that acid sites are associated with the hydrogen atoms which take place in hydrogen bonding. A comparison between the Hirshfeld charged predicted with DFT-PBE/DNP in this study and with BHL/DNP show that for the chain and spiro unit the range of charges appear to be larger for the BHL/DNP prediction, however overall all values are comparable.

	Mulliken	Hirshfeld	
	PBE/DNP	PBE/DNP	BHL/DNP[25]
Chain structure			
Si	1.551 – 1.617	0.521 – 0.527	0.458 – 0.489
O_b	-0.863 – -0.875	-0.282 – -0.294	-0.256 – -0.274
O_t	-0.640 – -0.712	-0.250 – -0.304	-0.212 – 0.293
H	0.287 – 0.330	0.114 – 0.181	0.096 – 0.192
Spiro unit			
Si	1.586 – 1.656	0.504 – 0.533	0.462 – 0.484
O_b	-0.881 – -0.894	-0.293 – -0.301	-0.257 – -0.274
O_t	-0.669 – -0.720	-0.245 – -0.315	-0.231 – -0.289
H	0.321 – 0.342	0.117 – 0.207	0.104 – 0.193

Table 6. 12: Mulliken and Hirshfeld charges of the silica pentamer.

Overall the DFT cluster calculations of chain silica fragments from a monomer to a pentamer have shown that the PBE/DNP functional have produced reliable results comparing well with other theoretical studies which have been cross referenced with NMR data. In the case of the trimer and tetramer the chain curves in a manner to maximise its hydrogen bonding, and unlike local DFT functionals the non-local PBE functional predicts realistic hydrogen bonds lengths without destabilising the acceptor OH bond. A comparison between all 1T to 5T fragments has shown that by increasing the number of T atoms the surface area of each fragment increases. However an increase in the surface area does not affect the strength of the acid sites, since all fragments are predicted to have acid sites of similar strengths

The combination of the PBE functional and DNP basis set has been successful in studying silicate clusters to produce results similar to previous studies. As a result, the same functional and basis set can be utilised to reliably predict the structure and

stability of aluminosilicate clusters, which can be systematically analysed and compared with the silica clusters.

6.4.2 Aluminosilicate clusters

To date, there are no studies which systematically investigate aluminosilicate clusters, work found in literature have considered totally siliceous clusters, therefore in this study a consistent approach is used to examine aluminosilicate clusters with the same level of theory (DFT-PBE/DNP) utilised to minimise the silica clusters. Modelling the $Al(OH)_4^-$ charged species in solution is a very complex process, consequently as a first approximation only charge neutral clusters have been examined, thus every two $Al(OH)_4^-$ units have been charge balanced with a barium cation, which is expected at high super saturation levels. Any cation may be chosen; however in this case a barium cation was employed since it is the extra framework cation found in bulk EDI. Aluminium species in the form $Al(OH)_4^-$ have been chosen as they have been identified as the major aluminium species in an alkaline solutions (*e.g.* basic zeolite sol-gel solutions).[40,41]

The position of aluminium atoms in the clusters have been selected according to Lowenstein's rule,[42] which states that two adjacent aluminium T atoms cannot be found within a zeolite. A theoretical study by Catlow *et al.*[43] has shown that the presence of aluminium in clusters play an important part in influencing the Si/Al ratio within zeolites. Their work concludes that the condensation of two aluminium monomers to form an aluminium dimer is an endothermic reaction, and unlikely to occur, thus the presence of an Al-O-Al link in small clusters, zeolites and other solids is forbidden, which is the basis of Lowenstein's rule. As a result, this work does not sample any clusters with an Al-O-Al link.

As with the analysis of silica clusters, the following sections will discuss the structural properties of each of the minimised aluminosilicate clusters. An examination of the strength of the acid sites of these clusters along with a comparison of the acid sites within silica and aluminosilicate clusters will be made.

6.4.2.1 Alumina monomer

In order to study an alumina monomer, a charge neutral cluster was formed by combining two individual monomers $Al(OH)_4^-$ in the presence of a barium cation. Figure 6. 10 illustrates the two alumina monomers charge balanced with the barium cation minimised to the DFT-PBE/DNP level of approximation. A comparison between both aluminium monomers show that both appear to minimise in very similar conformations. We also find that the position of the hydroxyl groups in the aluminium monomers lie within a similar arrangement as the silicon monomer in the C_1 space group (see Figure 6. 4(a) for the silicon monomer S1).

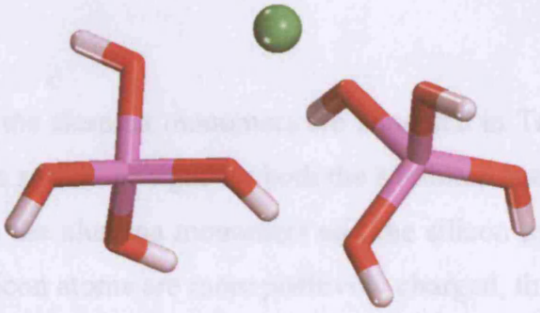

A1 A2

Figure 6. 10: Two alumina monomers and a barium cation, $Ba^{2+}2Al(OH)_4$, minimised with the DFT-PBE/DNP level of approximation.

The range and average values of the bond lengths and average bond angles of both monomers have been tabulated in Table 6. 13, on the whole the bond lengths and angles of both monomer units compare very well to one another. We find that each unit is at a similar distance from the barium cation and the Al-O bond is longer than the Si-O bond length, this is consistent with expectation since aluminosilicate bond lengths measured by XRD, as silicon is more electronegative therefore will create a stronger shorter bond than the less electronegative aluminium atom.

PBE/DNP	A1	A2
Bond Length (Å)		
AlO_t	1.74 – 1.82 (1.79)	1.75 – 1.85 (1.79)
OH	0.97 – 0.99 (0.97)	0.97
Ba...O_t	1.52, 1.59	2.62, 2.67
Ba...Al	3.46	3.43
O...H		
Bond Angle (°)		
O_tAlO_t	91.69 – 120.85 (109.00)	92.09 – 116.10 (109.12)
AlO_tH	113.91 – 117.87 (116.31)	115.30 – 119.92 (117.51)

Table 6. 13: Structural properties of both aluminium monomers and a barium cation in vacuo, with bond lengths given in angstroms (Å) and bond angles given in degrees(°). Average values are given in parentheses.

The atomic charges of the alumina monomers are tabulated in Table 6. 14, both the A1 and A2 monomers have similar charges for both the Mulliken and Hirshfeld predictions. A comparison between the alumina monomers and the silicon monomers (see Table 6. 2) highlight that the silicon atoms are more positively charged, this is expected since the silicon has a formal charge of +4, whereas the aluminium has a formal charge of +3. It is also found by comparison with earlier work on silica monomers that the silica monomer has similar hydrogen charges, however the oxygen atoms are more negative in the alumina monomer than in the silica monomer. The increase in negative charge is due to the alumina monomer containing a net negative charge; as a result the oxygen atoms have extra negative charge available to be dispersed between them.

	Mulliken		Hirshfeld	
	A1	A2	A1	A2
Al	1.126	1.137	0.454	0.464
O_t	-0.662 – -0.801	-0.654 – -0.762	-0.336 – -0.340	-0.327 – -0.381
H	0.253 – 0.345	0.252 – 0.281	0.104 – 0.152	0.135 – 0.157
Ba	1.336		0.799	

Table 6. 14: Mulliken and Hirshfeld charges of the alumina monomer.

6.4.2.2 Aluminosilicate trimer

Figure 6. 11 displays aluminosilicate trimer minimised to the DFT-PBE/DNP level of approximation. The aluminosilicate trimer chain minimises in a quasi cyclic formation, similar to the siliceous trimer conformation, however with the siliceous trimer the cycle is completed with hydrogen bonds, whereas with the aluminosilicate trimer the barium cation is in between the two ends of the chain, consequently the hydrogen atoms are repelled from the barium cation, and there are no hydrogen bonds formed between the two ends of the chain.

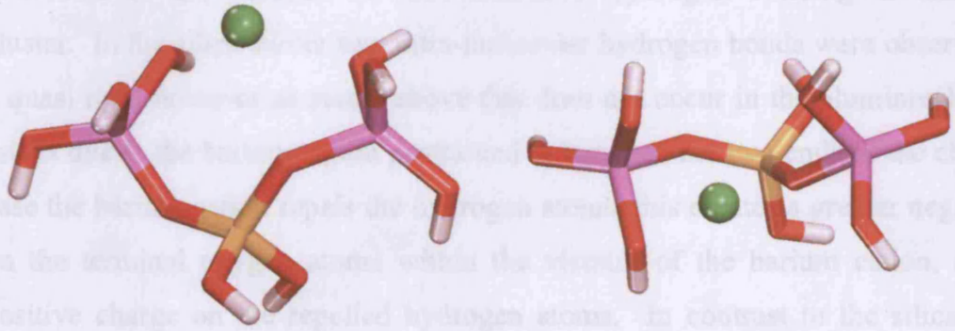

Figure 6. 11: Aluminosilicate trimer $BaSiAl_2O_2(OH)_8$ minimised with the DFT-PBE/DNP level of approximation.

Table 6. 15 lists all bond angles and bond lengths of the aluminosilicate trimer.

PBE/DNP		Al-Si-Al	
Bond Lengths (Å)		Bond Angles(°)	
AlO_t	1.73 – 1.83 (1.79)	AlO_bSi	132.40 – 137.40 (134.90)
AlO_b	1.77 – 1.81 (1.79)	OSiO	105.01 – 113.04 (109.47)
SiO_b	1.62 – 1.65 (1.63)	OAlO	91.25 – 120.51 (108.82)
SiO_t	1.67	SiOH	113.08 – 114.12 (113.60)
BaO	2.62 – 3.99	AlOH	114.62 – 117.46 (116.37)
BaAl	3.16 – 3.42		
BaSi	3.93		

Table 6. 15: Structural properties of a aluminosilicate trimer and a barium cation, $BaSiAl_2O_2(OH)_8$, with bond lengths measured in angstoms (Å) and bond angles measured in degrees (°). The average values are quoted in parentheses.

A comparison between this structure and the siliceous trimer show the T-O bond lengths are larger, this would be expected since the Al-O bond is weaker than the Si-O bond. The average TOT bond angle is smaller than the siliceous trimer by 10°, this is due to the attraction between the aluminium and the barium cation, and results in the chain adopting a staggered conformation.

As seen with the alumina monomer the silicon is more positively charged than the aluminium atoms (see Table 6. 16). A comparison with charge densities of the silica trimer illustrates the hydrogen atoms in the aluminosilicate trimer are less acidic, this is correlated to the absence of intra-molecular hydrogen bonding in aluminosilicate cluster. In the silica trimer two intra-molecular hydrogen bonds were observed creating a quasi ring, however as stated above this does not occur in the aluminosilicate trimer, this is due to the barium cation positioned in between the two ends of the chain. In this case the barium cation repels the hydrogen atoms, this creates a greater negative charge on the terminal oxygen atoms within the vicinity of the barium cation, and a small positive charge on the repelled hydrogen atoms. In contrast to the silica trimer, the greatest hydrogen charge resides on the hydroxyl attached to the central (silicon) atom, this is the reverse to what is observed for the silica trimer.

	Mulliken	Hirshfeld
Al	1.156 – 1.191	0.461 – 0.473
Si	1.574	0.481
O_t	-0.651 – -0.762	-0.298 – -0.377
O_b	-0.858 – -0.935	-0.334 – -0.359
H	0.261 – 0.281	0.136 – 0.161
Ba	1.349	0.772

Table 6. 16: Mulliken and Hirshfeld charges of the aluminosilicate trimer.

6.4.2.3 Aluminosilicate tetramer

For a complete analysis three different configurations of the aluminosilicate tetramer were studied, a four membered ring and two chains. The two chains contained aluminium atoms in different positions, the first contained an alternating aluminium silicon sequence, with aluminiums in position 1 and 3 (*i.e* Al-Si-Al-Si), and the second

contains two aluminium atoms at the ends of the chain, which is position 1 and 4 (*i.e* Al-Si-Si-Al). As with the previous aluminosilicates, each cluster have been charge balanced with a barium cation.

All three minimised fragments are illustrated in Figure 6. 12. Figure 6. 12(a) displays how the minimised ring, adopts a curved structure where the two aluminium atoms and hydroxyl oxygen atoms are attracted towards the barium cation and the two silicon atoms are furthest away. A study of the siliceous tetramer ring[25] with the DFT-BHL/DNP level of approximation minimises in a crown configuration which allows the formation of four hydrogen bonds, however in this case, the aluminosilicate ring shows no evidence of intra-molecular hydrogen bonding, with O…H distances ranging from 2.63 to 3.74Å.

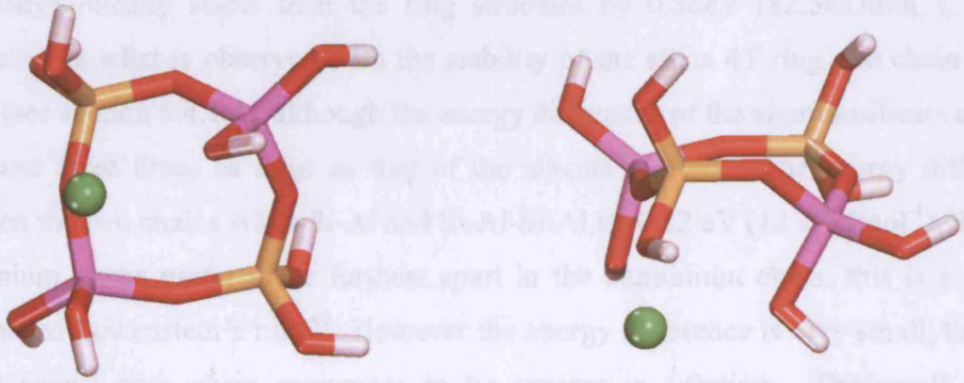

(a) Si-Al-Si-Al ring

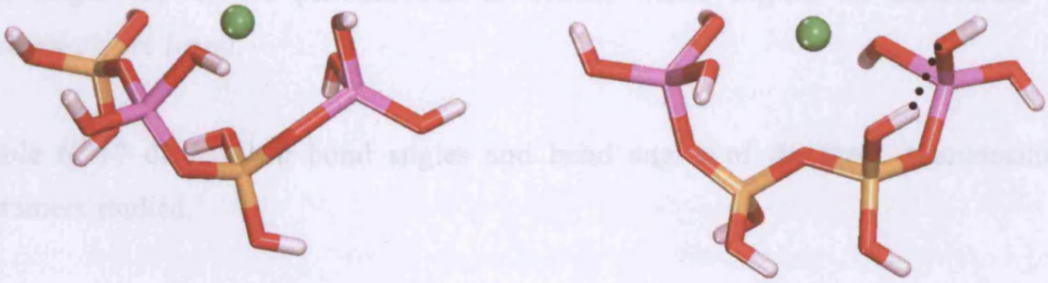

(b) Si-Al-Si-Al chain **(c) Al-Si-Si-Al chain**

Figure 6. 12: Aluminosilicate tetramer $BaSi_2Al_2O_3(OH)_8$ minimised with the DFT-PBE/DNP level of approximation. (a) tetramer ring $BaSi_2Al_2O_4(OH)_8$, (b) tetramer chain, $BaSi_2Al_2O_3(OH)_{10}$ with Al-Si-Al-Si sequence, (c) tetramer chain, $BaSi_2Al_2O_3(OH)_{10}$, with the Al-Si-Si-Al sequence.

Figure 6. 12(b) and (c) illustrates the two aluminosilicate tetramer chains, a common feature of both is the way in which the aluminium atoms and proximate hydroxyl oxygens coordinate to the barium cation. It is also found that the hydrogen bonding is very limited, within the Si-Al-Si-Al sequence no intra-molecular hydrogen bonding is observed, and the Al-Si-Si-Al structure contains only one intra-molecular hydrogen bond with a length of 1.93Å. With a large number of hydroxyls within close proximity one would expect the occurrence of more extensive hydrogen bonding. The small number of hydrogen bonds maybe a result of the underestimation of hydrogen bonding by the PBE/DNP functional, however since there are no experimental studies or theoretical studies of aluminosilicate clusters in vacuum or water, so there is no point of reference.

The total energy of the three 4T fragments show that the two linear chains are more thermodynamically stable than the ring structure by 0.86eV (82.54kJmol^{-1}), this is consistent to what is observed with the stability of the silica 4T ring and chain in this study (see section 6.4.1.4), although the energy difference of the aluminosilicate clusters is almost three times as large as that of the silicate clusters. The energy difference between the two chains Al-Si-Si-Al and Si-Al-Si-Al is -0.12 eV (12.17kJmol^{-1}), thus the aluminium atoms prefer to be furthest apart in the aluminium chain, this is a further example of Lowenstein's rule.[42] However the energy difference is very small, thus one would expect both chain sequences to be present in solution. The small energy difference suggests that there is little preference for a Al-Si +Si-Al or Al-Si + Al-Si condensation reaction occurring, hence there is unselective behaviour. Interestingly, this might explain the phenomenon of zoning where regions of aluminium rich framework are found.

Table 6. 17 displays all bond angles and bond angles of the three aluminosilicate tetramers studied.

	Ring	Al-Si-Al-Si	Al-Si-Si-Al
Bond Lengths (Å)			
AlO_t	1.74 – 1.87 (1.80)	1.73 – 1.82 (1.78)	1.73 – 1.83 (1.79)
AlO_b	1.73 – 1.83 (1.77)	1.77 – 1.83 (1.80)	1.77 – 1.80 (1.79)
SiO_t	1.65 – 1.72 (1.68)	1.65 – 1.71 (1.67)	1.65 – 1.69 (1.66)
SiO_b	1.60 – 1.64 (1.62)	1.60 – 1.63 (1.62)	1.60 – 1.69 (1.64)
BaO	2.55 – 3.98	2.69 – 3.86	2.64 – 3.98
BaAl	3.47, 3.97	3.21, 3.49	3.45, 3.55
BaSi	3.35, 5.14	3.49, 3.61	3.48, 4.13
$O_{Al}H$	0.97	0.97	0.97
$O_{Si}H$	0.97	0.97 – 0.98 (0.97)	0.97 – 0.99 (0.98)
Bond Angles(°)			
SiO_bSi			134.75
AlO_bSi	130.90 – 156.72 (143.95)	129.76 – 146.43 (140.69)	122.88 – 138.33 (131.99)
OSiO	95.72 – 114.48 (109.33)	100.48 – 116.94 (109.40)	99.59 – 114.91 (109.39)
OAlO	90.41 – 117.3 (109.12)	92.12 – 121.62 (109.00)	91.30 – 119.02 (109.11)
SiOH	112.01 – 113.74 (112.79)	113.97 – 115.43 (114.80)	109.55 – 115.54 (112.85)
AlOH	104.29 – 117.06 (113.01)	114.05 – 119.49 (116.67)	114.14 – 119.73 (116.50)

Table 6. 17: Structural properties of all three configurations of the aluminosilicate tetramer, with bond lengths measured in angstoms (Å) and bond angles measured in degrees (°). Figures in parentheses are the mean value.

The Ba-T distances for each conformation show that the aluminium atoms are likely to minimise in a position closer to the barium cation than when the T atom is a silicon atom, the Ba-O distances also display an attraction between the two. The T-O bond lengths for all three structures are within the correct range with the Al-O bond lengths all longer (by ~0.15Å) than the Si-O bond lengths, as discussed previously, however we find that the Al-O and Si-O bridging bonds are both shorter for the ring structure than each of the chains, this highlights the effect of this strained conformation. Nevertheless the average T-O-T bond angle for the ring conformation is larger than for the chain structure, this increase in bond angle must act as a method of reducing the strain within the ring, this effect of increasing the angle to decrease strain is a similar effect to what is observed with the silicate tetramer ring.[25] The O-T-O and T-O-H bond angles are all consistent to what is observed previously and with other silicate clusters, this implies that the substitution of a silicon atom with a aluminium atom does change the bond angles.

Both the Mulliken and Hirshfeld charges (see Table 6. 18) show that the silicon atoms are more positively charged than the aluminium atoms, this is consistent with the previous aluminosilicate clusters. This analysis highlights that the acid sites are stronger on the chain structures compared to the ring structure, this also highlights a difference between the silica and aluminosilicate cluster, the silica ring and chain have very similar hydrogen charges, whereas the presence of barium and aluminium atoms vary the charge distribution on the terminal oxygen (O_t) atoms and hydrogen by increasing the negative charge of O_t in the vicinity of barium, this is consistent to what has been observed by the aluminosilicate trimer.

		Mulliken	
	Ring	Al-Si-Al-Si	Al-Si-Si-Al
Al	1.200, 1.245	1.137 – 1.180	1.157, 1.188
Si	1.537, 1.608	1.569 – 1.576	1.580, 1.626
O_b	-0.848 – -0.953	-0.841 – -0.904	-0.845 – -0.961
O_t	-0.645 – -0.795	-0.646 – -0.776	-0.644 – -0.776
H	0.257 – 0.292	0.253 – 0.337	0.255 – 0.318
Ba	1.314	1.333	1.376
		Hirshfeld	
	Ring	Al-Si-Al-Si	Al-Si-Si-Al
Al	0.469, 0.486	0.461, 0.473	0.472, 0.473
Si	0.471, 0.499	0.481, 0.514	0.499, 0.507
O_b	-0.323 – -0.364	-0.327 – -0.348	-0.271 – -0.357
O_t	-0.267 – -0.382	-0.258 – -0.374	-0.267 – -0.377
H	0.135 – 0.174	0.124 – 0.179	0.124 – 0.176
Ba	0.811	0.678	0.7243

Table 6. 18: Mulliken and Hirshfeld charges of the alumina tetramer.

6.4.2.4 Aluminosilicate pentamer

The final set of aluminosilicate clusters investigated is the pentamers, as with the tetramer clusters all permutations of aluminium within the pentamer chain were studied. A pentamer unit was also studied within a spiro unit arrangement, as found on the (110) surface. To find a suitable starting position for the barium cation a large number of calculations need to be carried out, with the barium in different positions with reference with each T atom within the chain. Subsequently this technique has to be repeated for each chain with the aluminium atoms in different sequences along the chain, this would

be unpractical and extremely computationally expensive, since each cluster is minimised at a high level of theory.

In order to minimise the number of calculations required and also find a suitable minimised structure, a number calculations were carried out for each pentamer confirmation with the initial starting position of barium determined by chemical intuition. Firstly the barium cation was placed the same distance from the cluster as that found in the bulk crystal, another two clusters were formed with the barium cation placed on each end of the chain within a distance of 2.5Å away from the aluminium atoms. A forcefield method could not be used to predict positions of the barium cation since the forcefield has been parameterised for a bulk crystal, and therefore do not describe aluminosilicate clusters correctly.

Figure 6. 13 illustrate the minimised structure of the five pentamer configurations studied, for brevity only the most stable structure of each conformation has been shown. Comparisons of all four linear chains have shown that each cluster will minimise in a conformation where the two aluminium atoms are coordinated towards the barium cation, this is a similar to the trends seen by the trimer and tetramer chains. However unlike the trimer and tetramer chains the pentamer chain is longer and contains more points of rotation, this leads to a more flexible structure which results in a greater number of sites available for intra-molecular hydrogen bonding. The intra-molecular hydrogen bonding present in all four pentamer chains are in the range of 1.70-2.25Å, these bonds have been highlighted with a dotted line in Figure 6. 13. It is found that the hydrogen bonds within the range of 1.95-2.25Å with OH bond length of the acceptor group within the range of 0.97-0.98Å are of reasonable strength, where as the shorter hydrogen bonds of length 1.70-1.92Å may be too strong, this is demonstrated by the increase in bond length of the acceptor OH group to 1.0Å. The spiro unit exhibits only one very weak hydrogen bond (O...H length of 2.67Å), this is a direct result of the rigidity of the spiro unit. The three four-membered rings within the spiro unit are under considerable strain and are unable to rotate at either the T atoms or bridging oxygen atoms in order to increase hydrogen bonding.

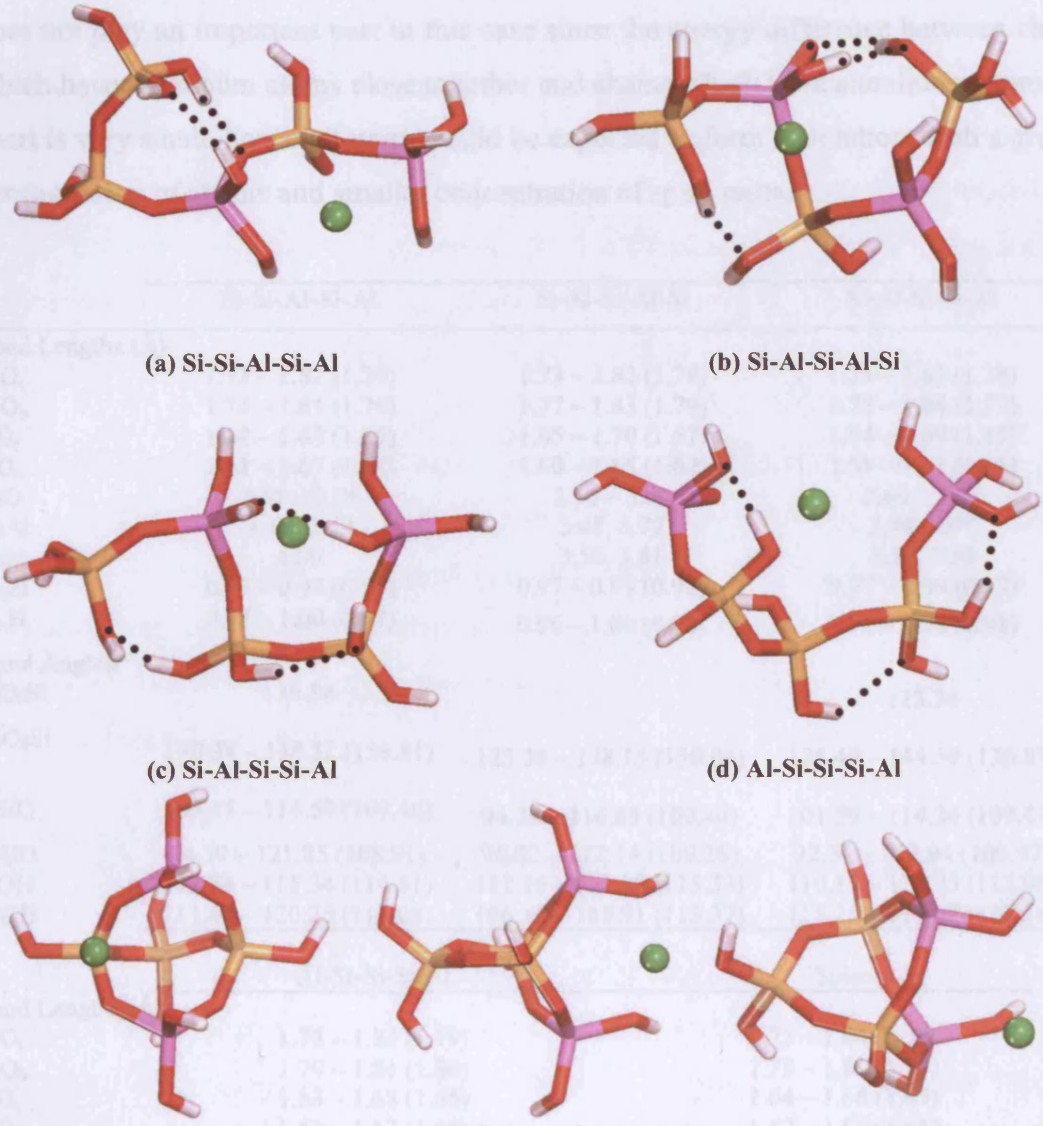

(a) Si-Si-Al-Si-Al **(b) Si-Al-Si-Al-Si**

(c) Si-Al-Si-Si-Al **(d) Al-Si-Si-Si-Al**

(e) Spiro unit

Figure 6. 13: Aluminosilicate pentamer minimised with the DFT-PBE/DNP level of approximation. Linear pentamer, $BaSi_3Al_2O_3(OH)_{12}$: (a) Si-Si-Al-Si-Al, (b) Si-Al-Si-Al-Si, (c) Si-Al-Si-Si-Al, (d) Al-Si-Si-Si-Al. (e) Spiro unit, $BaSi_3Al_2O_6(OH)_{10}$. Total energy of each cluster tabulated in Table 6. 24.

The energy difference between the spiro unit and the chain shows that the chain structure is more stable by -1.07 – -1.54eV (-103.31 – -148.12kJmol^{-1}) depending upon which chain structure the difference is calculated for. This result, along with the energy difference of the open and closed tetramer cluster highlights that open chains appear to be more stable than closed structures, this maybe a result of the high strain involved in ring structures with a small number of T atoms. Between the four T5 chain fragments the energy difference ranges from 0.06–0.46eV (5.94 – 44.81kJmol^{-1}), where the Al-Si-Si-Si-Al unit is the most thermodynamically stable, this trend is consistent with the

aluminosilicate tetramer and also obeys Lowenstein's rule,[42] However Dempseys[44] rule does not play an important part in this case since the energy difference between chains which have aluminum atoms close together and chains which have aluminium atoms far apart is very small, hence all units would be expected to form in solution, with a greater concentration of chains and smaller concentration of spiro units.

	Si-Si-Al-Si-Al	Si-Al-Si-Al-Si	Si-Al-Si-Si-Al
Bond Lengths (Å)			
AlO_t	1.73 – 1.82 (1.79)	1.73 – 1.82 (1.78)	1.74 – 1.82 (1.78)
AlO_b	1.74 – 1.81 (1.78)	1.77 – 1.83 (1.79)	1.75 – 1.84 (1.79)
SiO_t	1.64 – 1.67 (1.65)	1.65 – 1.70 (1.67)	1.64 – 1.69 (1.65)
SiO_b	1.61 – 1.67 (1.64)	1.60 – 1.65 (1.62)	1.61 – 1.67 (1.65)
BaO	2.61 – 2.76	2.56 – 3.00	2.60 – 3.12
BaAl	3.16, 3.40	3.48, 3.79	3.48, 3.47
BaSi	4.00	3.56, 3.81	3.56, 3.58
$O_{Al}H$	0.97 – 0.98 (0.97)	0.97 – 0.99 (0.98)	0.97 – 0.99 (0.97)
$O_{Si}H$	0.97 – 1.00 (0.97)	0.96 – 1.00 (0.98)	0.97 – 1.02 (0.98)
Bond Angles(°)			
SiO_bSi	139.84		123.74
AlO_bSi	130.38 – 148.52 (138.81)	123.30 – 138.15 (130.04)	125.49 – 144.59 (136.87)
OSiO	105.55 – 114.59 (109.46)	94.24 – 116.83 (109.40)	101.59 – 114.34 (109.43)
OAlO	94.39 – 121.85 (108.91)	96.02 – 122.14 (109.26)	92.31 – 117.94 (109.97)
SiOH	113.76 – 115.34 (114.61)	112.16 – 121.89 (115.33)	110.11 – 115.25 (112.98)
AlOH	111.40 – 120.25 (116.08)	106.12 – 118.91 (113.37)	115.25 – 119.07 (117.18)

	Al-Si-Si-Si-Al	Spiro
Bond Lengths (Å)		
AlO_t	1.73 – 1.83 (1.79)	1.73 – 1.84 (1.79)
AlO_b	1.79 – 1.81 (1.80)	1.75 – 1.82 (1.79)
SiO_t	1.63 – 1.68 (1.65)	1.64 – 1.66 (1.65)
SiO_b	1.63 – 1.67 (1.65)	1.62 – 1.68 (1.65)
BaO	2.65 – 2.97	2.57 – 4.00
BaAl	3.49, 3.59	3.41, 3.47
BaSi	3.61 – 3.86	3.31 – 5.60
$O_{Al}H$	0.97	0.97
$O_{Si}H$	0.97- 1.00 (0.98)	0.97
Bond Angles(°)		
SiO_bSi	129 12 – 132.68 (130.90)	131.93 – 150.13 (141.03)
AlO_bSi	131.11 – 131.55 (131.33)	129.21 – 144.98 (138.01)
OSiO	99.60 – 115.12 (109.41)	102.39 – 115.16 (109.42)
OAlO	95.52 – 117.35 (109.76)	92.85 – 118.07 (109.04)
SiOH	107.89 – 116.16 (112.87)	113.74 – 114.93 (114.32)
AlOH	114.40 – 121.31 (118.28)	115.00 – 118.42 (109.03)

Table 6. 19: Structural properties of all five configurations of the aluminosilicate pentamer, with bond lengths measured in angstoms (Å) and bond angles measured in degrees (°). Mean values are given in parentheses.

Table 6. 19 list all bond lengths and angles of all five pentamer aluminosilicates investigated. All Si-O and Al-O bond lengths are consistent with previous finding, the T...Ba lengths show that for all pentamer chains the Al...Ba distances are shorter than the Si...Ba distance, this is further evidence that the chains have minimised in a configuration which allows the aluminium to increase its coordination with the barium cation. Since the spiro unit is less flexible we find that the barium cation minimised in a position which is 0.1Å closer to the silicon atoms, however in this position the barium cation is able to coordinate at reasonable distances with both aluminium atoms.

All bond angles are at reasonable values and are consistent with previous results, all the chains appear to have values within the same limits of each other, however the T-O-T angles for the spiro unit are larger than the open chains when the T unit is both aluminium and silicon. The increase in angle is a means of decreasing the strain in the closed ring, this behaviour is consistent with what has been previously observed with the 4T aluminosilicate ring.

The Mulliken and Hirshfeld charges of all five pentamer clusters have been tabulated in Table 6. 20. The general trend of having a greater positive silicon charge than aluminium charge is also true for all pentamer fragments. All barium cation charges are within the same range (1.32-1.40); however the smallest barium charge is within the spiro unit, this occurs due to the larger distance between barium and the terminal oxygen atoms. Investigation of the acid sites shows that stronger acid sites are found in chains rather than the spiro unit. Also similar hydrogen and terminal oxygen charges are found for the pentamer units as calculated for previous aluminosilicate fragments.

A comparison between silica and aluminosilicate chains reveals a change in charge distribution due to the presence of aluminium and barium, this is consistent with previous aluminosilicate clusters containing less T atoms. For the silica and aluminosilicate pentamer units, the difference in Mulliken charge shows that stronger acid sites are observed in aluminosilicate clusters, however for the closed spiro unit stronger acid sites are found on the pure silica structure.

	Mulliken				
	Si-Si-Al-Si-Al	Si-Al-Si-Al-Si	Si-Al-Si-Si-Al	Al-Si-Si-Si-Al	Spiro
Al	1.175, 1.275	1.210, 1.232	1.175, 1.253	1.155 – 1.167	1.205, 1.218
Si	1.563 – 1.597	1.543 – 1.619	1.547 – 1.603	1.590 – 1.649	1.598 – 1.648
O_t	-0.651 – -0.796	-0.635 – -0.822	-0.635 – -0.774	-0.640 – -0.780	-0.643 – -0.768
O_b	-0.853 – -0.931	-0.835 – -0.956	-0.841 – -0.975	-0.866 – -0.932	-0.859 – -0.933
H	0.266 – 0.374	0.259 – 0.369	0.263 – 0.359	0.254 – 0.339	0.257 – 0.287
Ba	1.364	1.358	1.360	1.395	1.324
	Hirshfeld				
	Si-Si-Al-Si-Al	Si-Al-Si-Al-Si	Si-Al-Si-Si-Al	Al-Si-Si-Si-Al	Spiro
Al	0.476, 0.480	0.473, 0.479	0.474, 0.492	0.470, 0.471	0.470, 0.478
Si	0.494 – 0.507	0.492 – 0.502	0.501 – 0.504	0.502 – 0.531	0.476 – 0.516
O_t	-0.258 – -0.368	-0.249 – -0.374	-0.262 – -0.375	-0.255 – -0.381	-0.283 –0.331
O_b	-0.307 – -0.349	-0.331 – -0.357	-0.270 – -0.348	-0.269 – -0.357	-0.286 – 0.359
H	0.100 – 0.173	0.105 – 0.174	0.100 – 0.173	0.106 – 0.173	0.138 – 0.170
Ba	0.790	0.763	0.796	0.696	0.827

Table 6. 20: Mulliken and Hirshfeld charges of the alumina pentamer.

All the structures analysed up to this point have been minimised in vacuum, all silica clusters have relaxed into conformations which compare well with the previous studies. In the case of aluminosilicate clusters, where there is no data to make a direct comparison with, the structures are well behaved, with bond angles and lengths in correct proportions.

Investigation of acid sites shows that in cases where intra-molecular hydrogen bonding occurs, the strongest acid sites are correlated with the hydrogen atoms which take part in hydrogen bonding. In cases where there is no hydrogen bonding (*e.g.* aluminosilicate trimer) the strongest acid sites are located furthest away from the barium cation. A comparison between open and closed structures highlights that stronger acid sites arise in open structures, this again is correlated to the intra-molecular hydrogen bonds; since the closed structures are rigid, none or very little intra-molecular hydrogen bonding is present. An assessment of silica and aluminosilicate clusters highlights the strength of acid sites for both sets of clusters are of similar strength, this implies that the strength of the acid site is not dependent upon the type of T atom. Overall one may assume that the stronger the acid site the greater or more extensive the intra-molecular hydrogen bonding, since the intra-molecular hydrogen bonding would be expected to stabilise the cluster, the reactivity of the cluster would be expected to decrease.

Since the purpose of this study is to simulate clusters that could be found in the crystallisation process, the method is modified to include the effects of water surrounding the clusters, the results of which are analysed in the following section.

6.4.3 Hydrated structures

To model a hydrated cluster, each relaxed structure was minimised again using the same level of theory, the COSMO model was included to implicitly model water surrounding each cluster. Each cluster was found to be more thermodynamically stable for both silicate and aluminosilicate clusters, this point will be discussed in detail in section 6.4.4. As with the silicate and aluminosilicate clusters in vacuum, the structural properties and charge distribution of each of the hydrated cluster are analysed.

All bond angles and bond lengths of the silicate cluster have been listed in Table 6. 21.

DFT-PBE/DNP + COSMO	S1	S2	Dimer	Trimer
Bond lengths (Å)				
SiO_t	1.65 – 1.66 (1.65)	1.65	1.58 – 1.65 (1.64)	1.64 – 1.67 (1.65)
SiO_b			1.65	1.64
OH	0.97	0.97	0.97 – 0.98 (0.98)	0.97 – 0.99 (0.98)
O...H	2.62			1.86, 1.86
Bond Angles (°)				
SiO_bSi			137.18	144.61, 145.12 (144.64)
OSiO	100.95 – 114.09 (109.51)	106.73 – 115.00 (109.52)	103.71 – 114.80 (109.51)	103.59 – 113.28 (109.47)
SiO_tH	115.11 – 115.86 (115.44)	116.03 – 116.16 (116.09)	113.05 – 117.20 (115.56)	114.47 – 116.33 (115.36)

	Tetramer Chain	Tetramer Ring	Pentamer Chain	Spiro
Bond lengths (Å)				
SiO_t	1.64 – 1.66 (1.65)	1.64 – 1.65 (1.64)	1.64 – 1.66 (1.65)	1.63 – 1.66 (1.64)
SiO_b	1.63 – 1.65 (1.64)	1.64	1.64 – 1.66 (1.65)	1.64 – 1.66 (1.65)
OH	0.97 – 0.99 (0.98)	0.97	0.97 -0.99 (0.98)	0.97 – 0.99 (0.98)
O...H	1.80	2.62	1.75, 2.66	2.66
Bond Angles (°)				
SiO_bSi	140.63 – 154.01 (145.77)	142.89 – 157.63 (149.11)	113.47 – 151.04 (134.70)	136.83 – 141.20 (139.19)
OSiO	102.43 – 114.03 (109.49)	103.52 – 113.00 (109.47)	103.72 – 116.13 (109.47)	103.64 – 114.19 (109.46)
SiO_tH	114.47 – 118.01 (116.14)	115.40 – 116.47 (115.96)	112.46 – 119.13 (116.23)	114.05 – 117.40 (116.33)

Table 6. 21: Structural properties of all silicate clusters minimised at the DFT-PBE/DNP + COSMO level of theory, with bond lengths measured in angstoms (Å) and bond angles measured in degrees (°). Average values are given in parentheses.

It is found that all bond angles and bond lengths are within the range of 0 to 1% of the mean value of the clusters minimised in vacuum. The only exception is the hydrated silicate tetramer chain, which has a SiO_bSi angle 5.59% larger than the cluster minimised in vacuum. The conformation of the minimised tetramer cluster adopts a quasi cyclic structure, as observed by the clusters in vacuum, however previously there were two hydrogen bonds of length 1.91Å and 1.97Å between the two ends of the fragment, whereas the hydrated cluster only contains one hydrogen bond of 1.8Å. Overall, the conformations of the framework of all the hydrated structures are very similar to those shown previously, therefore for brevity these structures are not illustrated here.

Table 6. 22 lists the bond lengths and angles for each of the minimised hydrated aluminosilicate clusters, as with the silicate clusters, all structural parameters of the hydrated aluminosilicate clusters are in close correspondence with the properties of the clusters minimised in vacuum. The largest structural difference occurs in the 4T ring, where the SiOAl angle is 6.25% smaller than the 4T ring minimised in vacuum, however even after a decrease in the bond angle there is no hydrogen bonding. The Ba...T distances have only been tabulated for those under 4Å, the general trend shows that all clusters except the 4T ring minimise in a configuration where the aluminium atoms are closer to the barium cation than the silicon atoms. The 4T ring has values of 3.66 for Ba...Al and 3.35 for Ba...Si, this exception is due to the constraints of the ring confirmation, therefore unlike a chain it is unable to rotate at each oxygen atom.

Overall it is found that the OH bond lengths and OTO angle are all approximately equivalent, and the TO bond lengths are usually a maximum of 1% different when minimised in water compared to in vacuum. This implies that the effect of water on the tetrahedral nature of each T atom in the cluster is minimal. It is also found that the general trend for hydrated clusters is they tend to have a 0-6.3% smaller AlOH and AlOSi angles, and the SiOSi and SiOH angles tend to be 0-5.6% larger.

	T1	T2	Trimer	-Si-Al-Si-Al- (ring)
Bond Lengths (Å)				
AlO_t	1.77 – 1.81 (1.79)	1.77 – 1.81 (1.79)	1.75 – 1.80 (1.79)	1.76 – 1.81 (1.78)
AlO_b			1.78 – 1.79 (1.78)	1.77 – 1.81 (1.79)
SiO_t			1.67 – 1.68 (1.67)	1.66 – 1.69 (1.67)
SiO_b			1.63	1.63
BaO	2.73, 2.76	2.75, 2.76	2.73 – 3.06	2.67 – 2.89
BaAl	3.56	3.57	3.31, 3.57	3.66
BaSi				3.53
$O_{Al}H$	0.97 – 0.98 (0.98)	0.97 – 0.99 (0.97)	0.97	0.97
$O_{Si}H$			0.97	0.97 – 0.98 (0.97)
O...H	1.94, 1.98, 2.79			
Bond Angles(°)				
SiO_bSi				
AlO_bSi			127.88 – 140.00 (133.93)	126.58 – 143.69 (134.56)
OSiO			105.44 – 112.46 (109.49)	98.53 – 113.88 (109.40)
OAlO	93.53 – 117.11 (109.56)	94.27 – 116.98 (109.23)	92.14 – 119.44 (109.12)	93.05 – 116.17 (109.38)
SiOH			114.26 – 114.41 (114.33)	109.14 – 116.15 (113.60)
AlOH	110.42 – 118.70 (115.35)	109.40 – 119.26 (113.07)	113.31 – 118.19 (115.98)	112.23 – 119.74 (115.19)

	Al-Si-Al-Si	Al-Si-Si-Al	Si-Si-Al-Si-Al	Si-Al-Si-Al-Si
Bond Lengths (Å)				
AlO_t	1.76 – 1.81 (1.74)	1.75 – 1.82 (1.79)	1.76 – 1.81 (1.79)	1.76 – 1.80 (1.78)
AlO_b	1.78 – 1.80 (1.79)	1.77 – 1.79 (1.78)	1.77 – 1.79 (1.78)	1.77 – 1.81 (1.79)
SiO_t	1.65 – 1.69 (1.67)	1.66 – 1.68 (1.67)	1.64 – 1.67 (1.66)	1.64 – 1.69 (1.67)
SiO_b	1.61 – 1.63 (1.62)	1.61 – 1.65 (1.63)	1.61 – 1.65 (1.64)	1.61 – 1.64 (1.63)
BaO	2.73 – 3.99	2.71 – 3.10	2.73 – 2.77	2.68 – 2.95
BaAl	3.51, 3.65	3.60, 3.64	3.59, 3.62	3.64
BaSi	3.71, 3.99			3.60
$O_{Al}H$	0.97	0.97	0.97	0.97 – 0.98 (0.97)
$O_{Si}H$	0.97 – 0.99 (0.98)	0.97 – 1.00 (0.98)	0.97 – 1.00 (0.98)	0.97 – 1.01 (0.98)
O...H		1.70	1.71	1.69, 1.81, 1.82
Bond Angles(°)				
SiO_bSi		145.60	140.41	
AlO_bSi	128.20– 149.39 (137.91)	125.14 – 143.99 (134.56)	132.00 – 147.53 (141.38)	123.96 – 141.25 (130.98)
OSiO	102.02 – 116.01 (109.45)	104.43 – 113.91 (109.48)	103.61 – 115.35 (109.45)	95.34 – 113.82 (109.44)
OAlO	92.62 – 119.54 (109.39)	93.17 – 116.86 (109.35)	91.86 – 116.83 (109.36)	96.43 – 115.50 (109.35)
SiOH	112.44 – 117.78 (115.15)	107.02 – 114.44 (112.44)	113.57 – 116.92 (115.47)	111.62 – 121.47 (116.17)
AlOH	113.94 – 118.27 (116.00)	115.21 – 119.73 (117.23)	114.45 – 121.18 (117.82)	109.49 – 119.21 (115.58)

Table continued below

	Si-Al-Si-Si-Al	Al-Si-Si-Si-Al	Spiro
Bond Lengths (Å)			
AlO_t	1.75 – 1.79 (1.78)	1.76 – 1.81 (1.79)	1.76 – 1.80 (1.78)
AlO_b	1.76 – 1.85 (1.81)	1.78 – 1.84 (1.81)	1.77 – 1.81 (1.79)
SiO_t	1.65 – 1.68 (1.66)	1.65 – 1.66 (1.65)	1.65 – 1.66 (1.66)
SiO_b	1.61 – 1.67 (1.64)	1.62 – 1.66 (1.64)	1.62 – 1.68 (1.64)
BaO	2.70 – 3.78	2.70 – 2.81	2.66 – 3.93
BaAl	3.62, 3.63	3.68	3.67, 3.69
BaSi	3.94, 3.95		3.49
$O_{Al}H$	0.97 – 1.00 (0.98)	0.97	0.97
$O_{Si}H$	0.97 – 1.03 (0.99)	0.97 – 1.05 (0.99)	0.97
O...H	1.61, 1.85, 1.99	1.51, 1.73, 2.41, 2.65	
Bond Angles(°)			
SiO_bSi	121.99	133.63 – 153.52 (143.57)	132.46 – 150.59 (141.52)
AlO_bSi	123.14 – 146.54 (133.99)	126.22 – 145.93 (136.08)	130.54 – 143.82 (138.48)
OSiO	102.74 – 114.44 (109.46)	101.83 – 114.52 (109.44)	102.54 – 115.06 (109.42)
OAlO	93.79 – 120.25 (108.99)	93.10 – 114.37 (109.01)	95.12 – 114.89 (109.32)
SiOH	109.53 – 115.77 (113.03)	110.73 – 116.72 (114.47)	114.55 – 115.81 (115.09)
AlOH	116.09 – 118.97 (117.20)	114.58 – 118.93 (116.30)	114.54 – 119.22 (116.78)

Table 6. 22: Structural properties of all aluminosilicate clusters minimised at the DFT-PBE/DNP + COSMO level of theory, with bond lengths measured in angstoms (Å) and bond angles measured in degrees (°). Mean values are given in parentheses.

It should be noted that where hydrogen bonding was present in the clusters minimised in vacuum, the clusters exhibit the same hydrogen bonding when minimised in implicit water, however all hydrogen bonds appear to be stronger, *i.e.* they are shorter. As seen previously with the clusters in vacuum, the Ba...Al distances are shorter than the Ba...Si distances, hence the aluminium atoms try to charge balance by coordinating to the barium cation.

As previously observed with the hydrated 5T silica units, it is found that the presence of implicit water has the greatest affect on clusters with a large number of T atoms, for example the 5T chains condense into smaller more dense units, where the overall outline of the clusters are more spherical rather than elongated, this has the effect of maximising the aluminium and oxygen coordination with the barium cation, regardless of the aluminium position within the chain. When the clusters become more spherical, the surface area of the clusters also decrease, however as stated above this does not increase the number of sites which take part in intra-molecular hydrogen bonding. It is also observed that when a cluster becomes more spherical, between one to four hydroxyl groups are directed within the centre of the cluster rather than exposed on the surface. This will have an affect on the rate of growth, as shown in chapter 4, the formation of key bonds on the surface of the growing crystal controls the growth rate,

therefore by decreasing the number of hydroxyls on the surface of the cluster will inherently decrease the probability of that cluster attaching onto the growing surface. If this simulation was repeated with explicit water, a change in the outline of the cluster maybe observed, since the cluster may be more stable by creating inter-molecular hydrogen bonds with the explicit water.

Table 6. 23 tabulates all Mulliken and Hirshfeld charge distributions for all clusters minimised in water using the COSMO model. A comparison between charges of silica clusters in vacuum and in implicit water show that the monomers, dimer, and trimer have almost identical charges. However a difference is observed when the cluster contains four or five silicon atoms; the tetramer chain and ring, and the pentamer chain and spiro predict an increase in the positive charge of hydrogen, and apart from the pentamer chain, all these three clusters have a greater negative charge on the terminal oxygen, this is most likely due to the increase in the strength of intra-molecular hydrogen bonding. These clusters may also form hydrogen bonds with the implicit water, however this can not be calculated. To confirm the presence of inter-molecular hydrogen bonding, calculations with explicit water surrounding the cluster would need to be carried out.

If the same comparison of charges is carried out on aluminosilicate clusters, it is difficult to measure the difference in charge for the alumina monomers, since both A1 and A2 clusters charges are determined within the same model, it is found that when one monomer has stronger acid sites in water the other will have weaker acid sites to compensate since there is a fixed amount of electrons to be distributed throughout the structure. Analysis of the remaining aluminosilicate cluster shows that the trimer, like the silica trimer, predicts very similar charges. The tetramer chain structure display a variation in charges, with the Al-Si-Al-Si containing stronger acid sites in water, whereas the Al-Si-Si-Al chain has a smaller (less positive) hydrogen charge but a more negative oxygen charge, and the reverse is true in the ring structure. However the variation of the oxygen and hydrogen charge in the Al-Si-Si-Al chain and ring structure is not large enough to make an assessment as to whether the acid sites become stronger.

Investigation of the aluminosilicate pentamer structures highlight that in water the spiro unit, Si-Si-Al-Si-Al and Si-Al-Si-Al-Si chain all show a decrease in the strength of acid

sites, whereas the Si-Al-Si-Si-Al and Al-Si-Si-Si-Al chains both show an increase in acid site strength. This may be a result of the position of the aluminium atoms within the chain, *i.e.* the further apart the aluminium atoms within the chain the stronger the acid sites, however this is unlikely since the tetramer chain does not show the same trend. It is unclear as to why this would occur since all four pentamer chains do exhibit intra-molecular hydrogen bonding.

Analysis of the barium charges do not bare any relational to either the strength of the acid site, it also does not display any trend with the number of T atoms present in the cluster.

Unlike the silica clusters, where one observes an increase in the T atoms increases the acid site strength in water, the aluminosilicate clusters do not display a simple trend, however one can conclude that for both silica and aluminosilicate clusters the acid sites are stronger for open structures compared to closed structures.

			Mulliken		
	S1	S2	Dimer	Trimer	Tetramer chain
Si	1.476	1.458	1.520 – 1.555	1.577 – 1.600	1.522 – 1.622
O_t	-0.655 – -0.656	-0.636 – -0.667	-0.638 – -0.705	-0.640 – -0.71	-0.637 – -0.720
O_b			-0.871	-0.875	-0.874 – -0.888
H	0.286 – 0.287	0.281 – 0.288	0.279 – 0.318	0.285 – 0.334	0.279 – 0.350
			Hirshfeld		
	S1	S2	Dimer	Trimer	Tetramer chain
Si	0.500	0.500	0.503 – 0.521	0.515 – 0.519	0.500 – 0.542
O_t	-0.295	-0.288 – -0.300	-0.258 – -0.295	-0.245 – -0.307	-0.232 – -0.313
O_b			-0.296	-0.291	-0.288 – -0.302
H	0.170	0.166 – 0.169	0.128 – 0.180	0.112 – 0.179	0.102 – 0.189

Table continued below

			Mulliken		
	Tetramer ring	Si Pentamer	Si Spiro	T1	T2
Al				1.129	1.132
Si	1.605 – 1.611	1.548 – 1.599	1.583 – 1.659		
O_t	-0.680 – -0.687	-0.639 – -0.703	-0.623 – -0.676	-0.654 – -0.767	-0.656 – -0.771
O_b	-0.877 – -0.886	-0.860 – -0.881	-0.863 – -0.887		
H	0.319 – 0.324	0.275 – 0.341	0.286 – 0.332	0.257 – 0.318	0.253 – 0.323
Ba				1.306	
			Hirshfeld		
	Tetramer ring	Si Pentamer	Si Spiro	T1	T2
Al				0.425	0.485
Si	0.518 – 0.522	0.510 – 0.532	0.507 – 0.529		
O_t	-0.301 – -0.307	-0.239 -0.298	-0.242 – -0.297	-0.331 – -0.375	-0.313 – -0.382
O_b	-0.288 – -0.295	-0.283 – -0.298	-0.281 – -0.298		
H	0.188 – 0.190	0.109 – 0.186	0.113 – 0.180	0.095 – 0.155	0.101 – 0.151
Ba				0.848	
			Mulliken		
	Al-Si-Al	-Al-Si-Al-SI- ring		Al-Si-Al-Si	Al-Si-Si-Al
Al	1.144 – 1.190	1.179 – 1.236		1.152 – 1.165	1.169 – 1.197
Si	1.556	1.545 – 1.613		1.551 – 1.575	1.571 – 1.584
O_t	-0.654 – -0.758	-0.654 – -0.777		-0.641 – -0.791	-0.638 – -0.784
O_b	-0.846 – -0.911	-0.840 – -0.934		-0.834 – -0.894	-0.838 – -0.879
H	0.262 – 0.283	0.262 – 0.299		0.248 – 0.343	0.246 – 0.308
Ba	1.329	1.289		1.349	1.339
			Hirshfeld		
	Trimer	Ring		Al-Si-Al-Si	Al-Si-Si-Al
Al	0.455 – 0.463	0.462 – 0.477		0.453 – 0.458	0.468 – 0.469
Si	0.471	0.456 – 0.493		0.467 – 0.515	0.489 – 0.491
O_t	-0.296 – -0.380	-0.263 – -0.381		-0.254 – -0.372	-0.279 – -0.379
O_b	-0.333 – -0.361	-0.325 – -0.363		-0.330 – -0.351	-0.287 – -0.361
H	0.127 – 0.161	0.115 – 0.178		0.115 – 0.185	0.100 – 0.163
Ba	0.826	0.844		0.756	0.809

			Mulliken		
	Si-Si-Al-Si-Al	Si-Al-Si-Al-Si	Si-Al-Si-Si-Al	Al-Si-Si-Si-Al	Spiro
Al	1.182 – 1.266	1.200 – 1.221	1.153 – 1.273	1.176 – 1.185	1.209 – 1.212
Si	1.562 – 1.582	1.580 – 1.601	1.539 – 1.588	1.570 – 1.631	1.597 – 1.615
O_t	-0.641 - -0.759	-0.632 - -0.799	-0.645 - -0.775	-0.643 - -0.864	-0.643 - -0.764
O_b	-0.847 - -0.933	-0.836 - -0.928	-0.849 - -0.950	-0.852 - -0.962	-0.856 - -0.912
H	0.260 – 0.347	0.257 – 0.361	0.260 – 0.362	0.258 – 0.402	0.260 – 0.288
Ba	1.319	1.350	1.378	1.373	1.309
			Hirshfeld		
	Si-Si-Al-Si-Al	Si-Al-Si-Al-Si	Si-Al-Si-Si-Al	Al-Si-Si-Si-Al	Spiro
Al	0.465 – 0.492	0.468 – 0.471	0.468 – 0.491	0.467 – 0.485	0.467 – 0.471
Si	0.470 – 0.491	0.474 – 0.502	0.487 – 0.496	0.484 – 0.515	0.471 – 0.509
O_t	-0.245 - -0.377	-0.253 - -0.374	-0.253 - -0.370	-0.267 - -0.381	-0.285 - -0.378
O_b	-0.306 - -0.350	-0.334 - -0.356	-0.292 - -0.349	-0.292 - -0.359	-0.288 - -0.359
H	0.102 – 0.165	0.096 – 0.183	0.090 – 0.174	0.096 – 0.166	0.134 – 1.167
Ba	0.863	0.814	0.884	0.869	0.877

Table 6. 23: Mulliken and Hirshfeld charges of the silica and aluminosilicate clusters water.

Since the hydrated aluminosilicate clusters appear very similar to the clusters minimised in vacuum, for brevity they have not been presented here. The following section examines the stability of each fragment.

6.4.4 Energetics of clusters

As stated above, the total energy of each cluster minimised with the COSMO model is more stable by 0.5-2.7eV, the energy of each cluster in vacuum and water have been listed in appendix C, table C.1. The larger differences in energy (1.7-2.7eV) occur in structures with a larger number of T atoms, therefore these large differences maybe a result of an exaggeration in stability due to the clusters becoming more spherical and artificially decreasing the total energy.

Since the energy of the clusters minimised using the COSMO model are more stable, the following analysis will be carried out with the clusters minimised with the COSMO model. Analysis of table C.1 in appendix C shows that from all the fragments and configurations considered (*i.e.* fragments containing one to five T atoms in all configurations), the five T atom chain is most thermodynamically stable. It is also found that the relative stability of each T atom is greatest when there are a greater number of T atoms in the cluster, for example the energy per T atom for a silica dimer is -30179ev, whereas for a silica pentamer the energy per T atoms is -72330eV. Therefore it is most probably that 5T clusters are likely to be available in solution, for ease of comparison the values of the five T fragments have been listed below in Table 6. 24.

The total energy of the 5T aluminosilicate chains are very similar, they differ by a maximum of 0.24eV, as with the clusters minimised in vacuum, this highlights that the ordering of aluminium atoms becomes less important as you increase the number of T atoms. The insensitivity of thermodynamic stability to aluminium ordering also violates Dempsey's rule[44] which predicts that aluminium atoms are most stable furthest apart. As a result one would expect to observe all 5T chain structures in solution.

When examining the total energies (see Table 6. 24) a comparison between silicate and aluminosilicate clusters cannot be made due to the presence of different constituents, however one can make a comparison between clusters containing the same type of

species. From the analysis of silica pentamer clusters minimised in vacuum (see section 6.4.1.5) the spiro unit was calculated to be less thermodynamically stable that than the silica 5T chain, in this hydrated model the difference in total energy is 0.99-1.16eV (95.97-119.12kJmol^{-1}) dependent upon which chain the spiro is compared to. The energy difference between the silica chain and silica spiro also illustrates that the chain is more thermodynamically stable by 0.12eV (11.18kJmol^{-1}). A comparison between the aluminosilicate and silica clusters predicts the same results, *i.e.* the spiro is less thermodynamically stable than the 5T chain.

		Total Energy (eV)	
Chain	Fragment	PBE/DNP	PBE/DNP+COSMO
1	Si-Si-Si-Si-Si	-72328.5714	-72330.22215
2	Si – Spiro	-68171.1573	-68172.50516
3	Si-Si-Al-Si-Al	-284356.9376	-284359.5606
4	Si-Al-Si-Al-Si	-284357.2726	-284359.8036
5	Si-Al-Si-Si-Al	-284356.9992	-284359.5861
6	Al-Si-Si-Si-Al	-284357.4021	-284359.7304
7	Al/Si - Spiro	-280198.8975	-280201.5965

Table 6. 24: Total energy of all 5T clusters investigated in vacuum and with implicit water.

Comparison of the total energies (see Table 6. 24) of the 5T aluminosilicate chains the most thermodynamically favourable 5T species formed will have the sequence: Al-Si-Si-Si-Al for clusters modelled in vacuum and Si-Al-Si-Al-Si using the COSMO model. When the Al atoms (which are negative with respect to the silicon framework) are situated at the ends of the chain, they are able to envelop the barium cation in order to get close coordination, as shown previously be Figure 6. 13(d), this appears to be sterically more difficult when the Al atoms reside within the chain. The maximisation of coordination between the aluminium atoms and the barium cation balances the negative charge on the aluminium and results in the stabilisation of the cluster. However, when the COSMO model is implemented the cluster minimises into a more dense structure, and so the positioning the aluminium within the chain rather than the ends still allows a strong coordination between the aluminium atoms and barium cation.

Using the total energies of each fragment the energy of condensation for each cluster can be calculated and subsequently the mechanistic pathway for the formation of each cluster in solution can be inferred. Before analysing the results one should note that during the crystallisation process fragments are constantly forming and dissolving in solution. However, the aim of this study is to deduce the mechanism of a natural zeolite, thus unlike laboratory synthesis which is usually carried out on a short time scale (*i.e.* a number of hours to a few months), on a geological timescale the zeolite may take hundreds of years to form. As a result the concentration of a given fragment in solution is likely to have achieved a near steady state.

A number of factors can affect can affect the rate at which oligomeric units will condense or dissolute in solution, such as the concentration or availability of precursor fragments, the number of species involved in a reaction, and the free-energy barrier between reactants and products. In this research only static calculations have been performed on clusters, as a result this study is unable cannot comment on the kinetic effects on the formation of clusters, however, general kinetic factors can be applied to this study. For instance, the accessible energy barrier heights are assumed to be equal to kT, and given the high temperature at which zeolite synthesis takes place (possibly in excess of 500K), the accessible energy barrier will be high. For these condensation reactions it is likely that the barrier heights are similar, consequently differences of just a few $kJmol^{-1}$ will result in condensation rates that differ by orders of magnitude. To create a model to simulate a large number of clusters in solution, which can calculate energy barriers at a high level of theory such that energies of less than $1\text{-}2kJmol^{-1}$ can be differentiated is beyond the capability of this study.

Although information on the kinetics of the reactions is not available, the calculated thermodynamics of condensation can be used as an indicator of the presence of an oligomeric species in solution. Since this study involves the formation of a natural zeolite, the process considered evolves over a geological time scale, thus the attempted collisions between small units in solution would be large. It would also be expected that a reaction between two fragments which leads to the release of a high condensation energy, would simultaneously lead to a high barrier to dissolution. As a result fragments with high condensation energies are expected to have a high concentration in solution. Conversely, laboratory time scales are much shorter, as a result there will be a

fewer number of collisions between species, and the concentration of fragments may not have reached a steady state. Therefore it would be expected that the solution would contain a high concentration of fragments which are formed by crossing small barrier heights, and a much lower concentration of units which have a condensation high barrier height. Consequently one can imagine that the time scale of condensation energy dictates what product is formed and this may be a component of kinetically controlled growth.

The condensation energies for all possible mechanistic pathways of forming 5T fragments have been listed in Table 6. 25, along with the associated condensation energy per bond formed, or it may be thought of as the condensation energy per collision.

The greatest condensation energy for all silica and aluminosilicate 5T fragments occur for the condensation of five monomers to form the cluster, thus this mechanistic pathway appears to be the most thermodynamically favourable. However it is statistically unlikely that a simultaneous condensation of five monomeric units would occur to form either a chain or spiro structure. There have also been studies of zeolite growth[45,46] which have deduced that multinuclear fragments are important in growth, as a result it would not be expected for the growth mechanism to proceed by continuous addition of monomeric species. Analysis of the condensation energy per collision provides further evidence that the mechanism is not governed by condensation of monomer, this value reveals that the most thermodynamically stable condensation energy per collision is not associated with the fragment with the highest overall condensation energy.

The energy released per bond formation can also be interpreted as the energy barrier to dissolution of a fragment, thus the greater the energy released upon forming the bond to create a fragment, the larger the energy require to sever the fragment into smaller units. As a result, clusters which release a larger amount of energy on forming a bond will have a longer lifetime, and unless used within the crystallisation process, will be at a higher concentration in solution. Since the formation of natural zeolites would occur over a long time scale, there will be a high number of attempted collisions between

species in solution, thus the concentration of a particular fragment will be related to the energy released per bond formation, or energy released per successful collision

For simplicity only the skeleton backbone of each fragment is shown.

For *e.g.* Si-Al-Si = $(OH)_3Si\text{-}O\text{-}Al(OH)_2\text{-}O\text{-}Si(OH)_3$

Chain	Fragment Formed	Mechanistic Pathway	Condensation Energy	Condensation Energy/Collision
1	Si-Si-Si-Si-Si	5×Si	-0.4620	-0.1155
		3×Si + Si-Si	-0.3537	-0.1179
		Si +Si-Si-Si-Si	-0.0162	-0.0162
2	Si –Spiro	5×Si	-0.3693	-0.0616
		3×Si +Si-Si	-0.2610	-0.0522
		Si +2×Si-Si	-0.1527	-0.0382
		-Si-Si-Si-Si- +Si	-0.0690	-0.0345
		Si-Si-Si-Si + Si	0.0766	0.0255
		Si-Si-Si-Si-Si	0.0927	0.0464
3	Si-Si-Al-Si-Al	3×Si + 2×Al	-0.9728	-0.2432
	Si-Si-Al-Si-Al	Si-Si + Si + 2×Al	-0.8645	-0.2882
	Si-Si-Al-Si-Al	Al-Si-Al + 2×Si	-0.7810	-0.3905
	Si-Si-Al-Si-Al	Al-Si-Al + Si-Si	-0.6727	-0.6727
	Si-Si-Al-Si-Al	Al-Si-Al-Si + Si	-0.3675	-0.3675
4	Si-Al-Si-Al-Si	3×Si + 2×Al	-1.267	-0.317
	Si-Al-Si-Al-Si	Al-Si-Al + 2×Si	-1.058	-0.529
	Si-Al-Si-Al-Si	Al-Si-Al-Si + Si	-0.627	-0.627
5	Si-Al-Si-Si-Al	3×Si + 2×Al	-1.049	-0.262
	Si-Al-Si-Si-Al	Si-Si + Si + 2×Al	-0.907	-0.302
	Si-Al-Si-Si-Al	Al-Si-Si-Al + Si	-0.428	-0.428
6	Al-Si-Si-Si-Al	3×Si + 2×Al	-1.1427	-0.2857
	Al-Si-Si-Si-Al	Si-Si + Si + 2×Al	-1.0344	-0.3448
	Al-Si-Si-Si-Al	Si-Si-Si + 2×Al	-0.8178	-0.4089
7	Spiro	3×Si + 2×Al	-0.661	-0.110
	Spiro	Si-Si-Si + 2×Al	-0.285	-0.071
	Spiro	Al-Si-Al + 2×Si	-0.452	-0.113
	Spiro	Al-Si-Al + Si-Si	-0.310	-0.103
	Spiro	Si-Al-Si-Al (ring) + Si	-0.044	-0.022
	Spiro	Si-Si-Al-Si-Al	0.3629	0.1814

Table 6. 25: Formation of a $BaSi_3Al_2O_4(OH)_{12}$ species in different sequences.

Table 6. 25 demonstrates that the condensation energy released per collision is considerably lower for the spiro unit than for each of the linear chains, thus it would be expected that the spiro unit will have a low concentration in solution, this is true for both silicate and aluminosilicate clusters. A comparison of the condensation energies between the two spiro units and the chains illustrate that for both open and closed structures it is more favourable to form the aluminosilicate analogue of the cluster, this may be one of the reasons by siliceous EDI does not form naturally.

According to the total energy of the four 5T chains, all would form in solution, however the differences in energy show that the Si-Al-Si-Al-Si and Al-Si-Si-Si-Al sequence would be of highest concentration in solution, followed by the Si-Al-Si-Si-Al chain. If the concentration of growth fragments differs substantially, the frequency with which the clusters impinge upon the crystal surface will vary dramatically and on *short* time scales, this could lead to 'diffusion' limited growth. This analysis of growth rate shows that the number of bonds per unit area is the crucial to the crystal growth rate-limiting step, and therefore the mobility of solution species cannot therefore be critical on the geological time-scale. It is believed that these critical units which are important in growth of EDI, do preassemble in solution and then attach onto to the surface of this material, and so the availability of these preformed units in solution can alter the rate at which the four morphologically important faces form, hence defining the crystal habit.

The analysis above states that the spiro unit is likely to form at a slow rate, thus a lower concentration of this species will be available to attach onto the surface, resulting in the slow formation of a crystal face. In section 6.2.1 the spiro unit was identified as growth unit for the (1 1 0) face, and in chapter 4 the crystal morphology of EDI illustrates a large (1 1 0) faces, which occurs from a slow growing face, thus the energetics of the spiro cluster have been able to confirm that the spiro unit is the building unit for the (1 1 0) face.

Conversely section 6.2.2 illustrates how the fast growing (0 0 1) surface can be constructed from both Si-Al-Si-Al-Si and Al-Si-Si-Si-Al units, which according to the condensation energies are readily available in solution for attachment onto the growing surface. Lastly the (1 1 1) and $(1\,\bar{1}\,1)$ faces have a growth rate intermediate of the (1 1 0)

and (001) surface and constructed from Si-Al-Si-Si-Al units, equally the stability of this unit lies in-between the stability of the units which make up the (110) and (001) face.

6.5 Conclusion

From this investigation, fundamental building units from which each of the four morphologically important faces can be constructed have been proposed. Moreover, each unit was selected to be composed of $BaSi_3Al_2O_5$, the same constituents as one formula unit of EDI, with each layer containing two building units.

By carrying out DFT calculations on these 5T units, and smaller fragments have provided information on the energetic stability structural conformations of these clusters in vacuum and in water. Analysis of each structure was able to determine the extent of intra-molecular hydrogen bonding and also the acid sites for each structure. This research on silica clusters was able to predict configurations with bond lengths and angles which compared well with previous studies. However, within this work the intra-molecular hydrogen bonding did not appear to be overestimated, as was observed in previous studies based upon local density functionals. It was also found that chain clusters which have three or more silicon atoms are most stable when they adopt quasi ring structures, where the ring is closed by a hydrogen bond.

Investigation of acid sites within all silica clusters, with 1 to 5 T atoms, revealed that the strengths are all comparable, irrespective of cluster size; this is exemplified by similar charges residing on hydrogen and terminal oxygen atoms. Stronger acid sites were also found to be associated with hydrogen atoms which took part in intra-molecular hydrogen bonding.

By applying the same systematic approach to aluminosilicate clusters, the thermodynamic stability of each cluster was determined and the most stable conformations were predicted. As with silica clusters, all bond angles and lengths were calculated and were found to be comparable to silicate clusters. Comparison with silica clusters highlighted differences; aluminosilicate clusters do not minimise in configurations which form quasi rings, this is due to the presence of the barium cation. In silica clusters, hydrogen bonds are formed between the two ends of the chain,

however in aluminosilicate clusters the barium cation distorts the structure, such that the terminal oxygen atoms bonded to aluminium are attracted to the barium, and the hydrogen atoms are repelled away. It is found that both the silicate and aluminosilicate clusters with a larger number of T atoms are more stable, *i.e.* the larger fragments have a lower energy per T atom. This is expected, since the size of cluster will converge on the bulk crystal. The condensation energy of all T chains with respect to their monomer units are similar, therefore the thermodynamics suggests that all fragments will be present in solution. However, no information on the barrier heights of formation in solution can be concluded.

Analysis of the energy difference between open and closed clusters reveal that open chain structures are more thermodynamically stable than closed ring and spiro structures; this is most likely due to the large amount of strain involved in forming a small ring. Chain structures have conformational flexibility, *i.e.* they have many nodes of rotation and by doing so are able to remove strain from the structure, however ring structures are unable to rotate, they are only able to remove stress by bending, however this also has a domino effect on other atoms within the cluster. Therefore the closed structures will always contain some strain in comparison the open clusters with the same number of T atoms.

Determination of the charge density of aluminosilicate clusters show that in clusters where intra-molecular hydrogen bonding exists, as with silica clusters, the strongest acid sites resides of the hydrogen atoms which take part in hydrogen bonding. However in cases where no intra-molecular hydrogen bonding exists, the strongest acid sites are associated with hydrogen atoms furthest away from the barium cation.

Minimisation of all clusters with implicit water appears not to effect the conformation of clusters with a small number of T atoms, however when there are 5T atoms within the fragment a difference is observed in the outline of the cluster. The 5T aluminosilicate chains appeared to condense from structures which had an elongated outline to a more spherical topology, this has the effect of reducing the surface area, and more importantly in the case of EDI growth, reduces the number of solvent accessible hydroxyl groups. A reduction in the number of hydroxyl groups on the surface of a cluster, reduces the number of sites on the cluster which can attach onto the growing

surface, which reduces the probability of the cluster attaching onto the surface. To determine whether this is a result of the presence of using implicit solvation schemes, these calculations should be repeated in the presence of explicit waters.

It is difficult to examine the absolute stability of each fragment, however examination of the total energies highlight that the larger the cluster the more stable the cluster, it also shows that the aluminosilicate clusters appear to be more stable than the equivalent silica cluster. A comparison between the four and five T chains illustrate that there is a very small energy difference between the chains which have aluminium atoms at different positions, as a result chains which have aluminium atoms in all sequences would be expected in solution. This might lead to local density of aluminium atoms (zoning) within a crystal, the effect of zoning has been observed experimentally.

Calculation of condensation energies and the condensation energy per collision has illustrated potential mechanistic pathways for the formation of each cluster. It is clear that the clusters are not formed by the spontaneous condensation of monomeric species, rather a stepwise process of multinuclear condensation take place. By investigating various mechanistic pathways of forming 5T clusters, as expected, it is deduced that the chain structures are formed more easily than spiro units. Comparison between different 5T units show that there is only a small difference in energy between 5T chains, however over a long time scale, the small difference in energy is expected to change their concentration in solution.

The rate limiting step in the growth of EDI is the related to the formation of bonds at key sites on the surface of each face, thus the crucial fragment in the growth of each face preassembles in solution and attaches onto the growth surface, as a result EDI crystallises *via* a surface (terrace) nucleation limited process. The thermodynamics states that all 1 to 5T clusters are stable in solution, and the surface structure dictates which bonds determine the rate of growth. These factors suggests that the (110) surface grows *via* the attachment of spiro units, since the surface structure (and N_{BB}/SA assessment) indicates that only two bonds may be formed. However, the remaining three faces have eight sites of attachment, and so growth may proceed by the attachment of monomer to pentamer units.

The rate of formation according to the thermodynamic stability of each 5T cluster, and the energy per collision is consistent with the rate of growth of each face. The Al-Si-Si-Si-Al and Si-Al-Si-Al-Si chains are proposed to be the fastest forming units, whereas the spiro is the slowest forming. Therefore the rapidly growing (001) face has a high concentration of Al-Si-Si-Si-Al and Si-Al-Si-Al-Si available for growth. On the other hand the slow growing (110) has a very low concentration of spiro units in solution, however since EDI crystallised over a geological time scale, the (110) surface will growth and appear dominant overall.

REFERENCES

1 M. Ebelmen. *Ann. Chimie Phys.* **16**, 129 (1846)

2 M. Ebelmen. *Acad. Sci.* **25**, 845 (1847)

3 T. Graham. *J. Chem. Soc.* **17**, 318 (1864)

4 R. E. Liesegang. *Photogr. Archiv.* (1896)

5 D. M. Roy and R. Roy. *American Mineralogist* **89**, 957 (1954)

6 R. Roy. *J. Am. Ceram. Soc.* **39**, 145 (1956)

7 R. Roy. *J. Am. Ceram. Soc.* **52**, 344 (1969)

8 G. J. McCarthy, R. Roy and J. M. McKay. *J. Am. Ceram. Soc.* **54**, 637 (1971)

9 L. L. Hench and J. K. West. *Chem. Rev.* **90**, 33 (1990)

10 R. M. Barrer. *Hydrothermal chemistry of zeolites* (Academic Press, London, 1982)

11 C. J. Brinker and G. W. Scherer. *Sol-gel science, the physics and chemistry of sol-gel processing.* (Academic Press, New York, 1989)

12 R. M. Barrer, J. W. Baynham, F. W. Bultitude and W. M. Meier. *J. Chem. Soc.* (1959)

13 R. K. Harris and C. T. G. Knight. *J. Mol. Struct.* **78**, 273 (1982)

14 R. K. Harris and C. T. G. Knight. *Journal of the Chemical Society-Faraday Transactions Ii* **79**, 1525 (1983)

15 R. K. Harris and C. T. G. Knight. *Journal of the Chemical Society-Faraday Transactions Ii* **79**, 1539 (1983)

16 G. Engelhardt and D. Hoebbel. *Zeitschrift Fur Chemie* **23**, 33 (1983)

17 G. Engelhardt and O. Rademacher. *J. Mol. Liq.* **27**, 125 (1984)

18 R. Ravishankar, C. E. A. Kirschhock, P. P. Knops-Gerrits, E. J. P. Feijen, P. J. Grobet, P. Vanoppen, F. C. De Schryver, G. Miehe, H. Fuess, B. J. Schoeman, P. A. Jacobs and J. A. Martens. *J. Phys. Chem. B* **103**, 4960 (1999)

19 C. E. A. Kirschhock, R. Ravishankar, F. Verspeurt, P. J. Grobet, P. A. Jacobs and J. A. Martens. *J. Phys. Chem. B* **103**, 4965 (1999)

20 C. E. A. Kirschhock, R. Ravishankar, L. Van Looveren, P. A. Jacobs and J. A. Martens. *J. Phys. Chem. B* **103**, 4972 (1999)

21 C. T. G. Knight and S. D. Kinrade. *J. Phys. Chem. B* **106**, 3329 (2002)

22 H. Ramanan, E. Kokkoli and M. Tsapatsis. *Angew. Chem. Int. Ed.* **43**, 4558 (2004)

23 B. Bussemer, K.-P. Schroder and J. Sauer. *Solid State Nuclear Magnetic Resonance* **9**, 155 (1997)

24 J. Sauer. *Chem. Rev.* **89**, 199 (1989)

25 C. R. A. Catlow, D. S. Coombes and J. C. G. Pereira. *Chem. Mat.* **10**, 3249 (1998)

26 Cerius^2. (Accelrys Inc., San Diego).

27 A. K. Rappe, C. J. Casewit, K. S. Colwell, W. A. Goddard-III and W. M. Skiff. *J. Am. Chem. Soc.* **114**, 10024 (1992)

28 B. Delley. *J. Chem. Phys.* **113**, 7756 (2000)

29 B. Delley. *Journal of Physical Chemistry* **91**, 508 (1990)

30 J. C. G. Pereira, C. R. A. Catlow and G. D. Price. *J. Phys. Chem. A* **103**, 3252 (1999)

31 J. C. G. Pereira, C. R. A. Catlow and G. D. Price. *J. Phys. Chem. A* **103**, 3268 (1999)

32 A. Klamt and G. Schuurmann. *J. Chem. Soc.-Perkin Trans. 2*, 799 (1993)

33 D. W. Lewis, R. G. Bell, P. A. Wright, C. R. A. Catlow and J. M. Thomas. in *Progress in zeolite and microporous materials, pts a-c* 2291 (1997).

34 J. C. G. Pereira, C. R. A. Catlow, G. D. Price and R. M. Almeida. *J. Sol-Gel Sci. Technol.* **8**, 55 (1997)

35 J. C. G. Pereira, C. R. A. Catlow and G. D. Price. *Chem. Commun.*, 1387 (1998)

36 F. Jensen. in *Introduction to computational chemistry* 53 (Wiley, 1999).

37 J. C. G. Pereira. in *Geological Sciences* (University College London, 1997).

38 U. von Barth and L. Hedin. *J. Phys. C.: Solid State Phys.* **5**, 1629 (1972)

39 L. Hedin and B. I. Lundqvist. *J. Phys. C.: Solid State Phys.* **4**, 2064 (1971)

40 R. J. Moolenaar, J. C. Evans and L. D. McKeever. *J. Phys. Chem.* **74**, 3629 (1970)

41 T. W. Swaddle. *Coordination Chemistry Reviews* **219-221**, 665 (2001)

42 W. Lowenstein. *American Mineralogist* **39**, 92 (1854)

43 C. R. A. Catlow, A. R. George and C. M. Freeman. *Chem. Commun.*, 1311 (1996)

44 E. Dempsey, G. H. Kuhl and D. H. Olson. *Journal of Physical Chemistry* **73**, 387 (1969)

45 J. R. Agger, N. Pervaiz, A. K. Cheetham and M. W. Anderson. *J. Am. Chem. Soc.* **120**, 10754 (1998)

46 B. Slater, C. R. A. Catlow, Z. Liu, T. Ohsuna, O. Terasaki and M. A. Camblor. *Angewandte Chemie-International Edition* **41**, 1235 (2002)

CHAPTER SEVEN

CONCLUSIONS AND FUTURE WORK

7.0 AIMS

As stated at the beginning of this thesis, the two main aims of this study were to (i) predict and characterise the surface structure, and (ii) obtain an insight into the fundamental processes of crystal growth. These objectives have been achieved by carrying out a systematic study on a simple zeolite EDI, which has a defined crystal structure and ordered aluminium sites, with a silicon to aluminium ratio of 3:2.

7.1 Surface structure predictions

In chapter four, classical methods were used to deduce the surface structure of EDI. Initially, it was firstly important to produce an accurate model of the bulk structure. The siliceous EDI and hydrated aluminosilicate EDI models reproduced the bulk structure of natural EDI accurately with the potentials used, since the bond lengths, bond angles and cell parameters all compare very well to that found experimentally. However since siliceous EDI has not been made in the laboratory or found occurring naturally, a favourable comparison with *ab initio* calculation by Civalleri *et al.*[1,2] was made. Consequently the results of the bulk geometry optimisation calculations can be considered as reliable given the agreement with experiment, and siliceous EDI (from *ab-initio* calculations), despite the dearth of experimental evidence.

It was found that by treating natural EDI, which contains framework aluminium, silicon and oxygen, extra framework cations, and molecular water within the unit cell as a siliceous framework, the bulk and surface properties can be predicted and understood. For both siliceous and hydrated aluminosilicate EDI the same surface structure or termination for each face were found, exhibiting the same density of under-saturated bonds, suggesting that the framework structure is important rather than the chemical constituents in dictating the terminating surface structure.

Assessment of the surface energies reveals the same order of stability of the different faces as found experimentally, which implies that the relative thermodynamic stability of the surface structures is an ingredient in determining the relative crystal growth rate. Calculating surface energies has also highlighted that lowest surface energy is associated with a cut that minimises the number of broken bonds, *i.e.* a surface which contains the least number of under-saturated sites.

Neither the inter-layer spacing or attachment energies appear to correlate in any way to rate of growth and consequently the crystal morphology; indicating that inter-layer spacing and attachment energies are not reliable schemes for assessing growth rates. The attachment energy places importance upon the strength of binding of layers to each other. The fact that it is necessary to calculate the total energetics of the system correctly using the surface energy suggests that the energy of the constituents within each layer are important in determining the growth rate of EDI, as opposed to growth proceeding by complete layers forming in solution and attaching on to each face. In this case, each layer consists of a network of spiro units. Since evaluating the strength of bonding between each unit and the layer is clearly important, this may be evidence that growth proceeds *via* a TLK mechanism rather than layer upon layer.

Calculations from both the siliceous and hydrated aluminosilicate EDI surfaces have shown that the (110) surface is the most dominant in the predicted and observed morphology and is hydroxylated. The (001), (111) and $(1\bar{1}1)$ faces are not hydroxylated and show less importance in the morphology. The form of the morphology is consistent with what one might expect given that synthesis is undertaken under aqueous and hence polar conditions. The sides of the crystal are relatively hydrophilic and hydroxylated, the cap of the crystal is relatively hydrophobic and unhydroxylated, and this also highlights the different reactivity observed for different faces of the same crystal.

In the case of purely siliceous EDI, qualitatively an excellent correspondence was found between experimental and theoretical predictions of morphology, based on a surface energy assessment. With similar aspect ratios to those observed experimentally, this suggests that the surface structures are correct and surface energetics are also valid. This indicates that we can determine many growth related properties of EDI by

considering the siliceous analogue only, and also indicates that the aluminium, extra framework cations and water do not play a role in determining the correct aspect ratio. Calculating surface energies has also shown that the order of thermodynamic stability of each face can be correlated to the rate of growth of each face (*i.e.* the aspect ratio of each face).

Initial predictions of hydrated aluminosilicate EDI found the faces to be in the correct order of stability, however the energy of (001) face was found to be too high. The origin of the instability within the surface was found to be due to an under-coordinated barium cation on the surface. The coordination number of the barium cation was fulfilled by the addition of a layer of water on top of the surface, this stabilised the surface and stopped the unfavourable distortion of the surface framework. By using the surface energy of the (001) face with an additional layer of water creates a smaller aspect ratio between the (001) face and the other three faces of EDI, and so the (001) face is observed in the predicted equilibrium morphology.

Preliminary work, which has not been presented here, of placing between one and three layers of molecular water on to each morphologically important face has shown a further stabilisation in energy. By systematically removing each water molecule consecutively, starting with the oxygen coordinate that is furthest away from the surface, the binding energy of each water molecule shows that on each face at least eight molecules can be added to release energy of greater than $40kJmol^{-1}$.* As a result, each face is predicted to be thermodynamically more stable with the addition of at least one layer of water.

Quantitative analysis of the predicted equilibrium morphology of both siliceous and hydrated aluminosilicate morphology has shown a disparity between the growth rate predicted by surface energy and that calculated from the natural crystal. By investigating which factors affect the growth rate, it was found that the density of under-coordinated sites on each face plays a determining role. Predicting the morphology by calculating the number of broken bonds on creating the surface per surface area (N_{BB}/SA) for each face, produces an excellent reproduction of the growth rate, with

* $40kJmol^{-1}$ is the standard enthaply of vapourisation of a water molecule.

errors less than 0.05%. This new N_{BB}/SA method suggests that by simply calculating the density of broken bonds the growth rate may be predicted. More importantly, this method also implies that there are key sites on each face, which determines the rate of crystal growth of each face and connect one layer with another.

Overall, from the results presented in chapter four we have determined that surface structure properties of this natural high density zeolite can be readily understood by considering the siliceous analogue and that the relative growth rates of those surfaces are apparently insensitive to the aluminium and water content. We find that interlayer spacing is in no meaningful way correlated with morphological importance. However, direct assessment of the relaxed surface energies gives an accurate way of assessing the morphological importance of each face. More surprisingly a new N_{BB}/SA method has been found which reproduces the relative growth rate with great accuracy, also by determining the growth rate by this method allows an insight into the mechanism of growth, implying that there are crucial points of attachment which influence the rate of growth.

As stated above, some work has been carried out on hydrating the surface of the crystal, however equally it is important to determine the effects of dehydrating the structure. Bulk and surface calculations (which have not been presented here) have been carried out on the dehydrated aluminosilicate EDI. The predicted morphology exhibited only two faces, and therefore was not comparable with the experimental morphology. However, this finding does provide evidence that water will escape at different rates from facetted crystals and the interesting possibility that faces may 'boil' at different temperatures. Work carried out on the systematic dehydration of hydrated aluminosilicate EDI has shown that there are preferential sites within the crystal where water may be lost, before a major change in the framework is observed. It would be beneficial to complete this systematic study on the hydration and dehydration of EDI, by doing so will allow a full analysis of the effects of water on the crystal, which will ultimately assist in discovering the effects of water on the mechanism of growth.

It would also be extremely useful to use periodic *ab initio* methods to determine the surface energy and the chemical composition of each surface structure. Some initial studies have been carried out on the (110) face and it has been concluded that the

positions of hydrogen atoms have not been accurately predicted. It is found that that the TOH angle is too large (by ~20°), this highlights that for future work it would be beneficial parameterise a new hydroxyl potential for external zeolite surfaces.

7.2 Number of broken bonds per surface area predictions

In chapter five, tests on a range of zeolites were carried out to determine to applicability of the N_{BB}/SA method. A full systematic surface energy analysis of MER predicted both morphologically important faces, with the (110) surface most stable in its hydrated form, and the (111) is most stable when unhydroxylated. The equilibrium morphology of MER displayed both faces, although the aspect ratios were not in agreement with natural crystals. The N_{BB}/SA method was also able to reproduce the crystal morphology, however qualitative analysis illustrated the aspect ratios of each face were in far better agreement than the morphology prediction using surface energies. This implies that the growth rate of each face of MER is also dependent upon the density of under-saturated bonds on the surface. The findings from both surface energy and N_{BB}/SA methods are correlated, which may suggest that MER is crystallised at a high supersaturation level.

A complete surface energy analysis was also carried out on ANA, which has two morphologically important faces. In this case the surface energy analysis predicted both surfaces to be more stable in their unhydroxylated form. As with previous cases there was a disparity between morphology predictions using surface energies and N_{BB}/SA. Surface energies predicted a dominant (211) face, where as N_{BB}/SA predicted a dominant (100) face, in this case both predictions are 'correct', since there are an array of crystal habits exhibited in natural crystals, all exposing the (211) and (100) face, ranging from a dominant (211) and minor (100) to dominant (100) to minor (211). The occurrence of a range of crystals must be a direct result of a change in conditions which can affect the composition of units in solution, which essentially alters the growth rate of each face. Another important factor which can alter the rate of growth of a crystal, especially where there is a disparity in the area of surface accessible sites is the supersaturation level. Where there is a low supersaturation level it is suggested that the number of fragments which diffuse onto the surface and collide onto accessible surface

sites is low. Therefore for the (100) surface, where the density of accessible surface sites is lower than the (211) surface, the rate of growth will be much slower, and the (100) surface will become more dominant in the morphology. Hence, consideration of supersaturation levels suggests that the synthetic ANA crystal is grown under low supersaturation levels, whereas the natural crystal is inferred to have grown under high supersaturation levels.

The latter half of chapter five tested only the N_{BB}/SA method on four different zeolites, this test highlighted the versatility of this technique. By using the N_{BB}/SA method, the growth rate of each face of natrolite, zeolite A and thomsonite was predicted, and the crystal habit of natrolite and zeolite A was reproduced. In the case of thomsonite, where there are minor faces that have a very small surface area, the relative growth rate tends to be very sensitive, and so even small changes in the relative growth rates can lead to the extinction of crystal faces from the crystal habit prediction.

LAU was also tested with the N_{BB}/SA method, however in this particular case the N_{BB}/SA technique was unable to predict the relative growth rate of each face and the crystal habit. The error most likely lies in the determination of the most stable surface structure, here it is assumed that the most stable surface structure is the cut which severs the least number of bonds. However, the surfaces of LAU are very complicated, and there are many cuts with very similar number of broken bonds. Therefore, it may be that a cut which results in the breakage of a slightly larger number of bonds which subsequently relaxes into a more thermodynamically stable configuration. This suggestion could be tested by carrying out a full surface energy analysis on LAU.

Overall, the most important finding from the work of chapter five is that for most zeolites there appears to be key sites of attachment on the surfaces of zeolites, and it is the attachment of oligomeric fragments from solution to these binding sites which is the rate determining step in the growth of zeolites. This event is equivalent to terrace nucleation on the surface of a *Kossel* crystal, as discussed in chapter 2.

Within this study, tests of the N_{BB}/SA method have been carried out on zeolites which belong to the fibrous, singly connect four ring, and doubly connected four ring groups,

however to complete a fully analysis of this technique it will be useful to apply this method to zeolites in the mordenite and heulandite group, and also synthetic zeolites.

7.3 Study of silicate and aluminosilicate fragments.

In chapter six the surface structure of the four morphologically important faces of EDI were examined, it was found that for each face a cluster with composition $BaSi_3Al_2O_4$ could be tessellated from the bulk to the surface termination. On the (110) face the cluster was arranged in a spiro conformation, and on the remaining three faces the fragments were assembled as linear chains with aluminium atoms located at different positions on the chain. By carrying out DFT cluster calculations on these units and all smaller monomer and oligomeric units, the stability of these clusters in vacuum and in water, using the COSMO model, was deduced.

All structural properties of the silica clusters are consistent with findings from previous literature. In the case of aluminosilicate clusters, where there is no literature to compare with, all structural properties were found to give values which are similar to the silica fragments in this study. Intra-molecular hydrogen bonding has also been predicted, without any severe increase in the bond length of the acceptor OH group. Therefore the hydrogen bond lengths predicted in this study are not expected to be overestimated, as was found by local density approximation calculations in previous studies.[3-5] A general trend is found between the strength of the acid sites found within each cluster and hydrogen bonding, the hydrogen atoms involved in intra-molecular hydrogen bonding are associated with the strongest acid sites in the cluster. In a selection of aluminosilicate clusters, where no intra-molecular hydrogen bonding exists, the strongest acid sites are associated with hydrogen atoms furthest away from the barium cations, this is a direct result of the negative charge being drawn towards the barium, and leaving a strong positive charge at a point furthest away.

The self energy of all clusters minimised in solution were found to be more stable than those minimised in vacuum, it was also concluded that the self energy of a fragment increased with the addition of T atoms, hence the 5T clusters were the most thermodynamically stable. In addition the relative stability of each cluster increased

with the number of T atoms, therefore there is no thermodynamic reason why the 5T cluster would not form in solution.

To determine the manner in which each 5T fragment was formed in solution, the condensation energy of all possible ways (taking Lowenstein's rule into account) of forming each fragment was calculated, this suggested that the most favourable manner of forming each fragment was by condensation of five monomeric fragments, however previous work has suggested this to be inaccurate. A more chemically meaningful quantity was to calculate the condensation energy per collision/bond formed, this suggests a preferred thermodynamic mechanistic pathway for the formation of each fragment. A high condensation energy per collision also implies that there will be a high energy of dissolution, hence the bond/fragment is unlikely to dissociate into substituent fragments.

By analysing the total energy of each fragment, along with the condensation energy per collision, a prediction of how energetically favourable the formation of each 5T fragment was determined. The 5T chain structures are found to be more thermodynamically stable than the spiro unit, and the condensation energy per collision also highlights that it is more energetically favourable to create open chains compared to closed spiro units. This also appears to correspond to the rate of growth for each morphologically important face. It would be expected that the spiro unit, which is recognised as the growth fragment for the slow growing (110) surface, forms over a long period of time since the gain from forming each bond is low. Conversely the linear chains, which have a higher energy gain from forming each bond, condense faster in solution and are predicted as the growth units for the three remaining faster growing faces.

It is unclear whether the initial formation of EDI forms *via* homogeneous or heterogeneous nucleation (as discussed in chapter 2 section 2.1), since there is no experimental evidence of the initial steps of nucleation for EDI. EDI is a naturally occurring crystal, and so there is equal possibility that the initial steps of nucleation will occur by homogeneous nucleation where only the atomic constituents of EDI assemble or *via* heterogeneous nucleation where an external substrate exists in the crystallising solution and acts as a seed for EDI to nucleation up on. However it can be deduced, that

in the later stages of growth once an ordered crystal has been formed, multiple nucleation points may exist on the crystal faces, examples of multiple nucleation point have been observes experimentally on zeolite A.[6] The occurrence of several nucleation points on the face of a growing crystal may be considered as heterogeneous nucleation since the ordered crystal is thought of as the substrate. In order to determine what occurs at the initial stages of nucleation it would require simulating the correct composition of the gel in which nucleation takes place, along with the correct temperature and alkaline conditions, both of which is currently unknown for EDI.

This work may be advanced by modelling the aggregation of clusters *via* Monte Carlo methods. It would also be useful to use simulated annealing techniques to generate multiple positions for the barium cation with respect to the cluster, this will present a more accurate method of sampling all cation positions around a fragment. These methods can also be utilised to determine accurate starting positions for explicit water in hydrated state. This investigation would also reveal the extent of intra- and inter-molecular hydrogen bonding in solution fragments.

It will also be useful to work out the energy of charged clusters, this will allow a more detailed analysis of determining the mechanistic pathway of the formation of growth fragments. To assess to influence of the operating conditions at which zeolite growth takes place, it would also be useful to carry out all these simulations at a range on temperatures and pH levels. Before pH levels of clusters can be modelled accurately, it will be essential to parameterise a suitable set of potentials for water that will allow bond breaking between hydrogen and oxygen atoms.

Overall this study has been successful in meeting its aims, stable surface structures of EDI, ANA and MER have been calculated, and crystal habits have been deduced. A new simple method that predicts crystal morphology by examining density of broken bonds on the surface has been suggested. The versatility of the new N_{BB}/SA method has been tested on a range on zeolites, and has succeeded in predicting crystal habits for a range of zeolites. Atomistic and *ab initio* methods have also been successful in predicting the conformation and determining self energies on a range of silicate and aluminosilicate structures, which has provided an insight into the growth mechanism of the natural zeolite EDI. The systematic approach used throughout this research can

easily be adapted to predict the surface structure and identify key growth fragments of other zeolites with more complicated framework structures.

REFERENCE

1 B. Civalleri, S. Casassa, E. Garrone, C. Pisani and P. Ugliengo. *J. Phys. Chem. B* **103**, 2165 (1999)

2 P. Ugliengo, B. Civalleri, R. Dovesi and C. M. Zicovich-Wilson. *PCCP Phys. Chem. Chem. Phys.* **1**, 545 (1999)

3 C. R. A. Catlow, D. S. Coombes and J. C. G. Pereira. *Chem. Mat.* **10**, 3249 (1998)

4 J. C. G. Pereira, C. R. A. Catlow and G. D. Price. *J. Phys. Chem. A* **103**, 3252 (1999)

5 J. C. G. Pereira, C. R. A. Catlow and G. D. Price. *J. Phys. Chem. A* **103**, 3268 (1999)

6 S. Dumrul, S. Bazzana, J. Warzywoda, R. R. Biederman and A. Sacco Jr. *Microporous Mesoporous Mat.* **54**, 79 (2002)

APPENDIX A

A.1 Interatomic potentials

The model was based on formal charges with a shell model to represent the polarisability of the framework oxygen. The zeolite framework was described by parameters from Sanders *et al.*[1] This set of parameters has been used effectively to reproduce the zeolite framework in many other studies, as described in chapter 3, section 3.4. The partial charge parameters for the hydroxyl groups were fitted for bridging hydroxyl groups in zeolitic catalysts by Schröder *et al.*[2], the formal charge water model is described by de Leeuw *et al.*[3] and the barium was fitted in this study, details of which are described in the following section. The potential parameters used in these calculations have been tabulated below.

In all of the tables O_{zeo} represents the oxygen within the zeolite framework, O_{hyd} denotes the hydroxyl oxygen, H_{hyd} stands for the hydroxyl hydrogen, O_{wat} represents the water oxygen and H_{wat} corresponds to the water hydrogen.

Ions	Charges		Core –Shell
	Core (e)	Shell (e)	Interaction (eV Å^{-2})
Si	+4.000		
Al	+3.000		
O_{zeo}	+0.860	-2.860	74.9200
Ba	+2.000		
O_{hyd}	-1.426		
H_{hyd}	+0.426		
O_{wat}	+1.25	-2.05	209.4500
H_{wat}	+0.4		

Table A 1: Table of charges

Buckingham potential	A(eV)	ρ(Å)	C(eVÅ)
$Si\text{-}O_{zeo}$	1283.9070	0.3205	10.6616
$Si\text{-}O_{hyd}$	1283.9070	0.3205	10.6616
$Al\text{-}O_{zeo}$	1460.3000	0.2991	0.0000
$Al\text{-}O_{hyd}$	1460.3000	0.2991	0.0000
$Ba\text{-}O_{hyd}$	931.7000	0.3949	0.0000
$Ba\text{-}O_{hyd}$	931.7000	0.3949	0.0000
$O_{zeo}\text{-}O_{zeo}$	22764.0000	0.1490	27.8800
$O_{zeo}\text{-}O_{hyd}$	22764.0000	0.1490	27.8800
$O_{hyd}\text{-}O_{hyd}$	22764.0000	0.1490	27.8800
$O_{zeo}\text{-}H_{hyd}$	311.9700	0.2500	0.0000
$O_{zeo}\text{-}O_{wat}$	22764.0000	0.1490	28.9200
$Al\text{-}O_{wat}$	1460.3000	0.2991	0.0000
$Si\text{-}O_{wat}$	1283.9070	0.3205	10.6600
$Ba\text{-}O_{wat}$	931.7000	0.3373	0.0000
$H_{wat}\text{-}O_{zeo}$	311.9700	0.2500	0.0000
$H_{wat}\text{-}O_{wat}$	396.2700	0.2500	10.0000
$O_{hyd}\text{-}H_{wat}$	311.9700	0.2500	0.0000
$O_{hyd}\text{-}O_{wat}$	22764.3000	0.1490	27.8710
$O_{wat}\text{-}H_{hyd}$	311.9700	0.2500	0.0000

Table A 2: Buckingham potential parameters

Intermolecular Buckingham potential	A(eV)	ρ(Å)	C(eVÅ)
$O_{hyd}\text{-}H_{hyd}$	311.9700	0.2500	0.0000

Table A 3: Interatomic Buckingham potential parameters

Morse potential	D(eV)	$\alpha(Å^{-1})$	$r_0(Å)$
$O_{hyd}\text{-}H_{hyd}$	7.0525	2.1986	0.9485
$H_{wat}\text{-}O_{wat}$	6.2037	2.2200	0.9238

Table A 4: Morse potential parameters

Three-Body potential	k(eVrad-2)	Θ_0
O_{zeo}-Si-O_{zeo}	2.0972	109.4700
O_{zeo}-Si-O_{hyd}	2.0972	109.4700
O_{hyd}-Si-O_{hyd}	2.0972	109.4700
O_{zeo}-Al-O_{zeo}	2.0972	109.4700
O_{zeo}-Al-O_{hyd}	2.0972	109.4700
O_{hyd}-Al-O_{hyd}	2.0972	120.4700
Si-O_{hyd}-H_{hyd}	1.8920	116.8300
Al-O_{hyd}-H_{hyd}	1.8920	116.8300
H_{wat}-O_{wat}-H_{wat}	4.1998	108.6900

Table A 5: Three body potential parameters

Lennard Jones	A(eV $Å^{12}$)	B(eV$Å^6$)
O_{wat}-O_{wat}	39344.9800	42.1500

Table A 6: Lennard-Jones potential parameters

Coulomb Subtract	
O_{wat}-H_{wat}	50%
H_{wat}-H_{wat}	50%

Table A 7: Coulomb subtraction from potentials

A.2 Fitting the barium potential

To fit the barium-framework oxygen buckingham potential, the fit functionality on in the code GULP was utilised. Starting with the buckingham potential of a calcium-framework oxygen potential, all lattice parameters and other potential parameters where held fixed. The Buckingham potential was then parameterised to reproduce the experimentally characterised bulk crystal structure of EDI. The GULP code carries out this procedure by minimising the sum of squares by varying the potential parameters. The Newton-Raphson functional minimisation approach is utilised since to minimise the sum of squares since it avoids storing large matrices, however the downside is it does not eliminate near redundant variables. Ideally the sum of squares should minimise to zero however this is possible only for trivial cases, thus values close to zero

are acceptable, this parameterisation was able to reduce the sum of squares value to 0.0003eV.

REFERENCES

1 M. J. Sanders, M. Leslie and C. R. A. Catlow. *J. Chem. Soc. Chem. Commun.*, 1271 (1984)

2 K. P. Schroder, J. Sauer, M. Leslie, C. R. A. Catlow and J. M. Thomas. *Chem. Phys. Lett.* **188**, 320 (1992)

3 N. H. de Leeuw, G. W. Watson and S. C. Parker. *J. Chem. Soc.-Faraday Trans.* **92**, 2081 (1996)

APPENDIX B

B.1 Surface Energy Correction Terms

Since zeolites are usually synthesised in hydrothermal conditions it is necessary to assess whether the models of zeolite surfaces can undergo a reaction with water, the result of this process is that the surface becomes hydroxylated. In order to correct the thermodynamic stability of the surfaces the surface energies computed for each face have to be corrected for the number of water molecules dissociated on to the surface. This is done by use of the following equation:

$$\gamma(hkl) = \frac{E_d - (E_b + nE_{Corr})}{A} \tag{B. 1}$$

where E_d represents the total energy of the surface block with water dissociated onto the surface, E_b represents the total energy of the same number of bulk ions as that on the surface block (*i.e.* a surface which is not hydroxylated but has the same number of bulk ions), n is the number of hydroxyl groups, and E_{Corr} is the correction energy due to the presence of each hydroxyl groups.

In order to calculate the correction energy term two values are needed, firstly the self-energy for the formation of two hydroxyl groups and secondly the dissociation energy of water. The self-energy for the formation of two hydroxyl groups are taken to be $-1434.8138 kJmol^{-1}$, which is equivalent to the dissociation constant in the Morse potential used to represent the hydroxyl group. The dissociation energy of a water molecule is calculated to be the energy of dissociation for the following reaction:

$$H_2O_{(g)} + O^{2-}_{(g)} \rightarrow 2OH^{-}_{(g)} \tag{B. 2}$$

In order to get the correct value for the energy of dissociation of water the second electron affinity of oxygen is required. The value of the second electron affinity of oxygen is unique to the material of study, we are unable to determine this quantity theoretically, and so this work has used the value determined by calculations modelling

the surface of α-Quartz.[1] The value for the dissociation energy of water for this material is $-1155.9 kJmol^{-1}$. Using these values E_{Corr} is calculated to be:

$$E_{corr} = E_{Form} - E_{H_2O} \tag{B. 3}$$

where E_{Form} represents the energy of formation of two OH^- groups and E_{H_2O} represents the dissociation energy of a water molecule

Zeolites which contain both silicon and aluminium have hydroxyl groups attached to both silicon and aluminium atoms at the surface. In order to correct the surface energy for an aluminosilicate two different values are required for the energy of dissociation of a water molecule. For hydroxyl groups attached to a silicon atom, the same value can be used as mentioned above. However for hydroxyl groups attached to an aluminium atom the correction energy has been taken from a surface study on gibbsite.[2] As a result when correcting these surface energies both the number of water molecules dissociated onto the surface and the type of atom it is bonded to have to be taken into account.

B.2 Hydration Energy

In order to accurately calculate whether dissociative adsorption of water is an energetically favourable process, we must calculate the energy of hydration. If the energy of hydration is exothermic, hydroxylation of the surface is predicted, whereas if the energy of hydration is endothermic, the surface is predicted to be more stable in its unhydroxylated state. The reaction which takes place during hydration of the surface can be defined as following:

$$\text{Unhydroxylayed Surface} + \text{Water} \xrightarrow{\Delta E_{Hydration}} \text{Hydroxylated Surface}$$

The energy of hydration can not be determined directly by subtracting the total energy of reactants from the total energy of the products, since the oxygen atoms on the surface of the unhydroxylated surface have been represented by formal charges, whereas the

hydroxyl oxygens in the hydroxylated surface are modelled using partial charges, this change in charge has to be accounted for when determining the energy of hydration. The following Born-Haber cycle illustrates the alternative route taken to calculate the energy of hydration:

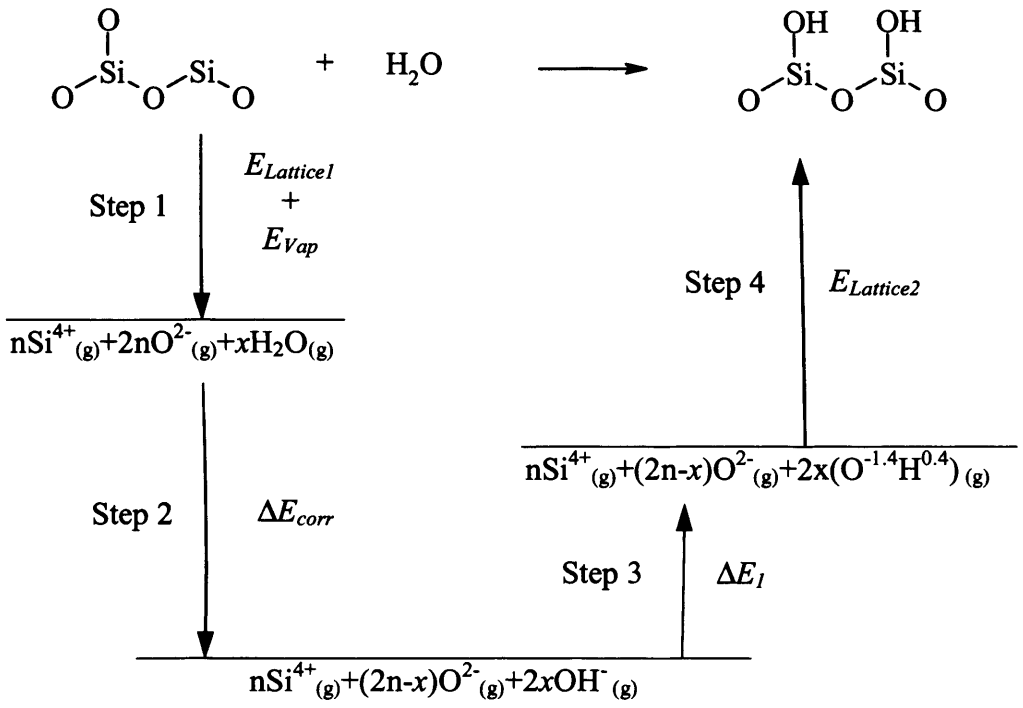

Figure B. 1: Born-Haber cycle used create an alternative route to calculate the energy of hydration.

Figure B. 1 illustrates that to calculate the hydration energy by the alternative route, four steps are necessary. Step 1 is the formation of gas ions from the unhydroxylated crystalline solid, *i.e.* the lattice enthalpy, plus the energy of vaporisation of the water. Step 2 is the energy of dissociation of water to form two hydroxyl groups as shown by equation (B. 2), this reaction energy has been previously defined as E_{corr} (see equation). Step 3 is the dissociation of the hydroxyl groups into gaseous ions with charges: $O^{-1.4}$ and $H^{0.4}$, this energy is the dissociation energy within the Morse potential used to describe the hydroxyl group. The final step, step 4, is the energy of forming a crystalline hydroxylated surface from gaseous ions, *i.e.* the negative of the lattice enthalpy.

REFERENCES

1 N. H. de Leeuw, F. M. Higgins and S. C. Parker. *J. Phys. Chem. B* **103**, 1270 (1999)

2 S. D. Fleming, A. L. Rohl, S. C. Parker and G. M. Parkinson. *Journal of Chemical Physics B* **105**, 5099 (2001)

APPENDIX C

C.1 Total energy of clusters

The following table lists the total energy of all clusters minimised at the DFT-PBE/DNP level of theory using the DMol^3 code. The first column lists the clusters, the third column is the minimised energy in vacuum and the last column is the total energy of the cluster modelled in water with the COSMO model.

		Total Energy (eV)	
	Composition	PBE/DNP	PBE/DNP+COSMO
Water	H_2O	-2078.4847	-2078.8006
Monomers			
S1	$Si(OH)_4$	-16128.2868	-16128.9756
S2	$Si(OH)_4$	-16128.3564	-16128.9925
2 x Al (*i.e.* A1 + A2)	$Ba[Al(OH)_4]_2$	-244284.7254	-244286.8125
Dimers			
Si-Si	$Si_2O(OH)_6$	-30178.3588	-30179.2927
Trimer			
Si-Si-Si	$Si_3O_2(OH)_8$	-44228.5587	-44229.7012
Al-Si-Al	$BaAlSi_2O_2(OH)_8$	-256256.3797	-256258.3957
Tetramer			
Si-Si-Si-Si	$Si_4O_3(OH)_{10}$	-58278.4343	-58280.0141
-Al-Si-Al-Si- (ring)	$BaAl_2Si_2O_3(OH)_8$	-268227.4500	-268230.1782
Al-Si-Al-Si	$BaAl_2Si_2O_3(OH)_{10}$	-270306.7901	-270309.0012
Al-Si-Si-Al	$BaAl_2Si_2O_3(OH)_{10}$	-270306.9125	-270308.9832

Total energy of pentamers have been included in main text, see chapter 6, Table 6.24

Table C. 1: Total energy of all clusters investigated, values given in eV. For simplicity only the skeleton backbone of each fragment is shown. For *e.g.* Si-Al-Si = $(OH)_3Si$-O-$Al(OH)_2$-O-$Si(OH)_3$

C.2 Pathway of formation of units

For completeness the following table has been included, which maps out all possible pathways (excluding Al-O-Al links) of forming a particular fragment, along with the associated condensation energy, and the condensation energy per bond formed.

Fragment Formed	Mechanistic Pathway	Condensation Energy	Condensation Energy / Bond
Si-Si	2×Si	-0.1083	-0.1083
Si-Si-Si	3×Si	-0.3249	-0.1624
Si-Si-Si	Si-Si + Si	-0.2165	-0.2165
Al-Si-Al	Si + 2×Al	-0.1919	-0.0959
Si-Si-Si-Si	4×Si	-0.4459	-0.1486
Si-Si-Si-Si	2×Si-Si	-0.2292	-0.2292
Si-Si-Si-Si	2×Si + Si-Si	-0.3376	-0.1688
-Si-Al-Si-Al- (ring)	2×Si + 2×Al	-0.5829	-0.1457
-Si-Al-Si-Al- (ring)	Al-Si-Al + Si	-0.3911	-0.1955
Al-Si-Al-Si	2×Si + 2×Al	-0.6054	-0.2018
Al-Si-Al-Si	Al-Si-Al + Si	-0.4135	-0.4135
Al-Si-Si-Al	2×Si + 2×Al	-0.5874	-0.1958
Al-Si-Si-Al	Si-Si + 2×Al	-0.4791	-0.2395

Table C. 2: Mechanistic pathway for the formation of clusters with one to four T atoms, the associated condensation energy and condensation energy per bond formed are given in eV.

As with the assessment of mechanistic pathways for 5T units in chapter 6, Table C. 2 shows that the most energy is gained from the condensation of monomer units, however as observed previously the condensation energy per bond highlights that that a higher energy gain can be achieved by a stepwise reaction rather than a spontaneous condensation of monomer units.